Identifying Ti-Cu-based alloys for biomedical applications

Libo Spotose

School of Chemical and Metallurgical Engineering,
University of the Witwatersrand, Johannesburg

A dissertation submitted to the Faculty of Engineering and the Built environment, University of the Witwatersrand, in fulfilment of the requirements for the degree of Masters of Science in Engineering.

December 2022

Declaration

I Libo Spotose declare that this dissertation is my own, unaided work. It is being submitted for the Degree of Masters of Science in Engineering at the University of the Witwatersrand, Johannesburg. It has not been submitted before for any degree or examination to any other university.

Date: 13 December 2022 Signature:

Abstract

Titanium alloys are widely-used in biomedicine for dental and orthopedic prosthesis implants, because of their good mechanical strength, biocompatibility and corrosion resistance. This work identified and made Ti-based alloys with similar phase proportions as Ti-6Al-4V, using Thermo-Calc. Beta-stabilisers are preferred as substitutional elements for Al and V since they give the good mechanical strength, biocompatible and corrosion resistance. For antibacterial properties, copper additions were made. Initially, calculations were done on phase proportions of chosen compositions, so that the two-phase proportions of Ti-6Al-4V were mimicked and different Cu additions were also calculated to determine how much Ti_2Cu would be formed.

Compositions with good phase proportions were selected for further work: Ti-6Ta-1.5Zr, Ti-6Ta-1.5Zr-0.2Ru, Ti-6Ta-1.5Zr-5Cu and Ti-6Ta-1.5Zr-0.2Ru-5Cu. Chemical analysis was done using SEM-EDX before etching; micrographs were obtained after etching with Kroll's reagent. X-ray diffraction, corrosion tests and hardness measurements were done on unetched samples. Microstructural and EDX analyses showed that Ti-6Ta-1.5Zr and Ti-6Ta-1.5Zr-0.2Ru alloys were two-phase. The Cu-containing alloys: Ti-6Ta-1.5Zr-5Cu and Ti-6Ta-1.5Zr-0.2Ru-5Cu had plate-like acicular α' martensite and retained β phase, with Ti_2Cu. The Ti-6Ta-1.5Zr alloy with coarse laths had low hardness, while Ti-6Ta-1.5Zr-0.2Ru and Ti-6Ta-1.5Zr-5Cu with fine laths had higher hardnesses, and Ti-6Ta-1.5Zr-0.2Ru-5Cu with plate-like phases had the highest hardness. In corrosion tests, the OCP vs time scans showed increasing passivation, while the potentiodynamic scans showed typical active-passive behaviour, shifting to the passive region, agreeing with OCP profiles. The OCP values did not reach stable potentials in a reasonable time, attributed to the α' metastable phase. The corrosion current densities of the alloys were similar. Corrosion rates were low and those of the Cu-containing alloys were similar to Ti-6Al-4V. The best alloys were Ti-6Ta-1.5Zr-5Cu and Ti-6Ta-1.5Zr-0.2Ru-5Cu, with the target phases α, β and Ti_2Cu and hardnesses comparable to reported Ti-6Al-4V and Ti-Cu alloys.

Acknowledgements

I would like to give a special thanks to the following people and organisations for their full support which made this work a success:

- My supervisor Prof. L.A. Cornish for continued and steadfast support and supervision. I would also extend my thanks for her constant guidance and making time to help me keep focus on this work. She has provided me with useful discussions which have helped a lot during this work. Her unwavering support has helped me with my personal and professional development.

- I would also like to extend my thanks to Prof. L.H. Chown, Dr M.O. Bodunrin and Prof. Susanne Norgren for their input in my project. To Prof. L.H. Chown, I appreciate your assiatance with the Thermo-Calc calculations, discussion and results. Dr M.O. Bodunrin gave advice and help in the laboratory.

- To the DSI-NRF Centre of Excellence in Strong Materials (CoE-SM) for financial support and funding this project. Prof. L.A. Cornish, thanks for organising funding, making this journey smooth and helping to make this work a success. I would also like to express my thanks to the African Materials Science and Engineering Network (AMSEN) for further funding. I appreciate Prof. L.A. Cornish for giving us as her students the opportunity to travel to the MSSA conference in Cape Town for the opportunity to network with other researchers.

- My sincere gratitude to Ms J. Jacobs and Mrs M. Labuschagne, I thank them for their support.

- I would like to extend my appreciation to Mintek, especially Ms Nomsombuluko Masia and Ms Melanie Smith for their assistance in performing my electrochemical tests, and Mr Edson Muhuma for assisting with the casting of my alloys.

- A special thanks to the staff members of the School of Chemical and Metallurgical Engineering, University of the Witwatersrand for providing with workplace, work equipment and laboratories which has all made valuable contribution to this work.

- A special thanks to my parents, Ms Z. Spotose and my grandma, Bangiwe Spotose for their emotional support and encouragement all through my masters. To the lovely daughter of my late sister, Lena Spotose, thank you so much for your love and support.

- To all my friends who have support me throughout my entire studies. Clinton M. Masemula, Kiyaasha Dyal Ukabhai, Percy Nthape Mphasha, Kgejepe Nape, Muzi Mavundla, Sibusiso Luthuli and Tandolwethu Manjezi.

Table of Contents

List of Figures ix

List of Tables xiv

List of abbreviations xv

1 Chapter 1: Introduction 1

1.1. Background of Ti and its alloys 1

1.2. Rationale of the Research 4

1.3. Problem statement 6

1.4. Aims and Objectives of the Research 6

1.5. Scope of the dissertation 7

2 Chapter 2: Literature Review 8

2.5. Overview of titanium and its alloys 8

2.1.1. The production of titanium 8

2.1.2. Phases in titanium 9

2.1.3. Classification of titanium alloys and general properties 10

2.1.4. Mechanical properties of Ti alloys 11

2.1.5. Effect of cooling rate on microstructure of titanium and its alloys 16

2.1.7. Effect of Interstitials or Impurities in Ti and its Alloys 23

2.1.8. Corrosion of Ti alloys 27

2.1.9. Application of titanium and its alloys 31

2.2. Titanium alloys in dental and orthopedic application 33

2.2.1. Importance of modulus of elasticity in implant materials 34

2.2.2. Biocompatibility and corrosion of titanium 36

2.2.3. Osseointegration 38

2.2.4. Effect of beta-stabiliser additions on implant materials 41

2.2.5. Copper additions and antibacterial Ti alloys 43

2.3. Summary of literature review and rationale of the project 51

3 Chapter 3: Experimental Procedure 53

3.1. Thermo-Calc Calculations 53

3.2. Alloy Manufacture 53
3.2.1. Materials 53
3.2.2. Arc melting 54
3.2.3. Cutting 54
3.2.4. Mounting 55
3.2.5. Grinding and polishing 55
3.2.6. Etching 55
3.2.7. Scanning electron microscopy and energy dispersive X-ray spectroscopy 55
3.2.8. X-ray diffraction 56
3.2.9. Hardness measurements 57
3.2.10. Corrosion tests 57
4 Chapter 4: Thermo-Calc Results 59
4.1. Thermo-Calc results for Ti-6Al-4V 59
4.2. Phase proportion calculation of Ti-6Ta-1.5Nb and Ti-6Ta-1.5Nb-0.5Ru-xCu 59
4.3. Phase proportion calculations of Ti-6Ta-1.5Zr and Ti-6Ta-1.5Zr-0.5Ru-xCu 62
4.4. Phase proportion calculations of Ti-5Nb-4Zr and Ti-5Nb-4Zr-0.5Ru-xCu 65
4.5. Phase Proportion calculations of Ti-6Zr and Ti-6Zr-0.5Ru-xCu 67
4.6. Effect of Ru on the Ti-6Ta-1.5Zr compositions 69
4.7. Preferred Compositions 70
5 Chapter 5: Experimental Results 71
5.1. EDX analyses 71
5.2. Optical micrographs and SEM–BSE images 71
5.3. XRD results 79
5.4. Hardness results 86
5.5. Corrosion tests 88
5.1.1. Open circuit potential profiles 88
5.1.2. Potentiodynamic polarisation curves 88
5.6. Post corrosion SEM images of tested as-cast alloys 91
6 Chapter 6: Discussion 95
6.1. Microstructures of the as-cast alloys 95
6.2. XRD results 96
6.3. Comparing SEM and XRD results 97

6.4. Comparing the Thermo-Calc phase calculation results 98
6.5. Comparing with published results 99
6.6. Relationship between microstructure and hardness 100
6.7. Corrosion 102
7 Chapter 7: Conclusions 109
References 110
Future work 133
APPENDIX 1: List of publications from this work 134
APPENDIX 2: Copies of the publications 135

List of Figures

Figure 1.1: Comparison of healthy and infected tissues around a dental implant. 3
Figure 2.1: Unit cells of (a) hcp α and (b) bcc β phases (Leyens and Peters, 2003). 10
Figure 2.2: Effect of alloying elements on phase diagram of Ti (Lütjering, 1998)...................11
Figure 2.3: Slip systems in the conceptual hcp unit cell (Leyens and Peters, 2003). 12
Figure 2.4: (a) SEM–EBSD image of Ti-6Al-4V showing a massive phase formed along prior-β grain boundaries and (b) SEM–BSE image showing massive phase on the prior-β grain boundaries (Lu et al., 2016). 15
Figure 2.5: Light micrograph (LM) of acicular martensite in Ti-6Al-4V alloy quenched from the β phase field (Lütjering et al., 2000). 16
Figure 2.6: SEM-BSE images of Ti-6Al-4V cooled from the β phase field, showing (a) α growing as lamellae into β grains and (b) colonies of lamellar oriented at different angles (Leyens and Peters, 2003). 17
Figure 2.7: Light micrography images showing lamellar microstructures: (a) slowly cooled Ti-6Al-4V (Lütjering et al., 2000) and (b) Ti-6Al-2Mo-2Cr (Sieniawski et al., 2013).....................17
Figure 2.8: Light microscopy images of Ti-6Al-4V after slow cooling at 50°C/h and water quenching from 1050°C, 800°C, and 650°C, showing α (light) and β (dark) phases (Leyens and Peters, 2003). 19
Figure 2.9: Optical micrographs (OM) showing microstructures of Ti-6Al-4V: (a) fine α equiaxed grains surrounded by small β boundaries, (b) coarse equiaxed α surrounded by β boundaries, (c) bimodal and (d) bimodal (TEM) (Leyens and Peters, 2003). 20
Figure 2.10: Light microscopy images showing basket-weave microstructure of Ti-6Al-4V cooled at (a) 15°C·s-1 (Ahmed and Rack, 1998) and (b) 9°C·s-1 (Sieniawski et al., 2013). 20
Figure 2.11: Schematic diagram of the processing route of bimodal Ti alloys. Shaded areas show the range of cooling rates depending on deformation (Lütjering, 1998). 22
Figure 2.12: Effect of different annealing temperatures and cooling rates on hardness (Jovanović et al., 2006). 26
Figure 2.13: Effect of different annealing temperatures and cooling rates on elongation and tensile strength (Jovanović et al., 2006). 27

Figure 2.14: Hardnesses of heat treated Ti-6Al-4V (Wanying et al., 2017) cooled at different rates: water quenched (WQ), air-cooled (AC) and furnace cooled (FC) (Wanying et al., 2017). 27
Figure 2.15: Hot tensile strength of Ti-6Al-4V cooled at different rates: water quenched (WQ), air-cooled (AC) and furnace cooled (FC) (Wanying et al., 2017). 28
Figure 2.16: Illustration of typical potentiodynamic polarisation curve showing active to passive state in an alloy (ASTM G3-89, 2010)...31
Figure 2.17: Healing process of fractured bone between 0-22 weeks after surgery (Niinomi et al., 2002). 43
Figure 2.18: Schematic illustration showing possible antibacterial mechanisms on the surface of Ti-6Al-4V-5Cu implants (Li et al., 2016). 46
Figure 2.19: TEM micrographs of treated Streptococcus mutans and Porphyromonas gingivalis (Liu et al., 2016). Peptidoglycan layer and cytoplasmic membrane are indicated by black and white arrows and red arrows indicate separation of cell wall and cell membrane, and release of content..47
Figure 2.20: TEM micrographs showing internal structure of Staphylococcus aureus (left) and Escherichia coli (right): (a and b) Untreated bacteria, (c and d) Bacteria treated with silver ion solution (0.2 ppm) (Jung et al., 2008). Black arrow indicates peptidoglycan, cytoplasmic membrane indicated by white arrow and separation of cell membrane from cell wall indicated by arrowhead. 48
Figure 2.21: Hardnesses of as-cast Ti-Cu alloys (Kikuchi et al., 2003). 49
Figure 2.22: Yield strength, tensile strength and elongation of as-cast Ti alloys (Kikuchi et al., 2003). 49
Figure 2.23: SEM–BSE images of Ti-5Cu alloys: (a) (Zhang et al., 2016b) and (b) (Liu et al., 2014), showing Ti_2Cu (arrows). 50
Figure 2.24: Cumulative Cu ion concentration (µg/L) curves released from Ti-5Cu binary alloys (a) (Ma et al., 2016) and (b) (Liu et al., 2016). 51
Figure 3.1: Button arc-melting furnace with oxygen-getter (Mintek). 54
Figure 4.1: Phase proportion diagram of Ti-6Al-4V (wt%). 59
Figure 4.2: Phase proportion diagrams of (a) Ti-6Ta-1.5Nb, (b) Ti-6Ta-1.5Nb-0.5Ru, and (c) Ti-6Ta-1.5Nb-0.5Ru-1Cu, (d) Ti-6Ta-1.5Nb-0.5Ru-2Cu, (e) Ti-6Ta-1.5Nb-0.5Ru-5Cu and (f) Ti-6Ta-1.5Nb-0.5Ru-7Cu (wt%). 60

Figure 4.3: Phase proportion diagrams of (a) Ti-6Ta-1.5Zr, (b) Ti-6Ta-1.5Zr-0.5Ru, (c) Ti-6Ta-1.5Zr-0.5Ru-1Cu, (d) Ti-6Ta-1.5Zr-0.5Ru-2Cu, (e) Ti-6Ta-1.5Zr-0.5Ru-5Cu and (f) Ti-6Ta-1.5Zr-0.5Ru-7Cu (wt%). 63
Figure 4.4: Phase proportion diagrams of (a) Ti-5Nb-4Zr, (b) Ti-5Nb-4Zr-0.5Ru, (c) Ti-5Nb-4Zr-0.5Ru-1Cu, (d) Ti-5Nb-4Zr-0.5Ru-2Cu, (e) Ti-5Nb-4Zr-0.5Ru-5Cu and (f) Ti-5Nb-4Zr-0.5Ru-7Cu (wt%). 65
Figure 4.5: Phase proportion diagrams of (a) Ti-6Zr, (b) Ti-6Zr-0.5Ru, (c) Ti-6Zr-0.5Ru-1Cu, (d) Ti-6Zr-0.5Ru-2Cu, (e) Ti-6Zr-0.5Ru-5Cu and (f) Ti-6Zr-0.5Ru-7Cu (wt%). 67
Figure 4.6: Effect of Ru on (a) Ti-6Ta-1.5Zr composition, with (b) Ti-6Ta-1.5Zr-0.2Ru, (c) Ti-6Ta-1.5Zr-0.4Ru, (d) Ti-6Ta-1.5Zr-0.6Ru, (e) Ti-6Ta-1.5Zr-0.8Ru and (f) Ti-6Ta-1.5Zr-1Ru (wt%). . 69
Figure 4.7: Phase proportion diagrams of (a) Ti-6Ta-1.5Zr-5Cu and (b) Ti-6Ta-1.5Zr-0.2Ru-5Cu (wt%). 70
Figure 5.1: OM images of (a, c, e) Ti-6Ta-1.5Zr, and (b, d, f) Ti-6Ta-1.5Zr-0.2Ru alloys showing Widmanstätten microstructures. 72
Figure 5.2: OM images of Ti-6Ta-1.5Zr-5Cu alloy showing (a) low magnification prior β grains, (b) prior β grains at higher magnification, (c) Widmanstätten microstructures low magnifications and (d) Widmanstätten microstructures at higher magnification. 73
Figure 5.3: OM images of Ti-6Ta-1.5Zr-0.2Ru-5Cu alloys showing Widmanstätten microstructures at different magnifications. Dark areas in (a) are holes caused by casting defects. 74
Figure 5.4: Typical positions of the EDX analyses of bright and dark phases in (a) Ti-6Ta-1.5Zr and (b) Ti-6Ta-1.5Zr-5Cu. 75
Figure 5.5: SEM-BSE images of the as-cast Ti-6Ta-1.5Zr alloy showing dendritic structure and (αTi) lamellae (white arrow) growing from the grain boundary into the matrix (dashed line), at: (a) low magnification showing the original light contrast dendrites and (b) high magnification. 76
Figure 5.6: SEM-BSE images of the as-cast Ti-6Ta-1.5Zr-0.2Ru alloys showing (αTi) (dark) phase (white arrows) and retained (βTi) matrix. 77
Figure 5.7: SEM-BSE images of the as-cast Ti-6Ta-1.5Zr-5Cu alloy showing (αTi) plates (white arrow) growing from prior (βTi) grain boundaries (dashed arrow). 77
Figure 5.8: SEM-BSE images of the as-cast Ti-6Ta-1.5Zr-0.2Ru-5Cu alloy showing: (a) light contrast dendrite (b) acicular (αTi) plates (white arrow) and parallel (αTi) plates (yellow

arrows) growing from β grain boundary (dashed arrow) (c) high magnification image with parallel (αTi) plates (yellow arrows) growing from β grain boundary (dashed arrow). 78
Figure 5.9: SEM-BSE images of (a, c) Ti-6Ta-1.5Zr-5Cu and (b, d) Ti-6Ta-1.5Zr-0.2Ru-5Cu alloy showing Ti_2Cu particles (arrows). 79
Figure 5.10: XRD diffractograms of the as-cast (a) Ti-6Ta-1.5Zr, (b) Ti-6Ta-1.5Zr-0.2Ru, (c) Ti-6Ta-1.5Zr-5Cu and (d) Ti-6Ta-1.5Zr-0.2Ru-5Cu alloys. 81
Figure 5.11: Superimposed XRD diffractograms of the as-cast alloys scanned for 17min. Symbols •, □ and ♦ represent reference line for the phases (αTi), Ti_2Cu and Ti_3Cu, respectively. The diffractograms are showing (αTi) found in Ti-6Ta-1.5Zr, Ti-6Ta-1.5Zr-0.2Ru and Ti-6Ta-1.5Zr-0.2Ru-5Cu, Ti_2Cu and Ti_3Cu found in Ti-6Ta-1.5Zr-0.2Ru-5Cu. The diffractogram of Ti-6Ta-1.5Zr-5Cu shows unmatched peaks that are similar to (αTi), Ti_2Cu and Ti_3Cu. 82
Figure 5.12: XRD diffractograms of the as-cast alloys scanned for 1 h. 84
Figure 5.13: Superimposed XRD diffractograms of the as-cast alloys scanned for 1 h. Symbols •, ★, □ and ♦ represent reference peaks for the phases (αTi), (βTi), Ti_2Cu and Ti_3Cu, respectively. 84
Figure 5.14: Hardness values measured across the sample surfaces. 87
Figure 5.15: Mean Vickers hardnesses of the alloys. 88
Figure 5.16: OCP profiles of the tested Ti alloys. 90
Figure 5.17: Potentiodynamic polarisation curves of the tested Ti alloys. 90
Figure 5.18: Corroded sample of Ti-6Ta-!.5Zr alloy: (a), (c), (d), (e) and (f) show SEM-BSE micrographs and (b) shows an SEM-SE image. 92
Figure 5.19: SEM-SE micrographs of Ti-6Ta-1.5Zr-0.2Ru after corrosion tests. 93
Figure 5.20: SEM-BSE images of corroded Ti-6Ta-1.5Zr-5Cu: (a) lower magnification and (b) higher magnification. 93
Figure 5.21: SEM-BSE images of corroded Ti-6Ta-1.5Zr-0.2Ru-5Cu at increasing magnifications. 94
Figure 5.22: EDX analysis of the pits after corrosion. 94
Figure 6.1: Mean hardness vs average lamellae thickness of the tested alloys. 101
Figure 6.2: Mean hardness vs average grain size of the tested alloys. 101
Figure 6.3: Corrosion current densities of Ti alloys processed different conditions: Ti-6Ta-1.5Zr, Ti-6Ta-1.5Zr-0.2Ru, Ti-6Ta-1.5Zr-5Cu and Ti-6Ta-1.5Zr-0.2Ru-5Cu (gold bars) (this work), wrought Ti-6Al-4V (blue bar) and electron-beam melted Ti-6Al-4V (black bar) (Bai et

al., 2017); Ti-6Al-4V as-cast, hot forged at 850°C, heat treated at 750°C/1h, air cooled (green bar) (Bai et al., 2012); Ti-6Al-4V as-cast, rolled, heat treated at 927°C/4h, cooled at 50°C/1h to 760°C subsequent air cooled. (red bars) corrosion was studied on all three surfaces of its rectangular sample (RD-TD), (RD-NB), (ND-TD) (Amirnejad et al., 2021); Ti-3Cu as-cast and annealed at 740°C/1h (orange bar~~s~~) (Siddiqui et al., 2021); as-cast Ti-5Cu (purple bar); Ti-5Cu as-cast and annealed at 900°C/2h, water quenched (yellow bar) (Masia et al., 2021). 106

List of Tables

Table 2.1: Yield stress ($\sigma_{0.2}$), ultimate tensile, elongation fracture toughness (σ_F) and reduction area results near-αTi alloys at room temperature and 600°C (Lütjering, 1998). 23

Table 2.2: Corrosion rates of Ti alloys and gum metal (Ti-23Nb-0.7Ta-2Zr-1.2O) (Revathi et al., 2014). 29

Table 2.3: Titanium alloys, condition and elastic moduli. 36

Table 2.4: Corrosion current densities of CP-Ti and Ti-6Al-4V alloy in different media at 37 ± 1°C. 39

Table 3.1: Grinding and polishing steps for Ti-6Ta-1.5Zr-xRu-yCu alloys. 56

Table 4.1: Phases calculated for Ti-6Ta-1.5Nb and Ti-6Ta-1.5Nb-0.5Ru-xCu for x = 0, 1, 2, 5 and 7 (wt%). 61

Table 4.2: Phases calculated for Ti-6Ta-1.5Zr and Ti-6Ta-1.5Zr-0.5Ru-xCu for x = 0, 1, 2, 5 and 7 (wt%). 64

Table 4.3: Phases calculated for Ti-5Nb-4Zr and Ti-5Nb-4Zr-0.5Ru-xCu for x = 0, 1, 2, 5 and 7 (wt%). 66

Table 4.4: Phases calculated for Ti-6Zr and Ti-6Zr-0.5Ru-xCu for x = 0, 1, 2, 5 and 7 (wt%)...68

Table 5.1: Targeted compositions and EDX results of the experimental alloys. 71

Table 5.2: EDX analysis of the bright and dark phases in (a) Ti-6Ta-1.5Zr and (b) Ti-6Ta-1.5Zr-5Cu. 75

Table 5.3: EDX results of polished samples and after etching. 76

Table 5.4a: Peak matches of the phases found the as-cast alloys. 85

Table 5.4b: Peak matches of the phases found the as-cast alloys. 86

Table 5.5: Polarisation results of the tested alloys. 91

Table 6.1: Phases predicted in Thermo-Calc compositions and formed in experimental alloys with different techniques. 99

Table 6.2: Hardness values and corresponding microstructures in Ti alloys. 104

List of abbreviations

$\alpha + \beta$	Alpha plus beta
AC	Air Cooling
BCC/bcc	body-centred cubic
BSE	Backscattered Electrons
CP-Ti	Commercially Pure Titanium
CRSS	Critical Resolved Shear Stress
EDX	Energy Dispersive X-Ray Spectroscopy
FC	Furnace Cooling
HCP/hcp	hexagonally-close packed
LM	Light Microscopy
OCP	Open Circuit Potential
OP	Optical Microscopy
PBS	Phosphate Buffered Saline (solution)
ROS	Reactive Oxygen Species
SCE	Saturated Calomel Electrode
SEM	Scanning Electron Microscopy
WE	Working Electrode
WQ	Water Quenched
XRD	X-Ray Diffraction

Chapter 1: Introduction

1.1. Background of Ti and its alloys

Titanium and its alloys are known for their good mechanical strength, biocompatibility and corrosion resistance (Leyens and Peters, 2003; Geetha et al., 2009; Chen et al., 2020). Titanium does not exist in pure form and is found on the earth's crust in oxide form, where rutile (TiO_2) and ilmenite ($FeTiO_3$) have the highest concentration of Ti (Lütjering and Williams, 2007). The commercially pure titanium (CP-Ti) Grades 1-4 differ in the amount of interstitials which influence their mechanical properties (Hidalgo et al., 2018). Titanium and its alloys are classified as α, α+β and β alloys (Leyens and Peters, 2003). Titanium alloys have greater strength to weight ratio than stainless steel by 50%, which makes Ti and its alloys better alternative for high load applications (Li et al., 2019). The mechanical properties of Ti alloy depend on the microstructures (Wang et al., 2019a), including volume fraction of specific phases, grain size, and distribution and type of precipitates. Alloying is commonly used to enhance mechanical properties and resistance to corrosion (Revathi et al., 2014). Alloys have been developed with different phases, they are either α, (α+β) and β alloys (Nicholson, 2020). The Ti-6Al-4V is the most widely-used two-phase (α+β) alloy. It is the most used Ti alloys due to its superior mechanical properties, good formability, weldability, high workability and corrosion resistance than CP-Ti (Revathi et al., 2014). Its microstructure can be easily manipulated by heat treatments (Yadav Saxena, 2020). Furthermore, heat treatments and quenching can be used to enhance the mechanical properties of Ti alloys (Leyens and Peters, 2003). Due to its properties, Ti and its alloys make them useful for many applications such as in aerospace, power generators, chemical processing, automotive, computer industry and medicine (Leyens and Peters, 2003).

Polymer and ceramics cannot serve as alternatives to metallic biomaterials since strength is an important requirement especially for load-bearing applications (Li et al., 2014). Titanium and its alloys have shown good performance as biomaterial (Saini et al., 2015). In biomedical application Ti alloys are used for dental and orthopedic prosthesis implants (Elias et al., 2008).

This is because they possess good mechanical properties, biocompatibility, corrosion resistance and the ability to integrate closely with the bone (Chen et al., 2020). When exposed to air, they form an inert oxide layer and for this reason, Ti and its alloys are resistant to corrosion (Zhang and Chen, 2019). The oxide film was found to be biocompatible (Guilherme et al., 2005) and promotes bone ingrowth, which allows firmer contact between the implant and the host bone. Osseointegration is considered as one of the prerequisites for success of implants (Viteri and Fuentes, 2013). The Ti-6Al-4V alloy is the most used alloy in dental and orthopedics due to its favoured properties compared to pure Ti (Leyens and Peters, 2003; Revathi et al., 2014). However, toxicity of the alloying constituents in Ti-6Al-4V, Al and V, could potentially occur as they were found to be harmful to the human cells (Bammidi et al., 2020; Haase et al., 2020). Additionally, the mismatch in mechanical properties of Ti and its alloys and the bone has limited its use for some biomedical applications. The high modulus of elasticity of implants causes stress shielding (Delannoy et al., 2020). Implant biocompatibility, surface quality and mechanical properties are major factors that determine the success of osseointegration (Parithimarkalaignan and Padmanabhan, 2013). Titanium alloys serve as the right candidate for these desired properties.

Commercially pure Ti and its alloys are used as dental implants. However, due to the chemistry in the oral environment these implants may corrode and wear. The ions and particles produced from corrosion and wear can cause tissue inflammation. This tissue response triggers bacterial colonialization causing peri-implantitis, which can lead to the implant having to be removed. To prevent implants from failing, it is necessary to prevent the build-up of bacteria, and this can be done by preventing the bacteria attaching. The process of peri-implantitis is linked to inflammation of tissue surrounding osseointegrated implants and leads to progressive bone loss. Figure 2.1 shows the comparison of a healthy tissue and inflamed tissue, bone loss and a contaminated implant surface. This need to stop bacteria adhering has encouraged investigation of implants with antibacterial properties by killing or inactivating bacteria adhering the implant surface (Hasan et al., 2013; Parithimarkalaignan and Padmanabhan, 2013). Silver or copper have antibacterial properties and have been used as doping and alloying elements (Zhang et al., 2016b; Fowler et al., 2019; Shi et al., 2020). The Ag and Cu ions damaged the cell envelopes and cause destruction of the bacterial DNA replication, leading to cell death (Zhang et al., 2016a; Shi et al., 2020). Both Ag and Cu were found to be relatively non-toxic to human cells (Zhang et al., 2012; Zhang et al., 2016a; Shi et al., 2020). Copper is more abundant on the Earth's crust than silver, which makes silver relatively expensive. This encouraged further investigation of Ti alloys containing Cu. The good Cu content for achieving good antibacterial properties was reported to be at least 3 wt% for as-cast and heat treated Ti-Cu alloy (Zhang et al., 2016a), while another study suggested that at least 5 wt% for a sintered (Liu et al., 2014) and as-cast, hot forged and heat treated Ti-Cu alloy (Ma et al., 2016). A 5 wt% Cu addition to Ti was reported to balance good mechanical strength and achieve good antibacterial efficacy (Liu et al., 2014; Zhang et al., 2016a).

Titanium alloys with low elastic modulus, superior corrosion resistance and mechanical strength have been targeted for biomedical applications (Nicholson et al., 2020). Alloys containing non-toxic and allergy-free β-stabilising elements have been investigated, and have low elastic modulus, high mechanical strength and superior corrosion resistance. Small ruthenium additions (<1 wt%) to Ti binary alloys significantly increased corrosion resistance of pure Ti (Schutz, 1996). When compared to titanium-palladium alloys they offer similar resistance to corrosion and also cost effective. Additionally, the increase in Ru content increased hardness in Ti alloys while at content ≥ 1wt% the corrosion resistance levelled off (Biesiekierski et al., 2014). But cost efficacy could be a major issue since Ru is expensive. Corrosion of biomedical implants was found to be one of the major factors that activate peri-implantitis (Mouhyi et al., 2012; Rodrigues et al., 2013).

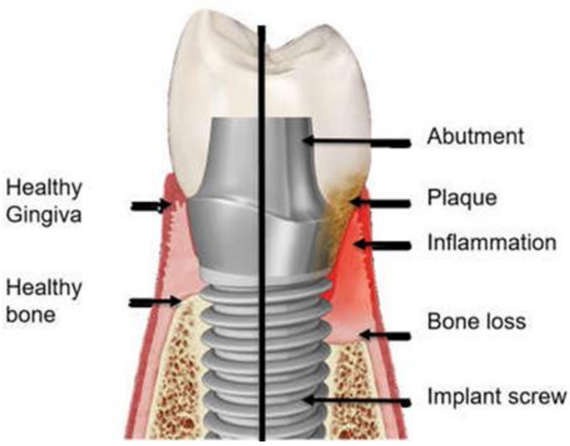

Figure 1.1: Comparison of healthy and infected tissues around a dental implant.

Titanium alloys have shown good tissue integration compared to other conventional alloys like stainless steel and Co-Cr alloys (Morias et al., 2007). This is attributed to their naturally forming oxide layers on their surfaces, mainly the outer porous oxide layer (Revathi et al., 2014). High strength is required to avoid failure of implants (Li et al., 2014). In addition, for implants to serve longer period high fracture toughness, wear resistance and fatigue strength are required (Li et al., 2014). Biomaterial implants should not show any toxic or allergy response to the body tissue (Sidhu et al., 2020). Accumulation of metal ions in human cells and tissues can cause adverse reactions (Sigel et al., 2015). Addition of β-stabilisers does not only enhance mechanical properties, also corrosion rates are significantly reduced (Revathi et al., 2014). The precipitation of Ti-Cu intermetallic phases plays a vital role in the antibacterial effects but decreases ductility (Kikuchi et al., 2003). The right Cu content which will not compromise other desired properties needs to be investigated.

1.2. Rationale of the Research

The human skeleton is composed of various bones which provide support for the body. When the bone has been damaged due to injury, arthritis or malformation, bone replacement becomes necessary to restore the normal function and improve mobility of the body. A good hard tissue replacement is achieved when the biomaterial is compatible with the human bone (Li et al, 2014). The properties required include good corrosion resistance, antibacterial properties, high mechanical strength and stability, good biocompatibility, and being allergy-free and non-toxic (Niinomi et al., 2002; Geetha et al., 2009). These properties are vital so that the biomaterials can withstand the possibly harsh body fluids, load bearing and to avoid rejection of the implant by host tissue (Rabiel, 2010). Metallic implants have been reported to be the best substitute for failed hard tissue or their replacement (Saini et al., 2015). It was estimated that more than 80% of biomaterials are made of metallic materials (Li et al., 2014). Various studies showed that titanium and its alloys have served as good substitutes for biomedical implants with good combinations of the desired properties compatible to bone (Saini et al., 2015; Sidhu et al., 2020). However, due to the high cost of Ti, their use has been limited, especially in economically underdeveloped countries where medical technology is also limited (Niinomi, 2003; Sidhu et al., 2020).

Titanium is very difficult to extract from its ore and because of its strong affinity to air at elevated temperatures (Koizumi et al., 2018; Koizumi et al., 2019). This makes Ti expensive and its applications limited to where there is no better substitute for it. There are many Ti-based alloys that have been developed over the past decades for various applications (Li et al., 2014; Chen et al., 2020), but a large proportion of these alloys have not achieved commercial status due to their manufacturing cost production (Bodunrin, 2016). These factors of production include their alloying elements, complex shape production, machining or finishing processes. The smaller proportion of these alloys that have been used were only utilised when there were no substitutes that could perform similar functions. For this reason, steel has been used for most applications since it has similar mechanical strength to Ti (Geetha et al., 2009; Li et al., 2014). Steel is cheaper and easy to process but it has higher density than Ti (Yamaguchi et al., 2000). Thus, Ti would be more beneficial if it was cheaper. For example, when used for car and aircraft body parts, fuel consumption and air pollution could be reduced (Yamaguchi et al., 2000). For manufacturing plants, its light weight can reduce machine breakdown and offer better performance as well as in corrosive environments (Chen et al., 2020; Nicholson, 2020). Similarly for implants, steel has large elastic modulus, susceptible to corrosion and higher density which are not compatible to bone (Niinomi et al., 2002). Recent studies have focused on designing Ti based alloys with low-cost alloying elements (Mn, Fe, Mo, Sn) (Xu et al., 2020; Sidhu et al., 2021). The main focus of these studies is the strengthening mechanisms and the ability to achieve high strength by addition of these inexpensive elements. To this author's knowledge, there are no low-cost elements that contain antibacterial effects when alloyed to Ti. Additive manufacturing, a 3D printing manufacturing technique can speed up complex shape designs by manufacturing in a single step, and be cost-effective (Vignesh et al., 2021). This reduces machining and eliminates waste removal from the bulk material (Morrow et al., 2007; Shunmugavel et al., 2015). However, it is difficult to identify the right correct manufacturing parameters for particular materials due to a wide range of 3D printing techniques (Vignesh et al., 2021).

The Ti-6Al-4V alloy became one of superior quality alloys and a benchmark alloy for other developed titanium alloys (Leyens and Peters, 2003; Li et al., 2014). The Ti-based alloys are the most suitable alternative for implants, especially for amputation (Cordeiro and Barão, 2017; Nicholson, 2020; Vignesh et al., 2021), with better health response and longevity than other conventional alloys. In addition, they have demonstrated minimal risk of mechanical failure. especially for load-bearing applications and show better performance implants with smaller dimension (Niinomi et al., 2002; Li et al., 2014; Saini et al., 2015). Although biomedical implant applications have broadened due to their improved patient satisfaction and with as little as 5% chance of rejection (Li et al., 2014; Romero-Pérez et al., 2014), patients with some mental or physical disabilities may be limited to implant placement due to their poor overall health (Romero-Pérez et al., 2014). Bruxism is a typical example of these conditions found commonly in children with brain damage. It characterised by grinding and clenching of teeth (Shetty, et al, 2010). Patients who suffered a loss of alveolar bone, implant rehabilitation will not be ideal for them.

The aim of this research is to develop a Ti-Cu based alloy with antibacterial properties, good corrosion resistance and improved mechanical strength and will be compared to the benchmark alloy Ti-6Al-4V.

1.3. Problem statement

A new α+β titanium alloy is needed which has good mechanical strength, low elastic modulus and good corrosion resistance, as the Ti-6Al-4V alloy, but not containing potentially harmful Al and V elements. Beta-stabilisers are preferred as substitutional elements for Al and V since they give the good mechanical strength, corrosion resistance and lower elastic modulus. Copper additions are needed for antibacterial properties.

1.4. Aims and Objectives of the Research

The aim of this research was to develop a new alloy that would have non-toxic elements which would have an $\alpha + \beta$ microstructure, and would also include copper for antimicrobial activity. This was achieved by the following objectives.

- To identify non-toxic β-stabilisers that would potentially lower the elastic modulus.
- To identify and investigate Ti-based alloys with Cu additions to achieve antibacterial properties, and retain the α+β phase in the new alloys when compared to Ti-6Al-4V.
- To investigate an optimum ruthenium content to improve the corrosion resistance of the Ti-Cu based alloys.

- To analyse the microstructure of the newly-developed Ti-Cu based alloys using scanning electron microscopy and X-ray diffraction.
- To measure the hardness and compare to cortical bone.

1.5. Scope of the dissertation

In this research, the compositions of Ti-based alloys were first identified using Thermo-Calc. Non-toxic β-stabilisers were identified to retain the desired α+β phases similar to Ti-6Al-4V. Based on previous work, 5 wt% Cu additions was sufficient to achieve antibacterial properties (although these were not measured). Buttons of 10g were prepared by arc melting under high purity argon. Samples were prepared metallographically, then studied using SEM, XRD, Vickers's hardness tests and corrosion was tested in a simulated physiological solution. The findings were compared to the newly-developed Ti-based alloys, Ti-6Al-4V alloy cortical bone.

Chapter 2: Literature Review

This chapter describes some aspects of titanium alloys and some of their applications, and then looks at the dental needs.

2.5. Overview of titanium and its alloys

2.1.1. The production of titanium

Titanium is found in oxide form as rutile and ilmenite on the earth's crust (Lütjering and Williams, 2007). It is difficult to extract Ti from its ores due to its strong affinity for oxygen and other interstitial elements (nitrogen, hydrogen and carbon). Titanium was successfully extracted from titanium tetrachloride ($TiCl_4$) (Kroll, 1940). The $TiCl_4$ was reduced using magnesium metal in an inert gas (argon) environment at about 1000°C. Magnesium has boiling point about 1107°C which is sufficient to separate Ti during reduction. It also does not absorb hydrogen and it is oxide and nitride free.

Pure Ti has a hexagonal-close packed (hcp) structure below 882°C and undergoes an allotropic transformation to form body-centred cubic (bcc) structure above this temperature (Leyens and Peters, 2003). The bcc structure remains stable until the melting point is reached. Titanium has its atoms held strongly by the electrostatic force, forming a firm metallic bonding and continuous lattice structure. To break these bonds more energy is required which results in its high melting point. Titanium has melting temperature of 1668°C. Its high chemical reactivity at these elevated temperatures makes it difficult to process. This makes Ti castings require special casting machines with inert gas environments which are oxygen-free to prevent metal contamination (Koizumi et al., 2018; Koizumi et al., 2019). An arc melting casting pressure machine with a non-reactive atmosphere with an argon gas pressure or centrifugal force was developed for Ti castings (Koizumi et al., 2019). Improved castability of wax patterned Ti was achieved when a centrifugal casting machine was utilised compared to a simple pressure casting machine (Koizumi et al., 2018). At high temperatures, Ti has strong affinity for oxygen and easily oxidizes, and reacts with the crucible during melting. Thus, Ti also required special moulding materials that contain nonreactive or more stable oxides than the melt. More stable oxides such as magnesia (MgO), zirconia (ZrO_2), alumina (Al_2O_3) and calcia (CaO) as components of cast investments which were found to be suitable for mouldings and castings Ti (Reza et al., 2010). This also reduces interfacial reactivity of Ti and contamination.

Additive manufacturing is a powder metallurgy manufacturing technique that uses 3D design software. It has gained much attention over the recent years due to its numerous advantages than other conventional manufacturing process (Morrow et al., 2007; Huang et al., 2013). It is cost-effective, less metal waste during fabrication, less tooling expenses and reduced fabrication time (Morrow et al., 2007; Shunmugavel et al., 2015; Alaghmandfard et al., 2021). This method also allows the manufacture and production of complicated geometries (or near-net shaped) with fully dense structures and good mechanical properties which are impossible with other conventional manufacturing processes (Huang et al., 2013). The Ti-6Al-4V alloys manufactured by this technique had higher yield and hardness than wrought Ti-6Al-4V (Brandl et al., 2011; Shunmugavel et al., 2017).

2.1.2. Phases in titanium

During cooling, titanium undergoes a crystal structure transformation, from bcc (β-phase) to hcp (α-phase) (Lütjering et al., 2000; Leyens and Peters, 2003). These two allotropic phases, α and β, occur at 882°C in pure Ti, its transus temperature (Lütjering et al., 2000; Lütjering and Williams, 2007). The precise transus temperature for commercially pure titanium (CP-Ti) is influenced by interstitial elements (Lütjering and Williams, 2007). The unit cell of the hexagonal close-packed (hcp) of αTi is illustrated in Figure 2.1a with close-packed planes and directions shown, and the lattice parameter at room temperature (Leyens and Peters, 2003). For pure αTi, the calculated ratio c/a is 1.587, smaller than the ideal ratio of the hexagonal-close packed crystal structure c/a = 1.633. Substitutional or interstitial elements increase the c/a ratio in αTi (Nayak et al., 2018). The unit cell of the body-centred cubic phase, βTi (above transus temperature) is shown in Figure 2.1b with slip plane and lattice parameter at 900°C (Lütjering et al., 2000; Lütjering and Williams, 2007).

The αTi phase has anisotropic behaviour, with hcp behaving differently in the *a* and *c* directions (Leyens and Peters, 2003). Diffusion rate, elastic and plastic deformation are closely related to the crystal structure (Lütjering et al., 2000). The Young's modulus of the αTi single crystal at 25°C consistently changes with the angle between the *c*-axis of the unit cell and the stress axis: 145 GPa for a load applied perpendicular to the basal plane and 100 GPa for load applied parallel to the basal plane (Leyens and Peters, 2003). The β-phase of pure Ti is not stable at room temperature, and can only be retained by alloying with β-stabilisers. Thus, additions of Mo and V can retain β phase in Ti when quenched from the β phase field (Zhao et al., 2012a; Zhao et al., 2012b; Zhang et al., 2015).

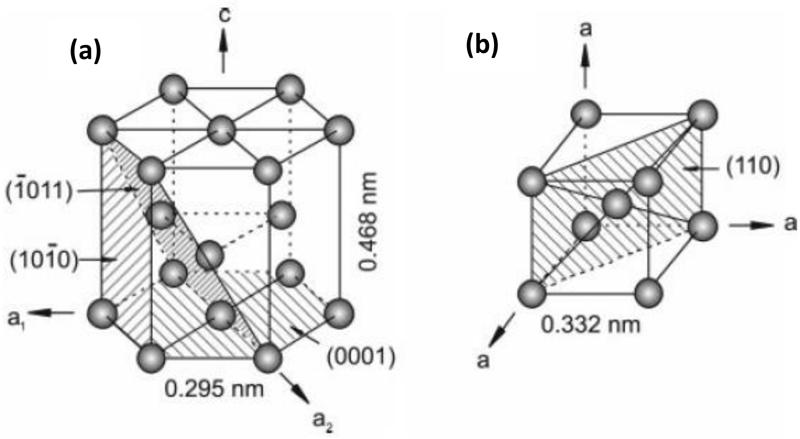

Figure 2.1: Unit cells of (a) hcp α and (b) bcc β phases (Leyens and Peters, 2003).

2.1.3. Classification of titanium alloys and general properties

Titanium alloys are categorized as α, α+β and β alloys (Gupta et al., 2018). The equilibrium constitution of the alloys varies with the concentration of the alloying elements (Lütjering and Williams, 2007). The alloying elements of CP-Ti have different categories: α-stabiliser, β-stabiliser and neutral, and also influence the phase transformation temperature. The effects of some alloying elements on Ti phase diagrams are illustrated in Figure 2.2. The addition of α-stabilising elements shifts the α phase field to higher temperatures, while β-stabiliser additions shift the β phase field to lower temperatures. Commercially pure Ti has various amounts of interstitial elements present in the order of 100 ppm (Lütjering et al., 2000; Weng et al., 2019). These non-metallic interstitial elements (oxygen, carbon and nitrogen) are also categorised as α-stabilisers and with aluminium being the most important α-stabilising element to CP-Ti. Alpha titanium alloys comprise various grades of CP-Ti and alloys containing α-stabilisers and/or neutral elements. Upon annealing below the transus temperature, small β phase proportions form which are stabilised by iron (Fe) found in the CP-Ti grades (Leyens and Peters, 2003; Lütjering and Williams, 2007). Beta-stabilisers are highly soluble in Ti and can also lead to the formation of intermetallic compounds even at low volume proportions. This happens through eutectoid decompositions (Figure 2.2). The neutral elements (tin and zirconium) have no influence on the phase transformation.

Classification of Ti alloys is further subdivided into near-α and metastable-β alloys. Near-α alloys are obtained when small amounts of β-stabilising elements are added. The most used class of alloys are the α+β alloys which contain significant volume fractions of α and β phases (Lütjering et al., 2000; Leyens and Peters, 2003). With high β-stabiliser additions, the transformation temperature lowers and β phase starts to transform by the martensitic process. On higher additions, the martensitic temperature shifts close to RT, and these alloys are called metastable-β alloys (Lütjering et al., 2000).

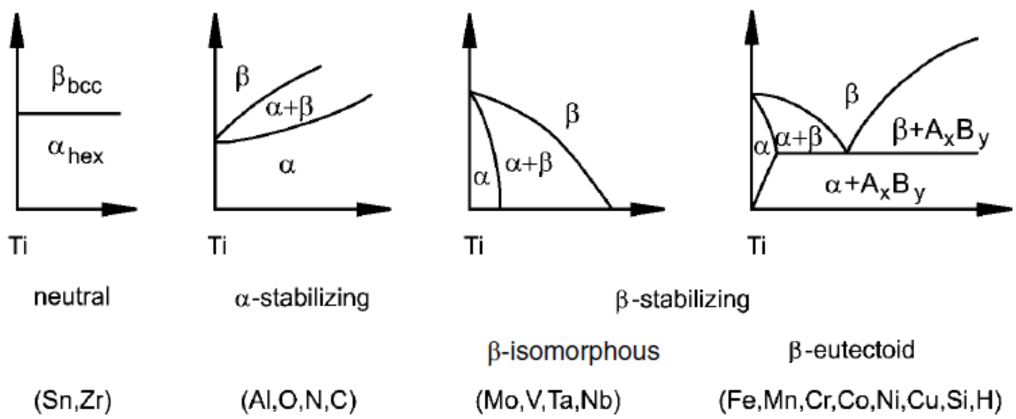

Figure 2.2: Effect of alloying elements on phase diagram of Ti (Lütjering, 1998).

2.1.4. Mechanical properties of Ti alloys

At room temperature the plastic deformation of αTi comprises both slip and twinning modes (Baral et al., 2018). Plastic deformation is induced when a shear stress is applied to a crystalline solid. These are crystallographic defects called dislocations. Dislocations are the main cause of plastic deformation in crystals, allowing deformation without fracture, producing ductility that makes metals workable (Clouet et al., 2015). Permanent plastic deformation occurs when dislocations move in a crystalline solid by glide and climb (Castany et al., 2007). Glide of dislocations results in slip of planes of atoms over one another. Each slip system has slip direction within a slip plane, and the product of the number of slip planes and number of slip directions is the number of slip systems (Leyens and Peters, 2003). There is greater probability of plastic deformation occurring in hcp than bcc lattice (Leyens and Peters, 2003; Lütjering and Williams, 2007). Dislocation movement is usually easier in a denser slip plane, i.e. a close-packed plane (Leyens and Peters, 2003), because the distances to move the atoms are smaller. Although the hcp lattice is close-packed and the bcc lattice is not, there are more slip systems in bcc (Leyens and Peters, 2003). Some slip systems of pure Ti are shown in Figure 2.3. The deformation of the two-phase Ti-6Al-4V alloy is controlled by the α phase as the β has only a small phase fraction.

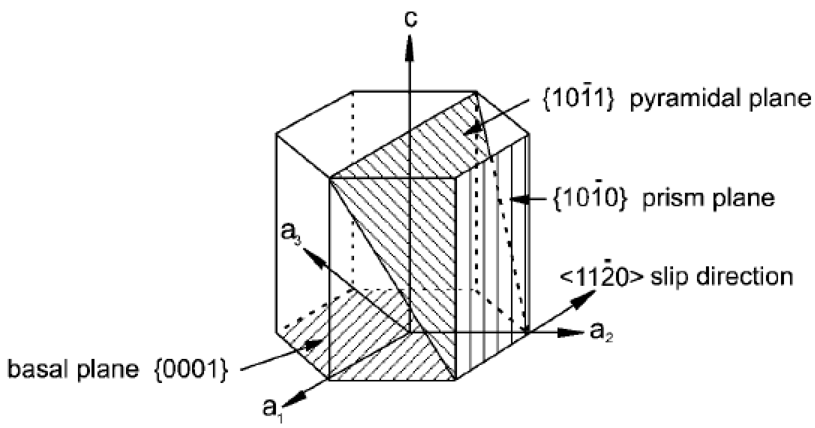

Figure 2.3: Slip systems in the conceptual hcp unit cell (Leyens and Peters, 2003).

For homogeneous plastic deformation to occur, five independent slip systems are required (Palumbo et al., 1998; Raabe et al., 2002), which satisfies the von Mises criterion. The αTi at room temperature has four independent slip systems: basal {0001} and prismatic {10$\bar{1}$0} slip planes with the <11$\bar{2}$0> direction of the <*a*> Burger's vector. An additional slip mode is required to fulfil the von Mises criterion and the required crystal orientation. The {10$\bar{1}$2} plane in the <11$\bar{2}$0> direction (<*a*> type) and {10$\bar{1}$1} plane in the <10$\bar{2}$3> direction (<*c*+*a*> type) are the first order slip modes. The {11$\bar{2}$2} in the <11$\bar{2}$3> direction (<*c*+*a*> type) is a second order slip plane. These first and second order slip systems are pyramidal slip planes, and they provide the addition slip systems to allow continuous plastic deformation.

The activation of the deformation modes depends on the critical resolved shear stress (CRSS). Different CRSS are reported since deformation depends on the material's chemical composition and microstructure. Pure Ti prismatic slip at room temperature is favoured and it does not allow strain along the *c*-axis (Zhou et al., 2021). This is associated with its low CRSS (30MPa and 120MPa) compared to the second order pyramidal slip shear stress (150MPa). This is also caused by the large Burgers vector. Prismatic slip is also the easiest to occur in Ti-6Al-4V with critical resolved shear stresses of 380MPa and 444MPa for basal slip (Alaghmandfard et al., 2021). These values are lower than for the second order pyramidal slip (630MPa). Both <*c*+*a*> slip systems of pure Ti and Ti-6Al-4V have higher CRSS than <*a*> glide.

Twinning is another form of deformation and may result from applied loads (Clayton, 2011; Zhu et al., 2012) where the CRSS is exceeded. Annealing may also produce twinning through atomic displacement at high temperature. In αTi $\{10\bar{1}2\}$ $<\bar{1}011>$, $\{11\bar{2}1\}$ $<\bar{1}\bar{1}26>$ and $\{11\bar{2}3\}$ $<\bar{1}\bar{1}22>$ are the activated twins during tension strain which lead to extension in the *c*-axis. The $\{11\bar{2}2\}$ $<11\bar{2}\bar{3}>$, $\{10\bar{1}1\}$ $<10\bar{1}\bar{2}>$ and $\{11\bar{2}4\}$ $<22\bar{4}\bar{3}>$ twins are activated when a compression load is applied parallel to the *c*-axis and reduce the c-axis. In pure Ti, $\{11\bar{2}3\}$ and $\{10\bar{1}1\}$ twins were not frequently found (Zhou et al., 2017). Grain rotation, grain boundary sliding, diffusion of atoms are deformation mechanisms that occur at relatively high temperatures, sometimes during annealing (Zhu and Langdon, 2005; Wang et al., 2014). Addition of solute atoms to pure αTi suppresses the occurrence of twinning.

Using additive manufacturing an electron–beam melted Ti-6Al-4V rod was deformed at 2100 s^{-1} strain rate had finer grains than a sample deformed at 700 s^{-1} (Alaghmandfard et al., 2021), resulting in the spacing between adjacent α-platelets being smaller in the as-built Ti-6Al-4V deformed at 2100 s^{-1} than for the sample deformed at 700 s^{-1}. This led to higher yield strength in the as-built Ti-6Al-4V deformed at a 2100 s^{-1} that the sample deformed at 700 s^{-1}. Alaghmandfard et al. (2021) found a significantly increased ratio of twin boundaries in the Ti-6Al-4V deformed under these high strain rates, which hindered dislocation movement and increased strength. The compressive twinning favoured the $\{10\bar{1}1\}$ planes, while the $\{10\bar{1}2\}$ planes were favoured during tension twinning at both strain rates.

The α phase of Ti-6Al-4V has slip systems with <*a*> and <*c*+*a*> type directions, activated during deformation. The basal slip <*a*> was the least favoured at elevated strain rates. The two slip directions $<11\overline{2}0>$ (<*a*> type) and $<11\overline{23}>$ (<*c*+*a*> type) are activated in the $\{1\overline{1}00\}$ prismatic slip plane during deformation, with the former being the favoured orientation for deformation. In Ti-6Al-4V, this is due to the least CRSS which is attributed to its lower *c/a* ratio than the perfect hcp crystal. Pyramidal slip has four first order slip planes in two directions <*a*> along $<11\overline{2}0>$ and <*c*+*a*> along $<11\overline{23}>$. Active slip for deformation was found to occur along the $<11\overline{23}>$ than $<11\overline{2}0>$.

High purity Ti goes through a complete phase transformation, β → α by cooling from β phase field (Dobromyslov and Elkin, 2006). At high temperature β grains grow large and α nucleates at β grain boundaries. The crystallographic orientation relationship between β and α, where $\{110\}_\beta$ // $\{0001\}_\alpha$ and $<111>_\beta$ // $<1120>_\alpha$ is called the Burgers relationship (Leyens and Peters, 2003; Tong et al., 2017). This relationship describes active slip planes and its direction in αTi (Tong et al., 2017). According to the Burgers relationship, bcc can transform into 12 hexagonal variants (Lütjering et al., 2000). This transformation can occur either by shear type process (martensitically) or by nucleation and growth, depending on the alloy composition and cooling rate (Lütjering et al., 2000, Britton et al., 2015). Within prior β grains, individual α lamellar packets nucleate and grow according to the 12 hexagonal orientation relationships (Lütjering and Williams, 2007; Britton et al., 2015).

The β/α phase transformation can result in diffusionless transformations (Behera et al., 2013), especially at high cooling rates. In this transformation, atomic shuffling across planes without atomic diffusion produces a martensitic transformation. This displacive transformation results in a microscopically homogenous transformation of the β phase into the α phase. Quenching from 900°C, β phase in CP-Ti and Ti alloys may transform into two different martensitic crystal structures, hexagonal martensite (α') and orthorhombic martensite (α'') (Leyens and Peters, 2003; Lütjering and Williams, 2007). Hexagonal martensite is the most common type and can exist in two morphologies: massive and acicular martensite (Lütjering et al., 2000). Massive martensite occurs only in alloys with low solute content, e.g. CP-Ti, whereas acicular martensite occurs in alloys with higher solute contents. Massive martensite consists of large irregular regions containing packets of small parallel α laths that belong to the same variant of Burgers relationship (Figure 2.4) (Lü et al., 2016). Figure 2.4a shows patchy phase regions, formed on prior-β grain boundaries. Figure 2.4b shows a massive phase sitting over the prior-β grain boundaries.

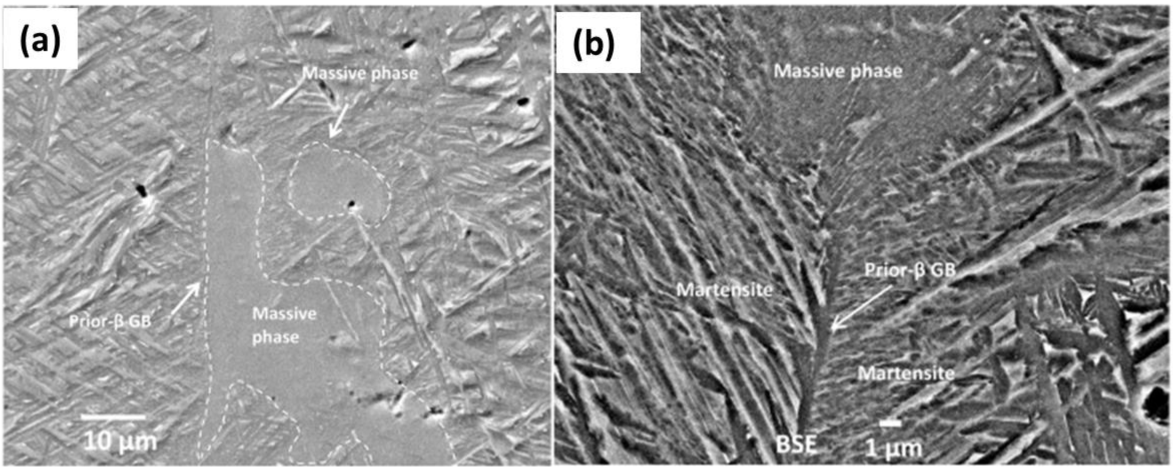

Figure 2.4: (a) SEM–EBSD image of Ti-6Al-4V showing a massive phase formed along prior-β grain boundaries and (b) SEM–BSE image showing massive phase on the prior-β grain boundaries (Lu et al., 2016).

The acicular martensite has a mixture of individual α laths (Figure 2.5) with each individual α lath having a different variant of the Burgers relationship (Lütjering et al., 2000). The martensite laths have high dislocation density and twins. The acicular martensite α’ is a supersaturated solid solution with β stabilisers (Lütjering and Williams, 2007; He et al., 2019). When annealed in the α+β phase region at 800-960°C, it decomposes to α+β by precipitating β particles at β phase layers at lath boundaries (Lütjering and Williams, 2007; Chong et al., 2019).

The nonequilibrium phase, α”, orthorhombic martensite forms in Ti alloys with high β-stabiliser additions and on quenching (Dobromyslov and Elkin, 2006; Lütjering and Williams, 2007; Banumathy et al., 2009). The concentration of α” increases with increasing period number and decreases with increasing group number (Dobromyslov and Elkin, 2006). This martensitic transformation occurs due to lattice strain and atomic rearrangement (Mei et al., 2017). The displacement of the β → α’ transformation is higher than that of the β → α” transformation, thus the β → α” transformation is considered as an incomplete transformation of the β → α’ transformation. This behaviour is found in Ti-V alloys.

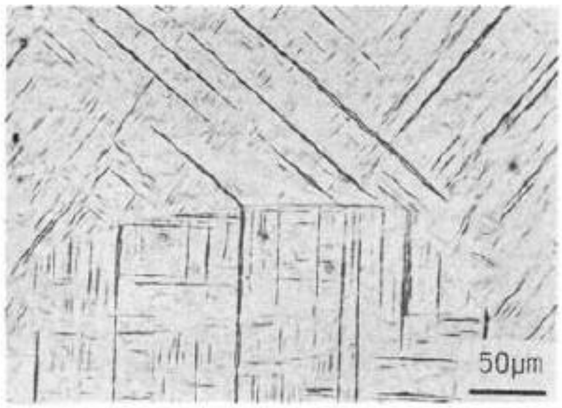

Figure 2.5: Light micrograph (LM) of acicular martensite in Ti-6Al-4V alloy quenched from the β phase field (Lütjering et al., 2000).

The βTi grains are large at high temperatures (Sieniawski et al., 2013). When Ti alloys are slowely cooled from high temperatures in the β phase field to the α+β phase field, the α phase first nucleates at β grain boundaries leading to a continuous α layer along β grain boundaries (Lütjering et al., 2000). Low cooling rates allow long-range diffusion of atoms, so the microstructure formed consists of colonies of parallel α plates, separated by plates of retained β phase (Lütjering and Williams, 2007; Tong et al., 2017). Each α plate within a colony belongs to a single variant of the Burgers relationship with the parent β matrix. Figure 2.7 shows typical microstructures of two different two-phase alloys: Ti-6Al-4V (Figure 2.7a) (Lütjering et al., 2000) and Ti-6Al-2Mo-2Cr (Figure 2.7b) (Sieniawski et al., 2013). The α plates in the same colony have the same crystallographic orientation, and the α and β plates have a lamellar microstructure (Lütjering et al., 2000). Figure 2.6 shows high temperature microstructure of the Ti-6Al-4V alloy when temperature is below the transus temperature: α nucleated at β grain boundaries and grew as lamellae into the β grains (Leyens and Peters, 2003).

2.1.5. Effect of cooling rate on microstructure of titanium and its alloys

Different microstructures affect the mechanical properties of Ti and its alloys (Gupta et al., 2018; Kang and Yang, 2019). These microstructures can be generated by thermomechanical treatments to achieve desired mechanical properties. The α and primary β phases define the microstructure of Ti alloys, and the properties of Ti alloys differ depending on the orientation of these two phases. Depending on the heat treatment and cooling rate or whether the temperature is below or above the phase transformation temperature, the microstructures formed are either equiaxed or lamellar (Meyer et al., 2008; Matsumoto et al., 2011; Gupta et al., 2018). Simple cooling from above the β transus temperature results in a pure lamellar microstructure.

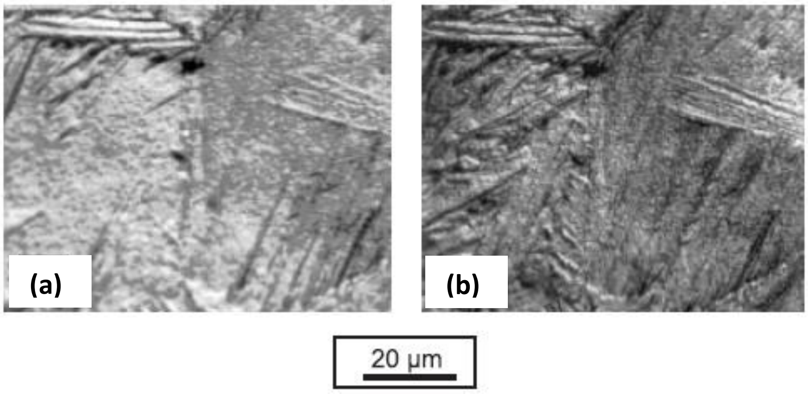

Figure 2.6: SEM-BSE images of Ti-6Al-4V cooled from the β phase field, showing (a) α growing as lamellae into β grains and (b) colonies of lamellar oriented at different angles (Leyens and Peters, 2003).

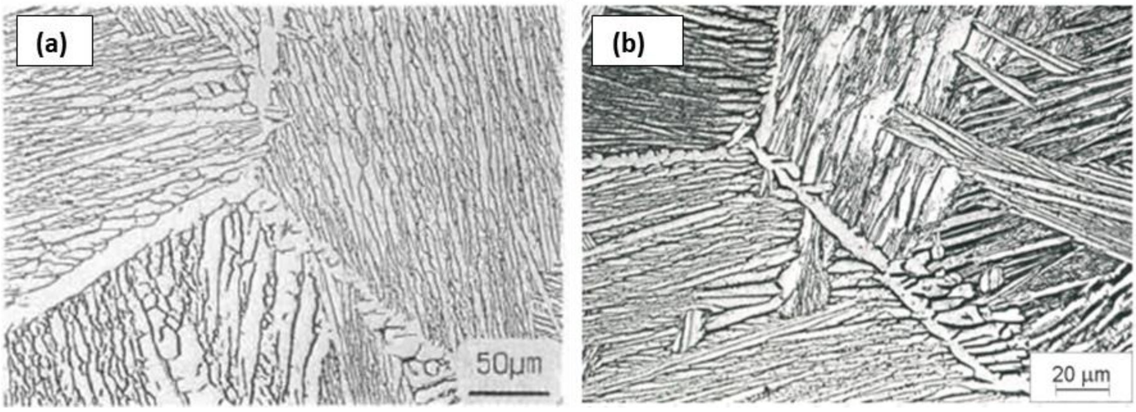

Figure 2.7: Light micrography images showing lamellar microstructures: (a) slowly cooled Ti-6Al-4V (Lütjering et al., 2000) and (b) Ti-6Al-2Mo-2Cr (Sieniawski et al., 2013).

Coarse lamellae (Figure 2.8a) are a result of slow cooling from the β-phase field. With reduced cooling rate the lamellae becomes coarser (Figure 2.8c, e). Acicular (or fine-scale) microstructure (Figure 2.8b) forms as a result of rapid quenching, which leads to martensitic transformation of the β phase. With rapid cooling or quenching from above the martensite start temperature and through the α+β phase field, β transforms to martensite (Figure 2.8d). The β volume fraction is further decreased at low temperatures and β no longer transforms into martensite at the martensitic finish temperature (Figure 2.8f). Slowly cooled specimens can show dendritic and interdendritic phases (Figure 2.8a, c, e).

Equiaxed microstructures have uniform α grains and β edges, and form by slow phase transformation (Figure 2.9 a,b) (Leyens and Peters, 2003). During fast cooling, the α colonies become smaller, the individual α plates become significantly smaller and the colonies start to nucleate independently of β grain boundaries (Lütjering et al., 2000; Leyens and Peters, 2003; Sieniawski et al., 2013). The distribution of these smaller colonies, with smaller numbers of platelets within the colonies leads to the Widmanstätten (or basket-weave) microstructure shown in Figure 2.10 (Lütjering et al., 2000; Sieniawski et al., 2013). The basket-weave microstructure in Ti alloys is observed in alloys with high β stabilising element contents (Leyens and Peters, 2003; Sieniawski et al., 2013). Basket-weave microstructures formed in the Ti-6.8Al-3.42Mo-1.9Zr-0.21Si alloy after being heat treated above its transus temperature, 1030°C and cooled at high rate (Mohandas et al., 1999). In Ti-6Al-4V, a basket-weave microstructure was observed when the alloy was solution treated at 1051°C for 30 min and cooled at rates between 15-1.5°C·s^{-1}, Figure 2.10a (Ahmed and Rack, 1998). Sieniawski et al. (2013) observed the Widmanstätten structure after cooling from the β phase field at the rate 9°C·s^{-1}, Figure 2.10b. With lower cooling rates the (≥1°C·s^{-1}) the lamellar became coarser (Kherrouba et al., 2016).

2.1.6. Effect of microstructure on mechanical properties

High fracture toughness and crack propagation resistance are typical for alloys with fully lamellar microstructures (Leyens and Peters, 2003). In α+β Ti alloys, the α colony size influences the mechanical properties (Meyer et al., 2008; Matsumoto et al., 2011; Gupta et al., 2018). The colony size and grain size determine the effective slip distance for dislocations during plastic deformation (Lütjering, 1998; Clemens et al., 2017). The colony and grain size depend on the cooling rate (Leyens and Peters, 2003). Work hardening from cold working can be used to strengthen metals (Clemens et al., 2017). Cold working produces dislocations so the mean path (distance) between individual dislocations is decreased. The dislocation movement becomes obstructed by other dislocations, because the dislocations interact more (Clemens et al., 2017).

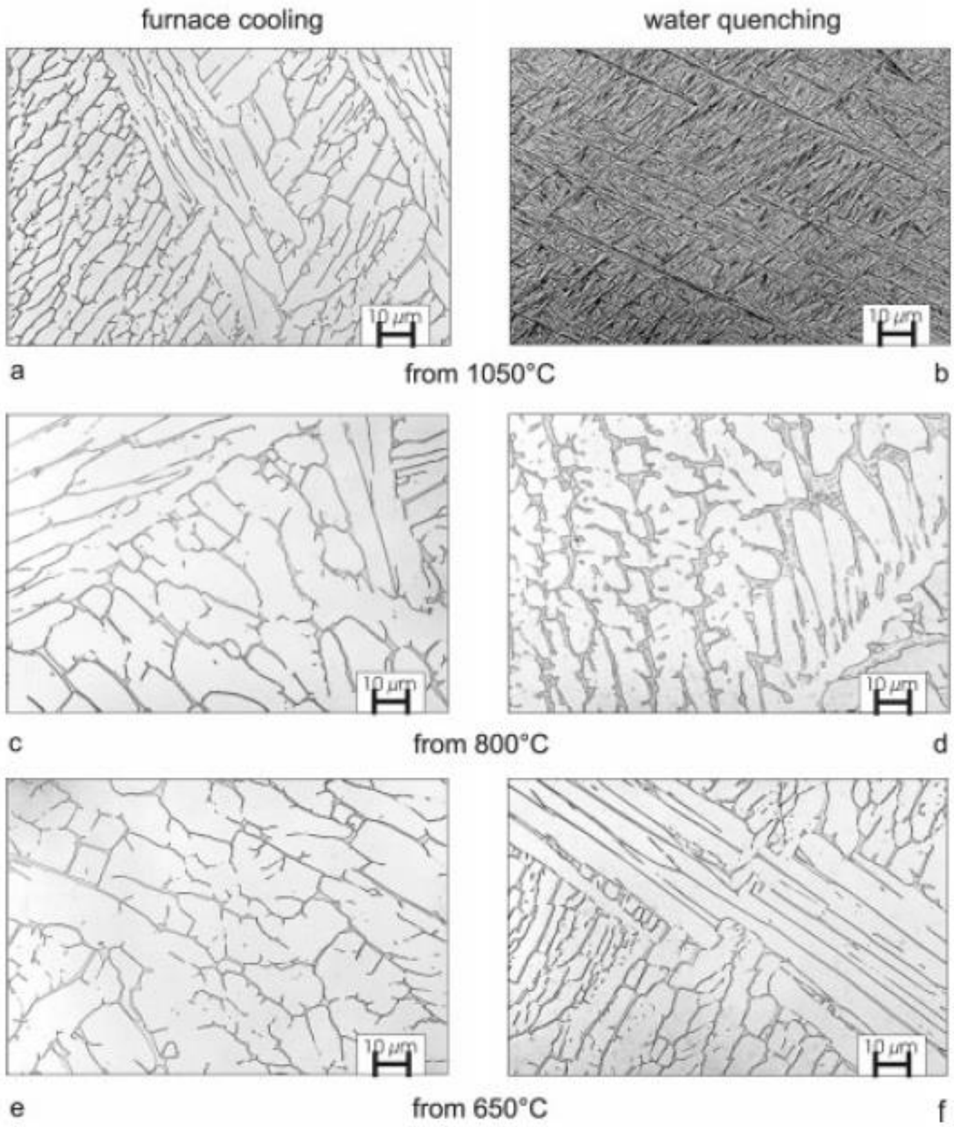

Figure 2.8: Light microscopy images of Ti-6Al-4V after slow cooling at 50°C/h and water quenching from 1050°C, 800°C, and 650°C, showing α (light) and β (dark) phases (Leyens and Peters, 2003).

Fine-grained materials are stronger at ambient temperatures than coarser grained materials, and the relationship between increasing yield strength with decreasing grain size is the Hall-Petch relationship (Hall, 1951; Petch, 1953). Finer grains have greater total grain boundary area to hinder dislocation motion than the coarse grains, and during plastic deformation, grain boundaries act as obstacles to dislocation movements. This is because individual grains have different crystallographic orientations, and if a dislocation passes into another grain, it has to change its direction of motion (Clemens et al., 2017). This process is increasingly hindered as the misorientation angle between the grains increases.

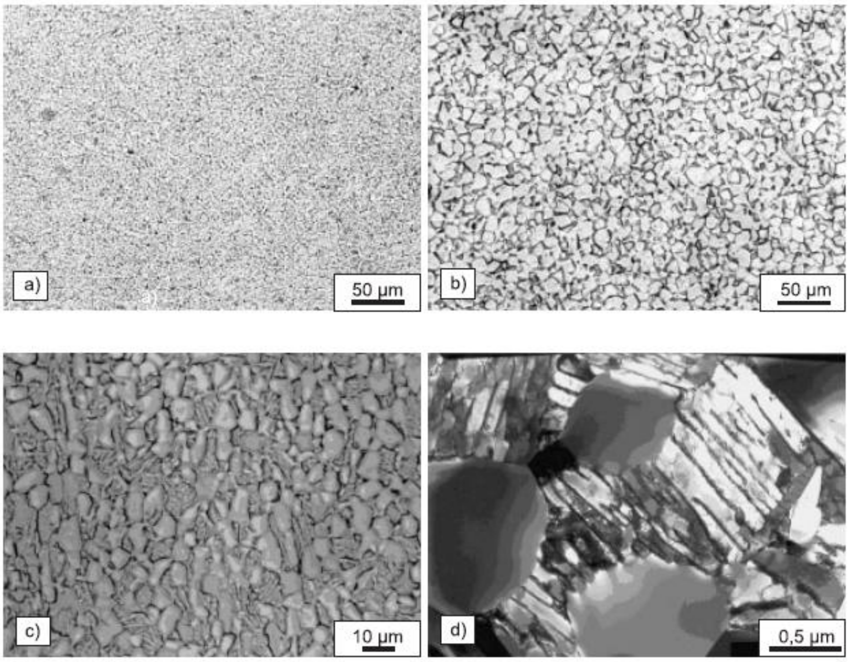

Figure 2.9: Optical micrographs (OM) showing microstructures of Ti-6Al-4V: (a) fine α equiaxed grains surrounded by small β boundaries, (b) coarse equiaxed α surrounded by β boundaries, (c) bimodal and (d) bimodal (TEM) (Leyens and Peters, 2003).

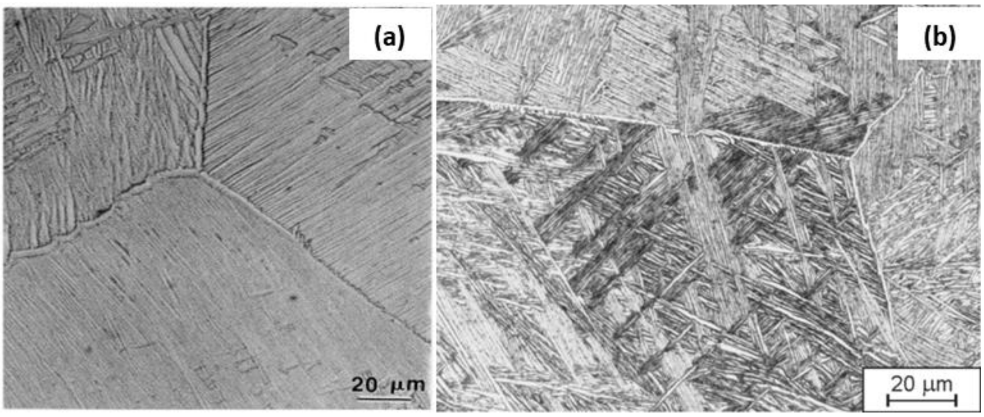

Figure 2.10: Light microscopy images showing basket-weave microstructure of Ti-6Al-4V cooled at (a) 15°C·s-1 (Ahmed and Rack, 1998) and (b) 9°C·s-1 (Sieniawski et al., 2013).

Yield strength, ductility and crack propagation resistance increase with decreased grain size and with increased cooling rate (Meyer et al., 2008; Matsumoto et al., 2011; Gupta et al., 2018). Finer microstructures have increased fracture toughness resistance because the fine structure slows down crack formation (Filip et al., 2003; Leyens and Peters, 2003). The yield strength of α+β Ti alloys increased with increasing cooling rate due to the finer microstructures produced (Lütjering, 1998). The yield strength also decreased with increasing average thickness of α lamellae. The yield and tensile strengths of Ti alloys increases as the grain size decreases (Chong et al., 2017; Leyens and Peters, 2003), since there is more obstruction of dislocations by grain boundaries. Equiaxed structures have high fatigue strength (Lütjering and Williams, 2007). Uniform elongation in equiaxed microstructure decreased when the grain size became smaller (Chong et al., 2017).

Bimodal microstructures combine equiaxed and lamellar microstructures (Figure 2.9c,d), and can be obtained in α+β Ti alloys (Leyens and Peters, 2003). They exhibit well-balanced mechanical properties (Lutjering, 1998; Filip et al., 2003; Leyens and Peters, 2003). The microstructure mainly comprises α grains (α_p) with equiaxed morphologies and transformed β regions that comprise secondary α lamellae, which transformed from equiaxed β grains during cooling after annealing, as well as retained β. Bimodal microstructures form as a result of the four thermomechanical processes: (i) homogenization in the β phase field, (ii) deformation in α+β phase, (iii) recrystallization in the α+β phase field and followed by (iv) aging at lower temperatures (Lutjering, 1998; Lütjering et al., 2000). The processing of bimodal microstructures is shown schematically in Figure 2.11. The important parameters to control in the resulting microstructural features in step I and step III is the cooling rate (shaded area). The mechanical properties are closely related to the size, volume fraction and distribution of α_p (recrystallized equiaxed α phase) and the transformed β regions. They have better yield strength, ductility and crack resistance than fully equiaxed microstructures (Chong et al., 2017: Leyens and Peters, 2003). This is attributed to blockage of dislocation glide when passing through one grain to another. The strengthening mechanism is also due to the finer β regions (Lütjering et al., 2000; Chong et al., 2018).

With increased annealing temperature, the volume fraction of α_p decreased and was more dispersed, while the volume fraction of the β grain gradually increased (Chong et al., 2018). Alloy element partitioning is the second parameter that influences the strength of the Ti-6Al-4V alloy with bimodal microstructures (Lütjering et al., 1998; Lütjering and Williams, 2007;

Chong et al., 2018). Partitioning is the separation of the alloying elements that occurs during phase transformations (Lütjering et al., 1998). Partitioning moves elements that are less soluble in a phase to other phases where they are more soluble. Aluminium is an α-stabiliser and vanadium is a β-stabiliser (Leyens and Peters, 2003), and Energy-dispersive X-ray mapping showed that Al partitioned to the α phase when the Ti-6Al-4V sample was annealed in the α+β region (Chong et al., 2018). There was higher Al content in α_p than in the transformed β grains, which gradually increased with increasing annealing temperature. Higher V contents were in the β regions. The increased strength and hardening in the α phase were caused mainly by the higher aluminium solubility than grain size reduction (Chong et al., 2018).

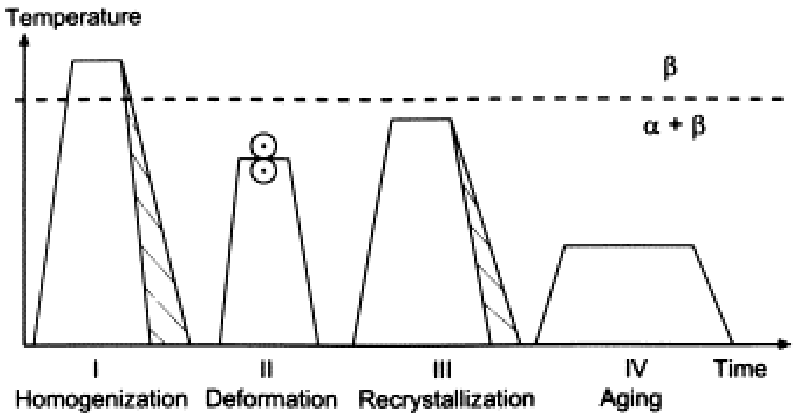

Figure 2.11: Schematic diagram of the processing route of bimodal Ti alloys. Shaded areas show the range of cooling rates depending on deformation (Lütjering, 1998).

The yield stress ($\sigma_{0.2}$) was highest between 10 and 20 vol.% percent α_p (Table 2.1), and depends on the α_p volume fraction, which is determined by the α colony size and element partitioning. This implies that the α colony size dominates at small volume fractions of α_p and element partitioning dominates at large volume fraction of α_p. The smaller decrease in yield strength at 600°C in the high α_p volume fraction region demonstrates that element partitioning at high temperature is less noticeable due to the effect of oxygen. Oxygen is an α-stabiliser and increased O content increases hardness and yield strength of CP-Ti. Thus, its solubility is low in α_p at 600°C and strengthening is reduced. The crack growth resistance (σ_F) at RT is reduced with increased α_p volume fraction. At high temperature, the σ_F is high for bimodal microstructures compared to fully lamellar microstructures, indicating that element partitioning is reduced at high temperature (Lütjering, 1998).

2.1.7. Effect of Interstitials or Impurities in Ti and its Alloys

Titanium and its alloys are normally utilised in the annealed condition (Lütjering et al., 2000; Leyens and Peters, 2003) to reduce residual stress from processing. However, annealing may compromise some desired properties even though it can increase ductility and fracture toughness. The mechanical properties of CP-Ti grades depend on the amounts of interstitial elements in solid solution. These interstitials are either impurities or additions (doping or alloying elements (Nayak et al., 2018)). The interstitial elements cause solid solution strengthening and reduced grain size thus improving yield and tensile strength with little effect on density and ductility. Alloying is another technique that strengthens metals by solid solution strengthening or precipitation of intermetallic phases (Clemens et al., 2017). When an alloying atom dissolves in a solid metal it may act as obstacle to dislocation motion. The precipitation of second phases in the matrix hinders dislocation motion by not allowing them to cut (pass through) (Clemens et al., 2017) which means they must be looped. Commercially pure Ti Grades 1-4 have oxygen contents between 0.18-0.40 wt% and 0.2-0.5 wt% for iron (Lütjering et al., 2000).

Table 2.1: Yield stress ($\sigma_{0.2}$), ultimate tensile, elongation fracture toughness (σ_F) and reduction area results near-αTi alloys at room temperature and 600°C (Lütjering, 1998).

Microstructure	Test Temp.	$\sigma_{0.2}$ (MPa)	UTS (MPa)	σ_F (MPa)	El. (%)	RA (%)
Lamellar	RT	925	1015	1145	5.2	12
Bi-modal (20% α_p)	RT	995	1100	1350	12.9	20
Bi-modal (30% α_p)	RT	955	1060	1365	12.6	26
Lamellar	600°C	515	640	800	10.5	26
Bi-modal (10% α_p)	600°C	570	695	885	9.9	30
Bi-modal (40% α_p)	600°C	565	670	910	14.4	36

Although Ti can be resistant to some chemicals, when it is exposed to hydrogen-containing media or environments it can pick up hydrogen atoms which have deleterious effects on some of its properties after certain concentration (Tal-Gutelmacher and Eliezer, 2005). These effects become more pronounced when Ti is exposed to hydrogen at elevated temperatures and for longer times (Dwivedi and Vishwakarma, 2018). Hydrogen's reaction with Ti includes an eutectoid transformation, with αTi and a hydride phase forming from the βTi phase (Figure 2.3). Some of the hydrogen induced damage is cracking. Residual hydrogen in Ti alloys induces cracks under low strain tensile loading and constant loads (Madina and Azkarate, 2009; Dwivedi and Vishwakarma, 2018). Sometimes an external load is not required to induce these cracks if there are residual stresses. In high strength alloys like Ti alloys, exposure to hydrogen environment induces hydrogen embrittlement, which decreases strength and ductility. The effect of hydrogen on pure titanium's mechanical and corrosion properties was recently studied in electrolytic hydrogen charging (Liu et al., 2020), and hydrides formed on the metal surface. These hydrides protected against corrosion at low concentrations, but increased hydride formation caused local strain in the Ti matrix, which increased the corrosion rates. Thus, with increased charging time (or exposure to hydrogen atmosphere), corrosion rates were initially low but increased with increased charging time. Two oxide layers were formed, a dense inner layer which provided good corrosion resistance, and an outer porous layer. Changed fracture modes and decreased ultimate tensile strength occurred as hydride formation increased. Fracture of hydrides in the matrix is induced at low densities, leaving space for crack nucleation and propagation (Robertson et al., 2015). With increased hydride formation, brittle fracture within the hydride occupies an increasingly larger area of the fracture surface. Different microstructures have different uptakes of hydrogen (Tal-Gutelmacher and Eliezer, 2005).

In the α+β alloys, there is a larger amount of β. In an electrochemical hydrogenated charged condition, a fully lamellar Ti-6Al-4V microstructure had more hydrogen than the duplex microstructure (Tal-Gutelmacher et al., 2004). When the current density was increased in both materials, the fully lamellar microstructure alloy had higher hydrogen uptake. Microstructures with elongated βTi, such as fully lamellar, will absorb more hydrogen than duplex microstructures with fine equiaxed α and small β edges. This is because the bcc βTi phase has a more open structure, allowing higher hydrogen diffusion and solubility (Nelson et al., 1972; Wang et al., 2001). Hydrogen also enters the two-phase alloys via grain boundaries. Iron on Ti surfaces aided hydrogen penetration, leaving voids for hydride formation and increasing hydrogen embrittlement in CP-Ti (Briant et al., 2002; Dwivedi and Vishwakarma, 2018). Pure Ti becomes susceptible in the presence of a notch (Tal-

Gutelmacher and Eliezer, 2005). Cracks are induced when there is a defect available in the alloy. In a hydrogen environment or dynamic loads, these cracks can grow and when they propagate to a sufficiently large length, propagation becomes difficult to hinder, resulting in failure. When a crack has propagated to sufficiently large length, fracture of the material occurs. Cracks propagate in a transgranular way in fine-grained microstructures, and intergranularly in elongated βTi phase microstructures (Tal-Gutelmacher and Eliezer, 2005; Zhang et al., 2018).

Oh et al. (2011) investigated the effect of oxygen on CP-Ti and Ti-6Al-4V. Increased oxygen increased Vickers hardness and tensile strength and decreased elongation. The CP-Ti Grades 1-5 have yield strengths of 170-795 MPa, ultimate tensile strengths of 240-860 MPa and elastic moduli of 103-120 GPa (Elias et al., 2008). The ductility of high purity Ti is 50% and for CP-Ti Grades 1-5, ductility decreases from 24% to 10% with increasing oxygen (Li et al., 2014). Rocha et al. (2006) measured the Vickers hardness of CP-Ti to be 200 $HV_{0.5}$ and 341 $HV_{0.5}$ for Ti-6Al-4V; similar results were found by Kikuchi et al. (2003). When subjected to different heat treatments, the Vickers hardness increased, for CP-Ti annealed at 955°C for 1h and aged at 620°C for 2h the hardness was 260 $HV_{0.5}$ and the specimen heat treated at 750°C for 2h had 202 $HV_{0.5}$. For Ti-6Al-4V, significant differences were found among the three specimens: control was 341 $HV_{0.5}$, heat treated at 750°C for 2h was 352 $HV_{0.5}$ and the sample annealed at 955°C for 1h and aged at 620°C for 2h was 369 $HV_{0.5}$ (Rocha et al., 2006). Venkatesh et al. (2009) demonstrated that yield strength and ultimate tensile strength can be increased by ageing and water quenching. Ti-6Al-4V annealed 1065°C and furnace cooled had a compressive strength of 960MPa and after water quenching the compressive stress was 1120MPa (Meyer et al., 2008). Brandes et al. (2012) undertook compression tests on Grades 1 and 4 CP-Ti under uniaxial conditions at RT. They observed tension-compression asymmetry, which was influenced by the oxygen content, activated dislocation systems and crystallographic orientation (Brandes et al., 2012). Jovanović et al. (2006) studied the effect annealing temperature and cooling rates on the hardness, tensile strength and elongation of arc melted Ti-6Al-4V. The annealing temperatures were between 800-1100°C for 1h. Three different cooling rates: air-cooling, water-quenching and furnace-cooling, were applied for each annealing temperature. The hardness values (Figure 2.12) and tensile strength (Figure

2.13) increased with increasing annealing temperature and cooling rate. With increasing annealing temperature, the elongation decreased.

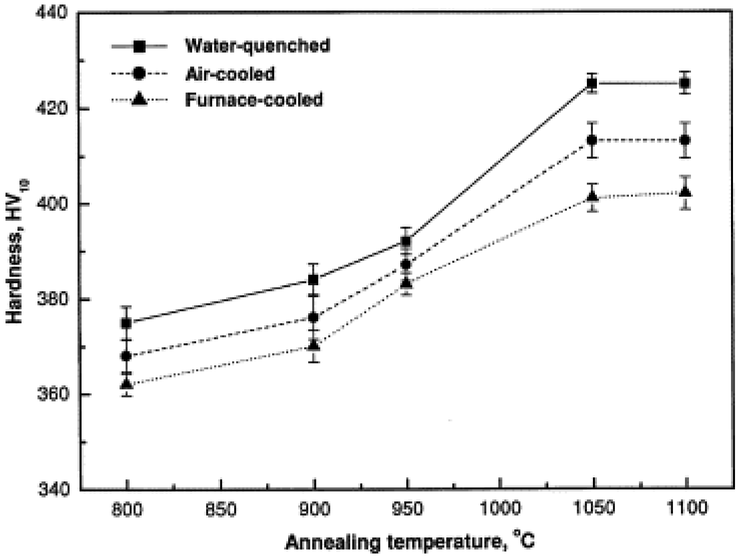

Figure 2.12: Effect of different annealing temperatures and cooling rates on hardness (Jovanović et al., 2006).

The effect of heat treatment and different cooling rates on the hardness and tensile strength of Ti-6Al-4V was investigated by Wanying et al. (2017). The sample bars were prepared by arc melting followed by forging. The samples were initially solution-treated at 930°C (α+β field) for 1h while other samples were held at 970°C above the transformation temperature for 1h. This was followed by different cooling rates: air-cooling, water-quenching and furnace-cooling. After cooling, all the samples were aged at 550°C for 6h. Figure 2.15 shows the effect of heat treatments and cooling conditions on the hardness. The hardness of the reference sample increased after solution-treatment followed by water quenching from 930°C and 970°C. No significant changes were observed after ageing. The tensile strength was performed after heat treatment to test the strength of the alloy at high temperatures (Figure 2.15). Water quenching increased hot tensile strength of the reference sample while air-cooling and furnace cooling decreased the hot tensile strength.

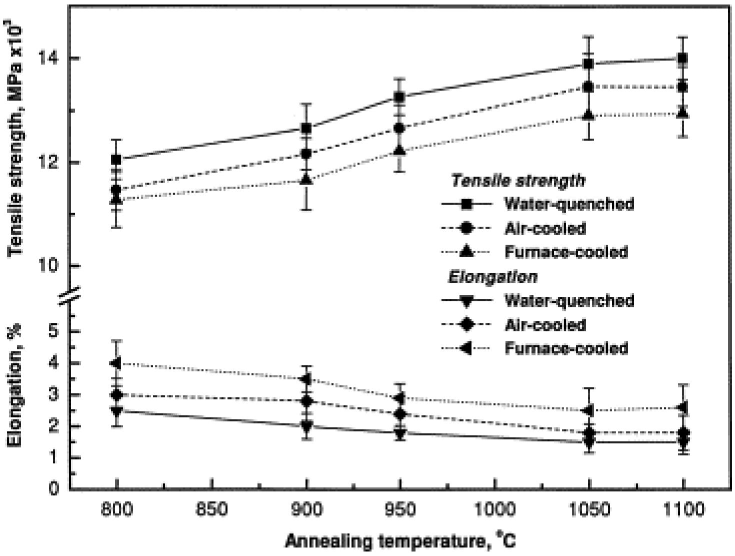

Figure 2.13: Effect of different annealing temperatures and cooling rates on elongation and tensile strength (Jovanović et al., 2006).

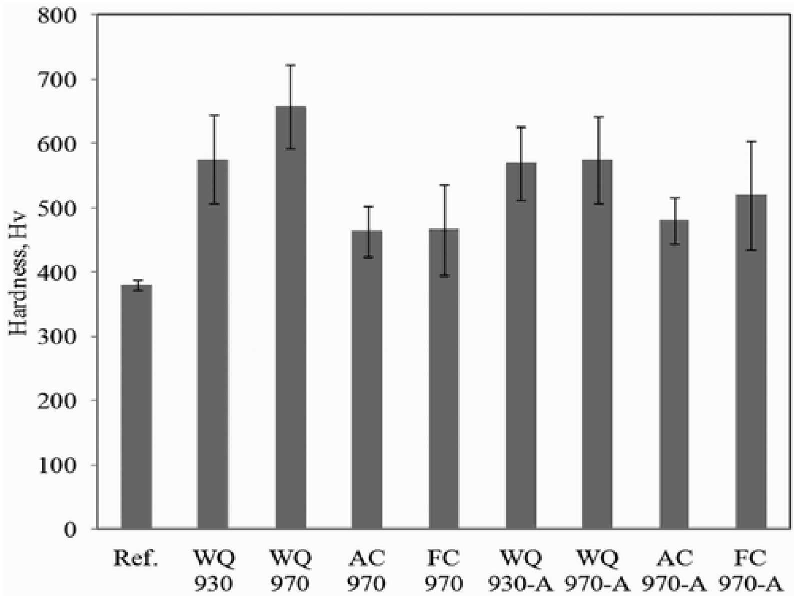

Figure 2.14: Hardnesses of heat treated Ti-6Al-4V (Wanying et al., 2017) cooled at different rates: water quenched (WQ), air-cooled (AC) and furnace cooled (FC) (Wanying et al., 2017).

2.1.8. Corrosion of Ti alloys

One of the major prerequisites for metallic materials is their ability to withstand corrosion and maintain their good properties even at elevated temperature (Lütjering and Williams, 2007; Chen et al., 2020). Such materials are needed for increased service life. A comprehensive knowledge of the underlying mechanisms of corrosion is needed to solve existing problems. Corrosion involves an electrochemical process (Pourbaix et al., 1959; Revathi et al., 2014). When Ti and its alloys are exposed to air or water (moist) they form an inert and highly stable oxide (mainly TiO_2) layer (Machnee et al., 1993; Guilherme et al., 2005). When damaged, the oxide layer spontaneously regenerates. The corrosion behaviour of Ti and its alloys depends on the environment, alloy compositions and microstructure (Chen et al., 2020). Titanium is preferred in environment with media solutions containing oxidants (Lütjering and Williams, 2007). For such environments unalloyed or pure Ti is preferred since corrosion is usually more important than the mechanical strength. An important technique for studying corrosion is the potentiodynamic polarisation. In potentiodynamic polarisation, the potential of the specimen is scanned and measured by a potentiostat. The potential is normally scanned in the noble direction until passivation at certain potential and current density is reached. The open circuit potential (OCP) is the stable potential, i_{corr} is the corrosion current density and E_{corr} is the corrosion potential. The cathodic and anodic Tafel slopes (β_c and β_a) are extrapolated in the linear cathodic and anodic region of the potentiodynamic curves (Choubey et al., 2004; Kakaei et al., 2019). From this, polarisation curves giving the corrosion rate of the test specimen can be done. Table 2.2 shows a series of Ti alloys with gum metal being Ti-23Nb-0.7Ta-2Zr-1.2O) and their corrosion data (Revathi et al., 2014).

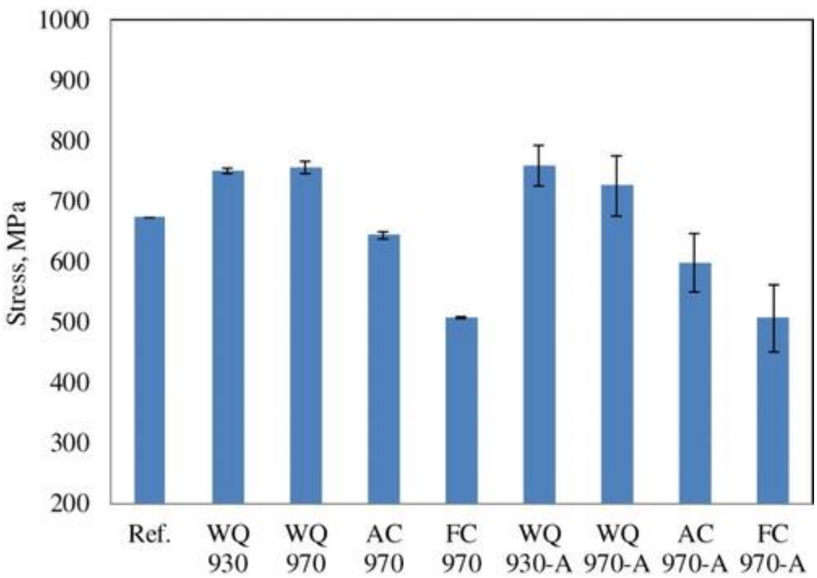

Figure 2.15: Hot tensile strength of Ti-6Al-4V cooled at different rates: water quenched (WQ), air-cooled (AC) and furnace cooled (FC) (Wanying et al., 2017).

Table 2.2: Corrosion rates of Ti alloys and gum metal (Ti-23Nb-0.7Ta-2Zr-1.2O) (Revathi et al., 2014).

Material	OCP	E_{corr}/mV	β_a/mV	β_c/mV	I_{corr}/$\mu A\ cm^{-2}$	Corrosion rate/mm $year^{-1}$ (mils $year^{-1}$)
Ti–13Nb–13Zr	−132	−21	114	96	0·0002	0·0007(0·0014)
Gum metal	−40	−49	150	107	0·0014	0·0012(0·0021)
Ti–20Nb–20Zr	−149	−452	174	123	0·0039	0·0024(0·0037)
Ti 15-3	−286	−476	187	154	0·0045	0·0027(0·0052)
Ti–20Nb–13Zr	−312	−485	197	206	0·0067	0·0030(0·0053)
Ti–6Al–4V	−361	−541	260	147	0·0104	0·0058(0·0096)
CP-Ti	−437	−576	284	125	0·0142	0·0060(0·0098)

In some chemical media, such as those containing reducing acids like dilute sulphuric acid (H_2SO_4) or hydrochloric acid (HCl), CP-Ti corrosion resistance is not enough (Bodunrin et al., 2020). These acids are strong enough to easily dissolve the protective oxide layer, so the metal corrodes (Tomashov et al., 1960; Tomashov et al., 1961; Cotton, 1967). Hydrides may form on the Ti surface if the acid concentration is enough. Alloys of Ti are resistant to pitting and microbial induced corrosion (Chaturvedi, 2009). Increased corrosion resistance or maintenance of its passive state is then required and selection of a material with low corrosion rates is done. This is achieved when the steady-state potential of the metal is shifted in the active (negative) or noble (positive) direction (Tomashov et al., 1960; Tomashov et al., 1961; Cotton, 1967). The former shift is obtained by external cathodic current or by using cathodic inhibitors in the corrodent (Stern and Wissenberg, 1959; Tomashov et al., 1960; Tomashov et al., 1961). The increased cathodic current leads to increased hydrogen overvoltage. In cathodic polarisation hydrogen absorption occurs and hydride formation at Ti surface occurs which affects its mechanical properties (Tomashov et al., 1960; Tomashov et al., 1961). Therefore, active shift is not efficient for Ti. On the other hand, noble potential is preferred for Ti, even in non-oxidising acids. This potential shift can be achieved by doping or alloying (Tomashov et al., 1961), external anodic polarization (Cotton, 1958; Cotton, 1967), by contacting Ti with a noble metal (Cotton, 1958), or introducing cations of a noble metal in the media containing the non-oxidising acid (Tomashov et al., 1961; Cotton, 1967).

Small additions of Pd to Ti can enhance its corrosion resistance even in reducing acids (Schutz, 1996; Handzlik and Fitzner, 2013). Stern and Wissenberg (1959) also showed the same effect wiith Pt, Pd, Re, Ru, Ir, Os, Rh and Au alloying elements in the same media. Schutz (1996) showed that small Ru additions to Ti alloys improved their corrosion resistance in boiling HCl acids and in hot NaCl brine media. The Ru-containing α, α+β and β Ti alloys were more cost effective than the corresponding Pd-containing Ti alloys (Schutz, 1996). With appropriate alloying, passivation of Ti can be increased owing to the shift of its potential to the steady-state, the region where Ti is completely passive (Stern and Wissenberg, 1959; Tomashov et al., 1961). Titanium may suffer anodic dissolution in aggressive media (Tomashov et al., 1960; Tomashov et al., 1961; Cotton, 1967). Alloying enhanced the stability (stable performance even at elevated temperature) and when alloyed with Cr and Mo, anodic dissolution was significantly reduced (Tomashov et al., 1961). Palladium additions to Ti forms the Ti_2Pd phase, even at low concentrations (Cotton, 1967), and also dissolves in the αTi matrix (Van der Lingen and de Villiers, 1994). Before passivation, Ti_2Pd undergoes partial dissolution and metallic Pd is precipitated at the material surface (Cotton, 1958; Cotton, 1967), which provide sites for reduced hydrogen overvoltage and depolarized hydrogen ion (H_3O^+) reduction, causing a potential shift to the noble direction, giving passivation (Tomashov et al., 1961; Cotton, 1967). Conversely, when Ti is exposed to an oxidising corrodent, it dissolves as Ti^{3+} and gets oxidized by Pd^{2+} which produces Pd and an unstable Ti^{4+}. The Ti^{4+} then reacts with oxygen species in the chemical media and precipitates as TiO_2. The high strength α+β Ti alloys are susceptible to corrosion in hot aqueous brine environments (Schutz, 1996). However, the corrosion deficiencies in these alloys can be significantly reduced by small Ru additions (Stern and Wissenberg, 1959; Schutz, 1996). Small additions of Pd salt in boiling non-oxidizing acid (H_2SO_4) can stop corrosion of unalloyed Ti with passivity initiating when concentrations of soluble Pd reach 10 ppm, and at 20 ppm metallic Pd precipitates at the Ti surface (Cotton, 1967).

Platinum group metals have been shown to be good cathodic modifiers when alloyed with Ti alloys in reducing acid media (Mwamba et al., 2014). Non-oxidising acids such as containing chloride and fluoride solution make titanium susceptible to pitting and crevice corrosion (Brossia and Cragnolino, 2001). Apart from platinum group metals, molybdenum also a beneficial cathodic modifier (Trufanov et al., 1989). Figure 2.16 shows a schematic polarisation scan, with an active-to-passive transition of an alloy. In addition to cathodic modification, the base alloy must have a small critical current density (i_{cr}) that will be surpassed by the current of the cathodic reaction of the alloying components (Potgieter et al., 1990; Mwamba et al., 2013; Mwamba et al., 2014). The alloying components must provide favourable surfaces for hydrogen evolution and inhibit anodic dissolution of the base metal (Potgieter et al., 1990). Furthermore, the passivation potential (E_p) of the base alloy has to be sufficiently negative to permit the introduced cathodic components to shift the corrosion potential (E_{corr}) of the base alloy to the passive region and more noble potentials. The shifted corrosion potential should be less than the potential associated with the onset of the transpassive process (E_{tr}). Lastly, the primary transpassive potential of the base alloy has to be sufficiently negative. This allows a wide range of passivation and shifts the corrosion potential of the cathodically-modified alloy in a more positive potential.

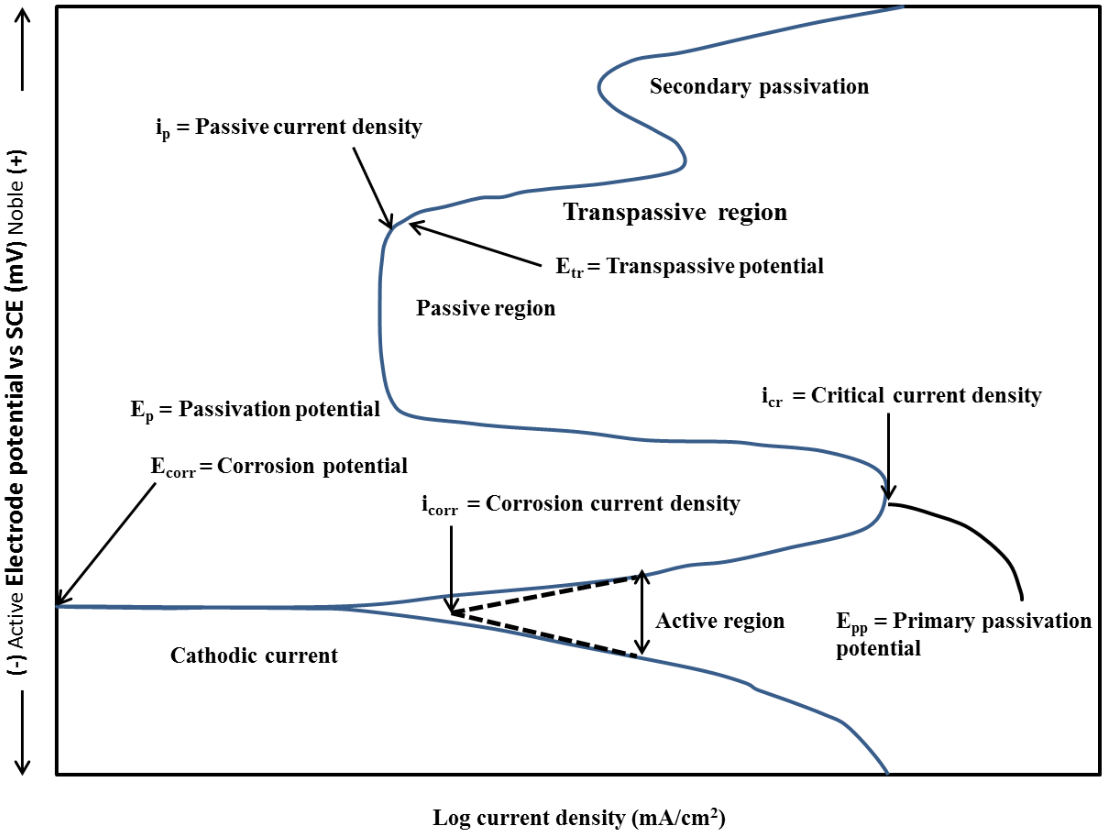

Figure 2.16: Illustration of typical potentiodynamic polarisation curve showing active to passive state in an alloy (ASTM G3-89, 2010).

2.1.9. Application of titanium and its alloys

Titanium and its alloys are widely used in aerospace, power generators, chemical processing, automotive, computer industry and medicine (Chen et al., 2020). In biomedicine they are used to replace hard tissue, make artificial joints and mend broken bones (Viteri and Fuentes, 2013;

Dutta et al., 2017). They are used for load-bearing implants because of their good corrosion resistance, strength and biocompatibility (Zhang and Chen, 2019; Nicholson et al., 2020). Titanium and its alloys have favourable corrosion resistance and better tissue tolerance than other conventional implants like stainless steel making them suitable for biomedical applications (Stenlund et al., 2015; Nicholson et al., 2020; Chen et al., 2020). Against cyclic stresses, materials need high fatigue strength (Geetha et al., 2009; Nicholson et al., 2020). The α+β and β alloys are mostly used in load-bearing applications, since they have superior mechanical properties and corrosion resistance than CP-Ti (Zhang and Chen, 2019; Nicholson et al., 2020; Chen et al., 2020).

High strength Ti alloys are obtained by alloying and processing (Kang and Yang, 2019). The α+β Ti alloys have yield strengths between 800-1200 MPa. Since the development of the Ti-6Al-4V alloy due to its favoured properties: corrosion resistance, formability, low density, high temperature stability and high mechanical strength compared to other conventional alloys, the applications Ti alloys have gradually increased (Gomez-Gallegos et al., 2018; Williams and Boyer, 2020). The weight reduction and high specific strength in Ti alloys are favoured for airframes and fuselages. Since titanium alloys are also resistant to crack growth, they substitute for many conventional alloys. In cases where high corrosion resistance and thermal stability are required, unalloyed Ti is used but it is low in strength. Some of the mostly used Ti alloys in aerospace are: Ti-10V-2Fe-3Al, Ti-6Al-4V, Ti-15V-3Cr-3Sn-3Al and Ti-6Al-2Sn-4Zr-2Mo (Gomez-Gallegos et al., 2018; Williams and Boyer, 2020). The metastable β Ti-10V-2Fe-3Al alloy is tough and used in high load applications (Leyens and Peters, 2003) and its forged parts are used to make main landing gear (Jackson et al., 2000). Its low transus temperature (800°C) (Lütjering et al., 2000) permits lower forging temperatures with cheaper tools (Jackson et al.,2000). Titanium mechanical properties and chemical compatibility with fuel gives pure Ti advantage over most conventional alloys for applications in engine components for spacecraft.

Automotive industries use Ti alloys for making engine components such as engine valves (Takahashi et al., 2020). The intake valve made from Ti-6Al-4V alloy and TI-6Al-4Zr-Sn-Nb-Mo-0.2Si-0.3O alloy, outlet valve (exhaust) is specially designed for durability at elevated temperatures (Yamaguchi at al., 2000). The latter alloy has dispersed reinforcing titaniumboride (TiB) for stability at high temperatures and to increase its mechanical properties (Yamaguchi at al., 2000; Saito, 2004). As a result of their low density, Ti alloys are more fuel efficient and eco-friendly than the conventional steel which is denser (Yamaguchi at al., 2000). Both alloys are manufactured by powder metallurgy (Yamaguchi at al., 2000) where the elements are blended into homogeneous mixtures and compacted under pressure. The compacted sample is heated to the forging temperature and then transferred to forging press where it is shaped to final ingot. Titanium alloys are also used for making automotive coil springs due to their higher specific strength, and lower shear and elastic moduli than conventional steels (Leyens and Peters, 2003). For this application, the β Ti-6.8Mo-4.5Fe-1.5Al alloy was preferred over the Ti-6Al-4V alloy owing to its low shear modulus and durability (Leyens and Peters, 2003). The reduced weight of Ti results in fewer turns thus it is cost effective.

In industries where aggressive media like non-oxidizing acids are encountered, metals with high corrosion resistance are required (Bodunrin et al., 2020), such as titanium and its alloys. They have been important in petrochemical refineries since they offer superior corrosion resistance. Their long equipment life and lower maintenance than conventional alloys makes them cost effective (Nicholson, 2020; Chen et al., 2020). For applications where outstanding corrosion resistance is required, like desalination plants, chemical and marine applications, alloyed Ti is utilised for good corrosion resistance (Wang et al., 2019b). Increased corrosion resistant alloys such as Ti Grade 7 (Ti-0.15Pd) and Grade 12 (Ti-0.3Mo-0.8Ni alloy) are used in chemical industries and where crevice corrosion is a problem (Schutz, 1996). Thin-walled tubes and pipes composed of Ti offer better heat transfer than conventional alloys like stainless steel (Takahashi et al., 2020). As a result of its good thermal conductivity Ti is also used for heat exchangers (Leyens and Peters, 2003). Beta Ti alloys have better performance in a variety of corrosive environments (Chen et al., 2020) and form a more stable oxide film than α and α+β alloys. 2.2.

2.2. Titanium alloys in dental and orthopedic application

Biomaterial implants need good mechanical strength, biocompatibility, low density, corrosion resistance and the ability to integrate closely with the bone (Chen et al., 2020). Biomaterials are used to replace hard tissue, mend broken bones, restore lost structures, hip replacements and replace damaged joints (Zhang and Chen, 2019; Nicholson, 2020; Chen et al., 2020). For dental and orthopaedic prostheses, Ti and its alloys have substituted for many alloys due to their good properties (Freese et al., 2001; Elias et al., 2008). Commercially pure Ti was first used as an alternative implant material to stainless steel and Co-Cr alloys due to its biocompatibility and better corrosion resistance (Li et al., 2014). Cobalt-chromium and stainless steel based alloys contained toxic elements which were harmful to the human body (Chen et al., 2020). However, the mechanical properties of CP-Ti were insufficient where high strength was required (Li et al., 2014). Ceramic and polymers cannot substitute for metallic implants because mechanical strength is one of the requirements for load-bearing applications (Li et al., 2014). Commercially pure Ti was then replaced by the α+β Ti-6Al-4V alloy which has superior mechanical strength than pure Ti (Revathiet al., 2014). The Ti-6Al-7Nb and Ti-5Al-2.5Fe alloys are also two-phase, comparable to Ti-6Al-4V. The two-phase alloys have good strength and corrosion resistance which are required for long term implantation (Chen et al., 2020). However, concerns have been raised about toxicity of the alloying elements, aluminium and vanadium, to the human cells (Zhang and Chen, 2019; Nicholson, 2020). When V ions accumulate in cells surrounding implants, they can cause toxicity and allergy while Al ions interfere with bone mineralisation. The mismatch in mechanical properties of Ti and its alloys and the bone has limited its use for some biomedical applications. This encouraged investigation of new biomedical implants. At present βTi alloys show good mechanical strength, low elastic modulus, corrosion resistance and biocompatibility (Zhang and Chen, 2019; Nicholson, 2020; Chen et al., 2020).

2.2.1. Importance of modulus of elasticity in implant materials

Higher modulus of elasticity of implant materials than human bone causes bone resorption due to stress shielding (Pohler, 2000; Elias et al., 2008). The mismatch between the mechanical properties and elastic moduli of the bone and the implant leads to biomechanical incompatibility (Saini et al., 2015). The α- and α+β Ti alloys have higher elastic moduli than human bone. Human cortical bone has tensile strength of 50-150 MPa, compressive strength of 20-193 MPa and elastic modulus of 4-30 GPa (Geetha et al., 2009; Mohamed and Shamaz, 2015). These mechanical properties are not similar to those of most biomaterials, e.g. Ti Grades 1-5 have ultimate tensile strengths of 240-860 MPa and elastic moduli of 100-120 GPa

(Elias et al., 2008). Originally, the load is supported by the bone, and when an implant is introduced, it shares the load with the surrounding bone, thus the bone is subjected to lowered stress and hence is stress is shielded (Ridzwan et al., 2007). When parts of the bone experience high load (i.e. stress) from the implant, the adjacent bone cells do not survive and bone growth is reduced (Geetha et al., 2009; Patel and Gohil, 2012; Mohammed et al., 2014). This stimulates colonisation of bacteria that cause inflammatory processes and resorption of the bone-cells around the implant, called atrophy, and leads to loosening of the implant (Mohammed et al., 2014). The elastic moduli of αTi and α+β Ti alloys are higher than those of β-type Ti alloys (Niinomi and Nakai, 2011; Li et al., 2014). Beta Ti alloys composed of non-toxic and allergy-free elements had low Young's moduli (Niinomi and Nakai, 2011; Mohammed, Khan, and Siddiquee 2014). The lower Young's modulus means less stress-shielding and hence bone resorption is inhibited, so bone integration with the material is enhanced. Many studies have focused on βTi alloys since they have advantageous properties such as low elastic modulus, high mechanical strength and superior corrosion resistance (Revathi et al., 2014; Li et al., 2014, Zhang and Chen, 2019; Nicholson, 2020; Chen et al., 2020). The Ti-13Nb-13Zr alloy is a βTi alloy that has been developed for biomedical implants (Schneider et al., 2000; Huang et al., 2018). The aged Ti-13Nb-13Zr alloy has a tensile strength of 1030 MPa, yield strength of 900 MPa, ductility of 15%, micro-Vickers hardness of 300 MPa, elastic modulus of 79-84 GPa and superior corrosion resistance than Ti and Ti-6Al-4V (Schneider et al., 2000; Revathi et al., 2014; Li et al., 2014; Huang et al., 2018). For dental implants a minimum elongation of 8% is required (Saini et al., 2015). Heat treatments, hot-working and cold-working can optimise the mechanical strength of the Ti-13Nb-13Zr alloy and give a lower elastic modulus, e.g. approximately 41-45 GPa can be achieved for a cold-worked alloy (Schneider et al., 2000; Davidson et al., 2014). Table 2.3 shows the elastic moduli of some α+β and β alloys.

Table 2.3: Titanium alloys, condition and elastic moduli.

Alloy	Condition	Elastic modulus (GPa)	Yield strength (MPa)	Elongation (%)	Reference
Ti-6Al-4V (ELI)	Annealed	101-110	795-875	10-15	Niinomi, 1998
Ti-6Al-4V	Annealed	110-114	825-869	6-10	Niinomi, 1998
Ti-10.1Ta-1.7Nb-1.6Zr	Forged, annealed	89	542	---	Stenlund et al., 2015
Ti-6Al-7Nb	wrought	114	880-950	8-15	Niinomi, 1998
Ti-29Nb-13Ta-4.6Zr	Solution-treated and aged	80	864	13.2	Niinomi, 2003
Ti-13Nb-13Zr	Heat treated, WQ, aged	79-84	836-908	10-16	Schneider et al., 2000
Ti-35Nb-7Zr-5Ta	Annealed	55	547	19	Li et al., 2014
Ti-15Mo	Annealed	78	544	21	Niinomi, 1998
Ti-$Nb_{22.3}$-$Zr_{4.6}$-$Ta_{1.6}$-Fe_6	Sintered (960°C)	75	2425	7	Li et al., 2013

2.2.2. Biocompatibility and corrosion of titanium

Biocompatibility is one of the prerequisites for implant materials. Success of implant surgery is evaluated by the reaction of the human body (Williams, 2008). Corrosion and wear resistance determine biocompatibility of an implant (Li et al., 2014). Degradation of biomaterials results in metal ion release which may lead to immune responses, toxicity and inflammation (Li et al., 2014). Corrosion resistance is one of the main properties an implant should possess for longevity of biomaterials. Corrosion rate and metal ions released are reduced as the Ti oxide layer thickens (Guilherme et al., 2005; Cvijovic-Alagic et al., 2011). Exposure of Ti based biomaterials to acidic environment, implant micro-motion, fluctuating or repeated stress and abnormal loads can result in the breakdown of the oxide layer (Rodrigues et al., 2013). Permanent breakdown of the oxide layer can expose the bulk metal to body electrolytes which initiates corrosion (Rodrigues et al., 2013). Under normal conditions the human body fluids have a pH of 7.4 (Abdel-Hady Gepreel and Niinomi, 2013), and are chemically stable and inert to Ti alloys. All metals release metal ions, even the passive Ti and Ti-6Al-4V (Morais et al. 2007). Metal ions are released from dental and prosthesis implants into the surrounding tissues by various mechanisms, including corrosion and wear (Saini et al., 2015).

Morais et al. (2007) inserted Ti-6Al-4V implants in rabbit tibiae to measure the amount of V ion release to the body during healing. After 1, 4 and 12 weeks of insertion, the lung, kidney and liver were extracted from the rabbit for analysis. From all the extracted parts, the V ion content increased after 1 week, and with further increase after 4 weeks. A decrease in V ion content was observed after 12 weeks but these values did not reach the 1-week values (Morais et al., 2007). In all weeks of analysis, the amount of V measured did not reach toxic level. The accumulation of these metal ions can cause allergy and damage to human cells when they reach toxic level (Sedarat et al., 2001; Okazaki et al., 2004; Morais et al., 2007; Athanasou, 2016). Debris may be generated from corrosion and abrasion (wear) at the surfaces of implants (Li et al., 2014). Soluble debris may enter the blood stream and be secreted through urine. Insoluble debris may build up in the human tissue and may have long term effects (chromosomal aberrations) or short-term effects (inflammation or damage of cells) (Abdel-Hady Gepreel and Niinomi, 2013; Li et al., 2014; Athanasou, 2016). The corrosion of implants has also been associated with implant failure since the corrosion is one of the factors that trigger peri-implantitis (Mouhyi et al., 2012; Rodrigues et al., 2013). Peri-implantitis is an infectious decease that causes destructive inflammation in soft and hard tissues surrounding osseointegrated implants, which leads to the development of an infected "pocket" between the implant and the tissue, damage to the supporting bone and loosening of the implant. Oral pathogens can form biofilms on the implant surfaces which activate peri-implantitis (Mouhyi et al., 2012). Inflammatory processes reduced the pH of the environment around the implant (Mathew et al., 2012; Rodrigues et al., 2013; Souza et al., 2010). Souza et al. (2010) found decreased corrosion resistance of CP-Ti Grade 2 in the presence of bacteria and suggested that the observed reduction in pH was promoted by pathogens which led to corrosion of the Ti (Souza et al., 2010). Localised corrosion in retrieved Ti samples was caused by biofilms and high metal ions contents were found in the surrounding tissues which could cause adverse tissue reactions (Guindy et al., 2004). Hydrogen peroxide (H_2O_2) was produced by bacteria during the inflammatory process (Pan et al., 1998), lactic acid and other organic acids, and were produced by bacterial strains in dental plaque (Koike and Fujii, 2001). Hydrogen peroxide and fluoride ions (F^-) in the oral environment corrode Ti and its alloys (Reclaru and Meyer, 1998; Mabilleau et al., 2006), but fluoride ions are unavoidable due to oral cleaning and dental cleaning. During the inflammation process the pH reduces due to the high levels of H_2O_2 (Handzlik and Fitzner, 2013). In simulated body fluids, the corrosion rates of CP-Ti and Ti-6Al-4V were lower at 25°C than at 37°C, showing temperature influences corrosion (Alves et al., 2009).

Table 2.4 shows the measured corrosion current densities of CP-Ti and Ti-6Al-4V processed with different conditions. The corrosion tests were conducted in different artificial physiological environments which had different pH values. These were phosphate buffered saline (PBS) solution, Ringer's solution and Hank's solution and their compositions are given in Table 2.4.

2.2.3. Osseointegration

Osseointegration is the direct structural and functional connection between living bone and the surface of a load-carrying implant (Parithimarkalaignan and Padmanabhan, 2013). It is one of the prerequisites for long-term clinical success and stability of biomedical implants (Parithimarkalaignan and Padmanabhan, 2013; Viteri and Fuentes, 2013). Osseointegration involves the efficient stress transfer between the bone and the implant and it also indicates that no relative motion occurred at the bone-implant interface (Steinemann, 1998). The bone-implant interface, biocompatibility and surface conditions determine the success of osseointegrated implant (Viteri and Fuentes, 2013). The surface conditions of the implant are determined by its mechanical properties and topological properties, all of which affect tissue reactions.

Table 2.4: Corrosion current densities of CP-Ti and Ti-6Al-4V alloy in different media at 37 ± 1°C.

Alloy	Processing condition	i_{corr} (mA/cm^2)	Reference
PBS solution (pH = 7.4) 8 NaCl, 0.2 KCl, 2.9 $Na_2HPO_4 \bullet 12H_2O$ and 0.2 KH_2PO_4 (g/L)			
Ti-6Al-4V (ELI)	Wrought	1.20E-05	Bai et al., 2017
	Electron beam melted	7.00E-06	
CP-Ti	As-cast, hot forged at 850°C, heat treated at 750°C/1h, air cooled	3.30E-05	Bai et al., 2012
Ti-6Al-4V		1.80E-05	
Ti-6Al-4V	RD-TD	4.30E-06	Amirnejad et al., 2021
	RD-ND	2.60E-05	
	ND-TD	1.20E-05	
Ti-6Al-4V	Commercial	1.88E-3	Hsu et al., 2004
Ti-3Cu	As-cast and annealed at 740°C/1h	8.60E-06	Siddiqui et al., 2021
Ti-5Cu	As-cast	3.00E-05	Masia et al., 2021
	Annealed at 900°C/2h, water quenched	3.10E-05	
Ringer's solution (pH = 7.0): 8.6 NaCl, 0.3 KCl and 0.33 $CaCl_2$ (g/L)			
CP-Ti	As-cast	3.60E-05	Kuphasuk et al., 2001
Ti-6Al-4V		2.00E-04	
Ti-6Al-4V (ELI)	Wrought	6.50E-05	Souza et al., 2009
Ringer's solution (pH = 7.5): 8.6 NaCl, 0.3 KCl and 0.33 $CaCl_2 \bullet 2H_2O$ (g/L)			
CP-Ti	As-cast	3.40E-04	Robin et al., 2008
Ti-6Al-4V		4.10E-04	
Hank's solution (pH = 7.4): 8 NaCl, 0.4 KCl, 0.06 $Na_2H_2PO_4 \bullet 2H_2O$, 0.06 $MgSO_4 \bullet 7H_2O$, 0.14 $CaCl_2$, 0.60 KH_2PO_4, 1.0 $C_6H_{12}O_6H_2O$, 0.35 $NaHCO_3$ and MgCl2•$6H_2O$ (g/L)			
Ti-6Al-4V	as-cast	1.60E-04	Choubey et al., 2004

The implant surface characteristics are determined by topographic properties, mechanical properties and physiochemical properties, all of which determine the tissue reaction to the oral implant (Parithimarkalaignan and Padmanabhan, 2013; Viteri and Fuentes, 2013). The mechanical properties of medical implants include hardness and stiffness (Parithimarkalaignan and Padmanabhan, 2013; Saini et al., 2015). Applied stresses may increase corrosion rates and relative movement of the implant against the host bone, which may cause wear (Parithimarkalaignan and Padmanabhan, 2013; Saini et al., 2015). The surface topography includes surface texture, roughness and orientation of the surface irregularities.

Surface roughness of implants promotes firmer bone fixation (Buser et al., 1991; Saini et al., 2015), and has different scales (micro- and nano-sized) which have different biological roles. In Ti, rough surfaces in the nanometre rage played an important role in adhesion of cells and protein adsorption (Le Guéhennec et al., 2007), whereas rougher surfaces in the micro-scale promote integration of mineralised bone and the implant. Bone quality of patient is related to the age, and its mechanical properties decrease with age (Saini et al., 2015), and affect the success of osseointegration.

Titanium has good tissue adsorption on the surface and the ability to bind with living cells (Shah et al., 2016). Depending on the manufacturing technique and machining conditions, both CP-Ti and Ti-6Al-4V have similar surface roughness (Palmquist et al., 2009; Shah et al., 2016). In some instances, Ti-6Al-4V alloy has lower surface roughness than CP-Ti, attributed to its higher micro-hardness. Commercially Pure Ti and Ti-6Al-4V undergo successful osseointegration with high bone ingrowth and high bone area as threaded implants and removed torque with no apparent adverse tissue reaction (Stenport and Johanssan, 2008; Palmquist et al., 2009; Shah et al., 2016). Higher removal toque is mostly found in CP Ti than Ti alloys (Stenport and Johanssan, 2008; Palmquist et al., 2009) after at least 8 weeks implantation (Palmquist et al., 2009). More mineralised bone tissues were found in CP-Ti than Ti-6Al-4V (Shah et al., 2016), where reduced minerals in the bone adjacent to Ti-6Al-4V was associated with the harmful alloying elements that hindered apatite formation. This shows that CP-Ti was biocompatible and promoted bone adsorption. These studies were carried out in rabbits or rats and most implants were threaded (Stenport and Johanssan, 2008; Palmquist et al., 2009; Stenlund et al., 2015; Shah et al., 2016).

Porous Ti-based implants have reduced elastic moduli and thus provide homogeneous stress transfer between the bone and the implant (Li et al., 2014). The pores provide biological fixation by promoting bone ingrowth into the pores of the implant. Furthermore, porous Ti based alloys have interconnected structures which provide sites for allowing stable blood supply and accommodating new bone tissue (Li et al., 2006). Interconnectivity also allows circulation of other body fluids. High porosity is vital for cell viability, adhesion, growth and differentiation (Li et al., 2006; Li et al., 2014). However, high porosity causes decreased the elastic modulus, yield and tensile strength (Li et al., 2014). Commercially pure Ti Grade 1 wire had elastic modulus of 116 GPa, yield strength of 300 MPa, tensile strength of 370 MPa (He et al., 2012). A 48% porous non-woven Ti wire decreased its elastic modulus to 1.05 GPa, yield strength to 75 MPa and tensile strength to 108 MPa. At 57.9% porosity, the values significantly decreased to 0.33 GPa, 24 MPa and 47.5 MPa, respectively.

2.2.4. Effect of beta-stabiliser additions on implant materials

Alloying Ti with β-stabilisers can reduce the melting temperature and reduce its reactivity with oxygen at high temperature (Okabe et al., 2001). Tantalum, Nb and Zr are beta-stabilisers which have the preferred mechanical properties, biocompatibility and anticorrosion properties (Eisenbarth et al., 2004). Beta-stabilisers in Ti also formed less soluble oxides thus, making the oxide film more stable and inert (Chen et al., 2020). The addition of β-stabilisers to Ti significantly reduced metal ion release (Geetha et al., 2009). Beta-alloys had improved fatigue resistance and superior resistance to abrasion and wear compared to α+β titanium alloys (Zhang and Chen, 2019). Commercially pure Ti has an elastic modulus close to 105 GPa and α+β alloys have the elastic modulus around 110 GPa. The Ti–6Al–4V alloy has been used in the biomedical applications because of its favoured mechanical properties. The mechanical and corrosion properties of Ti alloys are related to their microstructure including grain size (Li et al., 2013). Mechanical properties of TI alloys can be improved by heat treatments to tailor the properties required for specific applications. New β-type Ti alloys with non-toxic elements and low modulus of elasticity, improved mechanical strength and greater corrosion resistance are suitable for biomaterial implants (Mohammed et al., 2014). Beta stabilisers enhance the strength while keeping a low elastic modulus (Sidhu et al., 2020). A comparative study of electrochemical behaviour of CP-Ti and Ti-based alloys showed that the corrosion rate of Ti alloyed with Zr and Nb was lower than CP-Ti and Ti-6Al-4V (Revathi et al., 2014). The addition of Ta, Nb or Zr can impart great strength to Ti alloys (Zhang and Chen, 2019; Nicholson, 2020). The β alloy Ti-29Nb-13Ta-4.6Zr (TNTZ) demonstrated superior bone tissue response and excellent biocompatibility compared to Ti-6Al-4V alloy (Tane et al., 2008). A single crystal Ti-29Nb-13Ta-4.6Zr oriented in the <100> direction had a lower elastic modulus of 35 GPa (Tane et al., 2008). The strength of β Ti alloys can be increased while retaining the elastic modulus low by cold working after solution treatment (Niinomi et al., 2002) e.g 62 GPa for a hot forged and cold worked TNTZ alloy. After solution treating at 790°C (above the β transus) and water quenching, TNTZ had an elastic modulus of 65 GPa. After subsequent ageing at 400°C for 72h the elastic modulus was 97 GPa. The elastic modulus of β-type Ti alloys increases with increased strength and precipitation of α or β phases by ageing (Niinomi et al., 2002). Figure 2.17 shows the healing process of a fractured rabbit bone, with a series of implanted alloys (Niinomi et al., 2002). The low elastic modulus of the TNTZ alloy enhanced bone healing and bone remodelling (Figure 2.17a) more than the Ti-6Al-4V (ELI) (Figure 2.18b) alloy and stainless steel (Figure 2.17c).

Alloys Ti-6Al-4V, Ti-6Al-7Nb and Ti-13Nb-13Zr were immersed in balanced salt solutions with a constant physiological pH of 6.2 for 56 hours (de Assis et al., 2006), and the solution was naturally aerated at 37°C. A rapid increase in corrosion potentials with time was observed, which was related to formation and growth of the oxide film responsible for corrosion resistance (Lavos-Valereto et al., 2002; de Assis et al., 2006). Conversely, increased potential with current density in polarisation curves was associated with the thinning of the oxide films (Karthega et al., 2007; Lavos-Valereto et al., 2002). The high impendence suggested high corrosion resistance (Lavos-Valereto et al., 2006; de Assis et al., 2006). Lavos-Valereto et al. (2004) found a two-layer oxide film on Ti-6Al-7Nb alloy in Hank's solution, similar to Lavos-Valereto et al. (2006) and Karthega et al. (2007) on the TNTZ alloy. The bilayer oxide film had an outer porous layer (Lavos-Valereto et al., 2004; de Assis et al., 2006; Karthega et al., 2007), and the high impedance value was associated with the inner barrier layer. Corrosion resistance of these alloys was due to inner layer and osseointegration was associated with the outer porous layer (Lavos-Valereto et al., 2004). It was assumed that after implantation, bone cells tend to occupy the microscopic pores on the passive film, and this interpenetration speeds implant anchorage, accelerating osseointegration.

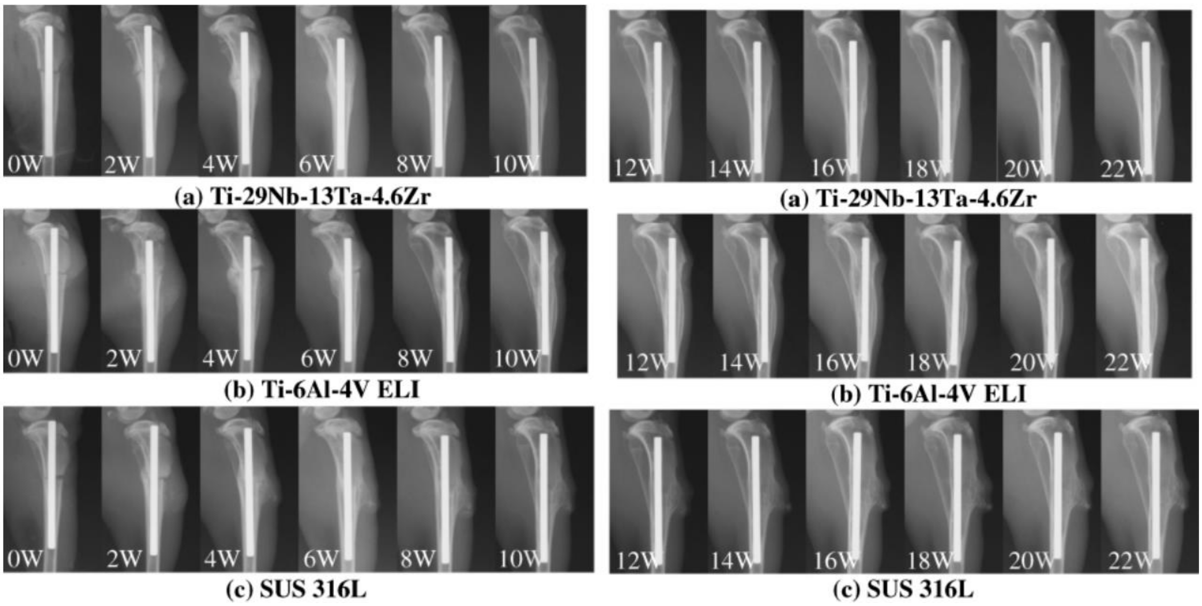

Figure 2.17: Healing process of fractured bone between 0-22 weeks after surgery (Niinomi et al., 2002).

The Ti-10.1Ta-1.7Nb-1.6Zr alloy has similar phase proportions to Ti-6Al-4V (Stenlund et al., 2015). Heat treated Ti-10.1Ta-1.7Nb-1.6Zr had a hardness of 223 HV_5, elastic modulus of 89 GPa, ultimate tensile of 542 MPa and yield strength of 502 MPa. The bone response demonstrated better biocompatibility, less inflammatory response and better osseointegration than CP-Ti. Biomechanical evaluation after 7 and 28 days of healing showed a strong anchorage.

2.2.5. Copper additions and antibacterial Ti alloys

Different antibacterial surface approaches have been designed to kill bacteria attaching to the implant surfaces, or by inhibiting the attachment of bacteria to the implant surfaces. Surface coatings and surface modification have the disadvantage that they are non-uniform, mechanically weak and lack long-term stability (Hasan et al., 2013). The reported procedures used in eliminating the inflammatory lesions have been effective, but to achieve reosseointegration to the once-contaminated surface was impossible (Mouhyi et al., 2012). Bacteria developing resistance to antibiotics has restricted the use of antibiotics for treatment of bacterial films (Stewart et al., 2001). Poor tissue response or cellular attachment caused by unfavourable chemistry on antibacterial surface coatings (Hasan et al., 2013) has identified the need for biomedical implants with antibacterial properties. Alloying Ti with elements with an antimicrobial property is the solution. Copper and silver have antibacterial properties (Yoon et al., 2007; Arciola et al., 2012; Olczak et al., 2012). The antibacterial activity of Cu- and Ag-containing alloys can be achieved by distal and contact killing (Shi et al., 2020). Distal killing is reported to be achieved by the release of Cu and Ag ions from the surface of the metal containing the elements. Contact killing is achieved by the precipitated Ti_2Cu and Ti_2Ag particles at the surface of the alloys. Shi et al. (2020) reported that the Ag ions released by Ti-*x*Ag (*x* = 7, 9 and 11 wt%) did not reach toxic levels. Similarly, the presence of Ti_2Ag precipitates did not show cytotoxicity. The antibacterial activity of Ag-containing alloys is not influenced by the content. Li et al. (2009) reported that Ti with 1 wt% Ag gave good antibacterial properties. Good mechanical strength and high elongations were retained even at 20 wt% Ag in Ti-Ag alloys (Takahashi et al., 2002). Better corrosion resistance was found in Ti-Ag alloys than pure Ti (Shim et al., 2005; Zhang et al., 2009). Different human cells are affected by Ag ions differently depending on the ion concentrations. Galandáková et al. (2016) reported that cytotoxicity occurred at 25 µg/mL where Ag ions were released from Ag nanoparticles. Tweden et al. (1997) reported cytotoxity at 12 µg/mL. Both Ag and Cu ions can cause tissue damage when they reached high concentrations (Oliveira et al., 2018; Shi et al., 2020). Some studies have reported that to achieve good antibacterial activity Ti-Ag must be surface treated. Antibacterial effects occurred when the alloy was grit blasted with alumina particles and acid-etched (Kang et al., 2012). Shi et al. (2020) acid-etched the alloys to increase the volume fraction of the Ti_2Ag particles at the surface and enhance the Ag ion release.

Silver nanoparticles were mostly used to study the mechanism of bacteria inactivation (Morones et al., 2005; Marambio-Jones and Hoek, 2010; Reidy et al., 2013). The Ag nanoparticles in the range of 1–10 nm adhere on the surface of the cell, envelop it and are destructive to its permeability and respiration, thus drastically disturbing the cells' viability. The nanoparticles cause further damage by penetrating inside the bacteria. They then react with sulphur- and phosphorus-containing compounds such as DNA. The nanoparticles release Ag ions, which interact with the DNA molecules causing DNA denaturation. The molecules become condensed, so DNA replication is disturbed. The Ag ions also interact with thiol groups in the proteins, which alters the protein shape, causing the bacteria to loose cell viability which leads to bacteria inactivation (Feng et al., 2000; Morones et al., 2005).

Sato and Taya (2006) demonstrated photo-killing of bacteria on Cu/TiO_2 films. They suggested that in liquids Cu^{2+} that leached from the film surface received an electron from the photo-excited TiO_2 and was reduced to Cu^+ (1). The Cu^+ then reacted with H_2O_2 to produce •OH and OH^- in a Fenton-type reaction (2) (Sato and Taya, 2006):

$$Cu^{2+} + e^- \rightarrow Cu^+ \quad \text{(Equation 2.1)}$$

$$H_2O_2 + Cu^+ \rightarrow OH^- + \bullet OH + Cu^{2+} \quad \text{(Equation 2.2)}$$

Wojcieszak et al. (2015) studied the impact of Cu-Ti thin film surfaces on antibacterial activity and functioning of living cells, and showed that the Cu^{2+} ions were released from the film surfaces. The antibacterial activity was closely linked to Cu^+ ions.

In the oral environment, reactive oxygen species (ROS) are generated by inflammatory processes, dental materials and other chemical reactions (Zukowski et al., 2018). When a Ti implant is inserted in a human body it triggers adverse reactions like inflammation (Handzlik and Fitzner, 2013). The ROS such as hydroxyl radical (·OH), superoxide anions ($\cdot O_2^-$) and hydrogen peroxide (H_2O_2) are then generated at the Ti surface (Foster et al., 2011) by the inflammatory processes (Zukowski et al., 2018). These ROS are highly reactive and harmful to bacterial and mammalian cells at high concentrations. They act on the cell membranes, making the cells lose their proper functioning. The exposure of cells to ROS causes cell wall damage and increased permeability, exerts oxidative stress on the cytoplasmic membrane and oxidative damage to cell's DNA and eventually leads to cell death (Huang et al., 2000). Reactive oxygen species react with DNA bases disrupting DNA replication process (Dizdaroglu and Jaruga, 2012). These free radicals can also cause chronical diseases and cell death (Von Sonntag, 2006).

Li et al. (2016) investigated the antimicrobial mechanism of Ti-6Al-4V-5Cu which released Cu ions in saline solution. The destructive effect of Cu ions and the ROS are schematically illustrated in Figure 2.18 (Li et al., 2016). Cells with damaged cytoplasmic membranes were found on the Cu-containing alloy. With increased incubation time, the antibacterial effect of the alloy also increased. Outflow of the cellular content was observed on the cells, which Li et al. (2016) suggested was caused by the increased permeability of the cell envelope. Also, the Cu ions released from the surface of the alloy enhanced the generation of the ROS and interfered with the DNA replication of the bacterial cell.

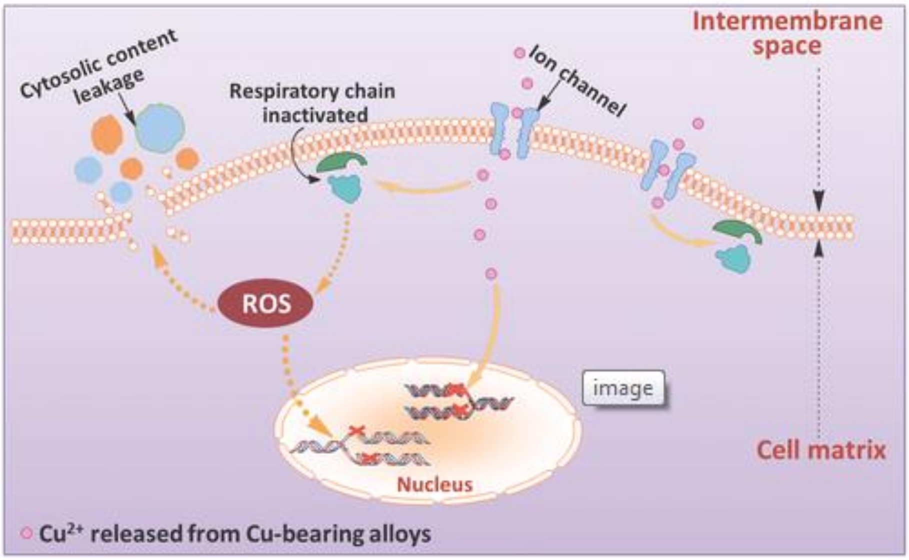

Figure 2.18: Schematic illustration showing possible antibacterial mechanisms on the surface of Ti-6Al-4V-5Cu implants (Li et al., 2016).

Liu et al. (2016) used a Ti-5Cu alloy to test the antibacterial effect on two different bacteria strains and compared the results to bacteria that were cultured on a pure Ti sample. TEM micrographs of both bacteria cultured on the pure Ti samples showed undamaged cell walls and membranes and well-maintained cytoplasmic membranes (Figure 2.19a, b, e, f). The morphological changes in both bacteria treated with the Ti-5Cu alloy had damaged cell envelopes (Figure 2.19c, d, g, h). The destructive effect of Cu led to decay of membrane layer (Figure 2.19c) and detachment of cell wall from the cell membrane (Figure 2.19d). A damaged cell wall and leakage of cytoplasm was observed in bacteria treated with Ti-Cu (Figure 2.19g, h). A similar study was conducted by Jung et al. (2008) who investigated the antimicrobial activity of two bacterial strains when exposed to a silver laundry machine that released Ag ions during washing and rinsing. TEM was used to analyse internal morphological changes in both silver-treated and nontreated bacterial strains. The untreated bacteria were normal, retaining their cell surface and cytoplasmic membranes (Figure 2.20a, b, left and right). After Ag ion treatment *Staphylococcus aureus* showed breakdown of cell walls and membranes, and decreased cytoplasm content (Figure 2.20c, d left). The *Escherichia coli* had damaged cells showing separation of cell wall from cell membrane and release of cellular content (Figure 2.20 c, d right) (Jung et al., 2008).

A series of Ti alloys, Ti-*xCu* (*x* = 0.5, 1, 2, 5 and 10 wt% Cu) was studied and shown to have good mechanical properties, anticorrosion and antibacterial properties (Kikuchi et al., 2003; Zhang et al., 2016b). The corrosion resistance of Ti-Cu alloys was better than CP-Ti (Zhang et al., 2013; Lui et al., 2014), with corrosion rates decreasing with increased Cu content. The Ti_2Cu phase was found in all the Ti-Cu alloys studied and phases like $TiCu_4$, TiCu, Ti_3Cu_4 or Ti_2Cu_3 were found in alloys with higher Cu contents (Zhang et al., 2013; Zhang et al., 2016a). Sufficient Ti_2Cu for good antimicrobial effects occurred in alloys with at least 5 wt% Cu (Zhang et al., 2013; Zhang et al., 2016a; Zhang et al., 2016b). Copper content influences the antibacterial rate (Liu et al., 2014b; Ma et al., 2016; Zhang et al., 2016b). Lui et al. (2014) reported that Ti-Cu sintered alloys needed at least 5 wt% Cu for good antibacterial properties.

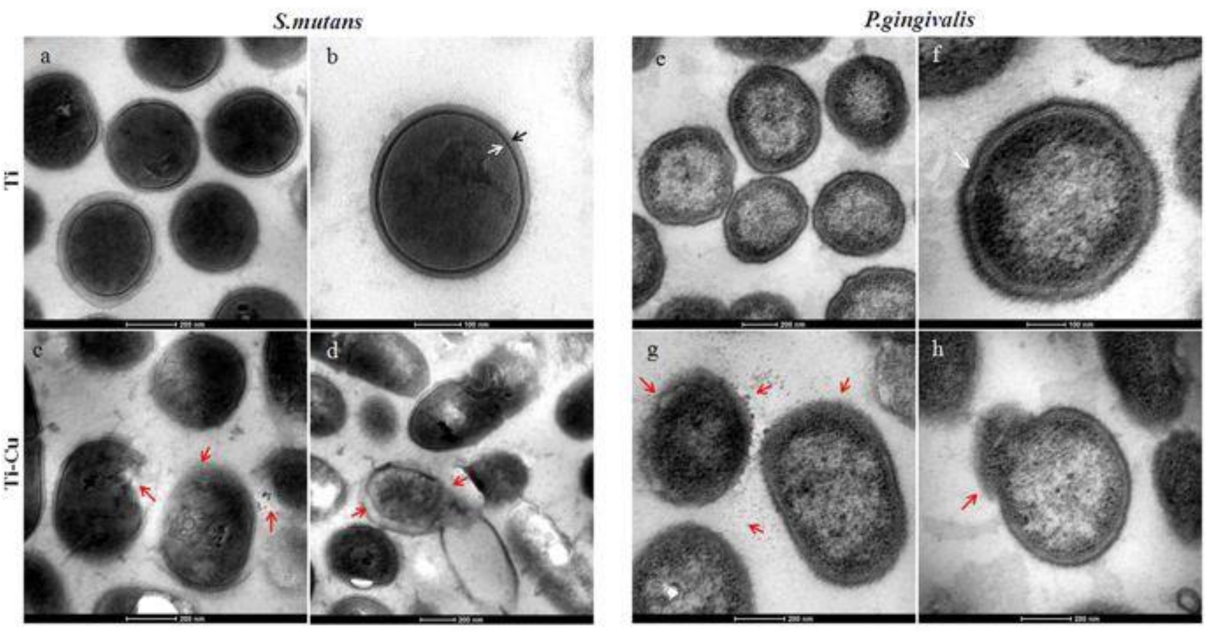

Figure 2.19: TEM micrographs of treated Streptococcus mutans and Porphyromonas gingivalis (Liu et al., 2016). Peptidoglycan layer and cytoplasmic membrane are indicated by black and white arrows and red arrows indicate separation of cell wall and cell membrane, and release of content.

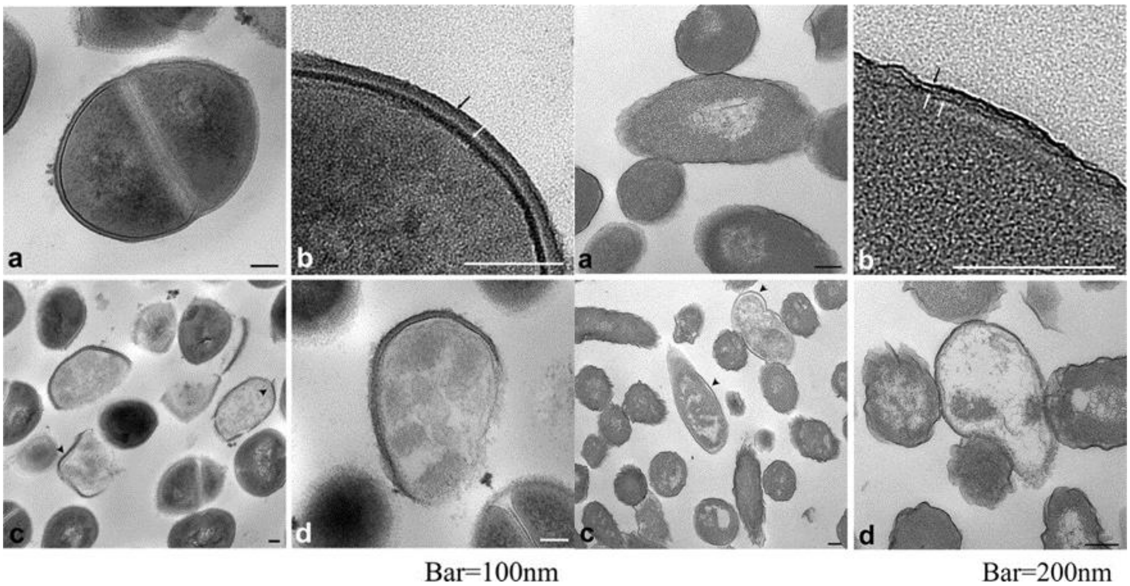

Figure 2.20: TEM micrographs showing internal structure of Staphylococcus aureus (left) and Escherichia coli (right): (a and b) Untreated bacteria, (c and d) Bacteria treated with silver ion solution (0.2 ppm) (Jung et al., 2008). Black arrow indicates peptidoglycan, cytoplasmic membrane indicated by white arrow and separation of cell membrane from cell wall indicated by arrowhead.

Killing of bacteria was achieved when bacteria was in contact with the alloys (Zhang et al., 2013). The right Cu content that will balance the good antibacterial properties and other properties needed to be investigated. The elongation of Ti-Cu alloys measured by Kikuchi et al. (2003) decreased with increased Cu content (Figure 2.22). However, high Cu content increased mechanical strength of Ti alloys (Takahashi et al., 2002; Kikuchi et al., 2003). The hardness values of the alloys were lower than Ti-6Al-4V (Figure 2.21). The Ti_2Cu intermetallic phase decreased ductility, increased mechanical strength and antibacterial properties (Lui et al., 2014; Zhang et al., 2016b). The tensile and yield strength measured by Kikuchi et al. (2003) was higher than CP-Ti, but lower than of Ti-6Al-4V (Figure 2.21). The measured elastic moduli of the series of alloys were between the values of CP-Ti and Ti-6Al-4V. Kikuchi et al. (2003) found cracks on the exterior surfaces of the 1 and 5 wt% Cu alloys after tensile tests. Fewer cracks were seen on higher Cu content alloys. Aoki et al. (2004) studied Ti-6Al-4V-*xCu* (*x* = 0, 1, 4 and 10 wt% Cu) alloys and measured their mechanical properties. The elongation decreased with increased Cu content, while tensile and yield strength increased with increasing Cu content. Copper additions also reduced the elastic modulus of the alloys except for the 10 wt% Cu which had highest value, and higher than CP-Ti (Aoki et al., 2004). Transverse cracks were seen on the exterior surfaces of the alloys, fewer cracks were seen with increased Cu content and no cracks were found on the 10 wt% Cu alloy.

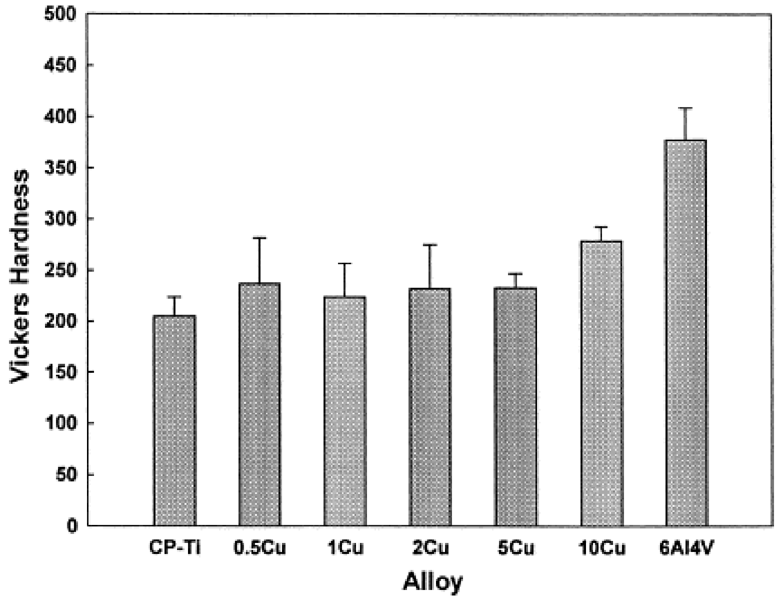

Figure 2.21: Hardnesses of as-cast Ti-Cu alloys (Kikuchi et al., 2003).

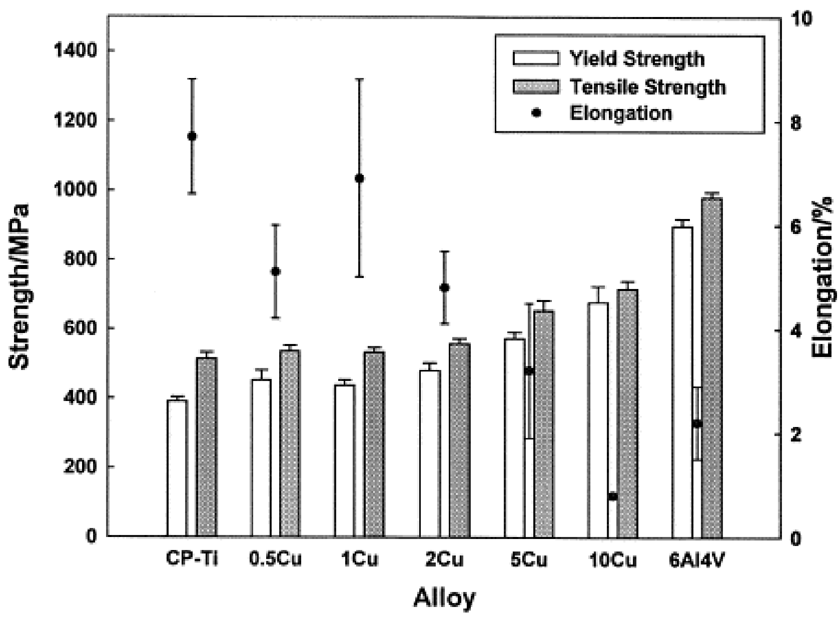

Figure 2.22: Yield strength, tensile strength and elongation of as-cast Ti alloys (Kikuchi et al., 2003).

A series of alloys, Ti-*xCu* (*x* = 2, 3 and 4 wt% Cu) was prepared by arc melting and remelted six times to obtain homogeneous chemical compositions (Zhang et al., 2016a). Some of the ingots were subjected to solid solution 900°C for 3h and some were subsequently aged at 400°C for 12h (Zhang et al., 2016a). Heat treatments improved the antibacterial rate significantly. The calculated antibacterial rates of as-cast Ti-Cu alloys were between 33-36% and 60-67% for the solution treated alloys, which were all less than 90% recommended for antibacterial ability (Zhang et al., 2016a). However, more than 90% antibacterial efficacy was achieved for Ti–3Cu and Ti–4Cu alloys, after a solid solution and ageing. Zhang et al. (2016a) suggested that the minimum content for achieving good antibacterial rate in as-cast and heat treated Ti-Cu alloys was 3 wt% Cu. Zhang et al. (2016b) observed that higher antibacterial rates (>99%) occurred in sintered alloys and the Ti_2Cu phase was mostly in these alloys. Figure 2.23 shows a typical microstructure of the Ti-5Cu alloys, with Figure 2.23a showing Ti_2Cu.

Cytotoxicity of the Ti-5Cu alloy on self-renewing stem cells, mesenchymal stem cells from rat bone was performed and the results were compared to the cells that were suspended on CP-Ti (Liu et al., 2016). Relative growth rates of these cells at 1-7 days showed non-cytotoxicity on both samples. Cell adhesion was observed on both CP-Ti and TI-5Cu after 4 hours of culturing, with more cells found on the Ti-5Cu alloy.

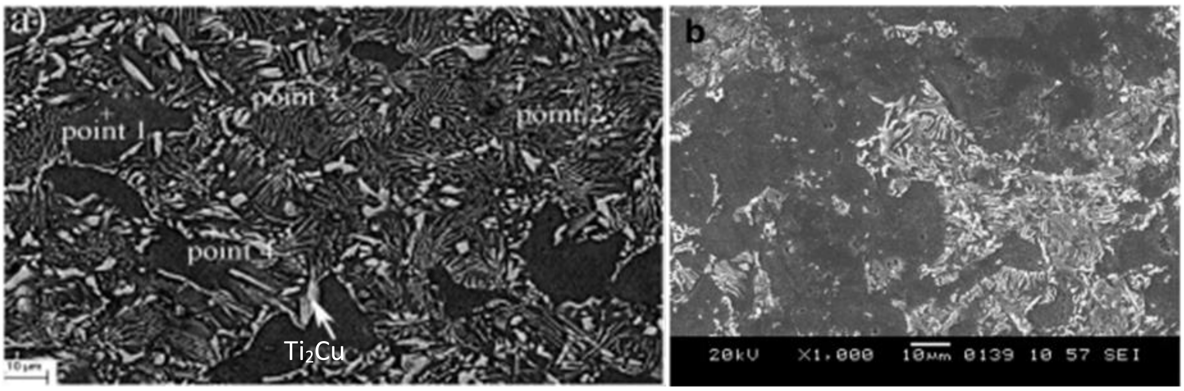

Figure 2.23: SEM–BSE images of Ti-5Cu alloys: (a) (Zhang et al., 2016b) and (b) (Liu et al., 2014), showing Ti_2Cu (arrows).

Figure 2.24 shows the accumulation of Cu ions released from Ti-5Cu alloys. The samples were prepared by arc melting and the ingots were remelted five times for homogeneity. The ingots were forged at 860°C and heat treated at 900°C for 2 hours then air cooled (Ma et al., 2016).

Liu et al. (2016) also prepared a Ti-5Cu alloy (Figure 2.24b) by arc melting. The ingot was forged, and heat treated at 850°C for 2 hours and furnace cooled. Ma et al. (2016) and Liu et al. (2016) machined their samples as discs with dimensions of 10mm in diameter and 2mm thickness, then immersed them in solutions of 0.9% NaCl at 37°C. Lui et al. (2016) estimated the average daily release rate of Cu ions from the Ti-5Cu alloy to be 1.584 x 10^{-4} µg/L/day.

Two different bacterial strains were used to calculate the minimum inhibitory concentration of Cu ions needed to kill them. The measured values were much higher than the estimated average daily release rate of Cu ions from the Ti-Cu alloy (Du et al., 2009), indicating that the Ti-5Cu alloy had efficient antibacterial properties. The copper limit for humans stated by the World Health Organization is 2-3 mg/day (Liu et al., 2016), which is higher than the estimated average daily release rate Cu ions by Ti-5Cu alloys (Liu et al., 2016).

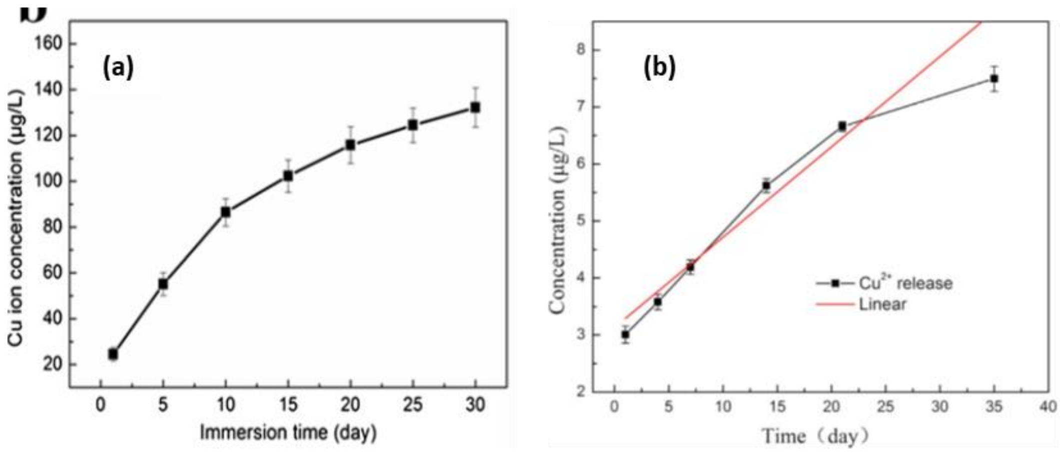

Figure 2.24: Cumulative Cu ion concentration (µg/L) curves released from Ti-5Cu binary alloys (a) (Ma et al., 2016) and (b) (Liu et al., 2016).

2.3. Summary of literature review and rationale of the project

From the literature survey, the widely used Ti-6Al-4V needs to be replaced due to potential harmful risks imposed by its alloying elements. Commercially pure Ti has good advantages such as biocompatibility and good tissue adsorption on the surface (Shah et al., 2016), but its mechanical properties were lower than the Ti-6Al-4V alloy (Li et al., 2014). Although Ti-6Al-4V promoted bone resorption (Shah et al., 2016), the demineralisation of the resorbed bones imposed by its harmful alloying elements encourages development of new Ti alloys (Shah et al., 2016; Chen et al., 2020).

Biomechanical incompatibility between the bone and implant is also the major issue in Ti-6Al-4V (Li et al., 2014). Its high stress transfer to the bone inhibits bone integration with the implant (Ridzwan et al., 2007). Titanium alloys with lower elastic moduli and high yield and tensile strength need to be identified. These Ti alloys need to contain toxic free alloying elements. From the literature non-toxic β-stabilisers were identified and were suggested as best alloying elements: Nb, Au, Zr, Ru, Sn and Ta (Biesiekierski et al., 2012)

Titanium-copper alloys have been suggested as the best alloys to inhibit bacterial colonisation (Zhange et al., 2016a). A minimum of 5 wt% Cu-containing Ti alloys gave good antibacterial properties and slightly enhanced corrosion resistance (Liu et al., 2016). However, their high elastic properties (Kikuchi et al., 2003) encourage investigation of new Ti alloys. Sintering of these alloys yielded higher antibacterial rates than as-cast alloys (Zhang et al., 2016b). However, sintering gave lower mechanical properties than as-cast alloys. Zhang et al. (2016a showed that solution treatment followed by ageing significantly improved the antibacterial properties of the as-cast Ti-Cu alloys.

Small Ru additions to CP-Ti and Ti-6Al-4V significantly increased resistance to corrosion in HCl acid and NaCl media (Schutz, 1996). Additions of <1 wt% Ru had no effect on the mechanical properties. These findings need to be evaluated on new Cu-containing alloys for dental applications. To evaluate better corrosion resistance of Ru-containing alloys for biomedical applications, the new Ti alloys need to be tested under artificial physiological solutions. Phosphate buffered saline (PBS) solution can be used to perform corrosion test since PBS does not change pH (Rosenbloom and Corbett, 2007).

Thus, the aim of this study was to develop alloys, with non-toxic β-stabilisers to lower the elastic modulus and retain the α+β phases as in the Ti-6Al-4V alloy. To achieve antibacterial properties copper elements were added to the α+β Ti alloy. Ruthenium additions were added to improve the corrosion resistance.

Chapter 3: Experimental Procedure

This chapter provides information on sample manufacturing, experimental set-ups and the experimental methods used in this research. The methods used to identify and develop the alloys are discussed in detail, starting with Thermo-Calc calculations to identify phases that were likely to be present in different compositions. The best compositions from the Thermo-Calc results were used to make samples. The characterisation techniques used in studying the sample's phases, microstructures and hardnesses are described and the corrosion testing.

3.1. Thermo-Calc Calculations

The Thermo-Calc software was used to calculate the phases of compositions likely to mimic the phase proportions in the Ti-6Al-4V alloy using the TTTI3 Titanium-Database (Andersson et al., 2002). The software was also utilised to provide information on the possible phases and transformation temperatures in the compositions input. The phase proportions were calculated between 400-2000°C. Using the chosen alloy components, the mass percentages were altered until the phase proportions were similar to Ti-6Al-4V alloy. Copper additions were altered between 1-5wt% although the compositions with 5 wt% Cu were chosen as the potential alloys.

3.2. Alloy Manufacture

This section describes the methods used to prepare the samples for characterisation and the techniques used for characterisation.

3.2.1. Materials

The powders used for the manufacturing the alloys were: high purity titanium (99.7%), tantalum (99.9%), zirconium (slurry), ruthenium (99.99%) and copper (99.5%) from Sigma-Aldrich. Sample compaction was then performed to avoid sample "fluttering" and hence powder loss in the arc melter.

3.2.2. Arc melting

The compacted samples were placed on a water-cooled copper hearth in the arc furnace, then melted. Prior to melting, the chamber was pumped out to $1x10^{-3}$ bar and pure argon gas was introduced, and flushed out three times. A titanium oxygen-getter was melted first to absorb the remaining oxygen and avoid oxidation of the samples (Figure 3.1). To encourage homogeneity, the samples were melted twice.

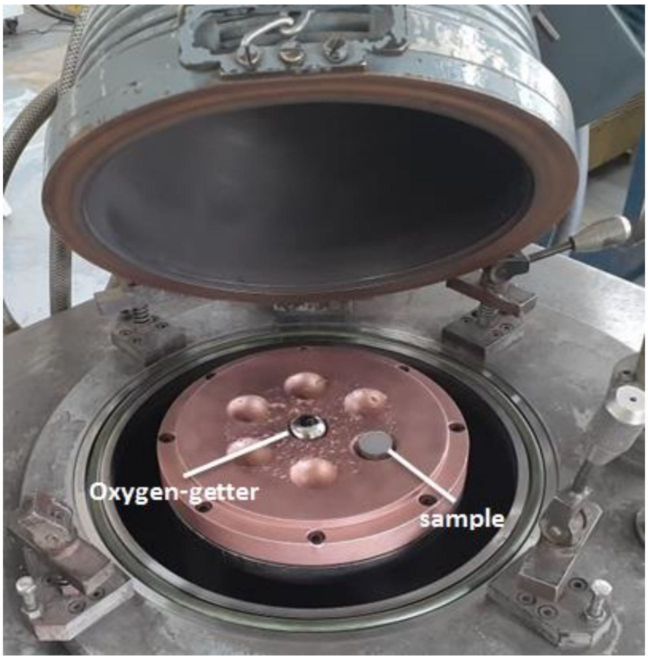

Figure 3.1: Button arc-melting furnace with oxygen-getter (Mintek).

3.2.3. Cutting

The machine used for cutting the samples required them to be mounted before cutting. Each sample alloy was mounted in thermoplastic transparent hot mounting powder for 3 minutes 30 seconds at 200°C under a pressure of 6 bar in an OPAL 410 mounting machine. For characterisation, the samples were cut across the middle to enable study of the cross-sectional area. The cutting used a diamond cut-off wheel with wheel speed of 3000 rpm, feed rate of 0.015 $mm \cdot s^{-1}$ for cut length of 50 mm using a Secotom-10 precision cutting machine. Water was the coolant to prevent the alloy from heating too much during cutting.

3.2.4. Mounting

The cut sections were mounted in a black Bakelite hot mounting resin (MultiFast Black) with the sections of interest facing the exterior. This was because the dimensions of the cut samples were too small to handle for the grinding and polishing. The entire process, heating and cooling took 8 min and 30 s at 180 °C, pressure of 6 bar with water as a coolant.

3.2.5. Grinding and polishing

The mounted samples were ground using automatic (SAPHIR 520) and manual grinding machines (IMPETECH 201). Grinding was done using silicon carbide (SiC) grinding paper with different particle sizes (grades), with water as a coolant. The steps for grinding and polishing were adapted from information on metallographic preparation of Ti alloys (Vander Voort, 1999; Vander Voort, 2006), Table 3.2. Polishing was done on a manual polishing machine (Tegramin-20, Struers) using MD-Chem polishing cloths. A 5:1 solution of colloidal silica and hydrogen peroxide (50%) was used as a suspension (Okawa and Watanabe, 2009). This mixture gave good results as the mirror-like images were achieved, even though the method was different from Vander Voort (1999) where the suspension contained 30% H_2O_2.

3.2.6. Etching

To study the microstructure of the alloys, the samples were cotton-swabbed with Kroll's reagent (Vander Voort, 1999). The etchant was composed of 92 ml deionised water, 6 ml nitric acid and 2 ml hydrofluoric acid. Since the solution contained a dangerous acid, HF, it handled with care, avoiding direct contact with the acid by using gloves, goggles and protective laboratory clothes. After etching the samples were cleaned with ethanol.

3.2.7. Scanning electron microscopy and energy dispersive X-ray spectroscopy

The microstructures of the as-polished and etched alloys were initially checked using a Leica DM 6000 optical microscope. Scanning electron microscopy (SEM) was used to study the samples, obtain micrographs and measure the compositions. This was performed using a field emission ZEISS Sigma 300 VP at an accelerating voltage of 20kV. Secondary electron mode imaging was used to check the overall topography (holes etc.) of the sample at low magnification. Backscattered electron imaging was used to obtain micrographs across the sample. To identify the phases present, several magnifications, 1.04k, 3.04k and 10k X, were used.

Table 3.1: Grinding and polishing steps for Ti-6Ta-1.5Zr-*x*Ru-*y*Cu alloys.

Parameters	Steps					
	1	2	3	4	5	6
Abrasive Discs (Silicon Carbide P Grade)/Polishing cloth	P500	P800	P1000	P1200	P2400	MD Chem
Lubricant	water	water	water	water	water	Colloidal Silica + 50% hydrogen peroxide (5:1) solution
Platen speed/direction	150 rpm/ counter rotation	170 rpm	170 rpm	170 rpm	170 rpm	180 rpm
Force	20 N	Hand	Hand	Hand	Hand	Hand
Time	5 min	1 min	1 min	1 min	2 min	15 min

An EDX detector (OXFORD INTRUMENS x-act PentaFET Precision) and EDS software (Oxford iNCA) was used to analyse the samples. Low magnification was used to analyse five different large areas on each unetched sample to give overall analyses. On each area, three spots were analysed on each phase. The spot analyses were done on phases that were at least 2 microns across (larger than the interaction volume) and for good results the spot was directed at the centre of the phase, to reduce pick-up from the surrounding phases.

3.2.8. X-ray diffraction

To identify the phases present, X-ray diffraction was performed on the polished samples (Table 3.1) using a Bruker D2 Phaser diffractometer. A Co Kα radiation source with wavelength of 1.78897 Å and a nickel filter were used. The measurements were done between 10-140° (2θ) with no spin for 17 min at room temperature. Samples that had unmatched peaks were ran for longer, 1 hour with no spin. The DIFFRAC.SUITE EVA software was used to evaluate the diffraction data and analyse the diffractions peaks to confirm the phases of interest using the PLU2018: 398726 database. Phase identification was done by matching three strongest peaks with the reference lines (Young, 1993; Pecharsky and Zavalij, 2009). The PDF file sources accessed under the PLU2018: 398726 database were used to further confirm the reasonable matches with corresponding phases.

3.2.9. Hardness measurements

The hardness of the ground and polished samples was tested using a Vickers hardness FutureTech Microhardness FM 700 machine. The indentation load was 0.5 kg and a dwell time of 10 s was used. The indentation sizes were measured using the attached low magnification optical microscope. Seven hardness indentations were made across each sample, spaced evenly, the values were recorded, and the means and standard deviations were calculated.

3.2.10. Corrosion tests

Corrosion tests were performed using a three-electrode cell: Pt electrode as the counter electrode, a saturated calomel electrode (SCE) as a reference electrode and the sample as the working electrode (WE). The cell set-up included a Luggin probe with a salt bridge that made the junction with the calomel electrode. The calomel electrode saturated with KCl^- (SCE) was the reference electrode was used between the WE. The Luggin probe tip was adjusted and brought close to the sample (WE). A graphite rod acted as an auxiliary electrode. The rod was inserted through the auxiliary electrode holder to the solution and its other end was connected to the potentiostat.

A thermometer was inserted in the solution to monitor the temperature. An artificial physiological solution, phosphate buffered saline (PBS) solution with a pH of 7.4 (Fowler et al., 2019) was prepared in a 1 L flask using deionised water. The pH of the solution should remain constant throughout (Rosenbloom and Corbett, 2007).

PBS solution:

- 8 g/L sodium chloride (NaCl)
- 0.2 g/L potassium chloride (KCl)
- 1.44 g/L sodium hydrogen phosphate (Na_2HPO_4)
- 0.24 g/L potassium dihydrogen phosphate (KH_2PO_4).

Prior to the experiment, the solution was heated and held 37±1 °C and with a thermostat immersed in the solution to control the temperature. The solution was kept purged with N_2 gas to remove oxygen and ensure anaerobic conditions. A freshly prepared solution was made for each sample tested.

A copper wire was soldered on the samples for electrical connection. The samples were mounted in a nonconductive epoxy resin. The surface exposed to the electrolyte was ground with 1200 grade silicon carbide paper and rinsed with deionised water.

After immersing the sample, the open circuit potential (OCP) vs time was recorded for 17 hours, or until it stablised using a potentiostat. Thereafter, each potentiodynamic polarisation scan was recorded in the range -250 mV to 1500 mV at a scan speed of 10 mV/min. The scan direction was not reversed. The electrochemical test was controlled by the sequencer software (AutoTafel, ACM Instrument).

Chapter 4: Thermo-Calc Results

This chapter gives the calculated phase proportions of chosen compositions. A series of compositions were identified, their phase proportions and phase formations results are shown in the figures and tables. The effect of Ru on BCC and HCP phases is discussed and Cu additions were calculated to see how much Ti_2Cu would be formed. In the last part of the chapter compositions with good phase proportions are identified and selected for future work.

4.1. Thermo-Calc results for Ti-6Al-4V

Figure 4.1 shows the two-phase proportions of Ti-6Al-4V that were mimicked in the identification of the alloys.

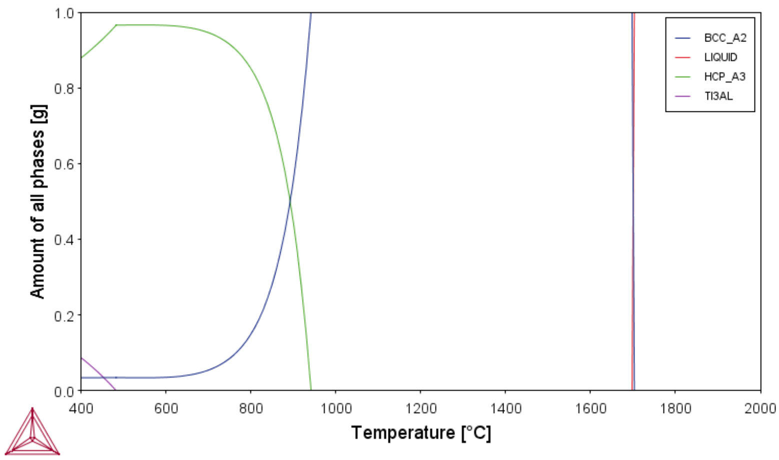

Figure 4.1: Phase proportion diagram of Ti-6Al-4V (wt%).

4.2. Phase proportion calculation of Ti-6Ta-1.5Nb and Ti-6Ta-1.5Nb-0.5Ru-*xCu*

Figure 4.2 shows the phase-proportion diagrams of Ti-6Ta-1.5Nb and Ti-6Ta-1.5Nb-0.5Ru-*xCu* (*x* = 0, 1, 2, 5, 7 wt% Cu) alloys and Table 4.1 gives details of the phases formed in the alloy compositions.

Between 718-842°C the base alloy, Ti-6Ta-1.5Nb (Figure 4.2a) formed HCP from BCC. At temperatures between 564-718°C the phase was entirely BCC and below 564°C, HCP reformed. On Ru addition, the phase proportions of Ti-6Ta-1.5Nb-0.5Ru compositions were similar to the phase proportions of Ti-6Al-4V alloy (Figure 4.1). At lower Cu additions, the Ti_2Cu phase formed at lower temperatures and stabilised at lower proportions than BCC. With increased Cu additions 5 and 7 wt% (Figure 4.2 e, f) more Ti_2Cu was stabilised at lower temperatures than BCC phase. At 5 wt% Cu the Ti_2Cu phase formed from the BCC at 753°C and HCP formed at 767°C. At 7 wt% Cu, Ti_2Cu phase occurred at 796°C, higher than the HCP formation temperature. In both 5 and 7 wt% Cu compositions, the HCP stabilised at higher proportions than BCC and Ti_2Cu at lower temperatures.

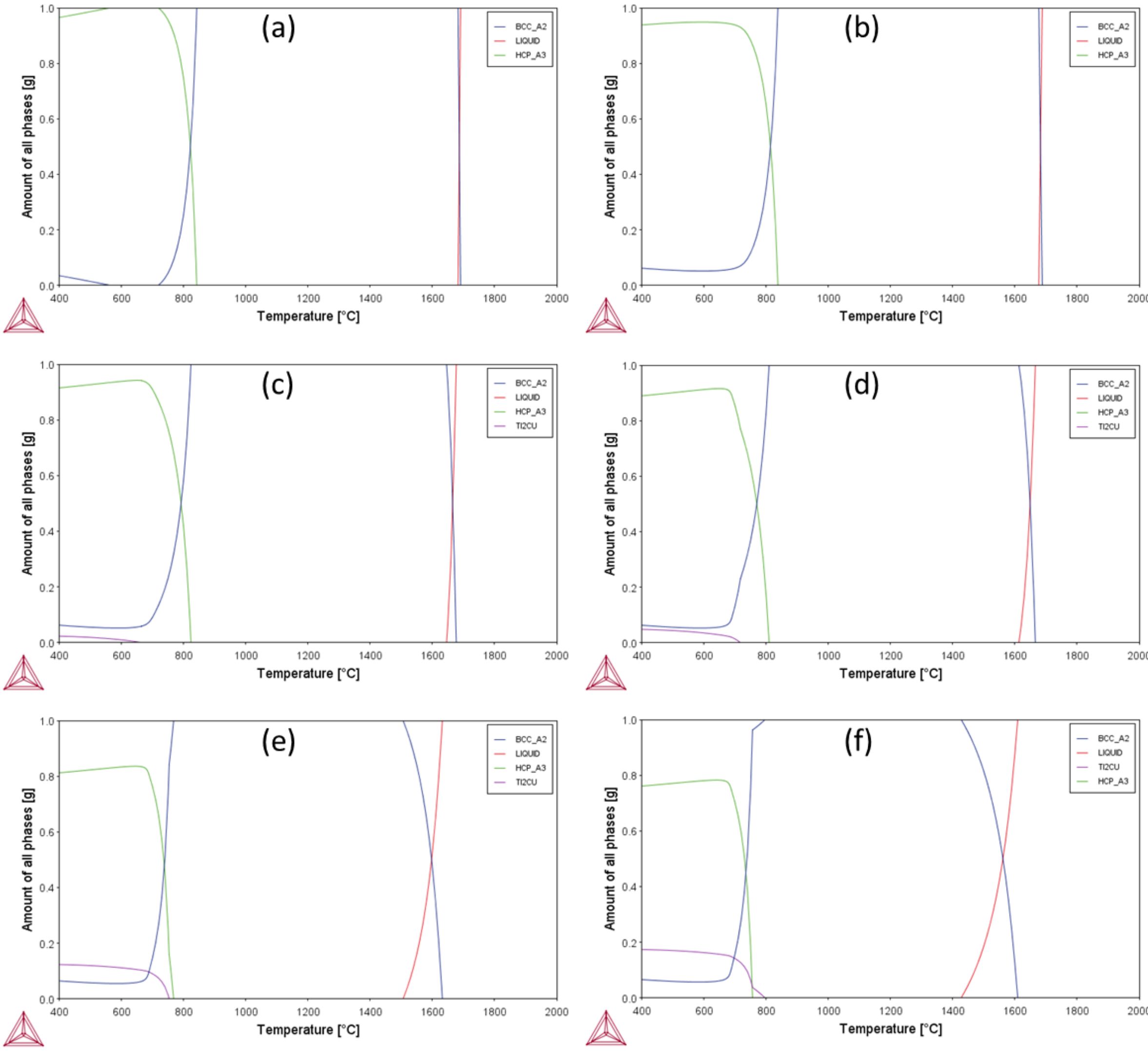

Figure 4.2: Phase proportion diagrams of (a) Ti-6Ta-1.5Nb, (b) Ti-6Ta-1.5Nb-0.5Ru, and (c) Ti-6Ta-1.5Nb-0.5Ru-1Cu, (d) Ti-6Ta-1.5Nb-0.5Ru-2Cu, (e) Ti-6Ta-1.5Nb-0.5Ru-5Cu and (f) Ti-6Ta-1.5Nb-0.5Ru-7Cu (wt%).

Table 4.1: Phases calculated for Ti-6Ta-1.5Nb and Ti-6Ta-1.5Nb-0.5Ru-*x*Cu for *x* = 0, 1, 2, 5 and 7 (wt%).

	Phase proportions (wt%)			
Temperature (°C)	**Amount of HCP**	**Amount of Liquid**	**Amount of BCC**	**Amount of Ti_2Cu**
Ti-6Ta-1.5Nb				
1690.98	---	1	Onset	---
1682.59	---	Onset	1	---
842.13	Onset	---	1	---
718.62	1	---	Onset	---
564.12	1	---	Onset	---
400.00	0.97	---	0.03	---
Ti-6Ta-1.5Nb-0.5Ru				
1676.87	---	Onset	1	---
1687.99	----	1	Onset	---
837.72	Onset	---	1	---
400	0.94	---	0.06	---
Ti-6Ta-1.5Nb-0.5Ru-1Cu				
1645.55	---	Onset	1	---
1677.01	---	1	Onset	
823.62	Onset	---	1	---
664.47	0.94	---	0.06	Onset
400	0.91	---	0.06	0.02
Ti-6Ta-1.5Nb-0.5Ru-2Cu				
1612.81	---	Onset	1	---
1665.92	---	1	Onset	---
809.58	Onset	---	1	---
717.27	0.77	---	0.23	Onset
400	0.89	---	0.06	0.05
Ti-6Ta-1.5Nb-0.5Ru-5Cu				
1505.65	---	Onset	1	---
1632.19	---	1	Onset	---
767.85	Onset	---	1	---
753.45	0.16	---	0.84	Onset
400	0.81	---	0.06	0.12
Ti-6Ta-1.5Nb-0.5Ru-7Cu				
1427.23	---	Onset	1	---
1609.13	---	1	Onset	---
796.64	---	---	1	Onset
756.10	Onset	---	0.96	0.04
400	0.76	---	0.06	0.17

4.3. Phase proportion calculations of Ti-6Ta-1.5Zr and Ti-6Ta-1.5Zr-0.5Ru-*x*Cu

Figure 4.3 shows the phase-proportion diagrams of Ti-6Ta-1.5Zr and Ti-6Ta-1.5Zr-0.5Ru-*xCu* (*x* = 0, 1, 2, 5, 7 wt% Cu) and Table 4.2 gives details of the phases formed in these compositions.

The Ti-6Ta-1.5Zr (Figure 4.3a) had HCP phase at low temperatures. On additions of Ru, HCP and BCC phases were predicted lower temperatures and their proportions were similar to the Ti-6Al-4V alloy. The Ti_2Cu phase formed at lower temperatures than the HCP (Figure 4.3b-d). The HCP formed between 800 - 900^{o}C. As the Cu content increased, the Ti_2Cu phase formed at higher temperatures and the HCP amount decreased. The Ti_2Cu phase formed from the BCC phase, before the HCP phase, above 700^{o}C, Figure 4.3e.

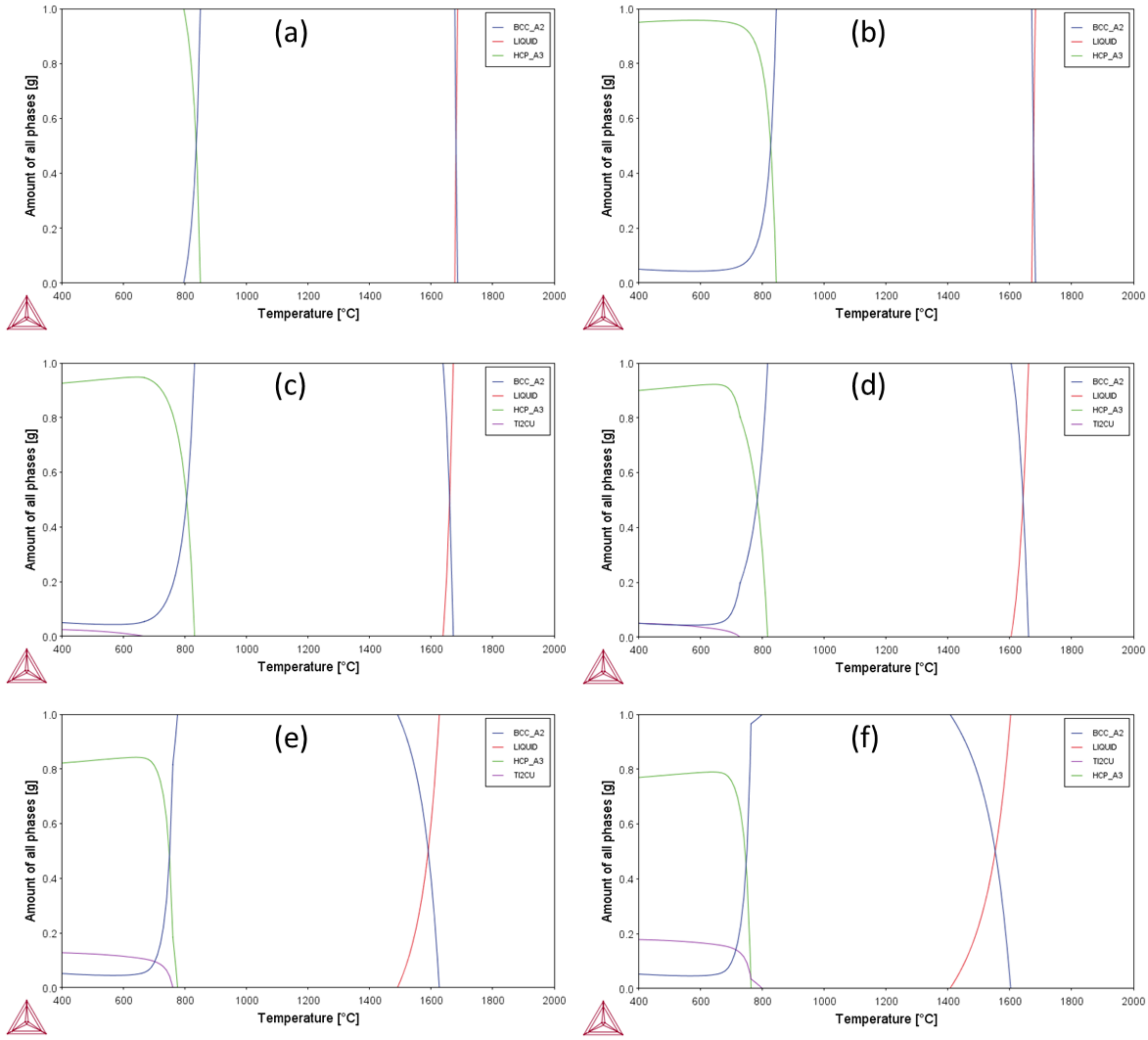

Figure 4.3: Phase proportion diagrams of (a) Ti-6Ta-1.5Zr, (b) Ti-6Ta-1.5Zr-0.5Ru, (c) Ti-6Ta-1.5Zr-0.5Ru-1Cu, (d) Ti-6Ta-1.5Zr-0.5Ru-2Cu, (e) Ti-6Ta-1.5Zr-0.5Ru-5Cu and (f) Ti-6Ta-1.5Zr-0.5Ru-7Cu (wt%).

Table 4.2: Phases calculated for Ti-6Ta-1.5Zr and Ti-6Ta-1.5Zr-0.5Ru-*x*Cu for *x* = 0, 1, 2, 5 and 7 (wt%).

	Phase proportions (wt%)			
Temperature (°C)	**Amount of HCP**	**Amount of Liquid**	**Amount of BCC**	**Amount of Ti_2Cu**
Ti-6Ta-1.5Zr				
1686.01	---	1	Onset	---
1676.99	---	Onset	1	---
849.84	Onset	---	1	---
795.39	1	---	Onset	---
400.00	1	---	---	---
Ti-6Ta-1.5Zr-0.5Ru				
1670.85	---	Onset	1	---
1682.97	---	1	Onset	---
844.84	Onset	---	1	---
400	0.95	---	0.05	---
Ti-6Ta-1.5Zr-0.5Ru-1Cu				
1638.28	---	Onset	1	---
1671.86	---	1	Onset	---
830.87	Onset	---	1	---
667.43	0.95	---	0.05	Onset
400	0.93	---	0.05	0.02
Ti-6Ta-1.5Zr-0.5Ru-2Cu				
1603.98	---	Onset	1	---
1660.64	---	1	Onset	---
816.99	Onset	---	1	---
727.83	0.8	---	0.2	Onset
400	0.9	---	0.05	0.05
Ti-6Ta-1.5Zr-0.5Ru-5Cu				
1490.46	---	Onset	1	---
1626.39	---	1	Onset	---
775.77	Onset	---	1	---
760.31	0.18	---	0.82	Onset
400	0.82	---	0.05	0.13
Ti-6Ta-1.5Zr-0.5Ru-7Cu				
1406.64	---	Onset	1	---
1602.87	---	1	Onset	---
799.78	---	---	1	Onset
763.11	Onset	---	0.97	0.034
400	0.77	---	0.05	0.18

4.4. Phase proportion calculations of Ti-5Nb-4Zr and Ti-5Nb-4Zr-0.5Ru-*x*Cu

Figure 4.4 shows the phase-proportion diagrams of Ti-5Nb-4Zr-0.5Ru-*x*Cu (*x* = 0, 1, 2, 5, 7 wt% Cu) and Table 4.3 gives details of the phases formed in these compositions.

Considering the phase proportions of the Ti-5Nb-4Zr and Ti-5Nb-4Zr-0.5Ru compositions, BCC and HCP were predicted at low temperatures (Figure 4.4a, b). The HCP phase formation was predicted at lower temperatures as the Cu content increased. The Ti_2Cu phase proportions increased, and the HCP formation decreased as the Cu contents increased. There was no effect on the BCC as the Cu content or Ti_2Cu phase increased.

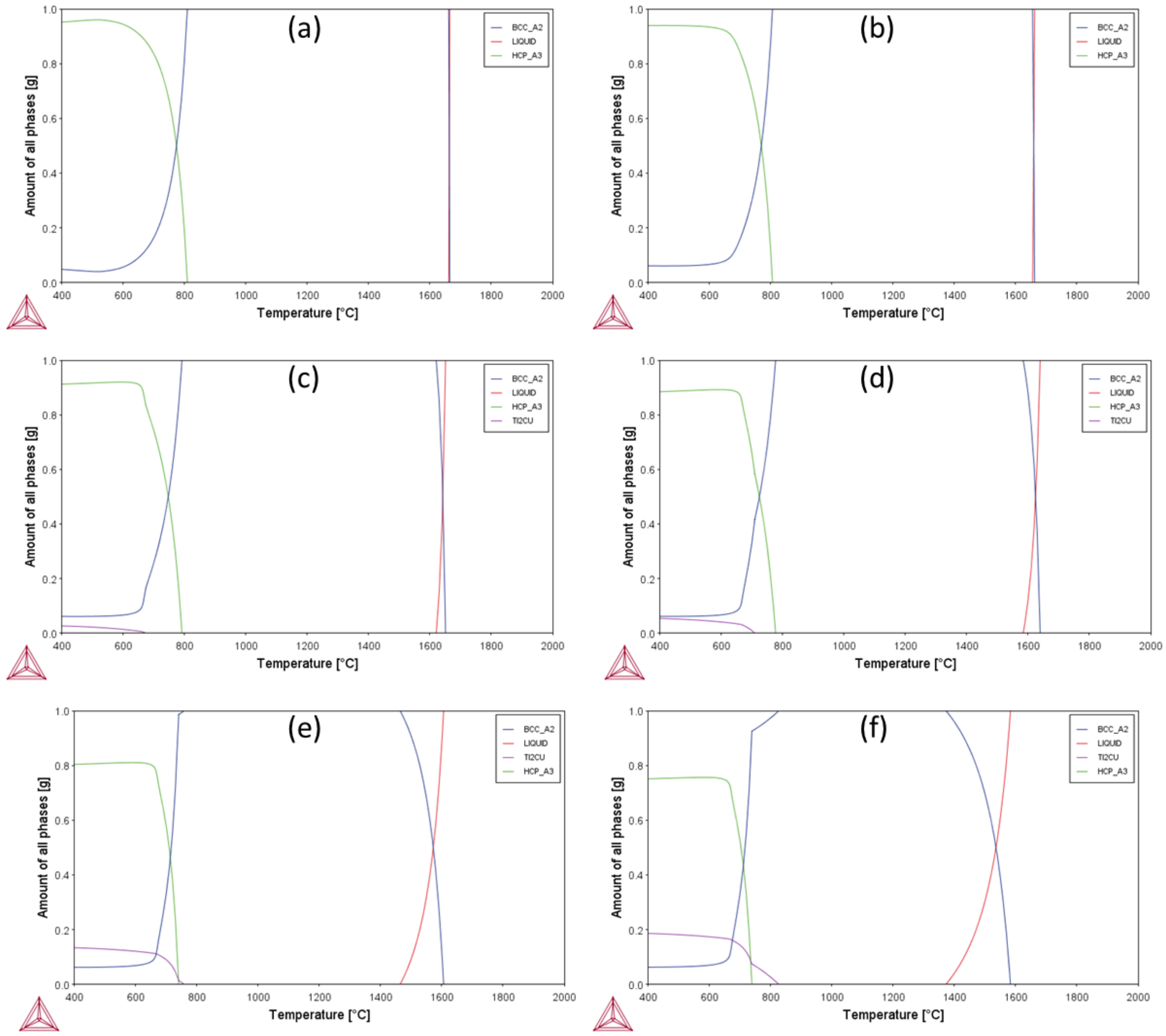

Figure 4.4: Phase proportion diagrams of (a) Ti-5Nb-4Zr, (b) Ti-5Nb-4Zr-0.5Ru, (c) Ti-5Nb-4Zr-0.5Ru-1Cu, (d) Ti-5Nb-4Zr-0.5Ru-2Cu, (e) Ti-5Nb-4Zr-0.5Ru-5Cu and (f) Ti-5Nb-4Zr-0.5Ru-7Cu (wt%).

Table 4.3: Phases calculated for Ti-5Nb-4Zr and Ti-5Nb-4Zr-0.5Ru-*x*Cu for *x* = 0, 1, 2, 5 and 7 (wt%).

	Phase proportions (wt%)			
Temperature (°C)	**Amount of HCP**	**Amount of Liquid**	**Amount of BCC**	**Amount of Ti_2Cu**
Ti-5Nb-4Zr				
1664.86	---	1	Onset	---
1661.37	---	Onset	1	---
809.38	Onset	---	1	---
400.00	0.95	---	0.05	---
Ti-5Nb-4Zr-0.5Ru				
1654.06	---	Onset	1	---
1660.48	---	1	Onset	---
814.45	Onset	---	1	---
400	0.95	---	0.05	---
Ti-5Nb-4Zr-0.5Ru-1Cu				
1619.5	---	Onset	1	---
1649.31	---	1	Onset	---
800.14	Onset	---	1	---
677.87	0.87	---	0.13	Onset
400	0.92	---	0.05	0.03
Ti-5Nb-4Zr-0.5Ru-2Cu				
1583.26	---	Onset	1	---
1638.09	---	1	Onset	---
785.89	Onset	---	1	---
714.26	0.63	---	0.37	Onset
400	0.89	---	0.05	0.05
Ti-5Nb-4Zr-0.5Ru-5Cu				
1463.03	---	Onset	1	---
1604.12	---	1	Onset	---
755.93	---	---	1	Onset
746.66	Onset	---	0.99	0.01
400	0.81	---	0.05	0.13
Ti-5Nb-4Zr-0.5Ru-7Cu				
1372.13	---	Onset	1	---
1581.16	---	1	Onset	---
823.53	---	---	1	Onset
745.12	Onset	---	0.93	0.07
400	0.76	---	0.05	0.19

4.5. Phase Proportion calculations of Ti-6Zr and Ti-6Zr-0.5Ru-*x*Cu

Figure 4.5 shows the phase-proportion diagrams of Ti-6Zr and Ti-6Zr-0.5Ru-*x*Cu (*x* = 0, 1, 2, 5, 7 wt% Cu) and Table 4.4 gives details of the phases formed in the alloys.

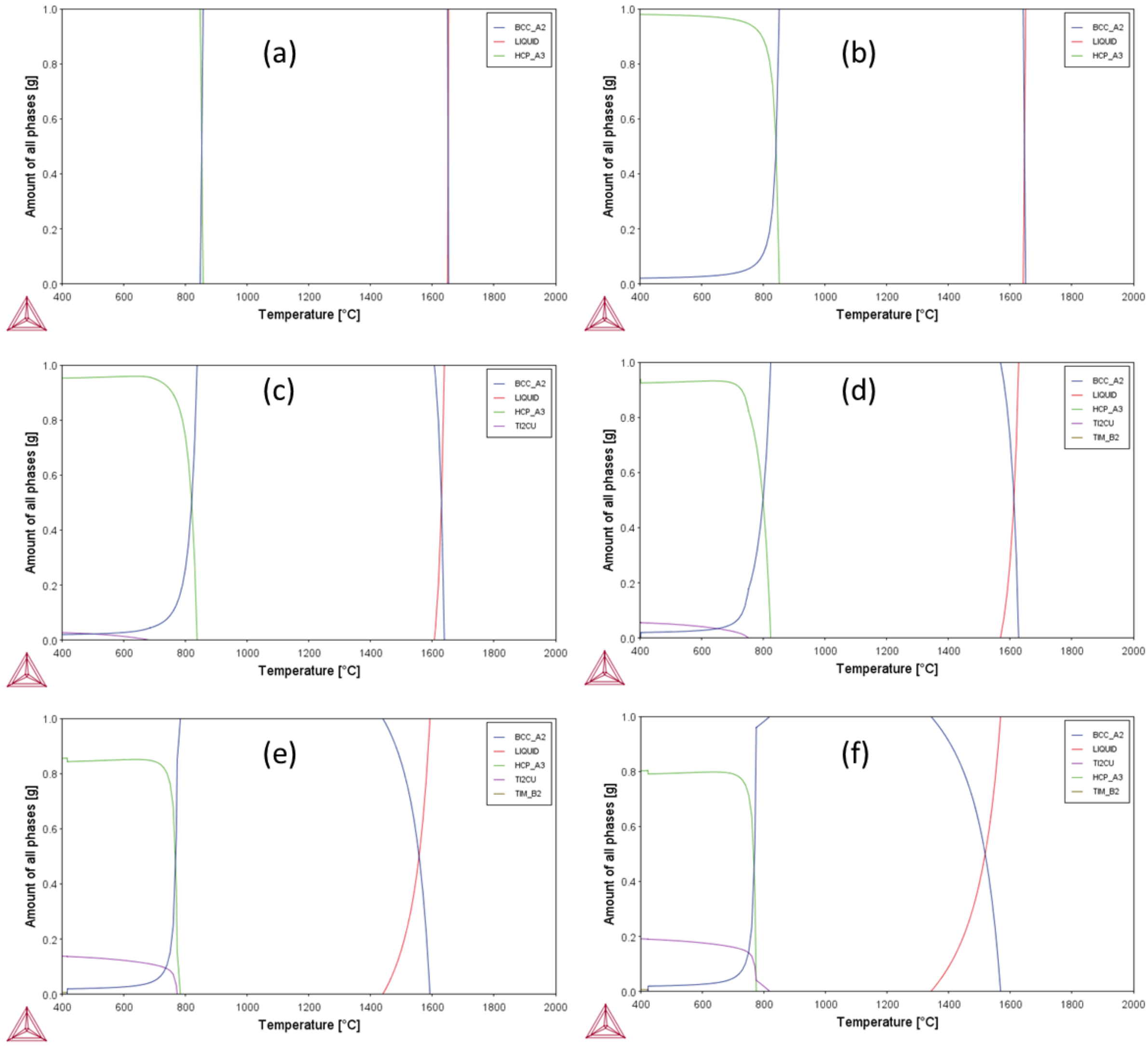

Figure 4.5: Phase proportion diagrams of (a) Ti-6Zr, (b) Ti-6Zr-0.5Ru, (c) Ti-6Zr-0.5Ru-1Cu, (d) Ti-6Zr-0.5Ru-2Cu, (e) Ti-6Zr-0.5Ru-5Cu and (f) Ti-6Zr-0.5Ru-7Cu (wt%).

The Ti_2Cu phase formed after HCP for the compositions with 1-5 wt% Cu. As Cu content increased, the Ti_2Cu phase fraction, at low temperature, increased. In compositions with 2.5 and 7 wt% Cu, Ti_2Cu phase proportion was more than the BCC phase at low temperature. For 7 wt% Cu, Ti_2Cu phase formed before the HCP. A new phase, TIM#2, was predicted for 2 wt% Cu composition (Figure 4.5c). The formation of the phase shifted to higher temperatures as the Cu content increased. At lower Cu contents, the Ti_2Cu phase was formed at lower temperatures.

Table 4.4: Phases calculated for Ti-6Zr and Ti-6Zr-0.5Ru-*x*Cu for *x* = 0, 1, 2, 5 and 7 (wt%).

	Phase proportions (wt%)			
Temperature (°C)	**Amount of HCP**	**Amount of Liquid**	**Amount of BCC**	**Amount of Ti_2Cu**
Ti-6Zr				
1653.22	---	1	Onset	---
1649.64	---	Onset	1	---
857.00	Onset	---	1	---
847.20	1	---	Onset	---
400.00	1	---	---	---
Ti-6Zr-0.5Ru				
1642.56	---	Onset	1	---
1650.31	---	1	Onset	---
851.22	Onset	---	1	---
400	0.98	---	0.02	---
Ti-6Zr-0.5Ru-1Cu				
1606.64	---	Onset	1	---
1638.96	---	1	Onset	---
837.45	Onset	---	1	---
685	0.95	---	0.04	Onset
400	0.95	---	0.021	0.027
Ti-6Zr-0.5Ru-2Cu				
1568.43	---	Onset	1	---
1627.51	---	1	Onset	---
823.77	Onset	---	1	---
751.69	0.82	---	0.18	Onset
400	0.98	---	---	0.06
Ti-6Zr-0.5Ru-5Cu				
1439.32	---	Onset	1	---
1592.43	---	1	Onset	---
783.22	Onset	---	1	---
773.01	0.15	---	0.85	Onset
400	0.85	---	---	0.14
Ti-6Zr-0.5Ru-7Cu				
1341.55	---	Onset	1	---
1568.27	---	1	Onset	---
818.67	---	---	1	Onset
774.53	Onset	---	0.96	0.04
400	0.8	--	---	0.19

4.6. Effect of Ru on the Ti-6Ta-1.5Zr compositions

The composition Ti-6Ta-1.5Zr had no BCC phase formed below 795°C (Figure 4.6a). For small additions of 0.2 wt% Ru, the BCC phase was predicted at low temperatures (Figure 4.6b). The phase proportions of the Ti-6Ta-1.5Zr-0.2Ru composition (Figure 4.6b) were similar to those of Ti-6Al-4V alloy (Figure 4.1). Ruthenium has a strong effect on stabilisation of the BCC phase in the base alloy at low temperatures. A notable amount of BCC can be seen in the phase proportions of all the < 1 wt% Ru additions to the base alloy. In all the Ru containing composition HCP formed around 840 °C.

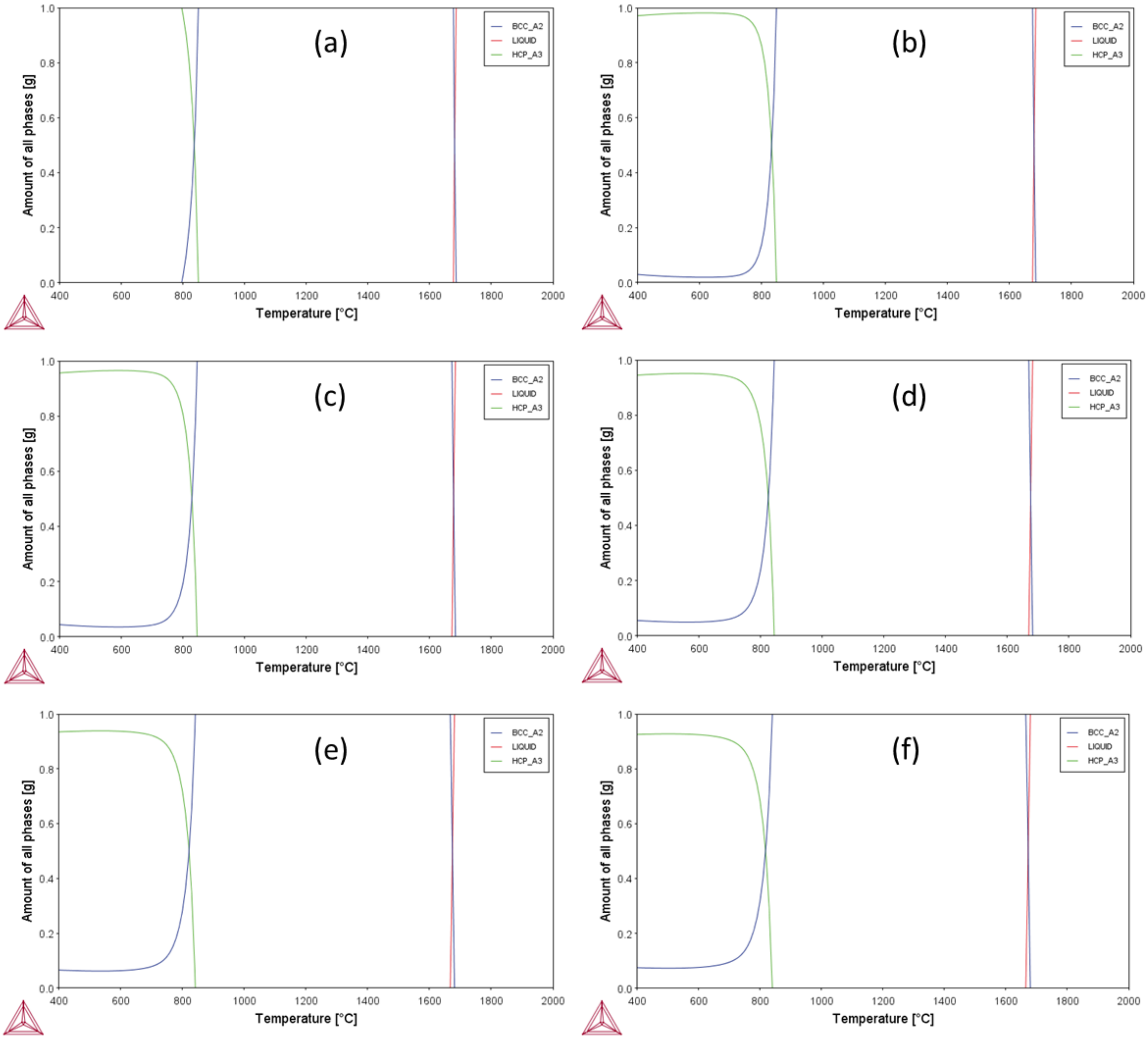

Figure 4.6: Effect of Ru on (a) Ti-6Ta-1.5Zr composition, with (b) Ti-6Ta-1.5Zr-0.2Ru, (c) Ti-6Ta-1.5Zr-0.4Ru, (d) Ti-6Ta-1.5Zr-0.6Ru, (e) Ti-6Ta-1.5Zr-0.8Ru and (f) Ti-6Ta-1.5Zr-1Ru (wt%).

The BCC and HCP phase proportions of the Ti-6Ta-1.5Zr-5Cu shown in Figure 4.7a were not desired because no BCC phase formed at low temperatures while Ti_2Cu phase was predicted. The HCP phase had low proportions at low temperatures. The Ti-6Ta-1.5Zr-0.2Ru-5Cu composition (Figure 4.7b) had both the BCC and HCP phases at lower temperatures with Ti_2Cu also predicted. The Ti_2Cu phase formed after the HCP between 700°C and 800°C. This indicated that the small additions of Ru had a significant impact in stabilising BCC phase. Hence in the Ti-6Ta-1.5Zr-0.2Ru-5Cu compositions, HCP, BCC and Ti_2Cu phases were stabilised at low temperatures.

4.7. Preferred Compositions

The compositions: Ti-6Ta-1.5Zr, Ti-6Ta-1.5Zr-0.2Ru, Ti-6Ta-1.5Zr-5Cu and Ti-6Ta-1.5Zr-0.2Ru-5Cu were the best compositions with the desired phases α, β and Ti_2Cu (for Cu containing compositions) with the required proportions which matched Ti-6Al-4V. These compositions were then manufactured as alloys. Other compositions had phase proportions that were not desired, especially after Cu additions. Their HCP and BCC phases proportions were dissimilar to the proportions in Ti-6Al-4V. In the Ti-6Ta-1.5Zr-0.2Ru composition the match between its phase proportions and that of Ti-6Al-4V was retained even after Cu additions.

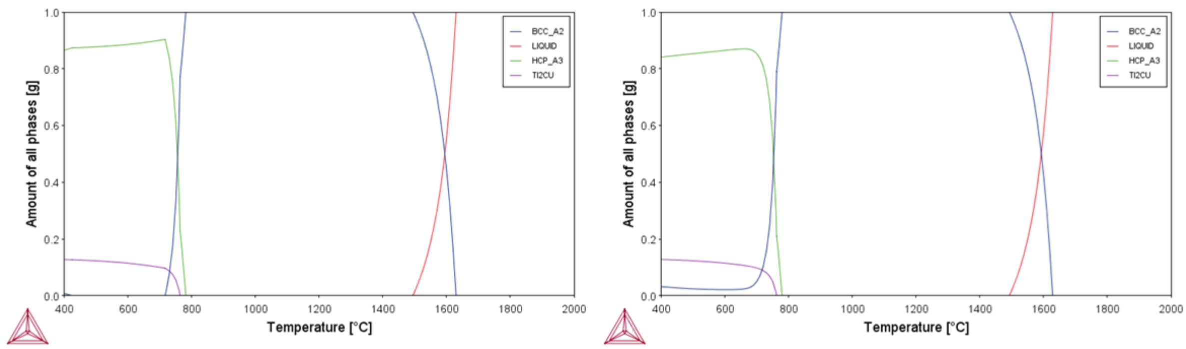

Figure 4.7: Phase proportion diagrams of (a) Ti-6Ta-1.5Zr-5Cu and (b) Ti-6Ta-1.5Zr-0.2Ru-5Cu (wt%).

Chapter 5: Experimental Results

This chapter gives the experimental results of the research. Light microscopy, scanning electron microscopy with EDX, XRD, hardness measurements and corrosion tests were done, and the results are presented.

5.1. EDX analyses

Table 5.1 shows the targeted compositions of each alloy. These EDX analyses were only carried out to determine the composition in each alloy. There were variations across the different areas, showing that the alloys were not homogeneous. In the Ti-6Ta-1.5Zr alloy the Ta analysis had a standard deviation >1 wt%. Ruthenium was not picked up in other areas of the Ti-6Ta-1.5Zr-0.2Ru alloy. In the Ti-6Ta-1.5Zr-5Cu alloy, Cu deviated between 0.7 wt% while in the Ti-6Ta-1.5Zr-0.2Ru-5Cu, a 1.7 error was calculated. In addition to the Ti-6Ta-1.5Zr-0.2Ru-5Cu, Ru was not found in other areas, and Ta and Zr had a standard deviation close to 1 wt%.

Table 5.1: Targeted compositions and EDX results of the experimental alloys.

	Targeted compositions (wt%)					**EDX analysis (wt%)**				
Alloy	**Ti**	**Ta**	**Zr**	**Ru**	**Cu**	**Ti**	**Ta**	**Zr**	**Ru**	**Cu**
Ti-6Ta-1.5Zr	92.5	6.0	1.5	-	-	92.0±0.7	8.1±1.1	0.2±0.3	-	-
Ti-6Ta-1.5Zr-0.2Ru	92.3	6.0	1.5	0.2	-	91.0±1.0	6.2±0.5	2.1±0.6	0.3±0.3	-
Ti-6Ta-1.5Zr-5Cu	87.5	6.0	1.5	-	5.0	86.0±1.2	5.9±0.5	3.1±0.5	-	4.9±0.7
Ti-6Ta-1.5Zr-0.2Ru-5Cu	87.3	6.0	1.5	0.2	5.0	86.0±1.6	7.4±0.9	2.0±0.8	0.4±0.6	4.5±1.5

5.2. Optical micrographs and SEM–BSE images

Figures 5.1 and 5.2 show the OM images of the etched samples at three different magnifications with and without Cu and Ru additions. These alloys had Widmanstätten (αTi) laths precipitated at the prior βTi grain boundaries. The (αTi) laths grew perpendicularly to the β grain boundaries, shown clearly in the alloys with no Cu (Figure 5.1). The Cu-

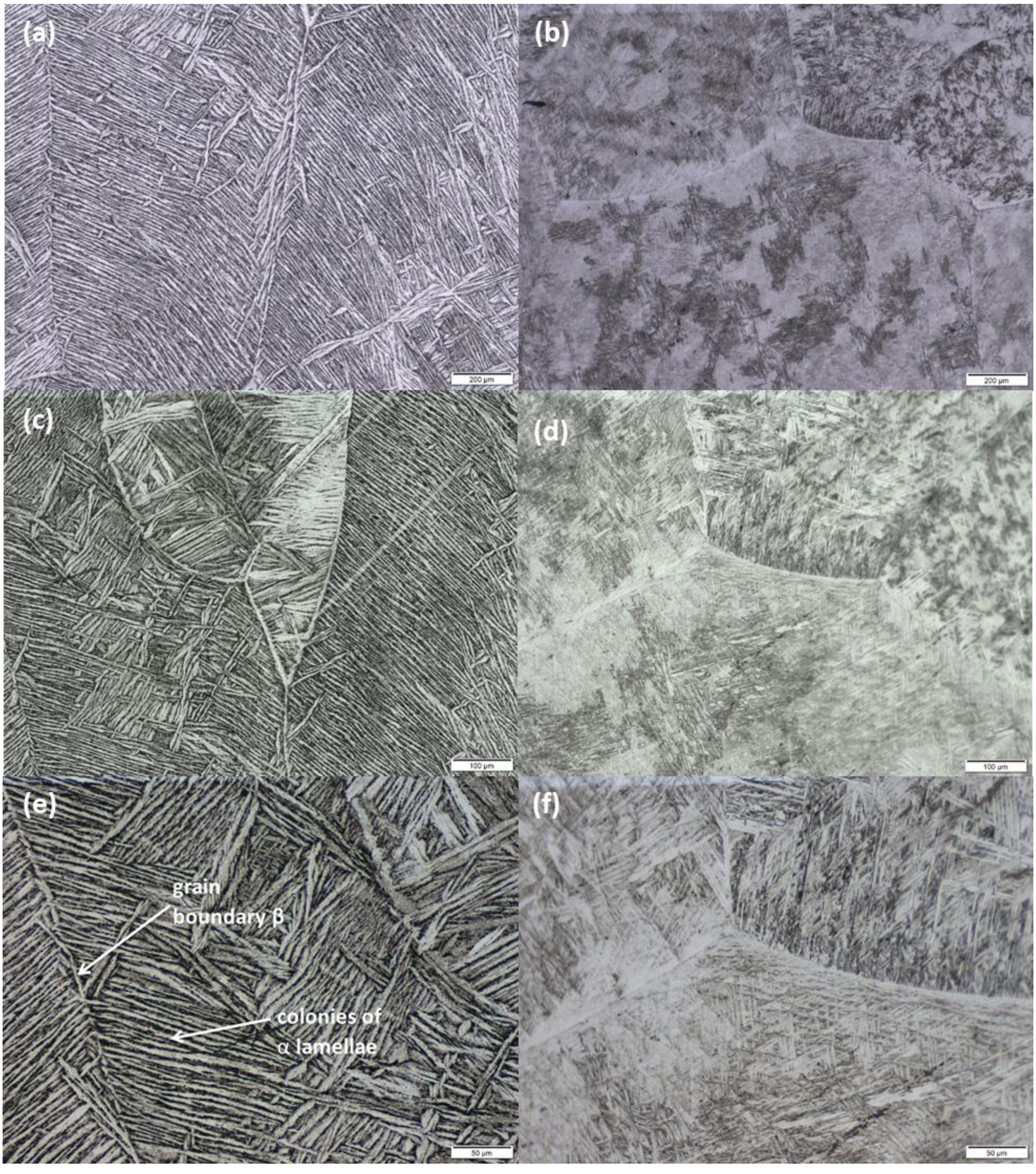

Figure 5.1: OM images of (a, c, e) Ti-6Ta-1.5Zr, and (b, d, f) Ti-6Ta-1.5Zr-0.2Ru alloys showing Widmanstätten microstructures.

containing alloys had reduced amounts of α plates and compared to zero Cu alloys. The Ti-6Ta-1.5Zr-5Cu alloy had equiaxed structure prior β phase (Figure 5.2a) with lamellae structure within the grains (Figure 5.2c). Parallel α laths forming basket-weave structure seen on higher magnification (Figure 5.2d). The Ti-6Ta-1.5Zr-0.2Ru-5Cu alloy had a plate-like acicular (αTi) microstructure (Figure 5.3). At higher magnification fine and parallel plates exist within the prior β grain and along the prior β grain boundary (Figure 5.3d).

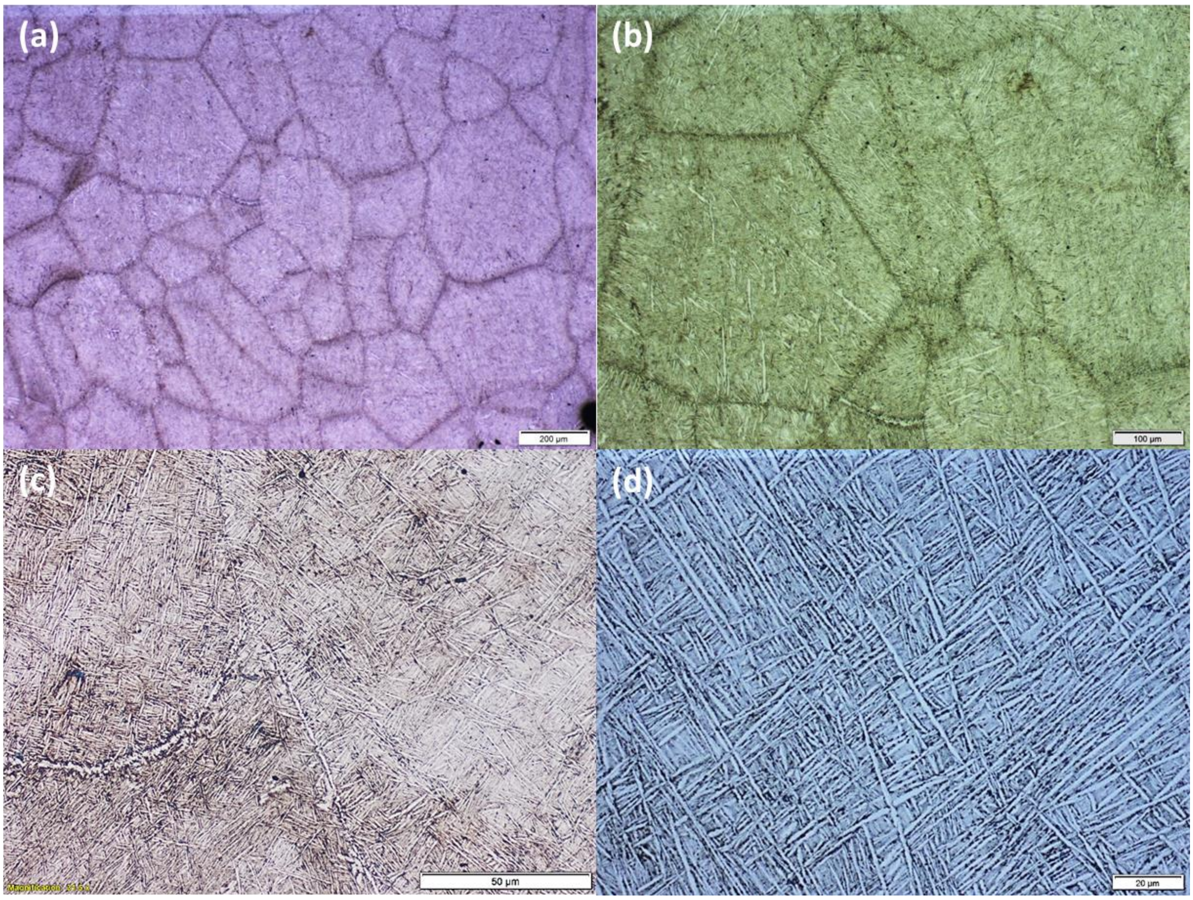

Figure 5.2: OM images of Ti-6Ta-1.5Zr-5Cu alloy showing (a) low magnification prior β grains, (b) prior β grains at higher magnification, (c) Widmanstätten microstructures low magnifications and (d) Widmanstätten microstructures at higher magnification.

To determine the compositions of the phases present in the alloys, spot analyses were carried on the dark and bright phases (Figure 5.4) and the analysis of each phase is shown in Table 5.2. In the Ti-6Ta-1.5Zr-5Cu alloy, the bright phase had higher Ta and Cu content and was (βTi). The dark phase had lower Ta and was (αTi). In the Cu-containing alloys, the bright phase had higher Cu content than the dark phase.

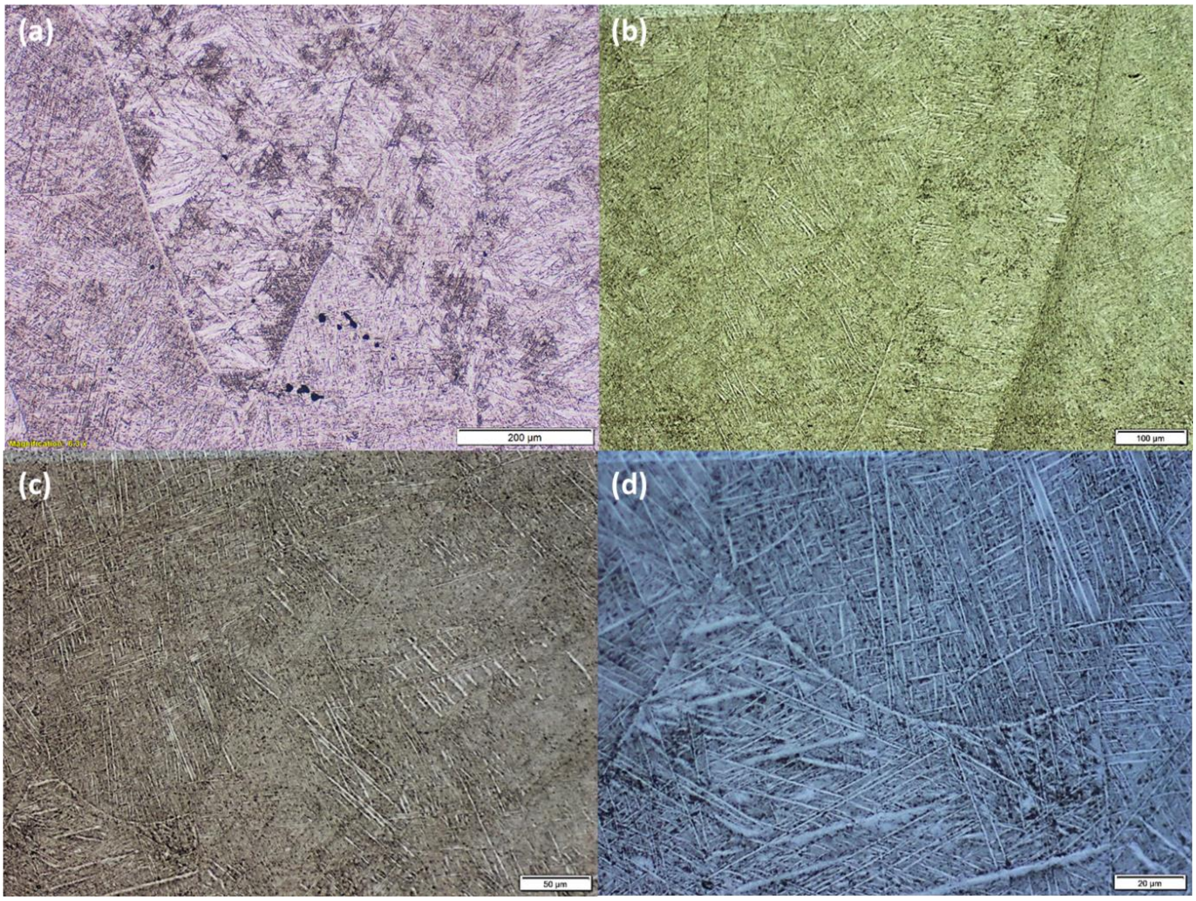

Figure 5.3: OM images of Ti-6Ta-1.5Zr-0.2Ru-5Cu alloys showing Widmanstätten microstructures at different magnifications. Dark areas in (a) are holes caused by casting defects.

The microstructures of the Ti-6Ta-1.5Zr alloy in Figure 5.5 consisted mostly of (αTi) as thick and thin α lamellae growing from the prior (βTi) grain boundaries and into the matrix. There were also much coarser lamellae as shown in Figure 5.5b. These (αTi) lamellae had high Ta content (Table 5.2). At low magnification, the original dendrites were visible. The Ti-6Ta-1.5Zr-0.2Ru microstructure (Figure 5.6) had plate-like (dark) (αTi) phases. The low magnification images showed coarse and parallel elongated (αTi) laths, and the original light contrast dendrites were visible. With Cu additions the microstructure of the alloys had plate-like, parallel (αTi) laths growing from the prior (βTi) grain boundary and into the matrix (Figure 5.6b and 5.7c). Acicular (αTi) grains formed in the Cu-containing alloys (Figure5.6a and 5.7a). Plate-like (αTi) regions were inclined at different angles to each other (Figure 5.8). In both alloys, no Ti_2Cu phase was found using SEM-EDX. Table 5.3 shows the overall EDX of the alloy compositions. Minor differences were found between the polished and after ectching sample’s compositions.

Table 5.2: EDX analysis of the bright and dark phases in (a) Ti-6Ta-1.5Zr and (b) Ti-6Ta-1.5Zr-5Cu.

	(a) Ti-6Ta-1.5Zr	**(b) Ti-6Ta-1.5Zr-Cu**
Bright phase (βTi)		
Element	wt%	wt%
Ti K	90.8±1.6	85.7±1.8
Cu K	---	5.5±1.5
Zr L	0.1±0.1	2.4±0.7
Ta M	9.1±1.5	6.5±1.1
Dark phase (αTi)		
Ti K	92.7±0.1	87.9±2.5
Cu K	---	4.8±1.9
Zr L	0.1±0.1	1.9±0.9
Ta M	7.2±0.1	5.4±1.3

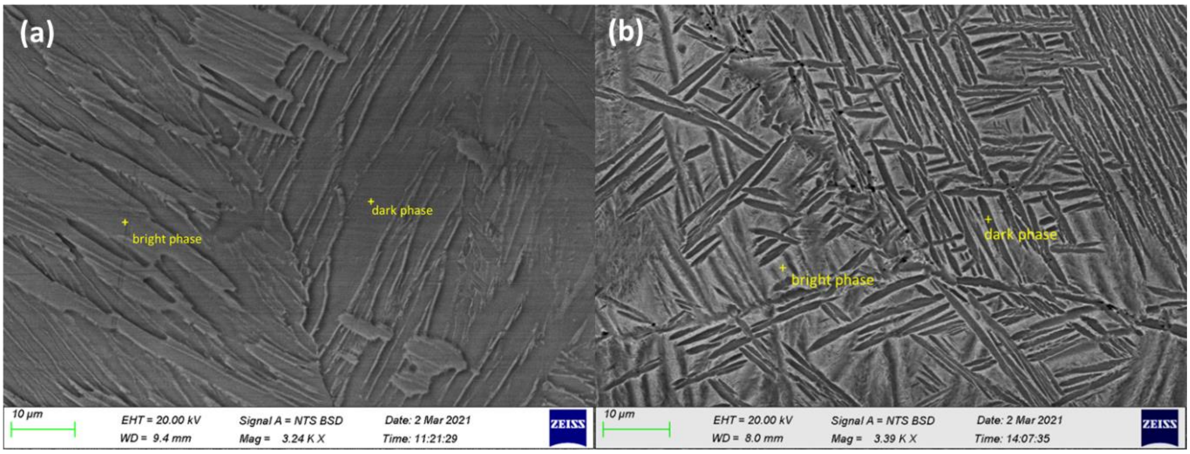

Figure 5.4: Typical positions of the EDX analyses of bright and dark phases in (a) Ti-6Ta-1.5Zr and (b) Ti-6Ta-1.5Zr-5Cu.

Table 5.3: EDX results of polished samples and after etching.

Alloy	EDX (wt%) after grinding and polishing				
	Ti	Ta	Zr	Ru	Cu
Ti-6Ta-1.5Zr	92.0±0.7	8.1±1.1	0.2±0.3	---	---
Ti-6Ta-1.5Zr-0.2Ru	91.0±1.0	6.2±0.5	2.1±0.6	0.3±0.3	---
Ti-6Ta-1.5Zr-5Cu	86.0±1.2	5.9±0.5	3.1±0.5	---	4.9±0.7
Ti-6Ta-1.5Zr-0.2Ru-5Cu	86.0±1.6	7.4±0.9	2.0±0.8	0.4±0.6	4.5±1.5
	EDX (wt%) after etching				
Ti-6Ta-1.5Zr	92.0±1.3	8.4±1.3	0.2±0.1	---	---
Ti-6Ta-1.5Zr-0.2Ru	90.0±1.7	6.7±1.5	2.8±0.6	0.6±0.04	---
Ti-6Ta-1.5Zr-5Cu	85.0±2.4	6.7±1.2	3.2±0.5	---	5.3±1.0
Ti-6Ta-1.5Zr-0.2Ru-5Cu	85.0±1.7	8.0±0.9	1.8±0.4	0.4±0.2	4.6±1.1

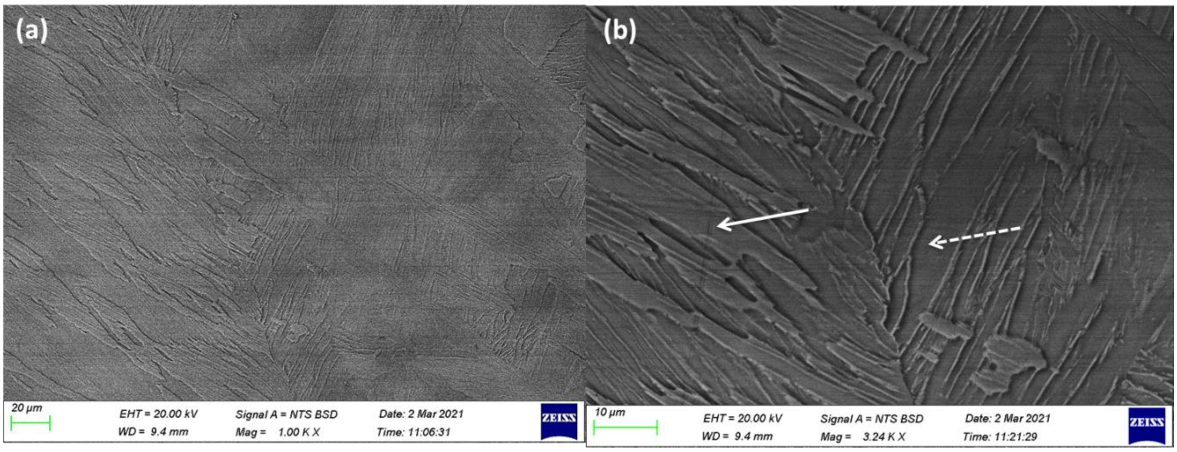

Figure 5.5: SEM-BSE images of the as-cast Ti-6Ta-1.5Zr alloy showing dendritic structure and (αTi) lamellae (white arrow) growing from the grain boundary into the matrix (dashed line), at: (a) low magnification showing the original light contrast dendrites and (b) high magnification.

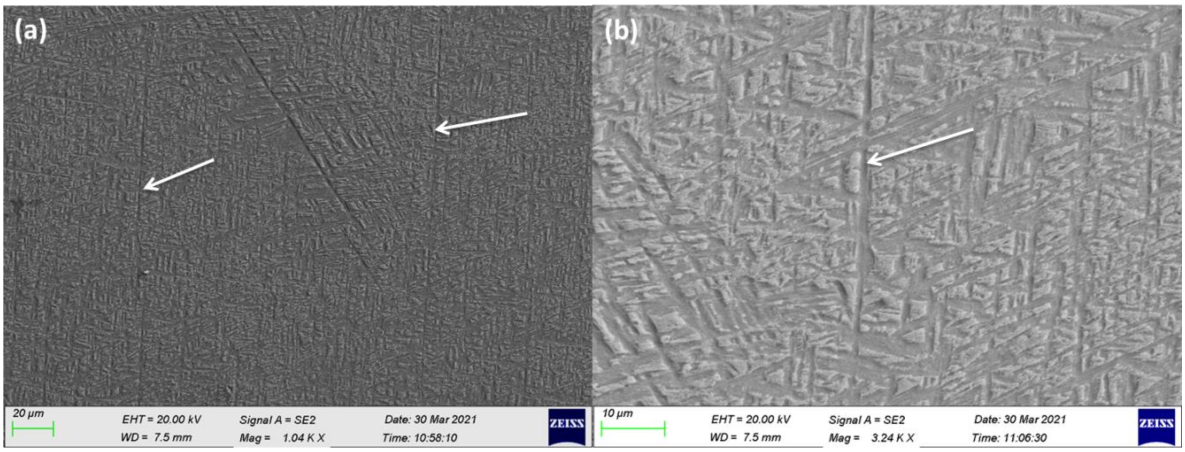

Figure 5.6: SEM-BSE images of the as-cast Ti-6Ta-1.5Zr-0.2Ru alloys showing (αTi) (dark) phase (white arrows) and retained (βTi) matrix.

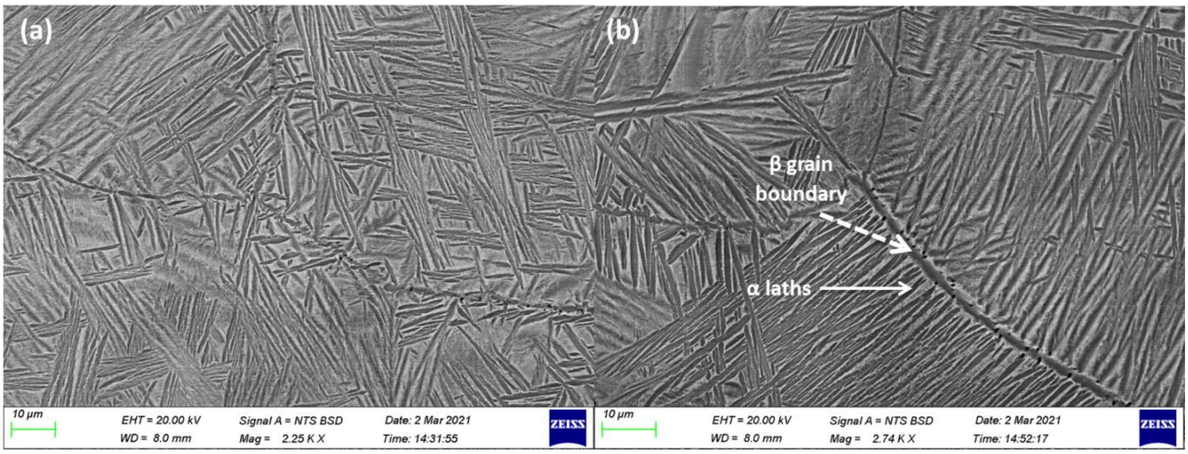

Figure 5.7: SEM-BSE images of the as-cast Ti-6Ta-1.5Zr-5Cu alloy showing (αTi) plates (white arrow) growing from prior (βTi) grain boundaries (dashed arrow).

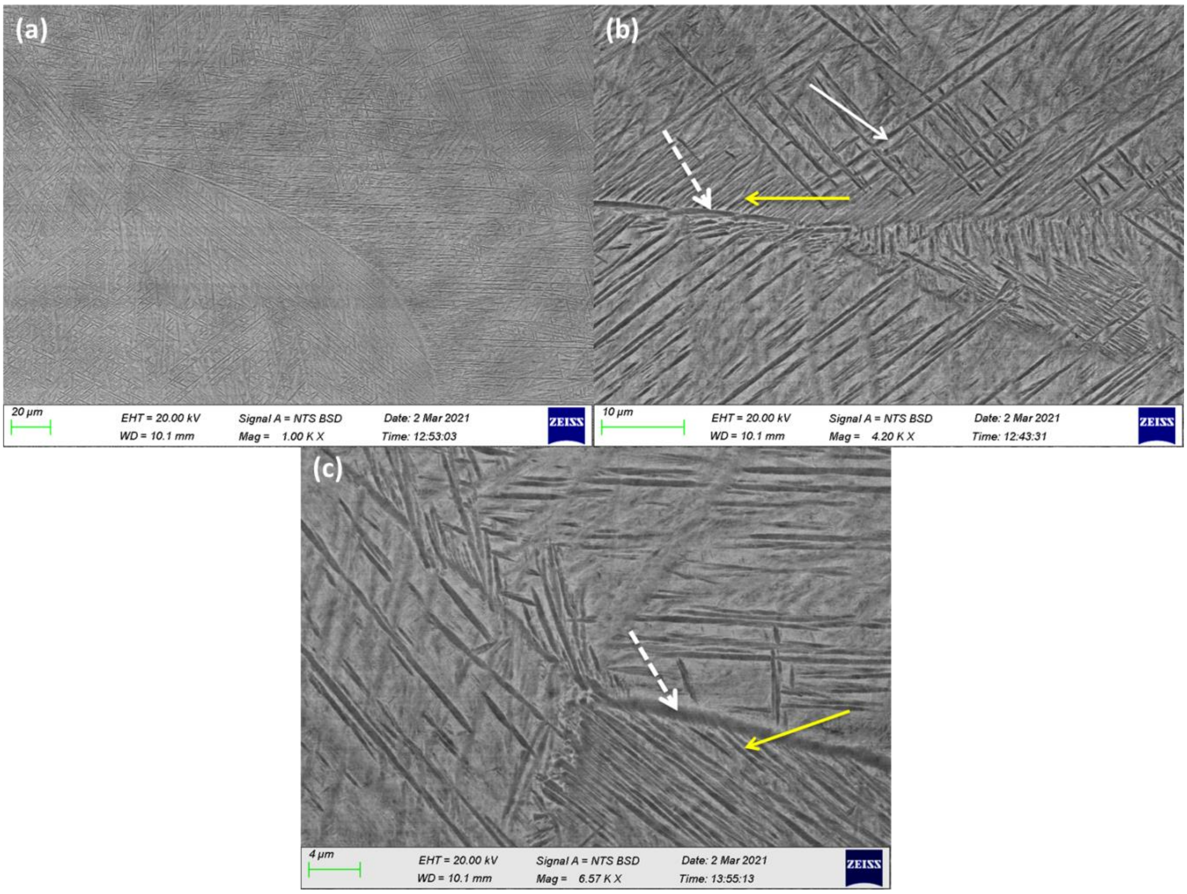

Figure 5.8: SEM-BSE images of the as-cast Ti-6Ta-1.5Zr-0.2Ru-5Cu alloy showing: (a) light contrast dendrite (b) acicular (αTi) plates (white arrow) and parallel (αTi) plates (yellow arrows) growing from β grain boundary (dashed arrow) (c) high magnification image with parallel (αTi) plates (yellow arrows) growing from β grain boundary (dashed arrow).

To identify the Ti_2Cu precipitates, the Ti-6Ta-1.5Zr-Cu and Ti-6Ta-1.5Zr-0.2Ru -Cu alloys were polished again for longer, 20 min, and then etched. Light contrast particles were then found, which were more pronounced in the Ti-6Ta-1.5Zr-0.2Ru -Cu alloy (Figure 5.9b) compared to the Ti-6Ta-1.5Zr-Cu alloy. The EDX analyses showed higher Cu content than in all other phases. Although these particles were smaller than the interaction volume, a high Cu content >17 wt% was found, indicating precipitation of a Ti-Cu phase, probably Ti_2Cu. The (αTi) laths were inclined at different angles were in the Ti-6Ta-1.5Zr-0.2Ru -Cu microstructure (Figure 5.9 b,d) while the Ti-6Ta-1.5Zr-Cu alloy had an acicular microstructure (Figure 5.9a,c).

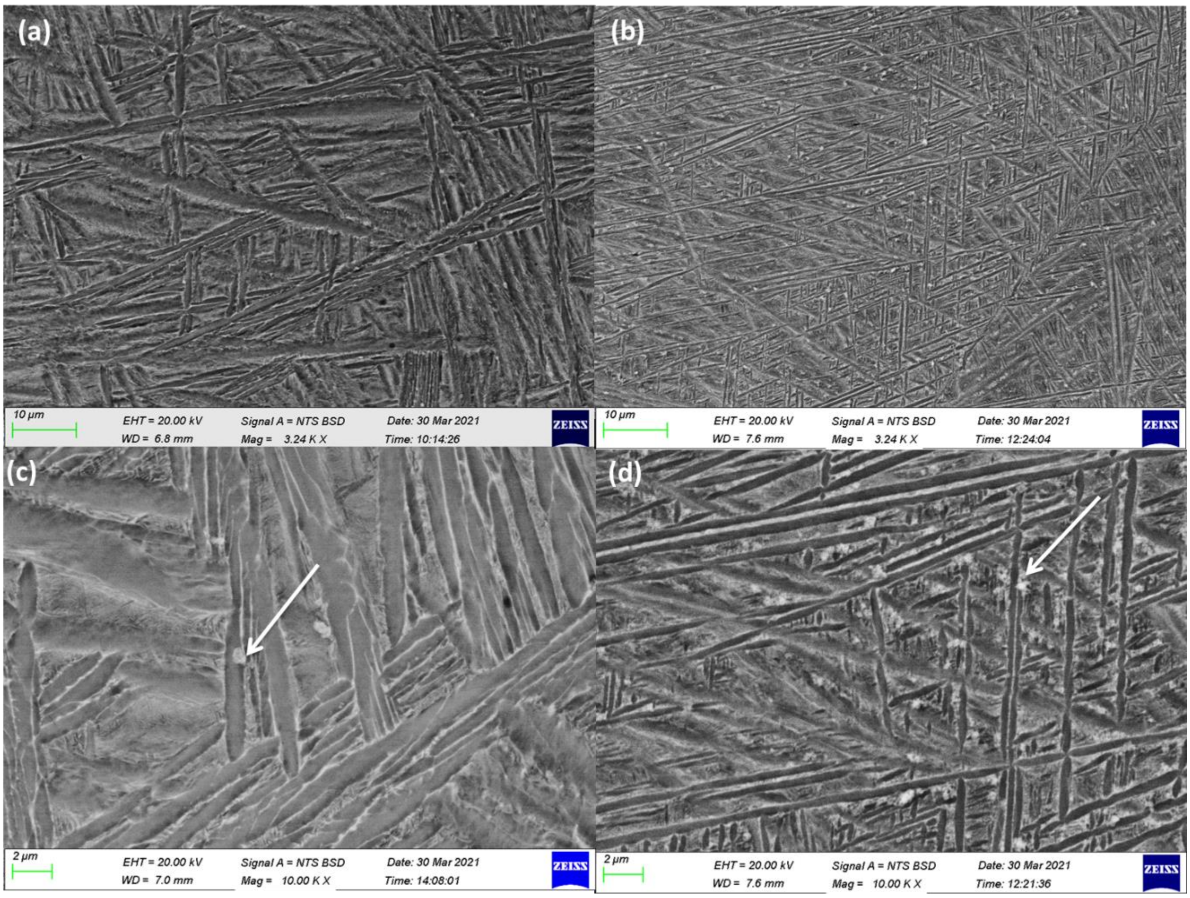

Figure 5.9: SEM-BSE images of (a, c) Ti-6Ta-1.5Zr-5Cu and (b, d) Ti-6Ta-1.5Zr-0.2Ru-5Cu alloy showing Ti_2Cu particles (arrows).

5.3. XRD results

The Ti-6Ta-1.5Zr alloy's XRD diffractogram had peaks corresponding to (αTi) (Figure 5.10a). The peak at 2θ = 44° was much higher than expected.

The Ti-6Ta-1.5Zr-0.2Ru alloy (Figure 5.10b) had peaks of (αTi) phase and no β phase peaks were identified in XRD pattern.

The Ti-6Ta-1.5Zr-Cu diffractogram (Figure 5.10c) had (αTi) phase only. No peaks matched β, Ti_3Cu and Ti_2Cu phases. The unmatched peaks were similar to Ti_2Cu and Ti_3Cu phases.

The XRD diffractogram of Ti-6Ta-1.5Zr-0.2Ru -Cu (Figure 5.10d) had (αTi) and Ti_2Cu peaks, although the Ti_3Cu peaks are very similar.

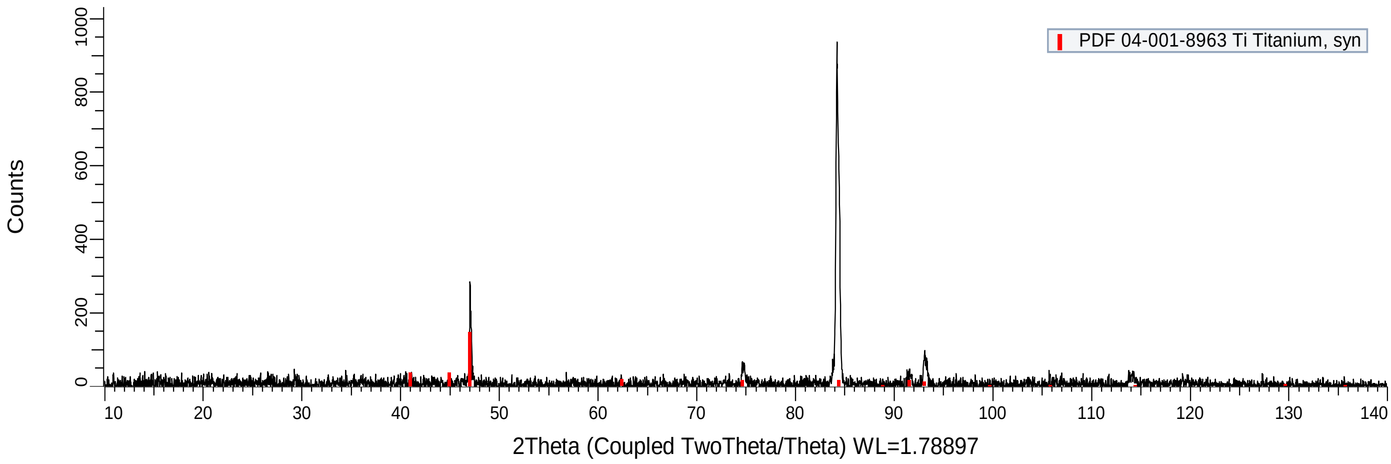

(a) XRD pattern for Ti-6Ta-1.5Zr showing (αTi).

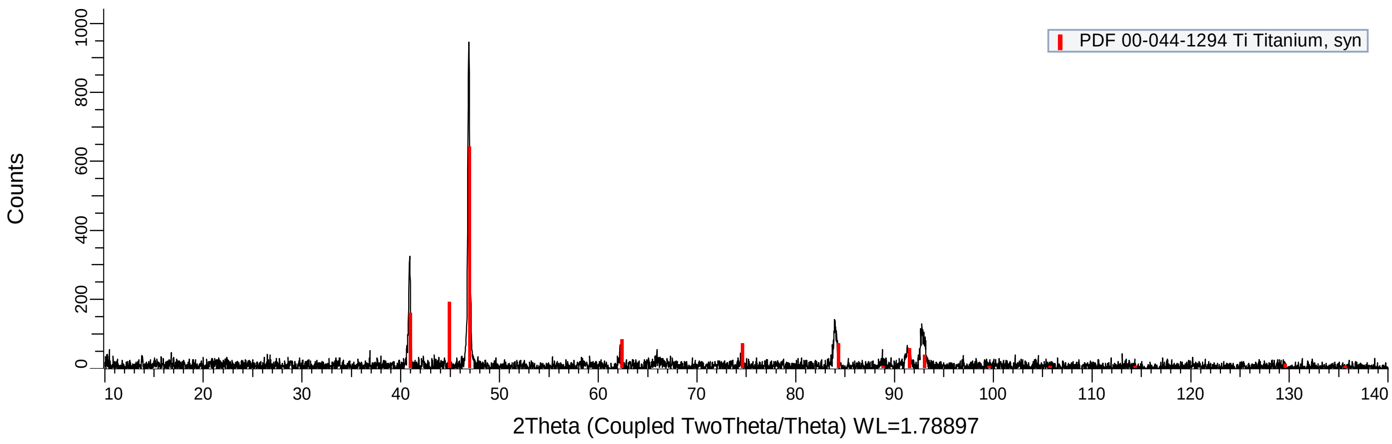

(b) XRD pattern for Ti-6Ta-1.5Zr-0.2Ru showing (αTi).

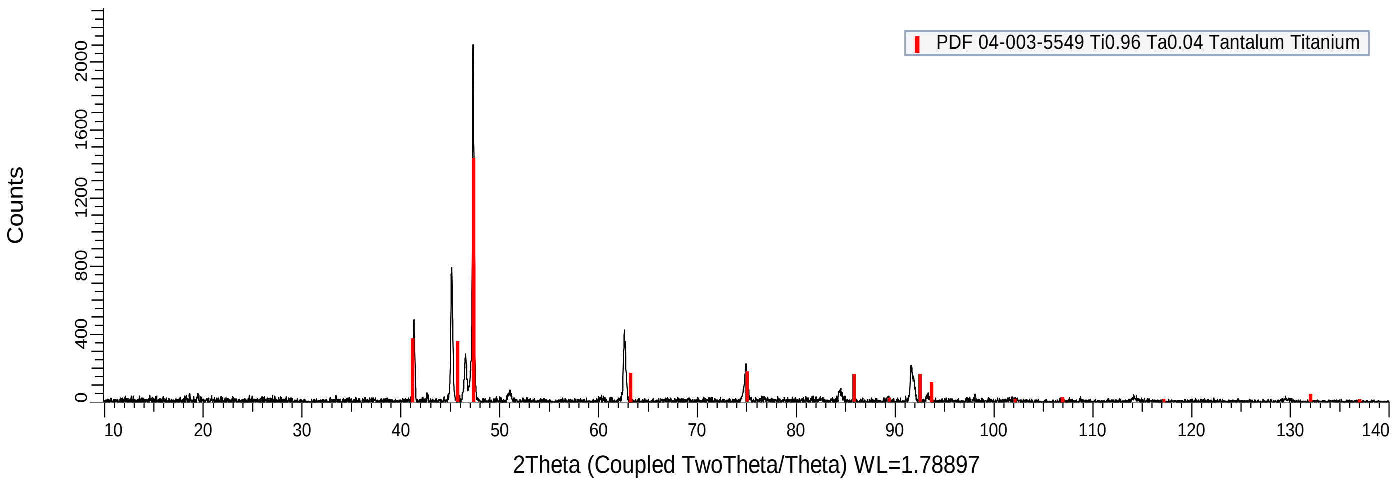

(c) XRD pattern for Ti-6Ta-1.5Zr-5Cu showing αTi and unmatched peaks which were similar to Ti_2Cu and Ti_3Cu phases (Figure 5.9d).

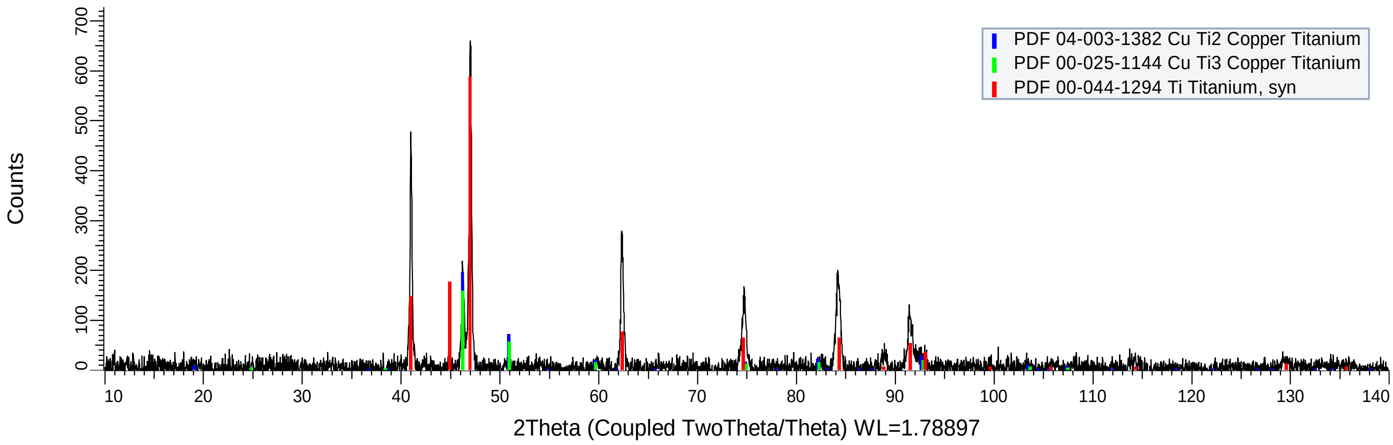

(d) XRD pattern for Ti-6Ta-1.5Zr-0.2Ru-5Cu showing (αTi) and $CuTi_2$, with $CuTi_3$ reference lines.

Figure 5.10: XRD diffractograms of the as-cast (a) Ti-6Ta-1.5Zr, (b) Ti-6Ta-1.5Zr-0.2Ru, (c) Ti-6Ta-1.5Zr-5Cu and (d) Ti-6Ta-1.5Zr-0.2Ru-5Cu alloys.

Figure 5.11 shows the superimposed XRD patterns of the as-cast scanned for 17min. The symbols •, □ and ♦ represent reference line for the (αTi), Ti_2Cu and Ti_3Cu phases, respectively, found in the as-cast alloys. The Ti_3Cu and Ti_2Cu phases found in the Ti-6Ta-1.5Zr-0.2Ru-5Cu are present by symbols □ and ♦. The XRD patterns of the alloys have some weak peaks that are lost due to background noise. The crystallographic data for the phases found in the alloys is presented in Table 5.4.

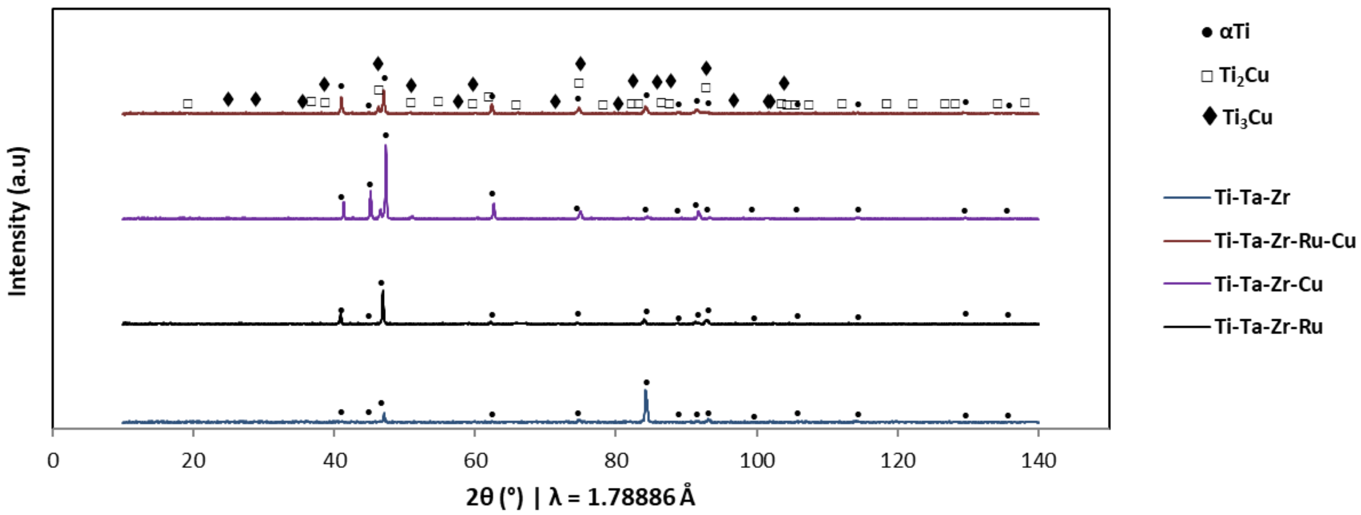

Figure 5.11: Superimposed XRD diffractograms of the as-cast alloys scanned for 17min. Symbols •, □ and ♦ represent reference line for the phases (αTi), Ti_2Cu and Ti_3Cu, respectively. The diffractograms are showing (αTi) found in Ti-6Ta-1.5Zr, Ti-6Ta-1.5Zr-0.2Ru and Ti-6Ta-1.5Zr-0.2Ru-5Cu, Ti_2Cu and Ti_3Cu found in Ti-6Ta-1.5Zr-0.2Ru-5Cu. The diffractogram of Ti-6Ta-1.5Zr-5Cu shows unmatched peaks that are similar to (αTi), Ti_2Cu and Ti_3Cu.

Figure 5.11 shows the diffractograms of the same samples that were ran for longer, 1 hour with no spin, to identify the unmatched peaks.

The Ti-6Ta-1.5Zr and Ti-6Ta-1.5Zr-0.2Ru alloys showed (αTi) phase. In the Ti-6Ta-1.5Zr-0.2Ru, no unique peaks indicative of (βTi) were found, since the peak at 2θ = ~45° was also shared with (αTi). There also unmathed peaks at 2θ = ~37°, ~48° and ~89°.

In both Cu-containing alloys, peaks matching (αTi) and (βTi) were found. The Ti_2Cu phase was also found, although the Ti_3Cu peaks are very similar (Karlsson, 1951; Mueller and Knott, 1963). The only differences are that Ti_2Cu has a 44% intensity peak at 2θ = 19.094° and a 14% intensity peak at 2θ = 36.717° (Mueller and Knott, 1963), whereas Ti_3Cu has a 15% intensity peak at 2θ = 24.845° and a 6% intensity peak at 2θ = 35.424° (Karlsson, 1951). Except for the 44% intensity peak Ti_2Cu, the other differentiating peaks have very small intensities, and were likely to be lost in the background.

In all diffractograms of the alloys no peaks indicative of α' martensite were found, even for the alloys with the acicular microstructure, so if present, it would have only been in small amounts.

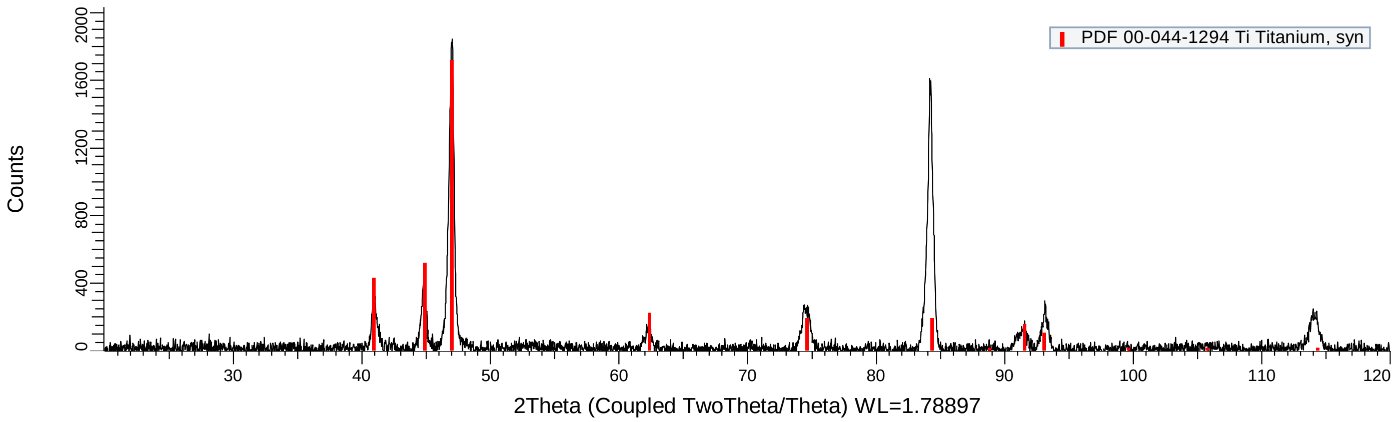

(a) XRD pattern for Ti-6Ta-1.5Zr showing (αTi).

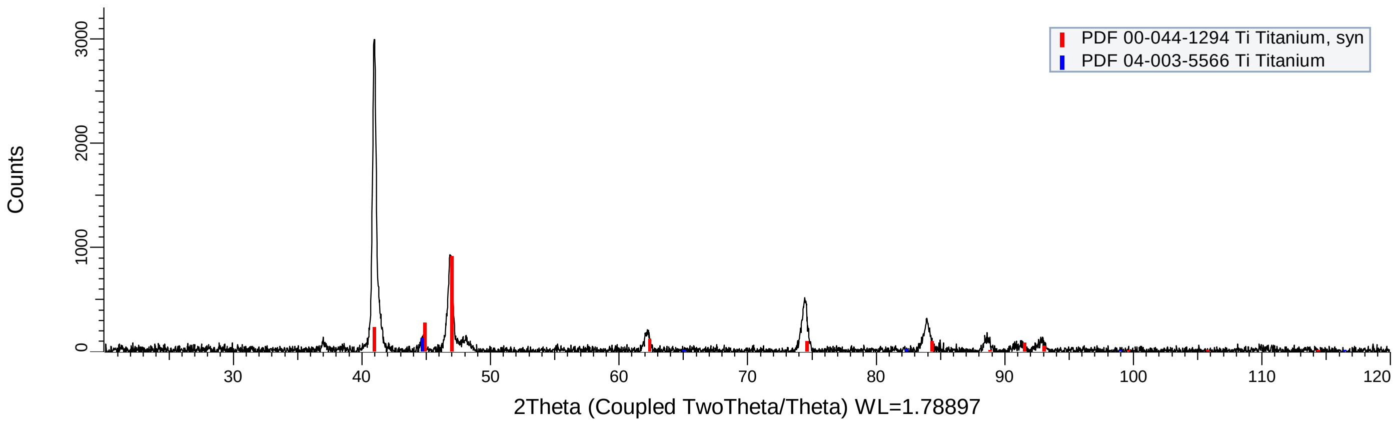

(b) XRD pattern for Ti-6Ta-1.5Zr-0.2Ru showing (αTi) and umatched peaks at 2θ = ~37°, ~48° and ~89°.

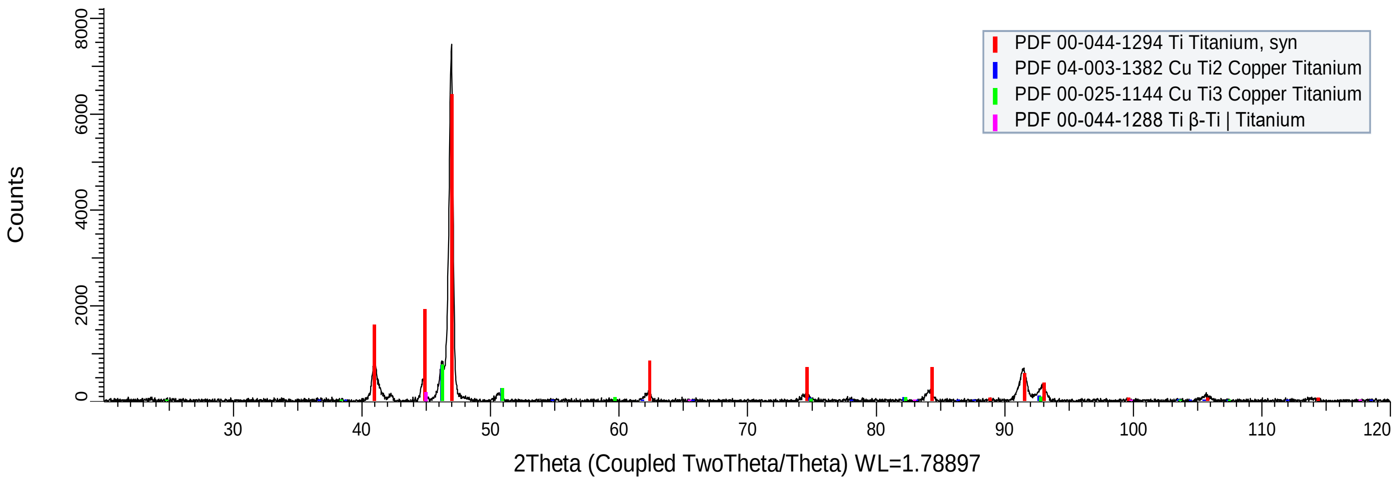

(c) XRD pattern for Ti-6Ta-1.5Zr-5Cu showing (αTi) and Ti_2Cu phases, with Ti_3Cu and βTi reference lines.

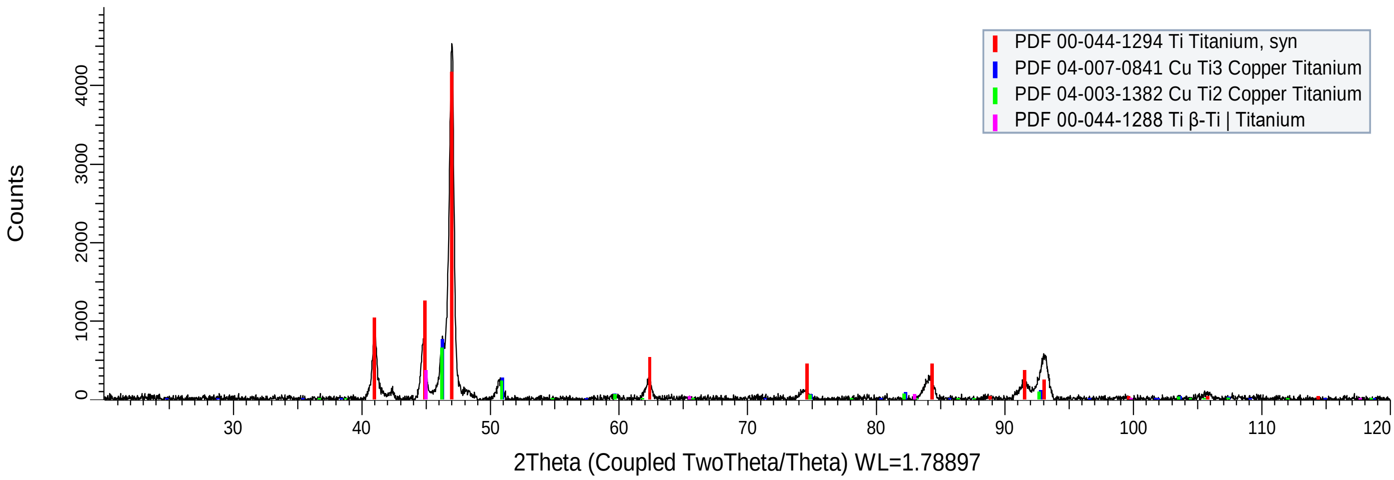

(d) XRD pattern for Ti-6Ta-1.5Zr-0.2Ru-5Cu showing (αTi) and Ti_2Cu phases, with βTi and Ti_3Cu reference peaks.

Figure 5.12: XRD diffractograms of the as-cast alloys scanned for 1 h.

Figure 5.12 shows the superimposed XRD patterns of the as-cast alloys scanned for 1 h. The symbols •, ★, □ and ♦ represent reference peaks for the phases (αTi), (βTi), Ti_2Cu and Ti_3Cu, respectively. Table 5.4 shows the crystallographic data of the phases found in the as-cast alloys. Alpha Ti was found in all the as-cast alloys, two different crystallographic data for βTi phase found in Ti-6Ta-1.5Zr-0.2Ru and Ti-6Ta-1.5Zr-5Cu and Ti-6Ta-1.5Zr-0.2Ru-5Cu is shown, and Ti_2Cu and Ti_3Cu found in the Cu-containing alloys is shown in Table 5.4.

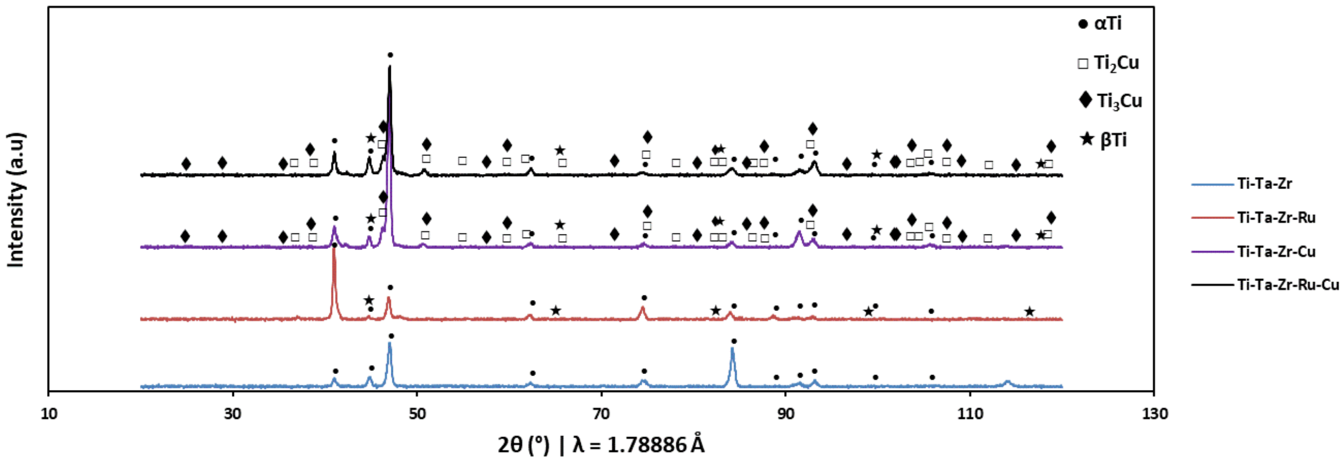

Figure 5.13: Superimposed XRD diffractograms of the as-cast alloys scanned for 1 h. Symbols •, ★, □ and ♦ represent reference peaks for the phases (αTi), (βTi), Ti_2Cu and Ti_3Cu, respectively.

Table 5.4a: Peak matches of the phases found the as-cast alloys.

αTi					
2θ (°)	**d (Å)**	**I**	**h**	**k**	**l**
40.986	2.555	25	1	0	0
44.927	2.341	30	0	0	2
47.005	2.243	100	1	0	1
62.42	1.7262	13	1	0	2
74.645	1.4753	11	1	1	0
84.371	1.332	11	1	0	3
88.874	1.2776	1	2	2	2
91.561	1.2481	9	1	1	1
93.071	1.2324	6	2	2	4
99.646	1.1707	1	0	0	2
105.798	1.1215	1	2	2	4
βTi found in Ti-6Ta-1.5Zr-0.2Ru					
44.694	2.35254	1000	1	1	0
65.056	1.6635	134	2	0	0
82.38	1.35824	214	2	1	1
99.006	1.17627	55	2	2	0
116.465	1.05209	67	3	1	0
βTi found in Ti-6Ta-1.5Zr-5Cu and Ti-6Ta-1.5Zr-0.2Ru-5Cu					
44.998	2.3375	100	1	1	0
65.512	1.6532	12	2	0	0
83.024	1.3496	17	2	1	1
99.855	1.1689	4	2	2	0
117.66	1.0454	5	3	1	0
Ti_2Cu found in Ti-6Ta-1.5Zr-5Cu and Ti-6Ta-1.5Zr-0.2Ru-5Cu					
19.094	5.39305	44	0	0	2
36.717	2.83993	14	1	0	1
38.746	2.69652	1	0	0	4
46.246	2.27771	1000	1	0	3
50.899	2.08158	366	1	1	0
54.853	1.94195	11	1	1	2
59.679	1.79768	100	0	0	6
61.869	1.74003	14	1	0	5
65.756	1.64774	1	1	1	4
74.847	1.4719	87	2	0	0
78.09	1.41996	3	2	0	2
82.211	1.36054	116	1	1	6
83.124	1.34826	2	0	0	8
86.389	1.30681	1	2	1	1
87.632	1.29196	1	2	0	4
92.697	1.23624	150	2	1	3
103.519	1.13886	50	2	0	6
104.454	1.13162	3	1	1	8

Table 5.5b: Peak matches of the phases found the as-cast alloys.

Ti2Cu found in Ti-6Ta-1.5Zr-5Cu and Ti-6Ta-1.5Zr-0.2Ru-5Cu *(continue)*					
105.493	1.12377	3	2	1	5
107.382	1.11	43	1	0	9
112.052	1.07861	1	0	0	10
118.504	1.04079	17	2	2	0
Ti_3Cu					
24.845	4.158	15	1	0	0
28.823	3.594	5	0	0	1
35.424	2.94015	6	1	1	0
38.412	2.71905	10	1	0	1
46.29	2.27567	1000	1	1	1
50.966	2.079	356	2	0	0
57.505	1.85951	3	2	1	0
59.704	1.797	102m	0	0	2
59.704	1.797	102m	2	0	1
71.376	1.53329	1	1	1	2
74.956	1.47008	86	2	2	0
80.387	1.386	1	3	0	0
82.285	1.35953	118m	2	0	2
82.285	1.35953	118m	2	2	1
85.73	1.31488	1	3	1	0
87.611	1.29221	1m	2	1	2
87.611	1.29221	1m	3	0	1
92.834	1.23483	150	3	1	1
96.601	1.198	1	0	0	3
101.726	1.15322	1	3	2	0
Ti_3Cu					
101.977	1.15117	1	1	0	3
103.649	1.13784	51	2	2	2
107.461	1.10944	45	1	1	3
109.093	1.09808	1m	3	0	2
109.093	1.09808	1m	3	2	1
114.904	1.06114	1	3	1	2
118.743	1.0395	17	4	0	0

5.4. Hardness results

The histogram shown in Figure 5.12 shows results taken from indentations made across the samples. For all samples, the measured hardness decreased when approaching the centre. The Ti-6Ta-1.5Zr had the lowest hardness, while Ti-6Ta-1.5Zr-0.2Ru-5Cu showed the highest. Thus, adding Cu and Ru increased the hardness. Indentation #1 and #5 (Figure 5.12) were close to the edge seemed to not make much of difference. The values at the edges were likely to be lower because the sample was less constrained.

The mean Vickers hardness of seven different indentations is shown in Figure 5.13. The Ti-6Ta-1.5Zr alloy had the lowest hardness of 252 ± 15.4 HV and Ti-6Ta-1.5Zr-0.2Ru-5Cu had the highest hardness, 368 ± 12 HV. The Ti-6Ta-1.5Zr-0.2Ru and Ti-6Ta-1.5Zr-5Cu samples had similar values: 335 ± 33 HV and 331 ± 29 HV, respectively, as well as fairly high standard deviations.

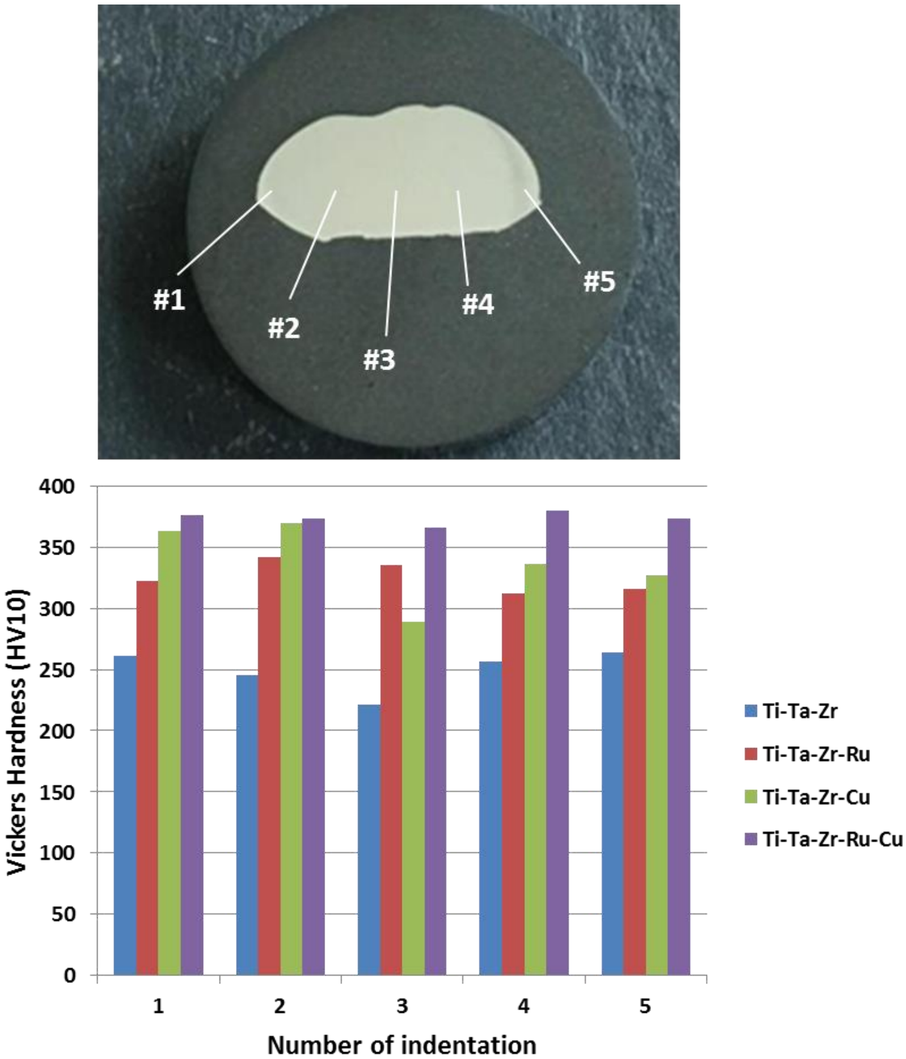

Figure 5.14: Hardness values measured across the sample surfaces.

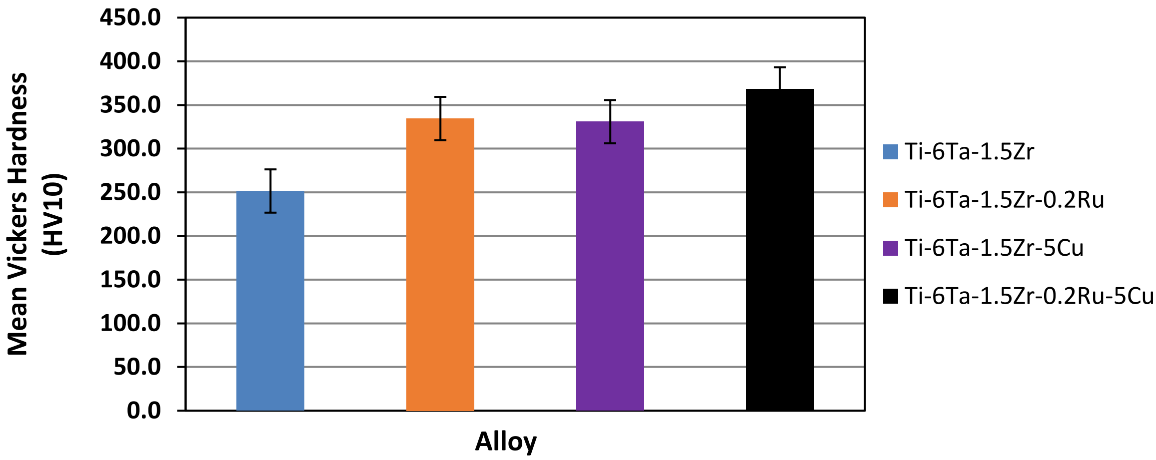

Figure 5.15: Mean Vickers hardnesses of the alloys.

5.5. Corrosion tests

Before corrosion test was performed the test samples were ground on 1200 grade SiC paper. However, for the Ti-6Ta-1.5Zr-0.2Ru sample this grinding paper alone did not give a good finish. Further grinding, followed by polishing was required. A 2400 grade SiC paper and MD-Chem polishing cloths with colloidal silica solution were used to produce a smoother surface.

5.1.1. Open circuit potential profiles

Open circuit potential graphs of the Ti alloys tested are shown in Figure 5.14. The Ti-6Ta-1.5Zr OCP showed a rapid increase in potential within the first few minutes compared to all other alloys. The increase in OCP with time indicated passivation of the alloys and formation of the oxide layer on their surfaces (Abou Shahbha et al., 2011). The Ti-6Ta-1.5Zr-0.2Ru OCP increased slowly and the potential shifted positively. The Ti-6Ta-1.5Zr-5Cu potential kept increasing at a constant potential rate and shifted to nobler potential, while Ti-6Ta-1.5Zr-0.2Ru-5Cu sharply increased within the first few minutes and thereafter increased at a slight potential rate. For all the tested samples, the OCP scan never reached stable values.

5.1.2. Potentiodynamic polarisation curves

Potentiodynamic polarisation curves of the tested samples shown in Figure 5.14 and all showed similar passivation behaviour. The Ti-6Ta-1.5Zr-0.2Ru alloy moved towards nobler potentials after the anodic reaction. The Ti-6Ta-1.5Zr-5Cu and Ti-6Ta-1.5Zr-0.2Ru-5Cu alloys also stabilised close to these potentials. The Ti-6Ta-1.5Zr alloy passivated slowly after the anodic reaction compared to other alloys.

Table 5.3 shows the corrosion potential, corrosion current density, Tafel slopes and corrosion rates of the tested samples. The calculated corrosion current density of all the samples was of the same order. The Ti-6Ta-1.5Zr-5Cu alloy had the lowest corrosion rate. The Ti-6Ta-1.5Zr and Ti-6Ta-1.5Zr-0.2Ru-5Cu samples had similar corrosion rates. The highest corrosion rate occurred in the Ti-6Ta-1.5Zr-0.2Ru alloy.

The corrosion parameters, E_{corr} and i_{corr}, of the alloys were estimated from the potentiodynamic polarisation curves (Figure 5.15) using the Tafel extrapolation method (Choubey et al., 2004) on Excel. The corrosion rates were calculated using the current density and adapting the Faraday's law with penetration units (mm/year):

Corrosion rate = $i_{corr}KW/n\rho$ (Equation 5.1)

where i_{corr} is the corrosion current density (mA/cm^2), W is the equivalent weight (47.88 g), ρ is density of the metal, K is a constant that define the units of corrosion rates (3,272 mm/(mA·cm·yr), W is atomic weight of the element in grams and n is the oxidation number of the element. In this analysis, the corroding species was assumed to be Ti since it has a large fraction. The density of the alloys was assumed to be of Ti (4.51 g/cm^3) (ASTM G 102).

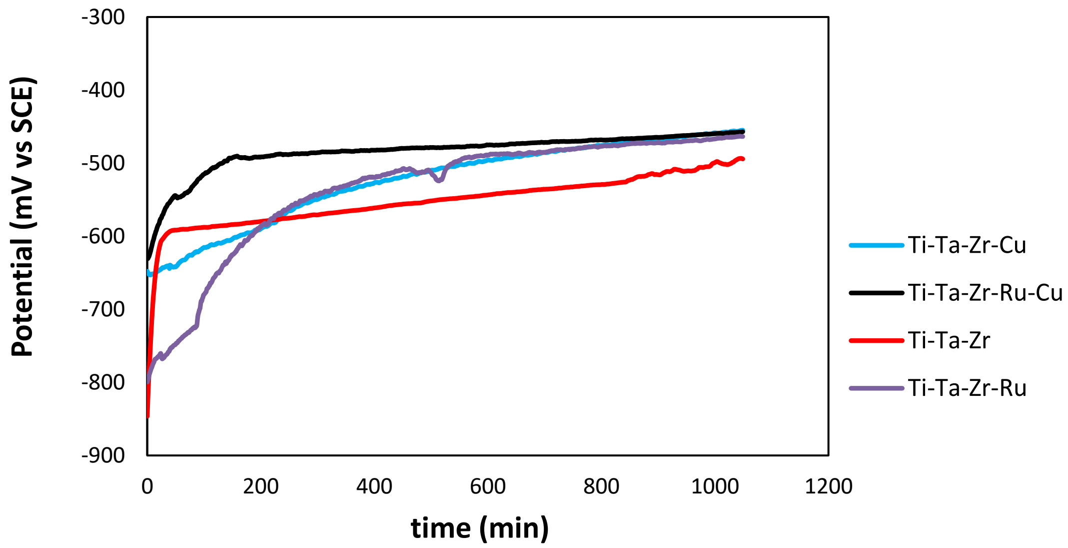

Figure 5.16: OCP profiles of the tested Ti alloys.

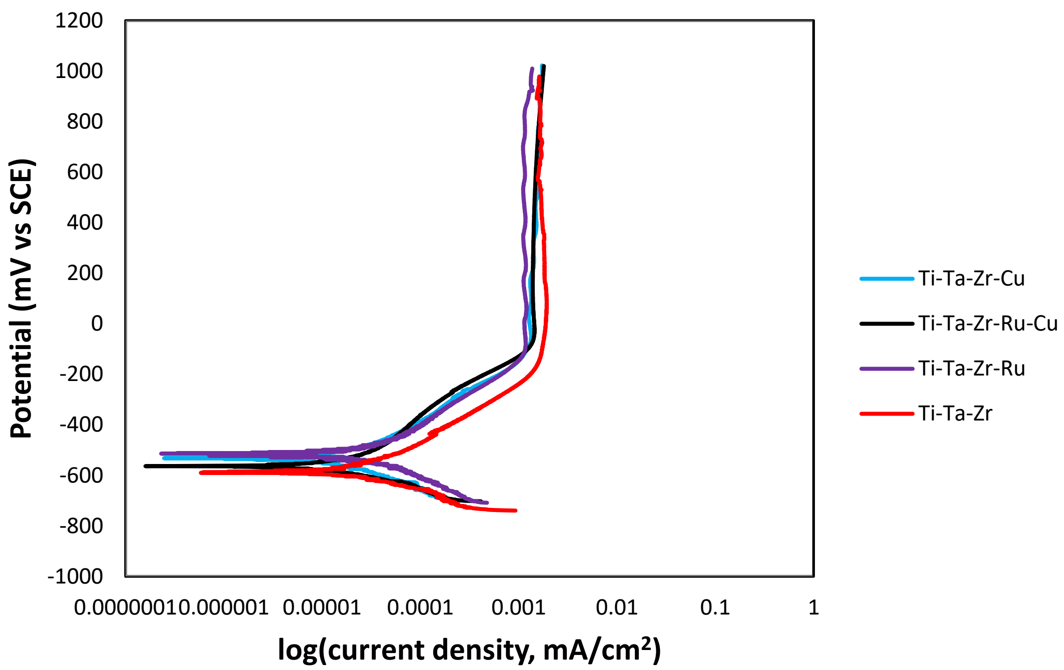

Figure 5.17: Potentiodynamic polarisation curves of the tested Ti alloys.

Table 5.6: Polarisation results of the tested alloys.

Alloy	E_{corr} (mV)	i_{corr} (mA/cm^2)	$\beta_{cathodic}$ (mV/decade)	β_{anodic} (mV/decade)	corr rate (mm/year)
Ti-6Ta-1.5Zr	-588.01	2.47E-05	-86219.02	246184.72	0.00021
Ti-6Ta-1.5Zr-0.2Ru	-512.69	3.51E-05	-199710.88	296010.11	0.00030
Ti-6Ta-1.5Zr-5Cu	-532.28	1.65E-05	-143067.29	245148.56	0.00014
Ti-6Ta-1.5Zr-0.2Ru-5Cu	-563.02	2.53E-05	-163867.31	375602.80	0.00022

5.6. Post corrosion SEM images of tested as-cast alloys

Figures 5.18, 5.19, 5.20 and 5.21 show the post corrosion surface morphologies of the as-cast alloys after polarisation tests in PBS solution at 37±1 °C. Different corrosion effects were found on the surface morphologies of the alloys. The green arrows indicate the pits formed on the surface exposed to the corrodent. Figure 5.22 shows the EDX analysis of the pits formed as result of corrosion, and some elements (chlorine, potassium and sodium) of the PBS solution were detected in the pits. The numerical values were not recorded since they would have been inaccurate, as the surface was not flat and some of the signal might have been lost. The Ti-6Ta-1.5Zr alloy had the most pits (Figure 5.18a). This is agreement with the polarization results shown in Figure 5.17.

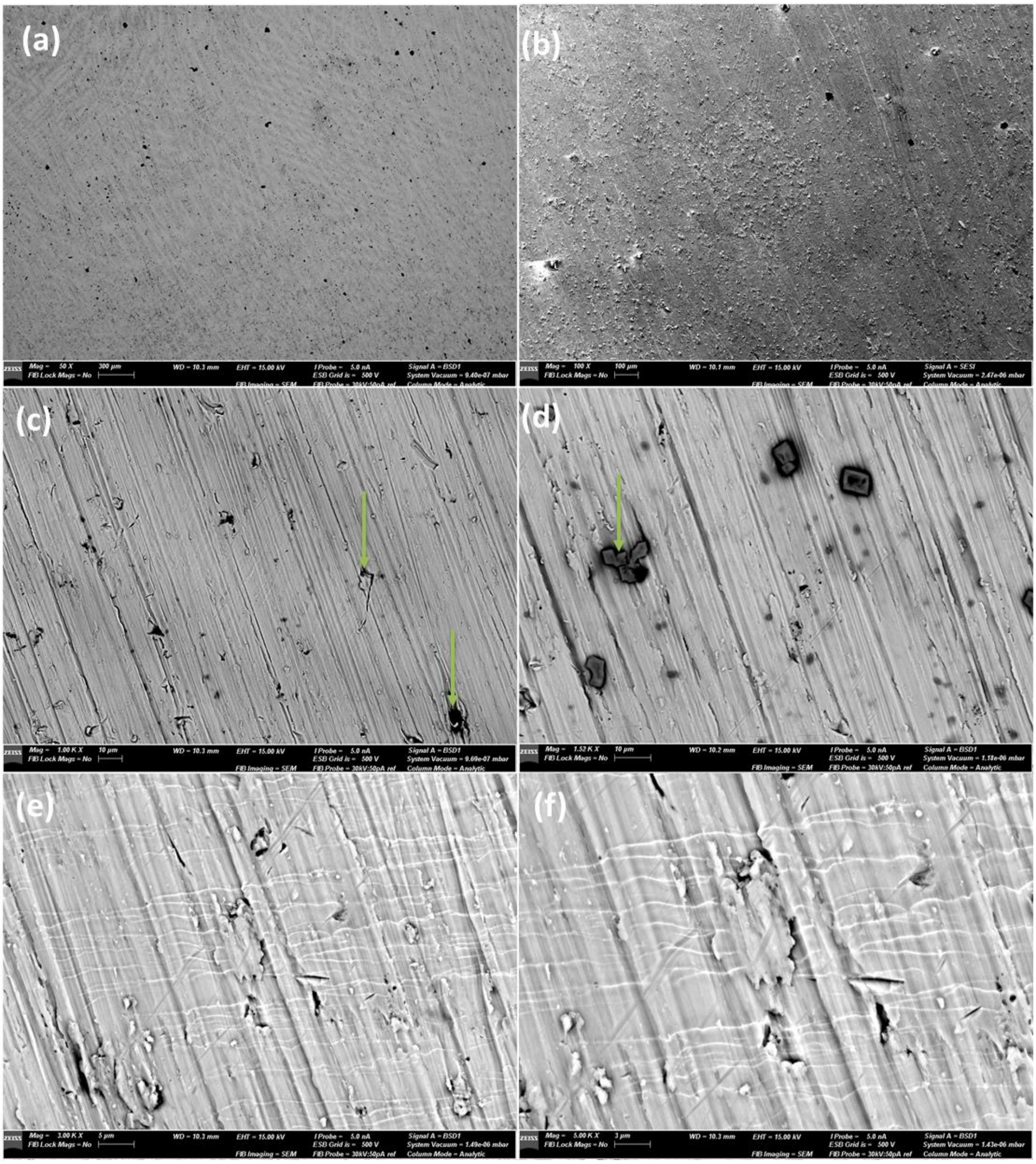

Figure 5.18: Corroded sample of Ti-6Ta-!.5Zr alloy: (a), (c), (d), (e) and (f) show SEM-BSE micrographs and (b) shows an SEM-SE image.

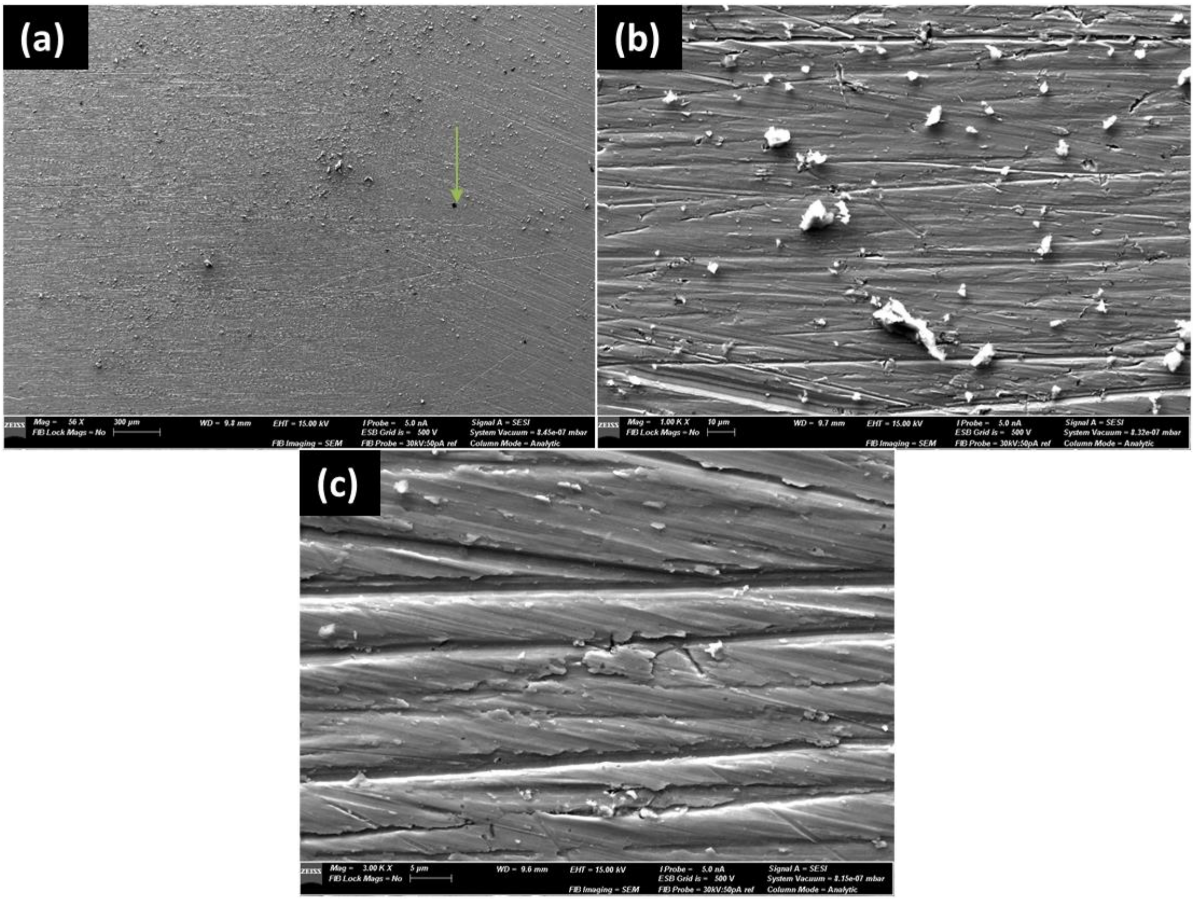

Figure 5.19: SEM-SE micrographs of Ti-6Ta-1.5Zr-0.2Ru after corrosion tests.

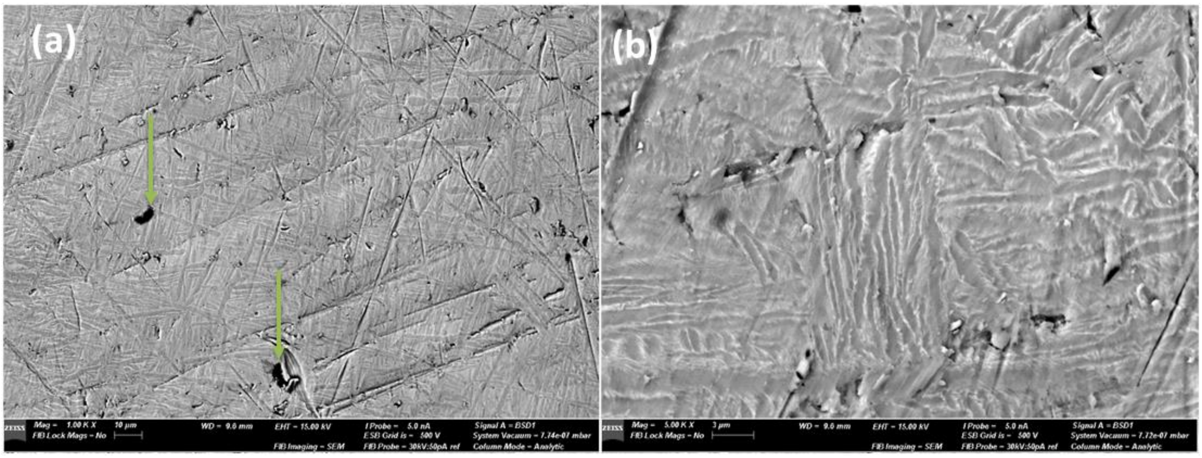

Figure 5.20: SEM-BSE images of corroded Ti-6Ta-1.5Zr-5Cu: (a) lower magnification and (b) higher magnification.

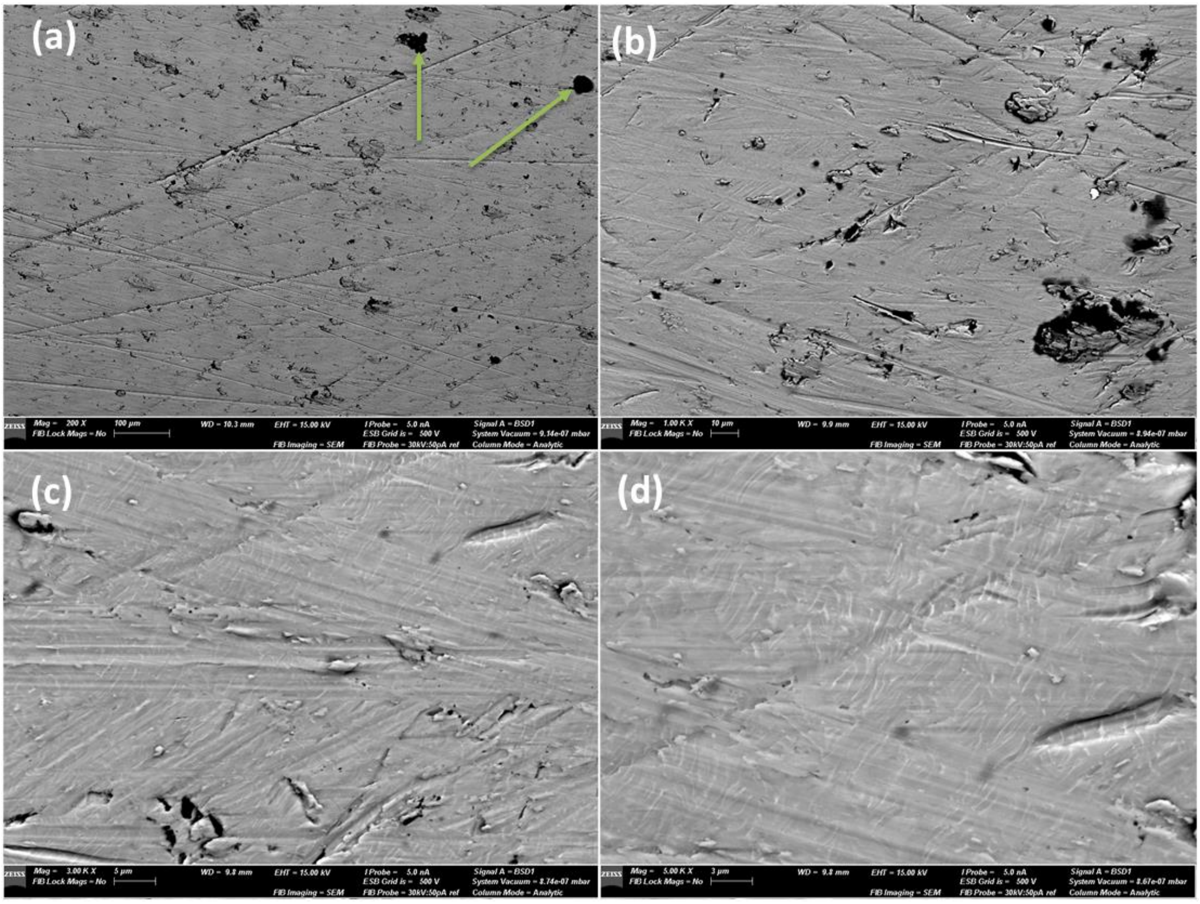

Figure 5.21: SEM-BSE images of corroded Ti-6Ta-1.5Zr-0.2Ru-5Cu at increasing magnifications.

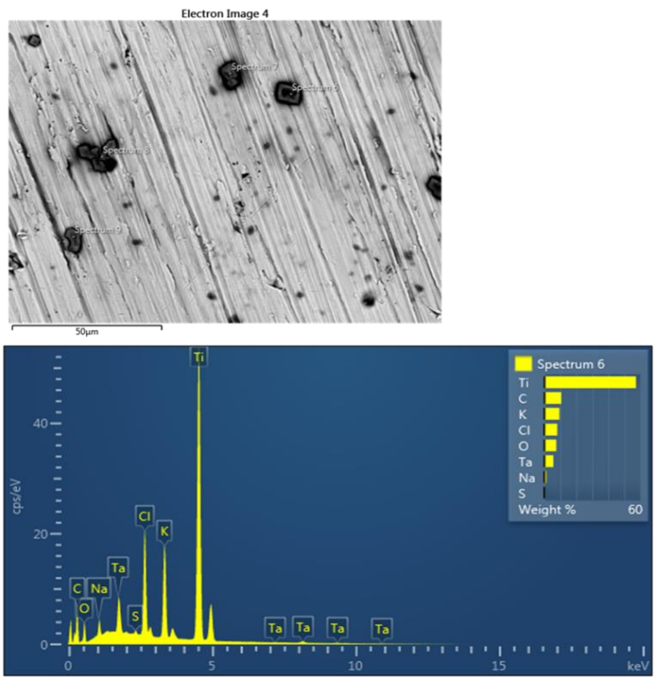

Figure 5.22: EDX analysis of the pits after corrosion.

Chapter 6: Discussion

6.1. Microstructures of the as-cast alloys

The microstructure of as-cast Ti-6Ta-1.5Zr was mostly α phase with range of α lamellae thickness growing from prior β grain boundaries (Figure 5.5). Light contrast original dendrites were also visible at low magnification (Figure 5.5a) which had transformed into lamellar microstructures. There was higher Ta content in the lamellae and lower Ta content in the interlamellar parts. This nonuniform distribution of Ta in the phases indicates that the Ti-6Ta-1.5Zr alloy was two-phase.

The microstructure of as-cast Ti-6Ta-1.5Zr-0.2Ru consisted of dark α phase and retained light β phase (Figure 5.6). In addition, some regions had parallel and plate-like structure (αTi) lath. Formation of plate-like laths is common in rapidly cooled Ti alloys with β-stabiliser additions (Davis et al., 1979; Banumathy et al., 2009; Salvador et al., 2016).

The microstructures of the Ti-6Ta-1.5Zr-5Cu and Ti-6Ta-1.5Zr-0.2Ru-5Cu alloys (Figures 5.6 and 5.7) had light retained (βTi) phase surrounded by dark fine laths, acicular α' martensitic structure. The repolished Ti-6Ta-1.5Zr-5Cu alloy had plate-like structure with light (βTi) layers (Figure 5.9 a,c). The as-cast Ti-6Ta-1.5Zr-0.2Ru-5Cu microstructure appeared dendritic at low magnification (Figure 5.9b), with fine dark laths within the dendrites, inclined at different angles. Plate-like structures were found in both Cu-containing alloys while in the Ti-6Ta-1.5Zr-0.2Ru-5Cu alloy they appeared as a colony of parallel laths (Figure 5.9 b,d). In addition, Ti_2Cu precipitates were present on both Cu-containing alloys microstructure indicated by light contrast particles. A similar microstructure was found in a 10 at.% hydrogenated Ti-6Al-4V alloy (Qazi et al., 2001). This microstructure had smooth regions of (αTi) phase some of which were plate-like structure (Qazi et al., 2001) similar to all the Cu-containing alloys in this work. While no precipitation of intermetallic phases was reported (Qazi et al., 2001), these regions were identified as α' and α" martensite, as shown by selective area diffraction in TEM. According to Dobromyslov and Elkin (2006), formation of α" martensite was not expected in Ti-9Cu at.% alloys due to the active eutectoid transformation. In this reaction βTi transforms to αTi + Ti_2Cu (Donthula et al., 2019). Those findings were in agreement with Kikuchi et al.

(2003), Alexandra et al. (2014), Zhang et al. (2016a), Ma et al. (2016) and Fowler et al. (2019) for binary Ti-Cu alloys. Alexandra et al. (2014) and Fowler et al. (2019) also found that the βTi phase was not formed as predicted in the calculations of their Ti-Cu compositions. In this work, calculations with Thermo-Calc of the Ti-6Ta-1.5Zr-5Cu composition predicted no β phase. However, the microstructures of both Ti-6Ta-1.5Zr-5Cu and Ti-6Ta-1.5Zr-0.2Ru-5Cu (Figure 5.7-5.8) had (αTi) and (βTi) phases. Above 882°C, pure Ti is bcc, and below is hcp. In the Ti-6Ta-1.5Zr-5Cu composition, Ti had a high content, and the eutectoid decomposition yielded αTi + Ti_2Cu (Donthula et al., 2019), hence, no (βTi) phase was predicted by Thermo-Calc. However, in the cast alloy, (βTi) was retained by fast cooling. In Ti-Cu-based alloys here, there were small amounts of β-stabilisers which helped to stabilise (βTi). Similarly, Cu-containing Ti-6Al-4V had (βTi) (Ren et al., 2014; Ma et al., 2015; Wang et al., 2015; Li et al., 2016).

6.2. XRD results

The XRD patterns obtained in 17 min did not give good match with the phases predicted by Thermo-Calc and found by SEM. In the 1h scans (Figure 5.11) no mismatch was found with the calculated phases. The XRD diffractogram of the cast Ti-6Ta-1.5Zr had peaks of (αTi). No peaks were indicative of (βTi) phase. The (βTi) phase in Ti-6Ta-1.5Zr-0.2Ru did not have any unique and significant diffraction peaks. The beta phase Ti has (110) (100% intensity (Eppelsheimer and Penman, 1950)), (200) (12% intensity (Eppelsheimer and Penman, 1950)) and (211) (17% intensity (Eppelsheimer and Penman, 1950)) as the strongest peaks, and in the as-cast alloys in this work, (βTi) was identified by the (110) peak which was also shared with αTi, with only very small (200) and (211) peaks, as expected from their reported intensities (Eppelsheimer and Penman, 1950). The missing (βTi) peaks in the diffractograms could be due to the small amount of β stabilisers giving only small β proportions. In the Cu-containing alloys, the missing (βTi) peaks were due to the eutectoid decomposition of the (βTi). In addition, crystal defects or distortion of crystalline structure could have occurred and caused reduced peaks while some could be lost in the background.

These results were similar to those of other researchers. Safdar et al. (2012) identified the βTi by the (200) peak and the (220) peak was shared with αTi while there was no significant (110) peak for electron-beam melted Ti-6Al-4V. The insignificance of the (110) peak was attributed to crystal defects or rearrangement of atoms such as ordering (Safdar et al., 2012). The observed β peaks in a grade 5 alloy were (110) and (211), and only (211) for a selective laser melted alloy (Dai et al., 2016a). The missing peaks (200) in the former alloys and (110) and (211) in latter were related to the small (βTi) phase fraction. The calculated β phase volume fraction for commercial grade 5 Ti alloy was 13.3% and selective-laser melted Ti-6Al-4V was 5% (Dai et al., 2016a). For a Ti-6Al-4V wire, Zeng and Bieler (2005) found the β phase was only identified by the (110) peak with a relatively small count. From XRD and TEM, they concluded that the missing (βTi) peaks were because the prior β phase had mostly transformed to the α phase. For as-cast Ti-6Al-4V, da Silva et al. (1999) found a unique (βTi) (110) peak, a weak (200) peak and a (211) peak which was shared with (αTi). In as-cast and hot isostatically pressed Ti-6Al-4V (Qazi et at., 2001), and a laser-deposited alloy (Dinda et al., 2008), βTi was only identified by the (110) peak. The amount of βTi phase calculated by XRD analysis in the as-cast and hot isostatically pressed Ti-6Al-4V was 7% (Qazi et at., 2001). For 5 wt% Cu as-cast and hot forged Ti-6Al-4V, (βTi) was identified by the (110) and (220) peaks (Ma et al., 2015; Li et al., 2016). The heat treated (at 900°C for 1h) alloy did not have any peaks for Ti_2Cu, instead the diffractograms had peaks of (αTi) and the (110) peak for (βTi). The diffractograms for the alloy aged at 600°C for 5h had peaks of (αTi), Ti_2Cu identified by (110) and (006), and (110) for (βTi) (Ma et al., 2015). Similar peaks and corresponding phases were observed in cast and hot forged Ti-6Al-4V with 5 wt% Cu (Wang et al., 2015). In a series of as-cast Ti-6Al-4V alloys with 1, 4 and 10 wt% Cu (Aoki et al., 2004) and as-cast Ti-6Al-4V with 1, 3 and 5 wt% Cu (Ren et al., 2014), more Ti_2Cu peaks were found with increased Cu content while peaks for β were suppressed. In all the alloys diffractograms there were no peaks indicative of martensites.

6.3. Comparing SEM and XRD results

In this study SEM was used to assess the microstructure of the samples and identify the phases formed. X-ray diffraction was used to confirm the presence of these phases. Table 6.1 shows the phases present in each alloy, identified by SEM and XRD. As-cast Ti-6Ta-1.5Zr and Ti-6Ta-1.5Zr-0.2Ru had two-phases, (Figures 5.5 and 5.6). Using EDX, the dark phase was (αTi) and the bright phase was (βTi). The as-cast Ti-6Ta-1.5Zr-5Cu and Ti-6Ta-1.5Zr-0.2Ru-5Cu alloys had three phases identified by SEM. Similarly, the dark phase was (αTi) and the bright phase was (βTi), and the very light contrast particles with higher Cu composition were identified as

Ti_2Cu phase (Figure 5.9). The plate-like dark phases were acicular α' martensite (Figures 5.7 and 5.8), found in both Cu-containing alloys. In all the alloys' diffractograms, α and β phases were found, with Ti_2Cu peaks for the Cu-containing alloys. No peaks for martensite phases (α' and/or α") were identified. The α and α' martensites have the same crystal structure (hexagonal). However, α' martensite is supersaturated in β-stabilising elements while primary α (and β) only exists in pure Ti (Motyka et al., 2014).

6.4. Comparing the Thermo-Calc phase calculation results

The developed alloys had phases that were predicted by Thermo-Calc and were observed in their microstructures and XRD results. In the phase calculations of the Ti-6Ta-1.5Zr composition, only a single-phase was predicted (Figure 4.6a). The microstructure characterisation of cast Ti-6Ta-1.5Zr showed mainly α phase by range of α lamellae thicknesses growing on and into the β gains (Figure 5.5). The EDX analyses showed a higher Ta content in the lamellae and low Ta content between the lamellae. Titanium alloys containing more than 2 wt% of β-stabilisers can stabilise 10-30% β phase to form a α+β alloy (Leyens and Peters, 2005). The EDX analysis showed a higher Ta content in the α lamellae of as-cast Ti-6Ta-1.5Zr (Figure 5.5) which indicated that Ta partitioned to the α phase. There was no clear variation in Zr content in the lamellae and interlamellar phases in this work and Zn has no effect on phase transformation (Leyens and Peters, 2003; Motyka et al., 2014). With Thermo-Calc, two phases were predicted in the Ti-6Ta-1.5Zr-0.2Ru composition and the as-cast alloy (Figure 4.6b) had a two-phase microstructure: retained β phase surrounded by α laths (Figure 5.6).

The microstructures of the Ti-6Ta-1.5Zr-5Cu and Ti-6Ta-1.5Zr-0.2Ru-5Cu alloys (Figures 5.6 and 5.7) had α and β phases. With Thermo-Calc, the Ti-6Ta-1.5Zr-0.2Ru-5Cu composition (Figure 4.7b) had α, β and Ti_2Cu phases, while for the Ti-6Ta-1.5Zr-5Cu composition (Figure 4.7a), only α and Ti_2Cu phases were predicted. Precipitation of Ti_2Cu in the alloys in this work was only discerned after they were repolished for longer time (Figure 5.9). In addition, the alloys also had acicular α' martensite indicated by dark fine laths, which could not be predicted by Thermo-Calc, since it is not an equilibrium phase. While (βTi) cannot be kept to lower temperature in binary Ti-Cu alloys (Murray, 1983; Motyka et al., 2014), both Cu-containing alloys in this work had retained (βTi) phase (Figures 5.7-5.9). Similarly, the two-phase Ti-6Al-4V with 5wt% Cu had (βTi) phase observed by XRD (Ren et al., 2014; Li et al., 2016). Table 6.1 shows the phases predicted in the Thermo-Calc calculations and the phases found in the experimental alloys.

Table 6.1: Phases predicted in Thermo-Calc compositions and formed in experimental alloys with different techniques.

Alloy	**Thermo-Calc results**	**Experimental alloys**	
		SEM	XRD
Ti-6Ta-1.5Zr	α	α and β	α
Ti-6Ta-1.5Zr-0.2Ru	α and β	α and β	α and β
Ti-6Ta-1.5Zr-5Cu	α, β and Ti_2Cu	α, β, Ti_2Cu and acicular α' martensite	α, β, Ti_2Cu and Ti_3Cu
Ti-6Ta-1.5Zr-0.2Ru-5Cu	α, β and Ti_2Cu	α, β, Ti_2Cu and acicular α' martensite	α, β, Ti_2Cu and Ti_3Cu

6.5. Comparing with published results

The as-cast Ti-6Ta-1.5Zr (Figure 5.1 a,b,c) and Ti-6Ta-1.5Zr-0.2Ru (Figure 5.1 d,e,f) alloys had basket-weave structures. The microstructures consisted of range of α laths surrounded by transformed β edges growing from prior β grain boundaries and into the prior β grains. These microstructures have been found in α+β-Ti alloys including Ti-6Al-4V since its microstructure can be manipulated by different cooling rates, thermomechanical and heat treatments (Lütjering, 1998; Leyens and Peters, 2003; Lütjering et al., 2007; Meyer et al., 2008). The thickness of the lamellae can be manipulated by range of cooling rates (Lütjering, 1998; Meyer et al., 2008; Sieniawski et al., 2013). Two-phase Ti alloys were also reported to possess a range of advantageous properties for many applications (Leyens an Peters, 2003; Sieniawski et al., 2013; Li et al., 2014). The Ti-6Al-7Nb, Ti-5Al-2.5Fe, Ti-6Al-2Mo-2Cr and Ti-6Al-5Mo-5V-1Cr-1Fe are some of the α+β-Ti with comparable microstructure with alloys in this work and they are used for different applications (Sieniawski et al., 2013; Li et al., 2014). This suggests that the alloys of the current work could also have multiple applications.

One of the other objectives of this present research is identifying an alloy that has antibacterial properties. Numerous studies have shown that this was achieved when alloying Cu to Ti and its alloys (Liu et al., 2014b; Ren et al., 2014; Li et al., 2016; Ma et al., 2016; Zhang et al., 2016b). Inactivation of bacteria attached to the surfaces of these alloys was caused by Ti_2Cu precipitates (Liu et al., 2014; Zhang et al., 2016b; Fowler et al., 2019). Copper-containing alloys in this work had sufficient Ti_2Cu precipitates (Figure 5.9) to be identified by XRD (Figure 5.11 c,d). In addition, the prior β grains transformed into α which grew from the prior β grain boundaries, and also formed the α laths which also grew into the prior β grains (Figure 5.2d and 5.3d). This led to acicular α' martensite microstructure. This typical microstructure was also found in Cu-containing Ti-6Al-4V and CP-Ti (Koike et al., 2005; Ren et al., 2014; Li et al., 2016; Zhang et al., 2016a). The mechanical and corrosion properties of these alloys were found to be sufficient for most biomedical applications (Aoki et al., 2004; Ren et al., 2014; Hayama et al., 2014; Zhang et al., 2016a).

6.6. Relationship between microstructure and hardness

The microstructure has strong relationships with alloy strength, hardness, fatigue resistance, fracture and creep behaviour (Lütjering, 1998; Poondla et al., 2009). Microstructural analysis can be utilised to assess susceptibility to failure and performance. For quick evaluation of mechanical properties, hardness testing is commonly used (Chandler, 1999). Low hardness values are expected for coarse lamellae (Meyer et al., 2008) like the Ti-6Ta-1.5Zr alloy (Figure 5.1), while increased hardness is expected for alloys with finer lamellae (Sieniawski et al., 2013) as in Ti-6Ta-1.5Zr-0.2Ru. The Ti-6Ta-1.5Zr alloy with coarse α lamellae had the lowest hardness value, 252 ± 15.4 HV of all the as-cast alloys. The Ti-6Ta-1.5Zr-0.2Ru with fine α lamellar increased the hardness to 335 ± 32.6 HV. Figures 6.1 and 6.2 shows this relationship between lamellae thickness and hardness. Figure 6.1 shows a plot of mean hardness values against lamellae thickness and Figure 6.2 shows a plot of mean hardness values against mean grain size (of parallel lamellae). In both cases, as the lamellae thickness or grain size decreased, the hardness decreased. The Ti-6Ta-1.5Zr alloy with low solute content had huge grain sizes than other cast alloys. The Ti-6Ta-1.5Zr-5Cu alloy consisted of a range of prior β grains sizes distributed through the microstructure (Figure 5.2a). Both Ti-6Ta-1.5Zr-5Cu and Ti-6Ta-1.5Zr-0.2Ru-5Cu alloys had microstructures consisting of α laths which grew from the β grain boundaries and into the prior β grains. (Figure 5.2 and 5.3). The Ti-6Ta-1.5Zr-0.2Ru-

5Cu alloy had thinner α laths compared to Ti-6Ta-1.5Zr-5Cu alloy and had the highest hardness value. Table 6.2 shows hardness values with corresponding microstructures of some reported Ti alloys and for the present work, and shows that the hardnesses of the current alloys were mostly within the same range, except for Ti-6Ta-1.5Zr which had coarse lamellae. This was encouraging since the current alloys were only as-cast and had not been optimised by heat treatment or other thermomechanical processing techniques

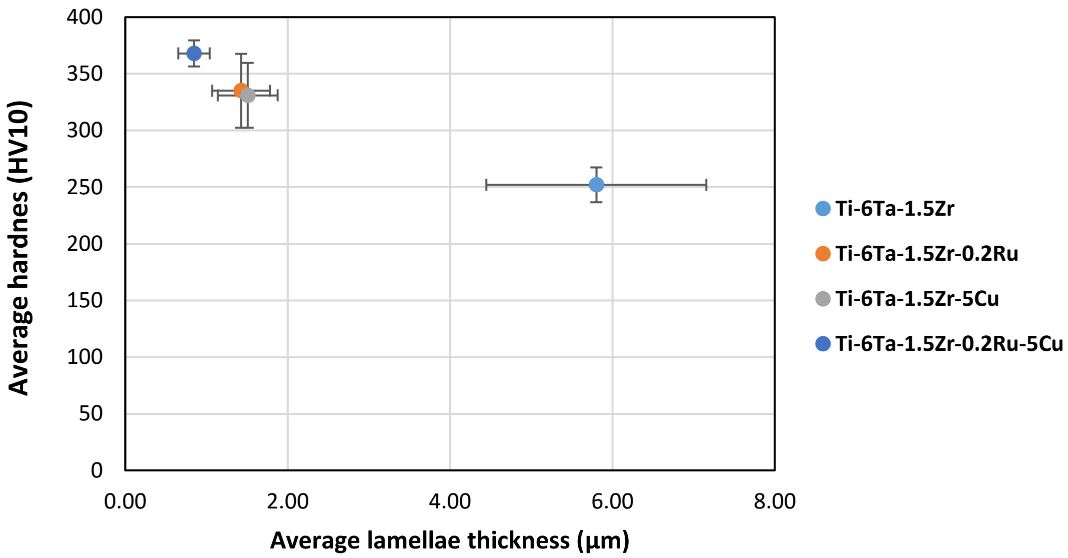

Figure 6.1: Mean hardness vs average lamellae thickness of the tested alloys.

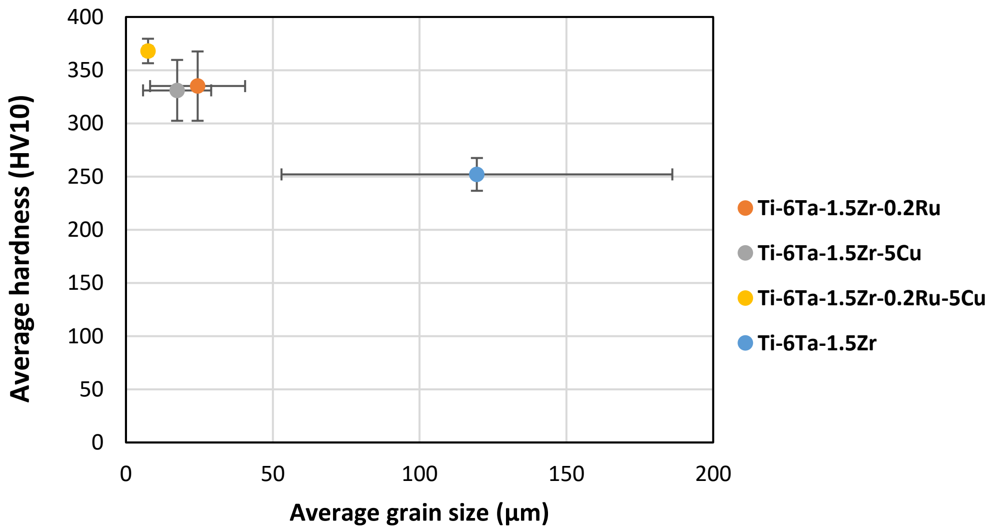

Figure 6.2: Mean hardness vs average grain size of the tested alloys.

The formation of the acicular α’ martensite in Ti alloys enhanced the hardness, tensile strength and compressive strength (Attar et al., 2014; Hayama et al., 2014; Wang et al., 2019). The Ti-6Ta-1.5Zr-0.2Ru-Cu alloy of this work had plate-like α’ martensite and had the highest hardness 368 ± 11.5 HV. A hardness close to the that measured in the Ti-6Ta-1.5Zr-0.2Ru-5Cu alloy was measured in as-cast Ti-10Cu (Hayama et al., 2014). The as-cast Ti-5Cu and Ti-7Cu with an acicular α’ martensite had hardness values close to 320 HV and 340 HV, respectively (Hayama et al., 2014), which were close to the value of 331 ± 28.6 HV of the Ti-6Ta-1.5Zr-5Cu alloy. This value was also close to the hardness measured in Ti-6Ta-1.5Zr-0.2Ru alloy. Alloys with martensite (α’ and α”) have good mechanical strength but low ductility (Lütjering et al., 2000; Attar et al., 2014; Hayama et al., 2014; Wang et al., 2019). These metastable phases (α’ and α” martensite) cause internal stresses which are detrimental to ductility (Lütjering et al., 2000). Such alloys have fully lamellar microstructures with the lamellae within the prior β grains which reduces the ductility (Lütjering, 1998; Lütjering et al., 2000). Lamellae colony size determines the slip length preferred for plastic deformation.

The average hardness values of the human cortical bone range between 33-44 $HV_{0.05}$ (Wu et al., 2019). Section of human radius were measured and were found to be 34.15 ± 6.48 $HV_{0.05}$ for proximal metaphysis, 35.24 ± 5.17 $HV_{0.05}$ for distal metaphysis and 42.54±5.59 $HV_{0.05}$ diaphysis which was measured to be the highest. The average value of the cortical bone measured by Zwierzak et al. (2009) and Öhman et al. (2013) was 42 $HV_{0.01}$. High values of hardness were found in the alloys of this work with values between 252-368 $HV_{0.5}$. High hardness is vital for biomedical implants to prevent fracture and wear (Saini et al., 2015).

6.7. Corrosion

The human body has different electrolytic substances which contain corrosive species that may increase corrosion in Ti alloys (Reclaru and Meyer, 1998; Mabilleau et al., 2006; Chen et al., 2020). Good corrosion resistance is one of the properties required for implant materials since biocompatibility is crucial (Mouhyi et al., 2012; Rodrigues et al., 2013).

Passivation of Ti and its alloys depends on the oxide layer, spontaneously formed on its surfaces (Machnee et al., 1993; Guilherme et al., 2005). The open circuit potentials of the alloys shifted in the positive direction indicating the formation and growth of an oxide layer on the alloy surfaces (Figure 5.11). No undulation was observed in all OCP curves, thus there was no dissolution of oxide film during the scan. The OCP values of the cast Ti-6Ta-1.5Zr, Ti-6Ta-1.5Zr-0.2Ru, Ti-6Ta-1.5Zr-5Cu and Ti-6Ta-1.5Zr-0.2Ru-5Cu at the 17min runs were -494 mV, -463 mV, -454 mV and -457 mV, respectively. Continuing passivation was observed for the as-cast alloys. The Ti-6Ta-1.5Zr alloy showed the highest passivation capacity due to the highest difference in its potential over the 17h of immersion. Passivation in selective-laser melted Ti-6Al-4V which had large fraction of acicular α' martensite was not achieved even after 48h in NaCl solution (Dai et al., 2016a). A series of as-cast Ti-6Al-4V-*x*Cu (*x* = 0, 1 and 4 wt% Cu) with acicular microstructure did not reach stable potentials in artificial saliva during their 16h of immersion (Koike et al., 2005). Similarly, the Ti-6Ta-1.5Zr-0.2Ru and Cu-containing alloys in this work had some martensite (Figures 5.6 and 5.7) and passivation was not achieved in 17h time. Dai et al. (2016a) suggested that long passivation found in the selective laser melted Ti-6Al-4V alloys demonstrated good passivation protection.

Table 2.4 shows CP-Ti and Ti-6Al-4V alloys and their corrosion current densities (i_{corr}) from literature (Hsu et al., 2004; Bai et al., 2012; Bai et al., 2017) studied under the same conditions as the alloys in this present study. Figure 6.3 shows a comparison i_{corr} of alloys in the present work, and Ti-6Al-4V and Ti-Cu alloys with different processing history. The alloys in this work and Ti-6Al-4V and TI-Cu alloys from literature (Bai et al., 2012; Bai et al., 2017; Amirnejad et al., 2021; Masia et al., 2021; Siddiqui et al., 2021) all had similar i_{corr}, 10^{-5}. Although the Ti-6Ta-1.5Zr-0.2Ru sample had the highest i_{corr} in Figure 6.3, most of the other alloys of this work were comparable to previous data (Bai et al., 2012; Bai et al., 2017; Amirnejad et al., 2021; Masia et al., 2021; Siddiqui et al., 2021). However, other alloys had much lower i_{corr} values (Bai et al., 2017; Amirnejad et al., 2021; Siddiqui et al., 2021). The different processing conditions result in different microstructures which has an effect on the i_{corr} and corrosion rates. The alloys in this work had slightly different microstructures, hence differences in their i_{corr} were found.

Table 6.2: Hardness values and corresponding microstructures in Ti alloys.

Alloy	Condition	Vickers Hardness (HV)	Microstructure	Reference
Ti-6Ta-1.5Zr	As-cast and fast cooled	252 ± 15.4	Coarse α lamellae	Current work
Ti-6Ta-1.5Zr-0.2Ru	As-cast and fast cooled	335 ± 32.6	Thin α lamellae	Current work
Ti-6Ta-1.5Zr-5Cu	As-cast and fast cooled	331 ± 28.6	Basket-weave structure with acicular α' martensite	Current work
Ti-6Ta-1.5Zr-0.2Ru-5Cu	As-cast and fast cooled	368 ± 11.5		Current work
Ti-3Cu	As-cast, solution treated 900°C/3h	325	Thin lamellae with acicular structure	Zhang et al., 2016a
Ti-5Cu	As-cast and fast cooled	~320	α' martensite with Ti_2Cu precipitates	Hayama et al., 2014
Ti-7Cu		~340		
Ti-6Al-4V-4Cu	As-cast	405	Basket-weave structure of acicular α' martensite	Aoki et al., 2004; Ren et al., 2014
Ti-6Al-4V	EBM, solution treated at 1050°C/2h and aged at 500°C/10h	350	Fine α laths and transformed β	Raghavan et al., 2018
Ti-6Al-4V	Annealed at 1065°C/1h, Furnace cooled	380	Plate-like, acicular α' martensite	Meyer et al., 2008

Unalloyed Ti has excellent corrosion resistance, and the addition of β-stabilisers significantly increases corrosion resistance and reduces metal ion release in a variety of corrosive environments (Geetha et al., 2009; Chen et al., 2020). These alloy additions affect the mechanism for protective oxide film formation. The components of the protective oxides of Ti, TiO_2 and other TiO variants are responsible for corrosion resistance (Machnee et al., 1993; Guilherme et al., 2005). Beta-stabilisers formed less soluble oxides, i.e. stable and inert oxides (Geetha et al., 2009). For example, Ta_2O_5, ZrO_2 and Nb_2O_5, are oxides of some β-stabilisers that were found to retard corrosion of Ti alloys (Yu et al., 1999; Guo et al, 2009; Atapour et al., 2011). In particular, Ta_2O_5 in the oxide layer improves corrosion resistance in solutions containing Cl (Guo et al, 2009) while Nb_2O_5 was reported to enhance stability at elevated temperatures, and ZrO_2 enhances resistance chemical dissolution (Yu et al., 1999). The alloys of this work have 6 wt% Ta and 1.5 wt% Zr additions, and even though not proven in this research the possibility of presence of these oxides could have aided in reduction the rate of corrosion. Blackwood and Peter (1989) found that the durability of the oxide layer depends on the rate at which they are formed. In their previous study, it was mentioned that solution composition and temperature were other factors that determine stability (Blackwood et al., 1988). Rapidly grown oxide layers had defect densities which are detrimental to corrosion resistance. The OCP profiles of the alloys in this work showed continuous growth and no undulations at any point. In addition, β-stabilisers increases passivation of Ti by shifting the potential to noble regions where it is completely passive (Tomashov et al., 1960; Tomashov et al., 1961; Cotton, 1967). Alloys of this work had comparable corrosion rates with Ti-6Al-4V without any heat treatment and their microstructures were martensitic which can be detrimental to corrosion resistance. Furthermore, αTi-alloys containing some β-stabilisers have rapid transitions to the passive state in comparison to alloys in the annealed state (Tomashov et al., 1974). Conversely, in alloys with two-phases, the β phase proportion was more stable while the α was dissolved in the active region. However, the β phase part was more dissolved in the transpassive regions. While the proportion of each phase was not calculated in each alloy, Ti-6Ta-1.5Zr was more susceptible to corrosion (Figure 5.17). In this alloy no β phase was found and was less corrosion resistant.

The polarisation curves of the alloys (Figure 5.15) showed typical active-passive behaviour, shifting to the passive region which agreed with the OCP curves. Low corrosion rates were obtained from potentiodynamic polarisation test for all alloys. There was no pitting breakdown was observed in all the potentiodynamic polarisation curves of the tested alloys. All the as-cast alloys had similar corrosion potentials, between -588.01 and -512.69 mV, Table 5.4.

The corrosion current densities of the current alloys were similar (Table 5.4). The slight differences in the i_{corr} cannot give reasonable comparison between alloys with and without Cu additions. The precipitation of Ti_2Cu was more pronounced in the Ti-6Ta-1.5Zr-0.2Ru-5Cu alloy (Figure 5.9 b,d) than the Ti-6Ta-1.5Zr-5Cu (Figure 5.9 a,c). Spacing between the particles

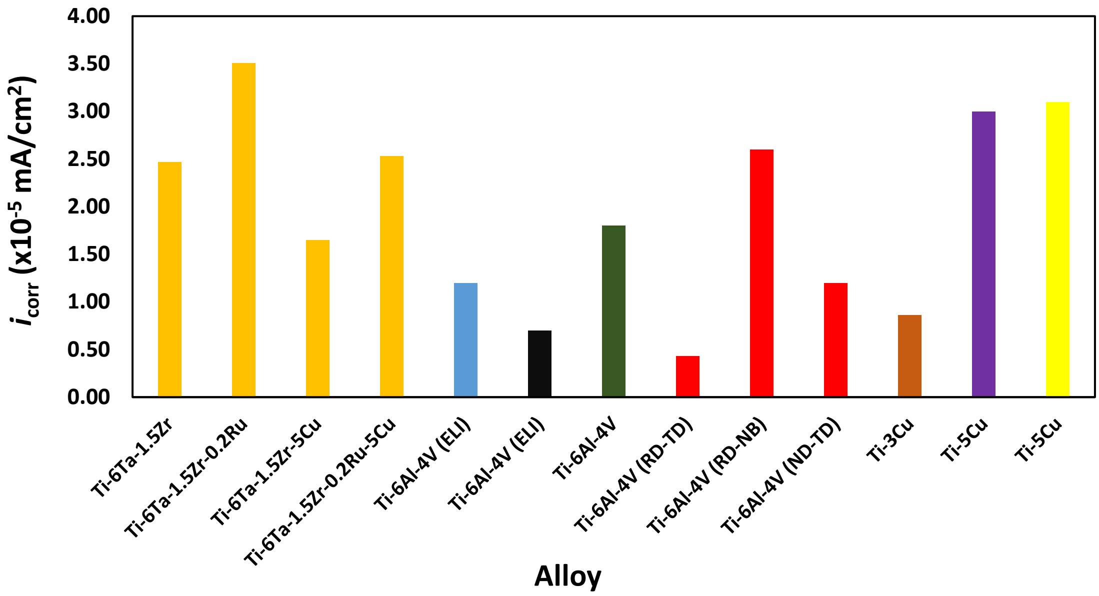

Figure 6.3: Corrosion current densities of Ti alloys processed different conditions: Ti-6Ta-1.5Zr, Ti-6Ta-1.5Zr-0.2Ru, Ti-6Ta-1.5Zr-5Cu and Ti-6Ta-1.5Zr-0.2Ru-5Cu (gold bars) (this work), wrought Ti-6Al-4V (blue bar) and electron-beam melted Ti-6Al-4V (black bar) (Bai et al., 2017); Ti-6Al-4V as-cast, hot forged at 850°C, heat treated at 750°C/1h, air cooled (green bar) (Bai et al., 2012); Ti-6Al-4V as-cast, rolled, heat treated at 927°C/4h, cooled at 50°C/1h to 760°C subsequent air cooled. (red bars) corrosion was studied on all three surfaces of its rectangular sample (RD-TD), (RD-NB), (ND-TD) (Amirnejad et al., 2021); Ti-3Cu as-cast and annealed at 740°C/1h (orange bars) (Siddiqui et al., 2021); as-cast Ti-5Cu (purple bar); Ti-5Cu as-cast and annealed at 900°C/2h, water quenched (yellow bar) (Masia et al., 2021).

was smaller in the Ti-6Ta-1.5Zr-0.2Ru-5Cu alloy which had slightly high corrosion rates compared to Ti-6Ta-1.5Zr-5Cu. Although higher volume fractions of Ti_2Cu lowered corrosion rates (Qin et al., 2018), the Ti-6Ta-1.5Zr-0.2Ru-5Cu alloy had finer (αTi) laths than Ti-6Ta-1.5Zr-5Cu. Acicular α’ and α in rapidly cooled α- and α+β-Ti alloys have similar crystal structure (Lütjering et al., 2000; Leyens and Peters, 2003), but α’ martensite is a metastable phase and has been reported to decrease corrosion resistance (Dai et al., 2016a; Dai et al., 2016b; Qin et al., 2018). Therefore, the higher corrosion rates for Ti-6Ta-1.5Zr-0.2Ru-5Cu alloy can be associated with deleterious α’ martensite.

Copper additions to as-cast Ti slightly increased corrosion resistance in various media (Osório et al., 2010; Zhang et al., 2016a; Zhang et al., 2016b; Ma et al., 2016; Qin et al., 2018). Similarly, for as-cast Ti-6Al-4V, Cu additions caused slight corrosion resistance improvements (Koike et al., 2005; Ren et al., 2014). The Ti_2Cu plays an important role in enhancing corrosion resistance and slight improvements in corrosion resistance were found as Cu content increased (Zhang et al., 2016a; Qin et al., 2018). The expected and accepted corrosion rate for biomedical materials is 0.13 mm/y (Bhola et al., 2011) which is more than the rates calculated in alloys in this present study, so shows these alloys were acceptable. The corrosion current densities are comparable to Ti-6Al-4V and Ti-Cu alloys.

The analyses and tests conducted in this study show that the Ti-6Ta-1.5Zr-5Cu and Ti-6Ta-1.5Zr-0.2Ru-5Cu alloys have potential for biomedical applications, even though the antimicrobial activity was assumed from the copper content and not actually measured. The microstructures showed that both alloys had three-phases, α, β and Ti_2Cu. The Ti_2Cu phase is mostly advantageous for antibacterial properties (Zhang et al., 2013; Lui et al., 2014; Zhang et al., 2016b). While α+β titanium alloys have been reported to have sufficient properties for biomedical applications (Geetha et al., 2009; Li et al., 2014), the formation of Ti_2Cu gives additional advantage in enhancing corrosion resistance (Zhang et al., 2013; Lui et al., 2014), hardness (Kikuchi et al., 2003) and strength (Kikuchi et al., 2003; Zhang et al., 2013). Comparable hardness values with those of Ti-6Al-4V (Meyer et al., 2008; Raghavan et al., 2018) and Ti-Cu alloys (Hayama et al., 2014; Zhang et al., 2016a) were obtained on both alloys. The long passivation period observed suggest good protection of the surface (Dai et al., 2016a). Low corrosion rates were found on both alloys which comparable to Ti-6Al-4V alloy. No pitting breakdown was observed within the potentials tested, which is beneficial.

Figures 5.18, 5.19, 5.20 and 5.21 show the SEM micrographs of the alloy samples of this work that were tested for corrosion. Localised pits were found on their surfaces while some holes were result of sample preparation. The pits that seemed to be a result of localised attack had some electrolyte species components. This was observed by EDX, Figure 5.22. The OCP curves of the developed alloys showed continuous growth as there was no stable potentials reached during the scans. The open circuit breakdown of the passive layer on Ti appeared to result from uniform chemical dissolution of the oxide rather than localised corrosion (Blackwood et al., 1988). No pitting breakdown was observed within the potentials tested. This could also be attributed to the possible formation of β-stabiliser oxides on surface exposed to the electrolyte (Yu et al., 1999; Guo et al, 2009; Atapour et al., 2011). Chlorine species are detrimental to the oxide layer and when they reach the surface of the metal could cause localised attack (Guo et al., 2009). The oxides of β-stabilisers also enhance the stability of TiO and its variants and inhibit its dissolution rate (Yu and Scully, 1997). This hinders the penetration of Cl species to the metal surface.

Chapter 7: Conclusions

In this work an attempt to identify Ti-Cu-based alloys for biomedical application was made. Phase proportions of the identified alloys were calculated by Thermo-Calc. The predicted phases identified the alloys for subsequent experiments: Ti-6Ta-1.5Zr, Ti-6Ta-1.5Zr-0.2Ru, Ti-6Ta-1.5Zr-5Cu and Ti-6Ta-1.5Zr-0.2Ru-5Cu. Microstructural and XRD analysis, hardness and corrosion tests were done and showed reasonable matches between the benchmark Ti-6Al-4V and Ti-Cu alloys.

The microstructural and EDX analyses showed that Ti-6Ta-1.5Zr and Ti-6Ta-1.5Zr-0.2Ru alloys were two-phase. The Cu-containing alloys; Ti-6Ta-1.5Zr-5Cu and Ti-6Ta-1.5Zr-0.2Ru-5Cu had fine laths, acicular α' martensite and retained β phase. The Ti_2Cu precipitates and plate-like regions were observed after repolishing.

The microstructures of the alloys in this work were similar to reported Ti-6Al-4V, Ti-6Al-4V-5Cu and Ti-Cu alloys. A reasonable match with hardness values was found. Precipitation of Ti_2Cu phase was found in Cu-containing alloys, which is crucial for antibacterial properties. The microstructures affected the measured hardness values and corrosion results. The Ti-6Ta-1.5Zr alloy with coarse laths had low hardness while Ti-6Ta-1.5Zr-0.2Ru and Ti-6Ta-1.5Zr-5Cu with fine laths had higher hardnesses. In addition, Ti-6Ta-1.5Zr-0.2Ru-5Cu with plate-like phases had highest hardness.

In corrosion tests, the OCP vs time scans showed increasing passivation, while the potentiodynamic scans showed a typical active-passive behaviour, shifting to the passive region which agreed with the OCP profiles. The OCP of the alloys did not reach stable potentials in a reasonable time, which was attributed to the metastable α' phase. The corrosion current densities of the alloys were similar. Corrosion rates were low and there were reasonable matches between these Cu-containing alloys and the Ti-6Al-4V alloy. From the results and analysis carried out for each alloy, Ti-6Ta-1.5Zr-5Cu and Ti-6Ta-1.5Zr-0.2Ru-5Cu were best alloys, with the target phases α, β and Ti_2Cu. Hardness values were comparable to Ti-6Al-4V and Ti-Cu alloys.

References

Abdel-Hady Gepreel M., Niinomi, M., 2013. Biocompatibility of Ti-alloys for long-term implantation. J. Mech. Behav. Biomed. Mater. 20, 407–415.

Abou Shahba, R.M., Ghannem, W.A., El-Shenawy, A.E.S., Ahmed, A.S. and Tantawy, S.M., 2011. Corrosion and inhibition of Ti-6Al-4V alloy in NaCl solution. International Journal of Electrochemical Science. 6, 5499-5509.

Adya, N., Alam, M., Ravindranath, T., Mubeen, A., Saluja, B., 2005. Corrosion in titanium dental implants: literature review. J. Indian Prosthodont. Soc. 5, 126-131.

Ahmed, T. and Rack, H.J., 1998. Phase transformations during cooling in α+β titanium alloys. Materials Science and Engineering. 243, 206-211.

Alaghmandfard, R., Chalasani, D., Odeshi, A. and Mohammadi, M., 2021. Activated slip and twin systems in electron beam melted Ti-6Al-4V subjected to elevated and high strain rate dynamic deformations. Materials Characterization. 172, 110866.

Alves, V.A., Reis, R.Q., Santos, I.C.B., Souza, D.G., Gonçalves, T.D.F., Pereira-da-Silva, M.A., Rossi, A., da Silva, L.A., 2009. In situ impedance spectroscopy study of the electrochemical corrosion of Ti and Ti-6Al-4V in simulated body fluid at 25°C and 37°C. Corrosion Science. 51, 2473–2482.

Amirnejad, M., Rajabi, M. and Jamaati, R., 2021. The effect of crystallographic texture as a distinct effective parameter on the biocorrosion performance of Ti6Al4V alloy in PBS solution. Corrosion Science. 179, 1-11.

Andersson, J.O., Helander, T., Höglund, L., Shi, P. and Sundman, B., 2002. Thermo-Calc & DICTRA, computational tools for materials science. Calphad. 26, 273-312.

Aoki, T., Okafor, I.C.I., Watanabe, I., Hattori, M., Oda, Y., Okabe, T., 2004. Mechanical properties of cast Ti-6Al-4V-*xCu* alloys. Journal Oral Rehabilitation. 31, 1109–1114.

Arciola, C.R., Campoccia, D., Speziale, P., Montanaro, L., Costerton, J.W., 2012. Biofilm formation in *Staphylococcus* implant infections. A review of molecular mechanisms and implications for biofilm-resistant materials. Biomaterials. 33, 5967–5982.

Askeland, D.R., Phulé, P.P., Wright, W.J. and Bhattacharya, D.K., 2003. The science and engineering of materials. Cengage Learning.

ASTM G3-89, 2010. Standard practice for conventions applicable to electrochemical measurements in corrosion testing. Annual Book of ASTM Standards.

Atapour, M., Pilchak, A.L., Frankel, G.S. and Williams, J.C., 2011. Corrosion behavior of β titanium alloys for biomedical applications. Materials Science and Engineering: C. 31, 885-891.

Athanasou, N.A., 2016. The pathobiology and pathology of aseptic implant failure. Bone and Joint Research. 5, 162–168.

Attar, H., Calin, M., Zhang, L.C., Scudino, S. and Eckert, J., 2014. Manufacture by selective laser melting and mechanical behavior of commercially pure titanium. Materials Science and Engineering: A. 593, 170-177.

Bai, Y., Gai, X., Li, S., Zhang, L.C., Liu, Y., Hao, Y., Zhang, X., Yang, R. and Gao, Y., 2017. Improved corrosion behaviour of electron beam melted Ti-6Al–4V alloy in phosphate buffered saline. Corrosion Science. 123, 289-296.

Bai, Y., Li, S.J., Prima, F., Hao, Y.L. and Yang, R., 2012. Electrochemical corrosion behavior of Ti–24Nb–4Zr–8Sn alloy in a simulated physiological environment. Applied surface science. 258, 4035-4040.

Bammidi, R. and Prasad, K.S., 2020. Ti-6Al-4V as Dental Implant. EAS Journal of Dentistry and Oral Medicine. 2, 14-18.

Banumathy, S., Mandal, R.K., Singh, A.K., 2009. Structure of orthorhombic martensitic phase in binary Ti–Nb alloys. Journal of Applied Physics. 106, 1-6.

Baral, M., Hama, T., Knudsen, E., Korkolis, Y.P., 2018. Plastic deformation of commercially-pure titanium: experiments and modeling. International Journal of Plasticity. 105, 164–194.

Blackwood, D.J. and Peter, L.M., 1989. The influence of growth rate on the properties of anodic oxide films on titanium. Electrochimica Acta. 34, 1505-1511.

Blackwood, D.J., Peter, L.M. and Williams, D.E., 1988. Stability and open circuit breakdown of the passive oxide film on titanium. Electrochimica Acta. 33, 1143-1149.

Brandl, E., Palm, F., Michailov, V., Viehweger, B. and Leyens, C., 2011. Mechanical properties of additive manufactured titanium (Ti–6Al–4V) blocks deposited by a solid-state laser and wire. Materials & Design. 32, 4665-4675.

Behera, M., Mythili, R., Raju, S. and Saroja, S., 2013. Effect of cooling rate on mechanism of β→ α phase transformation on continuous cooling in Ti–5Ta–1.8 Nb alloy. Journal of Alloys and Compounds. 553, 59-68.

Bhola, R., Bhola, S.M., Mishra, B. and Olson, D.L., 2011. Corrosion in titanium dental implants/prostheses–a review. Trends Biomater Artif Organs. 25, 34-46.

Biesiekierski, A., Ping, D.H., Yamabe-Mitarai, Y., Wen, C., 2014. Impact of ruthenium on microstructure and corrosion behavior of β-type Ti–Nb–Ru alloys for biomedical applications. Materials and Design. 59, 303–309.

Biesiekierski, A., Wang, J., Gepreel, M.A.H. and Wen, C., 2012. A new look at biomedical Ti-based shape memory alloys. Acta Biomaterialia. 8, 1661-1669.

Bodunrin, M.O., 2016. Titanium: metal of the future. Science Today. Available at: https://www.aasciences.africa/news/developing-affordable-titanium-implants-africa. (Accessed: 30 August 2022).

Brandes, M.C., Baughman, M., Mills, M.J. and Williams, J.C., 2012. The effect of oxygen and stress state on the yield behavior of commercially pure titanium. Materials Science and Engineering. 551, 13-18.

Briant, C.L., Wang, Z.F. and Chollocoop, N., 2002. Hydrogen embrittlement of commercial purity titanium. Corrosion Science. 44, 1875-1888.

Britton, T.B., Dunne, F.P.E. and Wilkinson, A.J., 2015. On the mechanistic basis of deformation at the microscale in hexagonal close-packed metals. Proceedings of the Royal Society A: Mathematical, Physical and Engineering Sciences. 471, 1-29.

Brossia, C.S. and Cragnolino, G.A., 2001. Effects of environmental and metallurgical conditions on the passive and localised dissolution of Ti-0.15%Pd. Corrosion. 9, 768–779.

Burstein, G.T. and Daymond, B.T., 2009. The remarkable passivity of austenitic stainless steel in sulphuric acid solution and the effect of repetitive temperature cycling. Corrosion science. 51, 2249-2252.

Castany, P., Pettinari-Sturmel, F., Crestou, J., Douin, J. and Coujou, A., 2007. Experimental study of dislocation mobility in a Ti–6Al–4V alloy. Acta Materialia. 55, 6284-6291.

Cardoso, F.F., Cremasco, A., Contieri, R.J., Lopes, E.S.N., Afonso, C.R.M. and Caram, R., 2011. Hexagonal martensite decomposition and phase precipitation in Ti–Cu alloys. Materials & Design. 32, 4608-4613.

Chandler, H., 1999. Introduction to hardness testing. Hardness testing. USA: ASM International. 1-13.

Chaturvedi, T.P., 2009. An overview of the corrosion aspect of dental implants (titanium and its alloys). Indian Journal of Dental Research, 20, 91-98.

Chen, J.R. and Tsai, W.T., 2011. In situ corrosion monitoring of Ti–6Al–4V alloy in H_2SO_4/HCl mixed solution using electrochemical AFM. Electrochimica Acta. 56, 1746-1751.

Chen, L.Y., Cui, Y.W. and Zhang, L.C., 2020. Recent development in beta titanium alloys for biomedical applications. Metals. 10, 1-29.

Chen, M., Zhang, E. and Zhang, L., 2016. Microstructure, mechanical properties, bio-corrosion properties and antibacterial properties of Ti–Ag sintered alloys. Materials Science and Engineering: C. 62, 350-360.

Chong, Y., Bhattacharjee, T., Park, M.H., Shibata, A. and Tsuji, N., 2018. Factors determining room temperature mechanical properties of bimodal microstructures in Ti-6Al-4V alloy. Materials Science and Engineering: A. 730, 217-222.

Chong, Y., Bhattacharjee, T., Shibata, A. and Tsuji, N., 2017, July. Investigation of the grain size effect on mechanical properties of Ti-6Al-4V alloy with equiaxed and bimodal microstructures. In IOP Conference Series: Materials Science and Engineering. 219, 1-7.

Chong, Y., Bhattacharjee, T., Tsuji, N., 2019. Bi-lamellar microstructure in Ti–6Al–4V: Microstructure evolution and mechanical properties. Materials Science and Engineering. 762, 1-8.

Clayton, J.D., 2011. Nonlinear Mechanics of Crystals, Solid Mechanics and Its Applications. Springer Netherlands, Dordrecht. 177, 379-394.

Clemens, H., Mayer, S. and Scheu, C., 2017. Microstructure and Properties of Engineering Materials. Neutrons and Synchrotron Radiation in Engineering Materials Science: From Fundamentals to Applications. WILEY-VCH Verlag GmbH & Co. KGaA. Weinhelm. 1-20.

Clouet, E., Caillard, D., Chaari, N., Onimus, F. and Rodney, D., 2015. Dislocation locking versus easy glide in titanium and zirconium. Nature Materials. 14, 931-936.

Cordeiro, J.M. and Barão, V.A., 2017. Is there scientific evidence favoring the substitution of commercially pure titanium with titanium alloys for the manufacture of dental implants? Materials Science and Engineering: C. 71, 1201-1215.

Cotton, J.B., 1958. Platinum-faced titanium for electrochemical anodes. Platinum Metals Review. 2, 45-47.

Cotton, J.B., 1967. The role of palladium in enhancing corrosion resistance of titanium. Platinum Metals Review. 11, 50-52.

Cotton, J.B. and Downing, B.P., 1957. Corrosion resistance of titanium to sea water. Transition Institution Marine Engineering. 69, 311-320.

Cvijovic-Alagic, J., Cvijovic, Z., Mitrovic, S., Panic, V. and Rakin, M., 2011. Wear and corrosion behavior of Ti-13Zr-13Nb and Ti-6Al-4V alloys in simulated physiological solution. Corrosion Science. 53, 796-808.

Dai, N., Zhang, L.C., Zhang, J., Chen, Q. and Wu, M., 2016a. Corrosion behavior of selective laser melted Ti-6Al-4 V alloy in NaCl solution. Corrosion Science. 102, 484-489.

Dai, N., Zhang, L.C., Zhang, J., Zhang, X., Ni, Q., Chen, Y., Wu, M. and Yang, C., 2016b. Distinction in corrosion resistance of selective laser melted Ti-6Al-4V alloy on different planes. Corrosion Science. 111, 703-710.

Davis, R., Flower, H.M. and West, D.R.F., 1979. Martensitic transformations in Ti-Mo alloys. Journal of Materials Science. 14, 712-722.

Delannoy, S., Sarah, B.A.Ï.Z., Laheurte, P., Jordan, l. and Prima, F., 2020. Development of elastically graded titanium alloys for biomedical applications. in MATEC Web of Conferences. 321, 1-7. EDP Sciences.

Dinda, G.P., Song, L. and Mazumder, J., 2008. Fabrication of Ti-6Al-4V scaffolds by direct metal deposition. Metallurgical and Materials Transactions A. 39, 2914-2922.

Dobromyslov, A.V., Elkin, V.A., 2006. The orthorhombic α″-phase in binary titanium-base alloys with d-metals of V–VIII groups. Materials Science and Engineering: A. 438–440, 324–326.

de Assis, S.L., Wolynec, S. and Costa, I., 2006. Corrosion characterization of titanium alloys by electrochemical techniques. Electrochimica Acta. 51, 1815-1819.

Du, W.L., Niu, S.S., Xu, Y.L., Xu, Z.R., Fan, C.L., 2009. Antibacterial activity of chitosan tripolyphosphate nanoparticles loaded with various metal ions. Carbohydrate Polymers. 75, 385–389.

Duarte, A., Viana, F. and Santos, H.M., 1999. As-cast titanium aluminides microstructure modification. Materials research. 2, 191-195.

Dutta, R.C., Dutta, A.K., Basu, B., 2017. Engineering implants for fractured bones; metals to tissue constructs. Journal of Materials Engineering and Applications. 1, 9-13.

Dwivedi, S.K. and Vishwakarma, M., 2018. Hydrogen embrittlement in different materials: a review. International Journal of Hydrogen Energy. 43, 21603-21616.

Eisenbarth, E., Velten, D., Müller, M., Thull, R., Breme, J., 2004. Biocompatibility of β-stabilizing elements of titanium alloys. Biomaterials. 25, 5705–5713.

Elias, C.N., Lima, J.H.C., Valiev, R., Meyers, M.A., 2008. Biomedical applications of titanium and its alloys. JOM. 60, 46–49.

Eppelsheimer, D.S. and Penman, R.R., 1950. Accurate Determination of the Lattice of Beta-Titanium at 900° C. Nature. 166, 960-960.

Feng, Q.L., Wu, J., Chen, G.Q., Cui, F.Z., Kim, T.N., Kim, J.O., 2000. A mechanistic study of the antibacterial effect of silver ions on *Escherichia coli* and *Staphylococcus aureus*. Journal of Biomedical Materials Research. 52, 662–668.

Filip, R., Kubiak, K., Ziaja, W. and Sieniawski, J., 2003. The effect of microstructure on the mechanical properties of two-phase titanium alloys. Journal of Materials Processing Technology. 133, 84-89.

Foster, H.A., Ditta, I.B., Varghese, S., Steele, A., 2011. Photocatalytic disinfection using titanium dioxide: spectrum and mechanism of antimicrobial activity. Applied Microbiology Biotechnology. 90, 1847–1868.

Fowler, L., Engqvist, H. and Öhman-Mägi, C., 2019. Effect of copper ion concentration on bacteria and cells. Materials. 12, 1-13.

Freese, H.L., Volas, M.G., Wood, J.R., 2001. Metallurgy and Technological Properties of Titanium and Titanium Alloys, in: Brunette, D.M., Tengvall, P., Textor, M., Thomsen, P. (Eds.), Titanium in Medicine: Material Science, Surface Science, Engineering, Biological Responses and Medical Applications, Engineering Materials. Springer Berlin Heidelberg, Berlin, Heidelberg. 25–51.

Galandáková, A., Franková, J., Ambrožová, N., Habartová, K., Pivodová, V., Zálešák, B., Šafářová, K., Smékalová, M. and Ulrichová, J., 2016. Effects of silver nanoparticles on human dermal fibroblasts and epidermal keratinocytes. Human & Experimental Toxicology. 35, 946-957.

Geetha, M., Singh, A.K., Asokamani, R., Gogia, A.K., 2009. Ti based biomaterials, the ultimate choice for orthopaedic implants – A review. Prog. Mater. Sci. 54, 397–425.

Gomez-Gallegos, A., Mandal, P., Gonzalez, D., Zuelli, N. and Blackwell, P., 2018. Studies on titanium alloys for aerospace application. In Defect and Diffusion Forum. Trans Tech Publications Ltd. 385, 419-423.

Guilherme, A.S., Henriques, G.E.P., Zavanelli, R.A., Mesquita, M.F., 2005. Surface roughness and fatigue performance of commercially pure titanium and Ti-6Al-4V alloy after different polishing protocols. J. Prosthet. Dent. 93, 378–385.

Guindy, J.S., Schiel, H., Schmidli, F., Wirz, J., 2004. Corrosion at the Marginal Gap of Implant-Supported Suprastructures and Implant Failure. Int. J. Oral Maxillofac. Implants 19, 826–831.

Guo, W.Y., Sun, J. and Wu, J.S., 2009. Electrochemical and XPS studies of corrosion behaviour of Ti–23Nb–0.7 Ta–2Zr–O alloy in Ringer's solution. Materials Chemistry and Physics. 113, 816-820.

Gupta, A., Khatirkar, R.K., Kumar, A. and Parihar, M.S., 2018. Investigations on the effect of heating temperature and cooling rate on evolution of microstructure in an α+ β titanium alloy. Journal of Materials Research. 33, 946-957.

Haase, F., Siemers, C., Klinge, L., Lu, C., Lang, P., Lederer, S., König, T. and Rösler, J., 2020. Aluminum-and Vanadium-free Titanium Alloys for Medical Applications. In MATEC Web of Conferences. 321, 1-6.

Hall, E.O., 1951. The deformation and ageing of mild steel: III Discussion of results. Proceedings of the Physical Society. Section B. 64, 747-752.

Hasan, J., Crawford, R.J., Ivanova, E.P., 2013. Antibacterial surfaces: the quest for a new generation of biomaterials. Trends Biotechnol. 31, 295–304.

Hayama, A.O., Andrade, P.N., Cremasco, A., Contieri, R.J., Afonso, C.R. and Caram, R., 2014. Effects of composition and heat treatment on the mechanical behavior of Ti–Cu alloys. Materials & Design. 55, 1006-1013.

He, G., Liu, P. and Tan, Q., 2012. Porous titanium materials with entangled wire structure for load-bearing biomedical applications. Journal of the Mechanical Behavior of Biomedical Materials. 5, 16-31.

He, J., Li, D., Jiang, W., Ke, L., Qin, G., Ye, Y., Qin, Q., Qiu, D., 2019. The Martensitic Transformation and Mechanical Properties of Ti-6Al-4V Prepared via Selective Laser Melting. Materials. 12, 1-14.

Hidalgo, A.A., Limberg, W., Ebel, T., Frykholm, R., Carreño-Morelli, E. and Pyczak, F., 2018. Influence of alloying elements in fatigue properties of α/β titanium alloys. Key Engineering Materials. 770, 80-86.

Hsu, R.W.W., Yang, C.C., Huang, C.A. and Chen, Y.S., 2004. Investigation on the corrosion behavior of Ti–6Al–4V implant alloy by electrochemical techniques. Materials chemistry and physics. 86, 269-278.

Huang, C.H., Chen, T.H., Chiang, C.C., Lin, S.Y., 2018. Electrochemical Corrosion and Mechanical Properties of two biomedical Titanium alloys. Int. J. Electrochem. Sci. 13, 2779-2790.

Jackson, M., Dashwood, R.J., Christodoulou, L. and Flower, H.M., 2000. Application of novel technique to examine thermomechanical processing of near β alloy Ti–10V–2Fe–3Al. Materials Science and Technology. 16, 1437-1444.

Jovanović, M.T., Tadić, S., Zec, S., Mišković, Z. and Bobić, I., 2006. The effect of annealing temperatures and cooling rates on microstructure and mechanical properties of investment cast Ti–6Al–4V alloy. Materials & Design. 27, 192-199.

Jung, W.K., Koo, H.C., Kim, K.W., Shin, S., Kim, S.H., Park, Y.H., 2008. Antibacterial Activity and Mechanism of Action of the Silver Ion in *Staphylococcus aureus* and *Escherichia coli*. Appl. Environ. Microbiol. 74, 2171–2178.

Kakaei, K., Esrafili, M.D. and Ehsani, A., 2019. Graphene and anticorrosive properties. In Interface science and technology. 27, 303-337.

Kang, L. and Yang, C., 2019. A Review on High-Strength Titanium Alloys: Microstructure, Strengthening, and Properties. Advanced Engineering Materials. 21, 1-27.

Kang, M.K., Moon, S.K., Kwon, J.S., Kim, K.M. and Kim, K.N., 2012. Antibacterial effect of sand blasted, large-grit, acid-etched treated Ti–Ag alloys. Materials Research Bulletin. 47, 2952-2955.

Karlsson, N., 1951. An X-Ray study of the Phases in the Copper Titanium System, J. Inst. Met, 79, 391-405.

Karthega, M., Raman, V. and Rajendran, N., 2007. Influence of potential on the electrochemical behaviour of β titanium alloys in Hank's solution. Acta Biomaterialia, 3, 1019-1023.

Kaur, M. and Singh, K., 2019. Review on titanium and titanium-based alloys as biomaterials for orthopaedic applications. Materials Science and Engineering: C. 102, 844-862.

Kherrouba, N., Bouabdallah, M., Badji, R., Carron, D. and Amir, M., 2016. Beta to alpha transformation kinetics and microstructure of Ti-6Al-4V alloy during continuous cooling. Materials Chemistry and Physics. 181, 462-469.

Kikuchi, M., Takada, Y., Kiyosue, S., Yoda, M., Woldu, M., Cai, Z., Okuno, O., Okabe, T., 2003. Mechanical properties and microstructures of cast Ti–Cu alloys. Dent. Mater. 19, 174–181.

Koike, M., Cai, Z., Oda, Y., Hattori, M., Fujii, H. and Okabe, T., 2005. Corrosion behavior of cast Ti-6Al-4V alloyed with Cu. Journal of Biomedical Materials Research Part B: Applied Biomaterials: An Official Journal of The Society for Biomaterials, The Japanese Society for Biomaterials, and The Australian Society for Biomaterials and the Korean Society for Biomaterials. 73, 368-374.

Koike, M., Fujii, H., 2001. The corrosion resistance of pure titanium in organic acids. Biomaterials. 22, 2931–2936.

Koizumi, H., Ishii, T., Okazaki, T., Kaketani, M., Matsumura, H. and Yoneyama, T., 2018. Castability and mechanical properties of Ti-15Mo-5Zr-3Al alloy in dental casting. Journal of Oral Science, 60, 285-292.

Koizumi, H., Takeuchi, Y., Imai, H., Kawai, T. and Yoneyama, T., 2019. Application of titanium and titanium alloys to fixed dental prostheses. Journal of Prosthodontic Research. 63, 266-270.

Kroll, W., 1940. The production of ductile titanium. Transactions of the Electrochemical Society. 78, 35-47.

Lavos-Valereto, I.C., Costa, I. and Wolynec, S., 2002. The electrochemical behavior of Ti-6Al-7Nb alloy with and without plasma-sprayed hydroxyapatite coating in Hank's solution. Journal of Biomedical Materials Research: An Official Journal of The Society for Biomaterials, The Japanese Society for Biomaterials, and The Australian Society for Biomaterials and the Korean Society for Biomaterials. 63, 664-670.

Lavos-Valereto, I.C., Wolynec, S., Ramires, I., Guastaldi, A.C. and Costa, I., 2004. Electrochemical impedance spectroscopy characterization of passive film formed on implant Ti–6Al–7Nb alloy in Hank's solution. Journal of Materials Science: Materials in Medicine. 15, 55-59.

Le Guéhennec, L., Soueidan, A., Layrolle, P. and Amouriq, Y., 2007. Surface treatments of titanium dental implants for rapid osseointegration. Dental materials, 23, 844-854.

Leyens, C., Peters, M., 2003. Titanium and Titanium Alloys: Fundamentals and Applications. John Wiley & Sons. WILEY-VCH Verlag GmbH & Co. KGaA. Weinhelm. 1-57.

Li, B., Liu, X., Meng, F., Chang, J. and Ding, C., 2009. Preparation and antibacterial properties of plasma sprayed nano-titania/silver coatings. Materials Chemistry and Physics. 118, 99-104.

Li, B.Q., Li, C.L., Wang, Z.X. and Lu, X., 2019. Preparation of Ti–Nb–Ta–Zr alloys for load-bearing biomedical applications. Rare Metals, 38, .571-576.

Li, J.C.M., 2000. Microstructure and Properties of Materials. University of Rochester. 2, 25-58.

Li, J.P., de Wijn, J.R., Van Blitterswijk, C.A. and de Groot, K., 2006. Porous Ti-6Al-4V scaffold directly fabricating by rapid prototyping: preparation and in vitro experiment. Biomaterials. 27, 1223-1235.

Li, M., Ma, Z., Zhu, Y., Xia, H., Yao, M., Chu, X., Wang, X., Yang, K., Yang, M., Zhang, Y., Mao, C., 2016. Toward a Molecular Understanding of the Antibacterial Mechanism of Copper-Bearing Titanium Alloys against *Staphylococcus aureus*. Advanced Healthcare Materials. 5, 557–566.

Li, Y., Yang, C., Zhao, H., Qu, S., Li, X. and Li, Y., 2014. New Developments of Ti-Based Alloys for Biomedical Applications. Materials. 7, 1709–1800.

Li, Y.Y.; Zou, L.M.; Yang, C.; Li, Y.H.; Li, L.J., 2013. Ultrafine-grained Ti-based composites with high strength and low modulus fabricated by spark plasma sintering. Materials Science and Engineering. 560, 857–861.

Liu, J., Li, F., Liu, C., Wang, H., Ren, B., Yang, K., Zhang, E., 2014. Effect of Cu content on the antibacterial activity of titanium–copper sintered alloys. Materials Science and Engineering. 35, 392–400.

Liu, R., Memarzadeh, K., Chang, B., Zhang, Y., Ma, Z., Allaker, R.P., Ren, L., Yang, K., 2016. Antibacterial effect of copper-bearing titanium alloy (Ti-Cu) against *Streptococcus mutans* and *Porphyromonas gingivalis*. Scientific Reports. 6, 1-10.

Liu, S., Zhang, Z., Xia, J. and Chen, Y., 2020. Effect of Hydrogen Precharging on Mechanical and Electrochemical Properties of Pure Titanium. Advanced Engineering Materials. 22, 1901182.

Lu, S.L., Qian, M., Tang, H.P., Yan, M., Wang, J. and St. John, D.H., 2016. Massive transformation in Ti–6Al–4V additively manufactured by selective electron beam melting. Acta Materialia, 104, 303-311.

Lui, J., Zhang. X., Wang., H., Ren, B., Yang., K, Zhang., E., 2014. The antibacterial properties and biocompatibility of a Ti-Cu sintered alloy for biomedical application. Biomedical Materials. 9, 1-11.

Lütjering, G.E.R.D., 1998. Influence of processing on microstructure and mechanical properties of (α+ β) titanium alloys. Materials Science and Engineering. 243, 32-45.

Lütjering, G., Williams, J.C., 2007. Titanium. Springer Science & Business Media. 15-47.

Lütjering, G., Williams, J.C. and Gysler, A., 2000. Microstructure and mechanical properties of titanium alloys. Microstructure and Properties of Materials. 2, 1-77.

Ma, Z., Li, M., Liu, R., Ren, L., Zhang, Y., Pan, H., Zhao, Y., Yang, K., 2016. In vitro study on an antibacterial Ti–5Cu alloy for medical application. Journal of Materials Science: Materials in Medicine. 27, 1-12.

Ma, Z., Yao, M., Liu, R., Yang, K., Ren, L., Zhang, Y., Liao, Z., Liu, W. and Qi, M., 2015. Study on antibacterial activity and cytocompatibility of Ti–6Al–4V–5Cu alloy. Materials Technology. 30, B80-B85.

Mabilleau, G., Bourdon, S., Joly-Guillou, M.L., Filmon, R., Baslé, M.F., Chappard, D., 2006. Influence of fluoride, hydrogen peroxide and lactic acid on the corrosion resistance of commercially pure titanium. Acta Biomaterials. 2, 121–129.

Machnee, C.H., Wagner, W.C., Jaarda, M.J. and Lang, B.R., 1993. Identification of oxide layers of commercially pure titanium in response to cleaning procedures. International Journal of Oral & Maxillofacial Implants. 8, 529-533.

Madina, V. and Azkarate, I., 2009. Compatibility of materials with hydrogen. Particular case: Hydrogen embrittlement of titanium alloys. International Journal of Hydrogen Energy. 34, 5976-5980.

Masia, N.D.E., Smit, M., Mwamba, I.A., Fowler, L., Chown, L.H., Norgren, S., Öhman-Mägi, C., Hashe, N. and Cornish, L.A., 2021. Corrosion performance of Ti-Cu alloys targeted for biomedical applications. Suid-Afrikaans Tydskrif vir Natuurwetenskap en Tegnologie/South African Journal of Science and Technology. 40, 244-250.

Mathew, M.T., Abbey, S., Hallab, N.J., Hall, D.J., Sukotjo, C., Wimmer, M.A., 2012. Influence of pH on the tribocorrosion behavior of CP-Ti in the oral environment: synergistic interactions of wear and corrosion. Journal of Biomedical Materials Research Part B: Applied Biomaterials. 100, 1662–1671.

Matsumoto, H., Yoneda, H., Sato, K., Kurosu, S., Maire, E., Fabregue, D., Konno, T.J. and Chiba, A., 2011. Room-temperature ductility of Ti–6Al–4V alloy with α′ martensite microstructure. Materials Science and Engineering. 528, 1512-1520.

Mei, W., Sun, J., Wen, Y., 2017. Martensitic transformation from β to α′ and α″ phases in Ti–V alloys: A first-principles study. Journal of Materials Research. 32, 3183–3190.

Meyer, L.W., Krüger, L., Sommer, K., Halle, T. and Hockauf, M., 2008. Dynamic strength and failure behaviour of titanium alloy Ti-6Al-4V for a variation of heat treatments. Mechanics of Time-Dependent Materials. 12, 237-247.

Mohammed, M.T., Khan, Z.A., Siddiquee, A.N., 2014. Beta Titanium Alloys: The Lowest Elastic Modulus for Biomedical Applications: A Review. International Journal of Chemical, Nuclear, Metallurgical and Materials Engineering. 8, 726-731

Mohamed, S., Shamaz, B.H., 2015. Bone Tissue Engineering and Bony Scaffolds. . International Journal of Dental & Oral Health. 1, 15-20.

Mohandas, T., Banerjee, D. and Rao, V.K., 1999. Fusion zone microstructure and porosity in electron beam welds of an α+ β titanium alloy. Metallurgical and Materials transactions. 30, 789-798.

Mombelli, A., 2002. Microbiology and antimicrobial therapy of peri-implantitis. Periodontololgy. 2000 28, 177–189.

Morones, J.R., Elechiguerra, J.L., Camacho, A., Holt, K., Kouri, J.B., Ramírez, J.T., Yacaman, M.J., 2005. The bactericidal effect of silver nanoparticles. Nanotechnology 16, 2346–2353.

Morais L.S., Serra G.G., Muller C.A., Andrade L.R., Palermo E.F.A., Elias C.N., Meyers M., 2007. Titanium alloy mini-implants for orthodontic anchorage: Immediate loading and metal ion release. Acta Biomaterialia. 3, 331-339.

Motyka, M., Kubiak, K., Sieniawski, J and Ziaja, W., 2014. Phase transformations and characterizations of α+β titanium alloys. Comprehensive materials processing. 2, 7-36.

Mouhyi, J., Ehrenfest, D.M.D., Albrektsson, T., 2012. The Peri-Implantitis: Implant Surfaces, Microstructure, and Physicochemical Aspects. Clin. Implant Dent. Relat. Res. 14, 170–183.

Mueller, M.H., Knott, H.W., 1963. The Crystal Structures of Ti_2Cu, Ti_2Ni, Ti_4Ni_2O, and Ti_4Cu_2O. Transactions of American Institute Metallurgical Engineers. 227, 674-678.

Murray, J.L., 1983. The Cu− Ti (copper-titanium) system. Bulletin of alloy phase diagrams. 4, 81-95.

Nayak, S.K., Hung, C.J., Sharma, V., Alpay, S.P., Dongare, A.M., Brindley, W.J. and Hebert, R.J., 2018. Insight into point defects and impurities in titanium from first principles. Computational Materials. 4, 1-10.

Nicholson, W.J., 2020. Titanium alloys for dental implants: A review. Prosthesis, 2, 100-116.

Niinomi, M., 1998. Mechanical properties of biomedical titanium alloys. Materials Science and Engineeering. A 243, 231–236.

Niinomi, M., 2003. Recent research and development in titanium alloys for biomedical applications and healthcare goods. Science and Technology of Advanced Materials. 4, 445-454.

Niinomi, M., Hattori, T., Morikawa, K., Kasuga, T., Suzuki, A., Fukui, H. and Niwa, S., 2002. Development of low rigidity β-type titanium alloy for biomedical applications. Materials Transactions. 43, 2970-2977.

Niinomi, M., Kuroda, D., Fukunaga, K., Morinaga, M., Kato, Y., Yashiro, T., Suzuki, A., 1999. Corrosion wear fracture of new beta type biomedical titanium alloys. Materials Science and Engineering. 263, 193-199.

Oh, J.M., Lee, B.G., Cho, S.W., Lee, S.W., Choi, G.S., Lim, J.W., 2011. Oxygen effects on the mechanical properties and lattice strain of Ti and Ti-6Al-4V. Metals and Materials International. 17, 733–736.

Oh, K.T., Shim, H.M. and Kim, K.N., 2005. Properties of titanium–silver alloys for dental application. Journal of Biomedical Materials Research Part B: Applied Biomaterials: An Official Journal of the Society for Biomaterials, The Japanese Society for Biomaterials, and The Australian Society for Biomaterials and the Korean Society for Biomaterials. 74, 649-658.

Öhman, C., Zwierzak, I., Baleani, M. and Viceconti, M., 2013. Human bone hardness seems to depend on tissue type but not on anatomical site in the long bones of an old subject. Proceedings of the Institution of Mechanical Engineers, Part H: Journal of Engineering in Medicine. 227, 200-206.

Okawa, S. and Watanabe, K., 2009. Chemical mechanical polishing of titanium with colloidal silica containing hydrogen peroxide—mirror polishing and surface properties. Dental Materials Journal. 28, 68-74.

Okazaki Y., Gotoh E., Manabe T., Kobayashi K., 2004. Comparison of metal concentration in rat tibia tissue with varios metallic implants. Biomaterials. 25, 5913-5920.

Olczak, T., Maszczak-Seneczko, D., Smalley, J.W., Olczak, M., 2012. Gallium(III), cobalt(III) and copper(II) protoporphyrin IX exhibit antimicrobial activity against Porphyromonas gingivalis by reducing planktonic and biofilm growth and invasion of host epithelial cells. Archives of Microbiology. 194, 719–724.

Oliveira, D.C., Nogueira-Pedro, A., Santos, E.W., Hastreiter, A., Silva, G.B., Borelli, P., Fock, R.A., 2018. A review of select minerals influencing the haematopoietic process. Nutrition Research Reviews 31, 267–280.

Palmquist, A., Lindberg, F., Emanuelsson, L., Brånemark, R., Engqvist, H. and Thomsen, P., 2009. Morphological studies on machined implants of commercially pure titanium and titanium alloy (Ti-6Al-4V) in the rabbit. Journal of Biomedical Materials Research Part B: Applied Biomaterials. 91, 309-319.

Palumbo, G., Lehockey, E.M. and Lin, P., 1998. Applications for grain boundary engineered materials. JOM. 50, 40-43.

Pan, J., Liao, H., Leygraf, C., Thierry, D. and Li, J., 1998. Variation of oxide films on titanium induced by osteoblast-like cell culture and the influence of an H_2O_2 pretreatment. Journal of Biomedical Materials Research: An Official Journal of The Society for Biomaterials, The Japanese Society for Biomaterials, and the Australian Society for Biomaterials, 40, 244-256.

Parithimarkalaignan, S., Padmanabhan, T.V., 2013. Osseointegration: An Update. Journal Indian Prosthodontic Society. 13, 2–6.

Patel, N.R., Gohil, P.P., 2012. A Review on Biomaterials: Scope, Applications & Human Anatomy Significance. Int. J. Emerg. Technol. Adv. Eng. 2, 2250-2459.

Pecharsky, V.K. and Zavalij, P.Y., 2009. The powder diffraction pattern. Fundamentals of Powder Diffraction and Structural Characterization of Materials. 151-202.

Peng, C., Zhang, S., Sun, Z., Ren, L. and Yang, K., 2018. Effect of annealing temperature on mechanical and antibacterial properties of Cu-bearing titanium alloy and its preliminary study of antibacterial mechanism. Materials Science and Engineering: C. 93, 495-504.

Petch, N.J., 1953. The cleavage strength of polycrystals. Journal of the Iron and Steel Institute. 174, 25-28.

Pohler, O.E.M., 2000. Unalloyed titanium for implants in bone surgery. Injury. 31, D7–D13.

Poondla, N., Srivatsan, T.S., Patnaik, A. and Petraroli, M., 2009. A study of the microstructure and hardness of two titanium alloys: Commercially pure and Ti–6Al–4V. Journal of Alloys and Compounds. 486, 162-167.

Potgieter, J.H., Heyns, A.M. and Skinner, W., 1990. Cathodic modification as a means of improving the corrosion resistance of alloys. Journal of applied electrochemistry. 20, 711-715.

Pourbaix, M.J.N., Van Muylder, J. and De Zoubov, N., 1959. Electrochemical properties of the platinum metals. Platinum Metals Review. 3, 47-53.

Qazi, J.I., Senkov, O.N., Rahim, J. and Froes, F.S., 2003. Kinetics of martensite decomposition in Ti–6Al–4V–*x*H alloys. Materials Science and Engineering: A. 359, 137-149.

Qazi, J.I., Rahim, J., Fores, F.S., Senkov, O.N. and Genc, A., 2001. Phase transformations in Ti-6Al-4V-*x*H alloys. Metallurgical and Materials Transactions A. 32, 2453-2463.

Qin, P., Liu, Y., Sercombe, T.B., Li, Y., Zhang, C., Cao, C., Sun, H., Zhang, L.-C., 2018. Improved Corrosion Resistance on Selective Laser Melting Produced Ti-5Cu Alloy after Heat Treatment. ACS Biomater. Sci. Eng. 4, 2633–2642.

Raabe, D., Zhao, Z., Park, S.J. and Roters, F., 2002. Theory of orientation gradients in plastically strained crystals. Acta Materialia. 50, 421-440.

Rabiei, A., 2010. Recent developments and the future of bone mimicking: materials for use in biomedical implants. Expert review of medical devices. 7, 727-729.

Raghavan, S., Nai, M.L.S., Wang, P., Sin, W.J., Li, T. and Wei, J., 2018. Heat treatment of electron beam melted (EBM) Ti-6Al-4V: Microstructure to mechanical property correlations. Rapid Prototyping Journal. 24, 774-783.

Reclaru, L., Meyer, J.-M., 1998. Effects of fluorides on titanium and other dental alloys in dentistry. Biomaterials 19, 85–92.

Reidy, B., Haase, A., Luch, A., Dawson, K.A. and Lynch, I., 2013. Mechanisms of silver nanoparticle release, transformation and toxicity: a critical review of current knowledge and recommendations for future studies and applications. Materials. 6, 2295-2350.

Ren, L., Ma, Z., Li, M., Zhang, Y., Liu, W., Liao, Z. and Yang, K., 2014. Antibacterial properties of Ti–6Al–4V–*xCu* alloys. Journal of Materials Science & Technology. 30, 699-705.

Revathi, A., Vijayalakshmi, U., Geetha, M., 2014. Comparative study of electrochemical behaviour of CP-titanium and Ti–6Al–4V with other titanium based alloys for biomedical applications. Materials Technology. 29, B49–B53.

Reza, F., Takahashi, H., Iwasaki, N. and Tamaki, Y., 2010. Effects of investment type and casting system on permeability and castability of CP titanium. The Journal of Prosthetic Dentistry. 104, 114-121.

Ridzwan, M.I.Z, Shuib, S., Hassan, A.Y., Shokri, A.A., Mohamad Ibrahim, M.N., 2007. Problem of stress shielding and Improvement to the Hip Implant Design; A Review. Journal of Medical Science. 7, 460-467.

Robertson, I.M., Sofronis, P., Nagao, A., Martin, M.L., Wang, S., Gross, D.W. and Nygren, K.E., 2015. Hydrogen embrittlement understood. Metallurgical and Materials Transactions B. 46, 1085-1103.

Robin, A., Carvalho, O.A.S., Schneider, S.G. and Schneider, S., 2008. Corrosion behaviour of Ti-xNb-13Zr alloys in Ringer's solution. Materials and corrosion, 59, 929-933.

Rocha, S.S. da, Adabo, G.L., Henriques, G.E.P., Nóbilo, M.A. de A., 2006. Vickers hardness of cast commercially pure titanium and Ti-6Al-4V alloy submitted to heat treatments. Brazilian Dental Journal. 17, 126–129.

Rodrigues, D.C., Valderrama, P., Wilson, T.G., Palmer, K., Thomas, A., Sridhar, S., Adapalli, A., Burbano, M., Wadhwani, C., 2013. Titanium Corrosion Mechanisms in the Oral Environment: A Retrieval Study. Materials 6, 5258–5274.

Romero-Pérez, M.J., Mang-de la Rosa, M.R., López-Jimenez, J., Fernández-Feijoo, J. and Cutando-Soriano, A., 2014. Implants in disabled patients: A review and update. Medicina Oral, Patologia Oral y Cirugia Bucal. 19, 478.

Rosenbloom, S.N. and Corbett, R.A., 2007. An assessment of ASTM F2129 electrochemical testing of small medical implants-lessons learned. Proceedings of the NACE Corrosion Conference & Exposition, Nashville, TN, USA. 11-15.

Saini, M., Singh, Y., Arora, P., Arora, V., Jain, K., 2015. Implant biomaterials: A comprehensive review. World Journal of Clinical Cases: WJCC. 3, 52–57.

Salvador, C.A., Lopes, E.S., Ospina, C.A. and Caram, R., 2016. Orthorhombic martensite formation upon aging in a Ti-30Nb-4Sn alloy. Materials Chemistry and Physics. 183, 238-246.

Sato, T. and Taya, M., 2006. Copper-aided photosterilization of microbial cells on TiO_2 film under irradiation from a white light fluorescent lamp. Biochemical Engineering Journal. 30, 199–204.

Saito, T., 2004. The automotive application of discontinuously reinforced TiB-Ti composites. JOM. 56, 33-36.

Schneider, S.G., Nunes, C.A., Rogero, S.O., Higa, O.Z. and Bressiani, J.C., 2000. Mechanical properties and cytotoxic evaluation of the Ti-13Nb-13Zr alloy. Biomechanics. 8, 84-87.

Schutz, R.W., 1996. Ruthenium Enhanced Titanium Alloys. Platinum Metals Review. 40, 54-61.

Sedarat, C., Harmand, M.F., Naji, A. and Nowzari, H., 2001. In vitro kinetic evaluation of titanium alloy biodegradation. Journal of Periodontal Research. 36, 269-274.

Shah, F.A., Trobos, M., Thomsen, P. and Palmquist, A., 2016. Commercially pure titanium (cp-Ti) versus titanium alloy (Ti6Al4V) materials as bone anchored implants—Is one truly better than the other? Materials Science and Engineering: C. 62, 960-966.

Shetty, S., Pitti, V., Satish Babu, C.L., Surendra Kumar, G.P. and Deepthi, B.C., 2010. Bruxism: a literature review. The Journal of Indian Prosthodontic Society. 10, 141-148.

Shi, X., Zeng, W., Sun, Y., Han, Y., Zhao, Y. and Guo, P., 2015. Microstructure-tensile properties correlation for the Ti-6Al-4V titanium alloy. Journal of materials engineering and performance. 24, 1754-1762.

Shim, H.M., Oh, K.T., Woo, J.Y., Hwang, C.J. and Kim, K.N., 2005. Corrosion resistance of titanium–silver alloys in an artificial saliva containing fluoride ions. Journal of Biomedical Materials Research Part B: Applied Biomaterials: An Official Journal of The Society for Biomaterials, The Japanese Society for Biomaterials, and The Australian Society for Biomaterials and the Korean Society for Biomaterials. 73, 252-259.

Shunmugavel, M., Polishetty, A., Goldberg, M., Singh, R. and Littlefair, G., 2017. A comparative study of mechanical properties and machinability of wrought and additive manufactured (selective laser melting) titanium alloy–Ti-6Al-4V. Rapid Prototyping Journal. 23, 295-304.

Shunmugavel, M., Polishetty, A. and Littlefair, G., 2015. Microstructure and mechanical properties of wrought and additive manufactured Ti-6Al-4V cylindrical bars. Procedia Technology. 20, 231-236.

Siddiqui, M.A., Ullah, I., Liu, H., Zhang, S., Ren, L. and Yang, K., 2021. Preliminary study of adsorption behavior of bovine serum albumin (BSA) protein and its effect on antibacterial and corrosion property of Ti-3Cu alloy. Journal of Materials Science & Technology. 80, 117-127.

Sidhu, S.S., Singh, H. and Gepreel, M.A.H., 2020. A Review on alloy design, biological response, and strengthening of β-Titanium Alloys as biomaterials. Materials Science and Engineering: C. 10, 1-16.

Sieniawski, J., Ziaja, W., Kubiak, K., Motyka, M., 2013. Microstructure and Mechanical Properties of High Strength Two-Phase Titanium Alloys. Titanium Alloys-Advances in Properties Control. 69-80.

Sigel, A., Sigel, H. and Sigel, R.K. (Eds.), 2015. Metal ions in toxicology: effects, interactions, interdependencies. Walter de Gruyter GmbH & Co KG. 8, 1-401.

Souza, J.C.M., Henriques, M., Oliveira, R., Teughels, W., Celis, J.-P., Rocha, L.A., 2010. Do oral biofilms influence the wear and corrosion behavior of titanium? Biofouling. 26, 471–478.

Sridhar, B.R., Devananda, G., Ramachandra, K. and Bhat, R., 2003. Effect of machining parameters and heat treatment on the residual stress distribution in titanium alloy IMI-834. Journal of Materials Processing Technology. 139, 628-634.

Steinemann, S.G., 1998. Titanium – the material of choice? Periodontology 2000. 17, 7–21.

Stenlund, P., Omar, O., Brohede, U., Norgren, S., Norlindh, B., Johansson, A., Lausmaa, J., Thomsen, P., Palmquist, A., 2015. Bone response to a novel Ti–Ta–Nb–Zr alloy. Acta Biomaterial. 20, 165–175.

Stenport, V.F. and Johansson, C.B., 2008. Evaluations of bone tissue integration to pure and alloyed titanium implants. Clinical Implant Dentistry and Related Research. 10, 191-199.

Stewart, P.S., William Costerton, J., 2001. Antibiotic resistance of bacteria in biofilms. The Lancet. 358, 135–138.

Sun, Y., Zeng, W., Han, Y., Zhao, Y., Wang, G., Dargusch, M.S. and Guo, P., 2011. Modeling the correlation between microstructure and the properties of the Ti–6Al–4V alloy based on an artificial neural network. Materials Science and Engineering: A. 528, 8757-8764.

Takahashi, K., Mori, K. and Takebe, H., 2020. Application of titanium and its alloys for automobile parts. MATEC Web of Conferences. EDP Sciences. 321, 1-10.

Takahashi, M., Kikuchi, M., Takada, Y. and Okuno, O., 2002. Mechanical properties and microstructures of dental cast Ti-Ag and Ti-Cu alloys. Dental Materials Journal. 21, 270-280.

Tal-Gutelmacher, E. and Eliezer, D., 2005. The hydrogen embrittlement of titanium-based alloys. JOM. 57, 46-49.

Tal-Gutelmacher, E., Eliezer, D. and Eylon, D., 2004. The effects of low fugacity hydrogen in duplex-and beta-annealed Ti–6Al–4V alloy. Materials Science and Engineering: A. 381, 230-236.

Tane, M., Akita, S., Nakano, T., Hagihara, K., Umakoshi, Y., Niinomi, M., 2008. Peculiar elastic behavior of Ti-Nb-Ta-Zr single crystals. Acta Materialia. 56, 2856–2863.

Tardelli, J.D.C., Bolfarini, C. and Dos Reis, A.C., 2020. Comparative analysis of corrosion resistance between beta titanium and Ti-6Al-4V alloys: A systematic review. Journal of Trace Elements in Medicine and Biology. 62, 1-5.

Tomashov, N.D., Altovsky, R.M. and Chemova, G.P., 1960. Increasing the stability of the passive state of titanium. Z. Phys. Chem. 214, 312-315.

Tomashov, N.D., Altovsky, R.M. and Chernova, G.P., 1961. Passivity and corrosion resistance of titanium and its alloys. Journal of the Electrochemical Society. 108, 113-119.

Tong, V., Joseph, S., Ackerman, A.K., Dye, D., Britton, T.B., 2017. Using transmission Kikuchi diffraction to characterise α variants in an α+β titanium alloy. Journal of Microscopy. 267, 318–329.

Trufanov, A.A., Katsov, K.B. and Chervonyi, M.V., 1989. Effect of Ni and Mo additions on the corrosion and mechanical properties of a Ti-Al alloy. Fiziko-Khimicheskaia Mekhanika Materialov. 25, 28-32.

Van der Lingen, E. and de Villiers Steyn, H., 1994. The potential of ruthenium as an alloying element in titanium. Titanium 1994: Products and Applications. 450-461.

Vander Voort, G., 1999. Metallographic preparation of titanium and its alloys. Buehler Tech-Notes. 3.

Vander Voort, G.F., 2006. Microstructure of titanium and its alloys. Industrial Heating, 73, 82-84.

Venkatesh, B.D., Chen, D.L., Bhole, S.D., 2009. Effect of heat treatment on mechanical properties of Ti–6Al–4V ELI alloy. Materials Science and Engineering. A 506, 117–124.

Viteri, V.S. de, Fuentes, E., 2013. Titanium and Titanium Alloys as Biomaterials. Tribology – Fundamentals and Advancements. InTech. 151-181.

Vignesh, M., Ranjith Kumar, G., Sathishkumar, M., Manikandan, M., Rajyalakshmi, G., Ramanujam, R. and Arivazhagan, N., 2021. Aspects of the Powder in Metal Additive Manufacturing: A Review. Journal of Materials Engineering and Performance, 30, 4735-4744.

Wang, C.P., Wang, H.Z., Ruan, G.L., Wang, S.H., Xiao, Y.X. and Jiang, L.D., 2019b. Applications and prospects of titanium and its alloys in seawater desalination industry. IOP Conference Series: Materials Science and Engineering. 688, 1-7.

Wang, L., Teng, J., Liu, P., Hirata, A., Ma, E., Zhang, Z., Chen, M., Han, X., 2014. Grain rotation mediated by grain boundary dislocations in nanocrystalline platinum. Nature Communications. 5, 1-7.

Wang, S., Ma, Z., Liao, Z., Song, J., Yang, K. and Liu, W., 2015. Study on improved tribological properties by alloying copper to CP-Ti and Ti–6Al–4V alloy. Materials Science and Engineering: C. 57, 123-132.

Wang, Z., Xiao, Z., Tse, Y., Huang, C. and Zhang, W., 2019a. Optimization of processing parameters and establishment of a relationship between microstructure and mechanical properties of SLM titanium alloy. Optics & Laser Technology, 112, 159-167.

Wanying, L., Yuanhua, L., Yuhai, C., Taihe, S. and Singh, A., 2017. Effect of different heat treatments on microstructure and mechanical properties of Ti6Al4V titanium alloy. Rare Metal Materials and Engineering, 46, 634-639.

Weng, W., Biesiekierski, A., Li, Y. and Wen, C., 2019. Effects of selected metallic and interstitial elements on the microstructure and mechanical properties of beta titanium alloys for orthopedic applications. Materialia. 6, 100323.

Wennerberg, A., 1998. The importance of surface roughness for implant incorporation. International Journal of Machine Tools and Manufacture. 38, 657–662.

Williams, D.F. 2008. On the mechanisms of biocompatibility. Biomaterials. 29, 2941–2953.

Williams, J.C. and Boyer, R.R., 2020. Opportunities and issues in the application of titanium alloys for aerospace components. Metals. 10, 1-22.

Wojcieszak, D., Kaczmarek, D., Antosiak, A., Mazur, M., Rybak, Z., Rusak, A., Osekowska, M., Poniedzialek, A., Gamian, A., Szponar, B., 2015. Influence of Cu–Ti thin film surface properties on antimicrobial activity and viability of living cells. Materials Science and Engineering: C. 56, 48–56.

Wu, W.W., Zhu, Y.B., Chen, W., Li, S., Yin, B., Wang, J.Z., Zhang, X.J., Liu, G.B., Hu, Z.S. and Zhang, Y.Z., 2019. Bone hardness of different anatomical regions of human radius and its impact on the pullout strength of screws. Orthopaedic Surgery. 11, 270-276.

Xu, Y., Gao, J., Huang, Y. and Rainforth, W.M., 2020. A low-cost metastable beta Ti alloy with high elastic admissible strain and enhanced ductility for orthopaedic application. Journal of Alloys and Compounds. 835, 155391.

Yamaguchi, T., Morishita, H., Iwase, S., Yamada, S., Furuta, T. and Saito, T., 2000. Development of P/M titanium engine valves. SAE transactions. 416-424.

Yoon, K.-Y., Hoon Byeon, J., Park, J.-H., Hwang, J., 2007. Susceptibility constants of Escherichia coli and Bacillus subtilis to silver and copper nanoparticles. Science of the Total Environment. 373, 572–575.

Young, R.A., 1993. The Rietveld method. International Union of Crystallography. 5, 1-38.

Yu, S.Y. and Scully, J.R., 1997. Corrosion and passivity of Ti-13% Nb-13% Zr in comparison to other biomedical implant alloys. Corrosion. 53, 1-12.

Yu, S.Y., Brodrick, C.W., Ryan, M.P. and Scully, J.R., 1999. Effects of Nb and Zr alloying additions on the activation behaviour of Ti in hydrochloric acid. Journal of the Electrochemical Society. 146, 4429.

Zeng, L. and Bieler, T.R., 2005. Effects of working, heat treatment, and aging on microstructural evolution and crystallographic texture of α, α′, α ″and β phases in Ti–6Al–4V wire. Materials Science and Engineering: A. 392, 403-414.

Zhang, B.B., Zheng, Y.F. and Liu, Y., 2009. Effect of Ag on the corrosion behavior of Ti–Ag alloys in artificial saliva solutions. Dental Materials. 25, 672-677.

Zhang, E., Li, F., Wang, H., Liu, J., Wang, C., Li, M., Yang, K., 2013. A new antibacterial titanium–copper sintered alloy: Preparation and antibacterial property. Materials Science and Engineering: C. 33, 4280–4287.

Zhang, E., Ren, J., Li, S., Yang, L., Qin, G., 2016a. Optimization of mechanical properties, biocorrosion properties and antibacterial properties of as-cast Ti–Cu alloys. Biomedical Material. 11, 1-13.

Zhang, E., Wang, X., Chen, M., Hou, B., 2016b. Effect of the existing form of Cu element on the mechanical properties, bio-corrosion and antibacterial properties of Ti-Cu alloys for biomedical application. Materials Science and Engineering: C. 69, 1210–1221.

Zhang, J., Zhu, J., Ding, S., Chen, L., Li, W. and Pang, H., 2018. Theoretical models of threshold stress intensity factor and critical hydride length for delayed hydride cracking considering thermal stresses. Nuclear Engineering and Technology. 50, 1138-1147.

Zhang, L.C. and Chen, L.Y., 2019. A review on biomedical titanium alloys: recent progress and prospect. Advanced Engineering Materials. 21, 1-29.

Zhang, W.D., Liu, Y., Wu, H., Song, M., Zhang, T.Y., Lan, X.D. and Yao, T.H., 2015. Elastic modulus of phases in Ti–Mo alloys. Materials Characterization. 106, 302-307.

Zhao, X., Niinomi, M., Nakai, M. and Hieda, J., 2012a. Beta type Ti–Mo alloys with changeable Young's modulus for spinal fixation applications. Acta biomaterialia. 8, 1990-1997.

Zhao, X., Niinomi, M., Nakai, M. and Hieda, J., 2012b. Effect of Deformation-Induced ½ Phase on the Mechanical Properties of Metastable ¢-Type Ti-V Alloys. Materials Transactions. 53, 1379-1384.

Zhou, B., Yang, R., Wang, B., Deng, L. and Zhang, Y., 2021. Twinning behavior of pure titanium during rolling at room and cryogenic temperatures. Materials Science and Engineering: A. 803, 140458.

Zhou, P., Xiao, D., Jiang, C., Sang, G. and Zou, D., 2017. Twin interactions in pure Ti under high strain rate compression. Metallurgical and Materials Transactions: A. 48, 126-138.

Zhu, Y.T., Liao, X.Z., Wu, X.L., 2012. Deformation twinning in nanocrystalline materials. Progress in Materials Science. 57, 1–62.

Zukowski, P., Maciejczyk, M., Waszkiel, D., 2018. Source of free radicals and oxidative stress in the oral environment. Archives of Oral Biology. 92, 8-17.

Zwierzak, I., Baleani, M. and Viceconti, M., 2009. Microindentation on cortical human bone: effects of tissue condition and indentation location on hardness values. Proceedings of the Institution of Mechanical Engineers, Part H: Journal of Engineering in Medicine. 223, 913-918.

Zychlinski, L., Byczkowski, J.Z. and Kulkarni, A.P., 1991. Toxic effect of long-term intratracheal administration of vanadium peroxide in rats. Archives of Environmental Contamination and Toxicology. 20, 295-298.

Future work

- One of the major reasons of the developed alloys was achieve antibacterial properties. Antibacterial tests were not performed due to a number of literature confirming that 5 wt% Cu will be sufficient to achieve these properties. The alloys microstructure had Ti_2Cu precipitates that were found in literature to be the primary cause of bacterial inactivation. Antibacterial test would be good attempt to assess this effect of Ti_2Cu precipitates.
- The hardness values of the tested alloys in this work are comparable to that of Ti-6Al-4V alloy, microstructure relationship to mechanical strength suggest that the developed alloys might have good mechanical strength. There for it would be good attempt to study the mechanical strength and ductility and measure their suitability for biomedical application. Furthermore, addition of β-stabilisers was to potentially lower the elastic modulus. Therefore, Young's modulus measurements would be beneficial on determining this property.
- The electrochemical test performed in this study were on PBS solution. It would be good attempt to study the developed alloys in other physiological solutions. In addition, the bilayer that was found on other Ti alloys in literature was found to be beneficial for corrosion resistance and to promote osteointegration. To confirm bilayer formation, electrochemical impedance spectroscopy should be performed.
- Polarised surfaces form β-stabiliser oxides. Therefore, it will be good to study the surface chemistries of the surfaces exposed to electrolyte. To study where the corrosion affects the microstructure, electrochemical test should be performed on the as-polished samples.
- X-ray Diffraction and SEM assessment were not enough to confirm the phases found on the SEM microstructure. Transmission Electron Microscopy or EBSD would be advisable to confirm the crystal structure and orientation on the surface of the alloys.
- With the tests performed on the alloys in this work they have shown potential for alloys for biomedical application and similar characteristics to Ti-6Al-4V. Heat treatments should be performed: to enhance corrosion resistance, remove residual stress, potentially lower the hardness and increase mechanical strength and ductility.

APPENDIX 1: List of publications from this work

L. Spotose, N.S. Phala, C. Polese, L.A. Cornish, Development and Characterisation of Antibacterial Titanium-Based Alloys with Copper for Biomedical Applications, Microscopy Society of Southern Africa-Proceedings- 2019. Vol. 49, p. 85.

Ukabhai, K.D., Nape, K.T., **Spotose, L**., Mavundla, M., Mwamba, I.A., Bodunrin, M.O., Chown, L.H. and Cornish, L.H., 2022. Thermo-mechanical processing and phase analysis of titanium alloys with copper additions. South African Journal of Science and Technology. 40, 84-90.

L. Spotose and L.A. Cornish. New Ti-Cu Based Alloys For Biomedical Applications. AfInMic PG Symposium, 2021.

N.G. Hashe, L. Fowler, W.E. Goosen, S. Norgren, N.D. Masia, L.A. Cornish, C. ÖhmanMägi, L.H. Chown, S. Magadla, K.T. Nape, M. Mavundla, **L. Spotose**. A microstructural analysis of a Ti-Ta-Cu-Nb-Zr alloy. Microscopy Society of Southern Africa-Proceedings, 2019. Vol. 48, p. 30.

Dyal Ukabhai, K., Fowler, L., Nape, K.T., Mavundla, M., **Spotose, L.**, Magadla, S., Masia, N.D., Klenam, D.E.P., Hashe, N.G., Öhman Mägi, C., Norgren, S., Chown, L.H., Cornish, L.A. Effect of Different Copper Additions To Ti-10.1Ta-1.7Nb-1.6Zr. Microscopy Society of Southern Africa-Proceedings- 2019. Vol. 48, p. 37.

APPENDIX 2: Copies of the publications

DEVELOPMENT AND CHARACTERISATION OF ANTIBACTERIAL TITANIUM-BASED ALLOYS WITH COPPER FOR BIOMEDICAL APPLICATIONS

L Spotose[1,2], N.S. Phala[1,2], C. Polese[1,3] and L.A. Cornish[1,2]

[1]School of Chemical and Metallurgical Engineering, University of the Witwatersrand, , [2]DSI-NRF CoE in Strong Materials, hosted by the University of the Witwatersrand, and DSI Collaborative Programme in Additive Manufacturing, [3]School of Mechanical, Aeronautical and Industrial Engineering, University of the Witwatersrand

Titanium and its alloys are used biomedically, including dental implants, due to their favourable combination of properties: low density, high strength, corrosion resistance, excellent biocompatibility and good osseointegration[1]. The widely used Ti-6Al-4V alloy has concerns as Al been associated with Alzheimer diseases and phosphorus deficiency in the blood and bone, while V appeared to be cytotoxic and show carcinogenic properties[1].Hence the development of new alloys with non–toxic elements is necessary.

The aim of this study is to develop a Ti-based alloy that is not toxic and has improved corrosion resistance as the human body has different electrolytes which contain corrosive species. The addition of 5 mass% copper promotes good antibacterial properties as well as balanced mechanical properties in Ti-Cu based alloys[2]. Small ruthenium additions enhance corrosion resistance without changing the microstructure of the alloy[3].

The titanium alloys were selected using Thermo-Calc and four alloys were chosen as their (α+β) phase proportions were similar to Ti-6Al-4V, which was used as a reference alloy[3]. The alloys were: Ti-6Ta-1.5Zr, Ti-6Ta-1.5Zr-5Cu, Ti-6Ta-1.5Zr-0.2Ru and Ti-6Ta-1.5Zr-5Cu-0.2Ru (mass%). High purity powders were mixed in the required ratios and cast in a button arc furnace. The samples were submerged in phosphate buffered solution to test their corrosion resistance. Open circuit potential was measured for up to 17 hours and potentiodynamic polarisation was carried out at 37°C.

The corrosion rates of all the alloys were: Ti-6Ta-1.5Zr (0.00021 mm/y), Ti-6Ta-1.5Zr-5Cu (0.00014 mm/y), Ti-6Ta-1.5Zr-0.2Ru (0.00030 mm/y) and Ti-6Ta-1.5Zr-0.2Ru-5Cu (0.00022 mm/y). Ti-6Ta-1.5Zr-0.2Ru had the highest corrosion rate as compared to other alloys and all were below the recommended rates[4] in biomedical applications which is 0.13 mm/y. Fig. 1 shows the microstructure of the Ti-6Ta-1.5Zr-0.2Ru before the corrosion test and Fig. 2 shows the microstructure of Ti-6Ta-1.5Zr-0.2Ru afterwards. There was corrosion damage, as well as some scratches from handling. Table 1 shows the EDX results of Ti-6Ta-1.5Zr-5Cu (mass%) before and after the corrosion tests, the EDX was done on an area of 20x20 μm^2 on five different places and the average was taken to represent the bulk composition. The EDX results shows that there were minor losses of Ta and Zr, but higher losses of Cu (almost 50%), which shows that some of the Cu was lost. However, this is beneficial since the antimicrobial action occurs when copper is in the surrounding solution[5].

References:
1. Jingjing, Z., et al. (2020), Calphad.
2. Liu, J., et al. (2014), Mat. Sci. Eng. C, 35, 392.
3. Spotose, L. and Cornish, L.A. (2021) African Inclusive Microscopy Network's Student Symposium.
4. Bhola, R., et al. (2011), Trends Biomater Artif. Organs, 25(1) 34
5. Li, M., et al. (2016), Adv. Healthc. Mater., 5(5), 557.

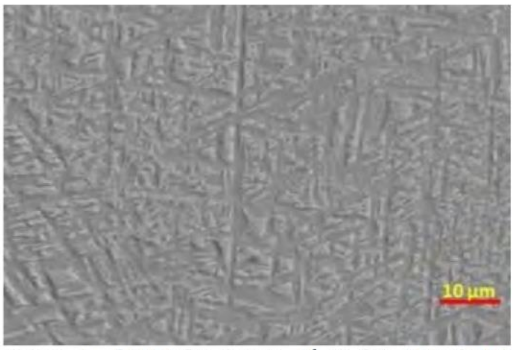

Figure 1. SEM-BSE image of Ti-6Ta-1.5Zr-0.2Ru (mass%) before corrosion, showing (βTi) (light contrast) and (αTi) (dark contrast).

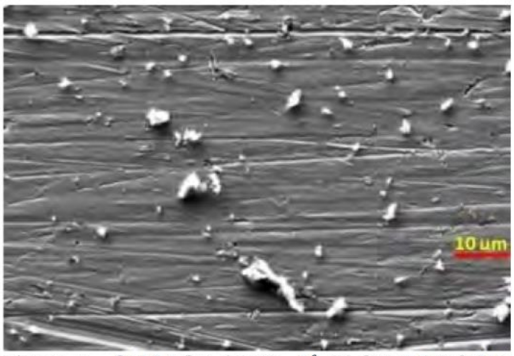

Figure 2. SEM-BSE image of Ti-6Ta-1.5Zr-0.2Ru (mass%) after corrosion, showing (βTi) (light contrast) and (αTi) (dark contrast).

Table 1. Overall EDX analyses of Ti-6Ta-1.5Zr-5Cu (mass%) before and after corrosion.

	EDX analysis (mass%)			
	Ti	Ta	Zr	Cu
Before corrosion	86.0±1.2	5.9±0.5	3.1±0.5	4.9±0.7
After corrosion	90.0±0.3	5.0±0.5	2.1±0.6	2.3 ±0.1

Corresponding author: 820850@students.wits.ac.za

Available online at https://doi.org/10.36303/SATNT.2021cosaami.17
Conference of the South African Advanced Materials Initiative

Thermo-mechanical processing and phase analysis of titanium alloys with copper additions

KD Ukabhai[a,b,*], KT Nape[a,b], L Spotose[a,b], M Mavundla[a,b], IA Mwamba[b,c], MO Bodunrin[a,b,d], LH Chown[a,b], LA Cornish[a,b]

[a] *School of Chemical and Metallurgical Engineering, University of the Witwatersrand, Private Bag 3, WITS, 2050, South Africa*
[b] *DSI-NRF Centre of Excellence in Strong Materials, hosted by the University of the Witwatersrand, Johannesburg, Private Bag 3, WITS, 2050, South Africa*
[c] *Advanced Materials Division, Mintek, Private Bag X3015, Randburg, 2125, South Africa*
[d] *African Academy of Sciences, P.O. Box 24916-00502, Nairobi, Kenya*
*Email: *669011@students.wits.ac.za, 573762@students.wits.ac.za, 2187508@students.wits.ac.za, 1597090@students.wits.ac.za, alainm@mintek.co.za, michael.bodunrin@wits.ac.za, lesleyhchown@gmail.com, Lesley.cornish@wits.ac.za*

Abstract

In dentistry and orthopaedics, to replace and mend broken bones, any replacement material needs to have: low density, high strength, good biocompatibility and must be able to integrate closely with the bone. Titanium-based alloys have these properties, although currently used alloys contain toxic elements, and commercially pure Ti does not have sufficient strength. Within ten years, 7% of dental implants have complete failure, mainly from bacterial infection. Therefore α + β type Ti-alloys were developed by adding b stabilisers, with similar phase proportions to Ti-6Al-4V without the toxic elements, with Cu additions for antibacterial properties and Ru for corrosion resistance. Deformation behaviour of Ti-6Al-4V and Ti-Ta-Nb-Zr alloys were also studied using a Gleeble thermomechanical simulator. The compositions of the new alloys were derived using Thermo-Calc. Ti-8Nb-4Zr alloys had bimodal microstructures and the addition of Cu formed the Ti_2Cu phase. The Ti-6Ta-1.5Zr and Ti-6Ta-1.5Zr-0.2Ru alloys with no Cu had coarse α lamellae, whereas the alloys with Cu had parallel α plates. The Gleeble results showed that higher flow stresses were obtained at higher strain rates and lower temperatures, agreeing with literature. At 850 °C, the Ti-6Al-4V alloy had higher flow stresses than Ti-10.1Ta-1.7Nb-1.6Zr. The Ti-6Al-4V and Ti-10.1Ta-1.7Nb-1.6Zr alloys had steady-state flow stresses at 950 °C, and continuous flow softening at 850 °C for both strain rates.

1. Introduction

Biomedical materials are used daily to improve the lives of many people. These materials are used in various parts of the human body as intravascular stents, heart valves, replacement implants in knees, hips, elbows, shoulders, ears and dentistry (Geetha et al., 2009; Zhang et al., 2011). With ageing populations, there is increased demand for biomedical materials with long life spans that do not require revision surgery once implanted. One of the main causes for failure of dental implants is peri-implantitis, which is a site-specific infectious disease that causes inflammation in soft tissues, and bone loss around an osseointegrated implant (Persson and Renvert, 2014).

Biomedical materials have been studied since the 1980s, and typically include 316L stainless steel, Co-Cr based alloys and Ti alloys (Navarro et al., 2008; Khan et al., 2006). However, there are issues with these materials. For example, stainless steel is prone to sudden failure (Bundy et al., 1983), whereas Co-Cr based alloys and Ti alloys such as Ti-6Al-4V can release unfavourable toxic metals into the body (Okazaki and Gotoh, 2005).

Biomedical materials need to have high corrosion and wear resistance, be highly biocompatible and have a comparable modulus to the bone. For these reasons Ti-alloys have been used in recent years, due to their high specific strength, excellent corrosion resistance, low elastic modulus, and superior biocompatibility (Calin et al., 2007; Zhang et al., 2007). Titanium alloys have been designed not only for medical use, but also for jewellery, aerospace, military, automobiles and mobile phones (Calin et al., 2007; Zhang et al., 2007). Compared to 316L stainless steel and Co-Cr, Ti-alloys have significantly lower densities, and their elastic modulus is much closer to those of the bone (Mitragotri and Lahann, 2009).

There are five types of Ti-alloys: α-type and near α type, α + β type, β-type and shape memory (Zhang et al., 2011). The α-type alloys have not been used due to low mechanical and fatigue strength in load bearing applications (Mitragotri and Lahann, 2009). The α + β type alloys have good corrosion resistance and excellent capability of osseointegration (integration of materials into bone) (Stenlund et al., 2015; Sidambe, 2014), although the elastic moduli are higher than of the bone (Lindahl and Lindgren, 1967; Burnstein et al., 1976). The β-type alloys are currently being developed the most, due to their low elastic moduli, and high strength for load bearing uses (Zhang et al., 2011). However, β-type alloys are expensive since their alloying elements are expensive, and not many thorough investigations have been done to determine their reliability in the human body during long term service (Zhang et al., 2011). However, currently used Ti-6Al-4V contains toxic vanadium (V) (Choubey et al., 2004; Tamilselvi et al., 2006). Ti-6Al-7Nb and Ti-5Al-2.5Fe were developed to replace Ti-6Al-4V (Choubey et al., 2004; Tamilselvi et al., 2006), but these alloys contain aluminium (Al), which can lead to diseases such as Alzheimer's (Li et al., 2014).

Thus, it would be advantageous to develop a Ti alloy with neither V nor Al, so α + β type alloys for dental screws were derived by adding α and β stabilisers to Ti, to mimic the beneficial α + β phase proportions of Ti-6Al-4V, which was used as a reference material. Zirconium, tantalum, niobium and molybdenum were proposed as potential non-toxic alloying elements, since they are β stabilizers (Eisenbarth et al., 2004). They are considered as biocompatible (Kuroda et al., 1998; Eisenbarth et al., 2004), because they minimize adverse tissue reactions originating from the release of metal ions from the implant (Meng et al., 2014). Other additions to the alloys considered were copper (Cu) and ruthenium (Ru). Copper is one of the most promising alloying elements for clinical applications because of its low toxicity and high cytocompatibility (Jin et al., 2015), and Ru is a noble element which improves corrosion resistance in Ti-alloys, even in extremely small amounts (Schutz, 1996). The alloy must mimic the phase proportions of Ti-6Al-4V, which is done by varying the alloy component proportions to achieve the targeted phase proportions, as Stenlund et al. (2015) did. The alloys should be fairly low cost, easy to manufacture, have good mechanical properties and be biocompatible with the human body. The moduli of the alloys must be comparable to that of the bone (10-40 GPa) (Nang et al., 2005).

The Ti-10.1Ta-1.7Nb-1.6Zr (TTNZ) alloy was developed as an implant material (Stenlund et al., 2015) to improve mechanical strength and osseointegration, and mimic the phases of Ti-6Al-4V. However, no studies were done on thermo-mechanical processing of the alloy, which could provide information for shaping it. Hot compression testing is a thermo-mechanical test, which can be used to study flow stress, stress-relaxation, hot workability, and flow softening behaviour due to recrystallisation and recovery (Jha and Kumar, 2010). Therefore, hot compression testing was done on Ti-10.1Ta-1.7Nb-1.6Zr and Ti-6Al-4V alloys using the Gleeble3500® to compare their behaviour. Thermo-mechanical studies done on Ti-6Al-4V showed that low strain rate at higher temperature improved the ductility, and higher flow stresses were observed at higher strain rate and lower deformation temperatures (Vanderhasten, 2008; Shaikh et al., 2015; Dos Santos, 2017; Bodunrin, 2018).

2. Experimental procedure

2.1 α + β alloys

The compositions of different alloys were determined using Thermo-Calc, with the TTTI3 database, and composition which gave similar α (hcp) and β (bcc) proportions to Ti-6Al-4V and Ti-10.1Ta-1.7Nb-1.6Zr were selected (Table 1). The compositions were then made up as arc melted buttons, by mixing 99.9% pure elemental powders. The weighed out mixed powders were cold compacted with a hydraulic press and then melted in a button arc furnace, which was purged with argon gas and used a titanium oxygen-getter, as commonly used. The buttons were then cut and prepared metallographically for analysis.

Table 1: Compositions of alloys determined from Thermo-Calc

Alloy	Composition (wt%)	
1	Ti-8Nb-4Zr	Ti-8Nb-4Zr-5Cu
2	Ti-6Ta-1.5Zr	Ti-6Ta-1.5Zr-5Cu
3	Ti-6Ta-1.5Zr-0.2Ru	Ti-6Ta-1.5Zr-0.2Ru-5Cu
4	Ti-2Ta-8Mo-8Sn	Ti-2Ta-8Mo-8Sn-5Cu

The buttons were cut using a Struers Secotm-10 cutting machine, with a diamond MOD13 blade. The pieces were mounted in polyfast using an ATM-Opal 410 hot mounting press, then ground (P400, P800, P1200 and P2400 papers) and polished (MD-Chem cloth) by hand on a Struers Tegramin-20® machine.

The samples were then etched using Kroll's reagent and examined on a cross-polarized and Leica DM 6000®-Light Optical Microscope (LOM) and a Sigma Zeiss scanning electron microscope (SEM) in backscattered (BSE) and secondary electron (SE) modes, and representative images are shown here. The phases of the samples were analysed by energy dispersive X-ray spectroscopy (EDS) in the SEM.

2.2 Thermo-mechanical testing

The as-received Ti-6Al-4V and Ti-10.1Ta-1.7Nb-1.6Zr (TTNZ) (Stenlund et al., 2015) alloys were subjected to isothermal compression testing using a Gleeble 3500® Thermomechanical Simulation Facility. Cylindrical samples of 8 mm diameter x 12 mm height were machined using electric discharge machining. Prior to compression testing, a chromel-alumel thermocouple was welded to the centre of the test samples using a spot welder, to measure the temperature. The samples were then placed on the Hydrawedge autoloader. Graphite foil and nickel paste were placed between the Iso-T tungsten carbide anvils and the sample to reduce the effect of friction during deformation.

The samples were heated at 5 °C/s to the deformation temperature, and held for 360 s for homogenisation, then deformed at the parameters specified in Table 2, followed by compressed air cooling. The test parameters were used in the Quicksim software using the (.hds) program, which was then converted to Gleeble Script Language (.gsl) before running each experiment.

Table 2: Hot compression testing parameters

Deformation parameters		Temperature (°C)	
Strain	Strain rate (s^{-1})		
0.6	0.1	850	950
0.6	10	850	950

3. Results

3.1 α + β alloys

Results from Thermo-Calc were used only as guidelines for the compositions as the database used did not have all the reported phases in the alloys. The b stabiliser amounts added (Ta, Zr and Nb) were varied until the phase proportion mimicked those of Figure 1a. The amount of Ru and Cu that was added was based on Jin et al. (2015) and Schutz (1996). Figures 1 and 2 show the phase proportion diagrams for the as-received alloys and the experimental

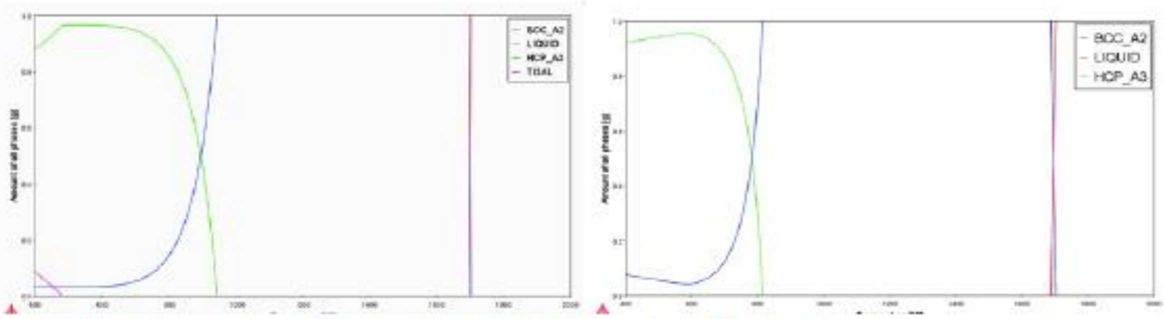

Figure 1. Phase proportion diagrams for: (a) Ti-6Al-4V (wt%) and (b) Ti-10.1Ta-1.7Nb-1.6Zr (wt%).

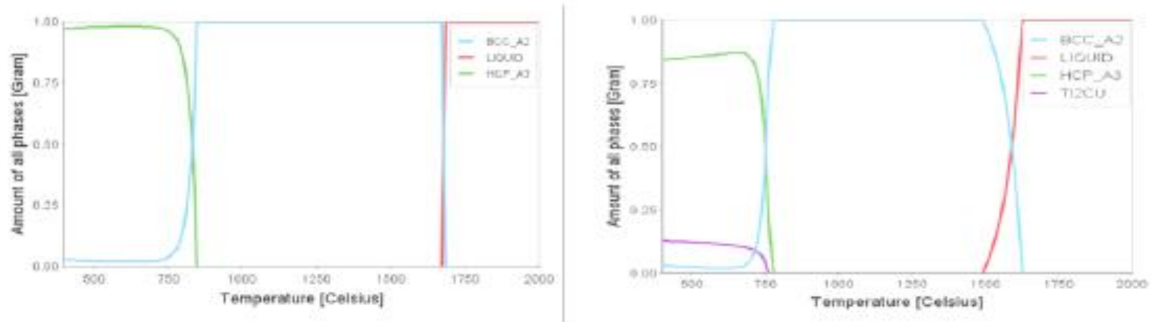

Figure 2: Phase proportion diagrams for: (a) Ti-6Ta-1.5Zr-0.2Ru (wt%) and (b) Ti-6Ta-1.5Zr-0.2Ru-5Cu (wt%)

alloys. Figures 1a and 1b show the phase proportions for Ti-6Al-4V are 0.88 αTi, 0.03 βTi and 0.09 Ti_3Cu, and for TTNZ are 0.92 αTi and 0.08 βTi at 400 °C (at lower temperatures the results are less reliable). From Figure 2a the phase proportions were 0.97 αTi and 0.03 βTi for Ti-6Ta-1.5Zr-0.2Ru and Ti-6Ta-1.5Zr-0.2Ru-5Cu had 0.84 αTi, 0.03 βTi and 0.13 Ti_2Cu at 400 °C as shown in Figure 2b. The phase proportions were quite similar, and when Cu was added the Ti_2Cu phase formed (Figure 2b).

Figure 3 shows the optical micrographs of the as-cast Ti-8Nb-4Zr-xCu (x = 0, 5 wt%) alloys. The bimodal microstructure of Alloy 1 (Figure 3a) consisted of clusters of α-laths within the transformed β matrix. The black precipitates were thought to be the Ti_2Cu phase (Figure 3b), which formed when 5 wt% Cu was added. The EDX results of the Ti-8Nb-4Zr-xCu (x = 0, 5 wt%) alloys indicated a higher Cu content in the light contrast βTi phase compared to the dark contrast αTi phase. The EDX analysis showed that the black precipitates (Figures 3b) were Ti_2Cu. The microstructures of Ti-8Nb-4Zr-xCu (x = 0.5 wt%) showed similar αTi, βTi and Ti_2Cu morphologies. The EDX analyses indicated higher Cu content in βTi phases than αTi in Ti-8Nb-4Zr-5Cu. The solid solubility of Cu in βTi was 4.5 ± 0.4 wt% for Ti-8Nb-4Zr-5Cu.

The SEM images are shown in Figures 4 and 5. Figures 4a and 5a show the Ti-6Ta-1.5Zr and Ti-6Ta-1.5Zr-0.2Ru alloy microstructures, and Figures 4b and 5b shows the same alloys with Cu additions. The microstructures comprised mostly αTi layers. The alloys in Figures 4 and 5 all had αTi laths which precipitated at the prior βTi grain boundaries. The Cu-containing alloys (Figures 4b and 5b) had less plate-like αTi phase and acicular αTi .

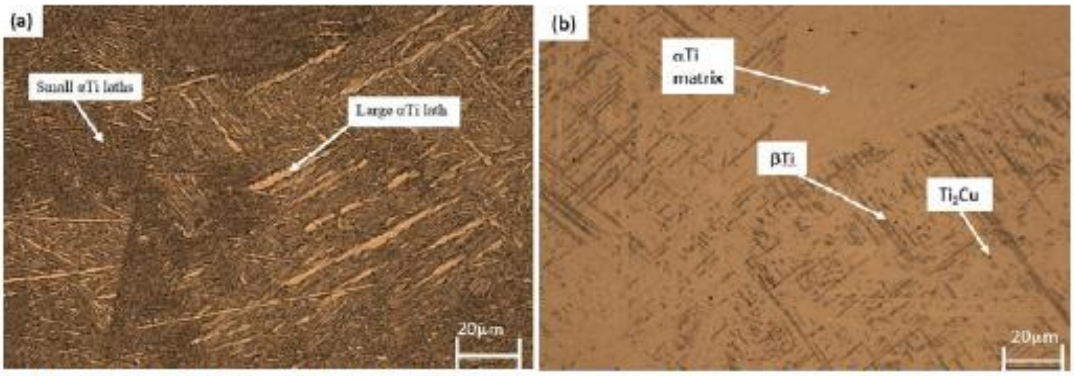

Figure 3: Optical micrographs of as-cast: (a) Ti-8Nb-4Zr showing clusters of αTi laths within prior βTi grains and (b) Ti-8Nb-4Zr-5Cu (wt%) showing βTi, αTi and Ti_2Cu phases

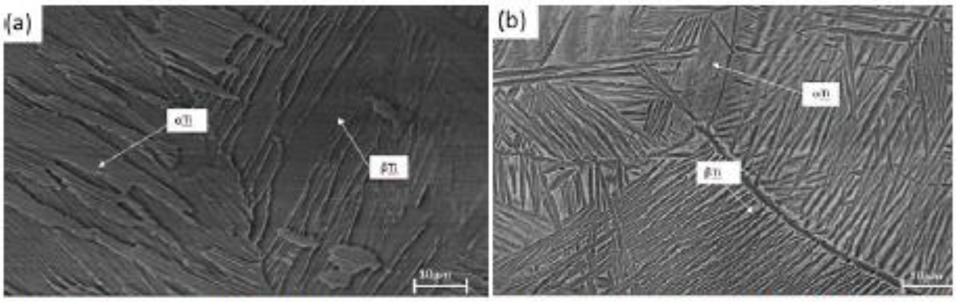

Figure 4: SEM-BSE images of as-cast: (a) Ti-6Ta-1.5Zr (wt%) and (b) Ti-6Ta-1.5Zr-5Cu showing thick and thin (αTi) lamellae, growing from prior βTi grain boundaries

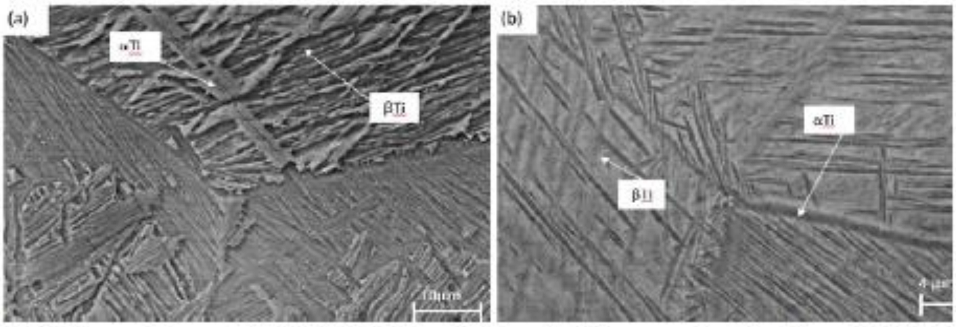

Figure 5: SEM-BSE images of as-cast: (a) Ti-6Ta-1.5Zr-0.2Ru (wt%) showing light contrast plate-like αTi, and (b) Ti-6Ta-1.5Zr-0.2Ru-5Cu showing parallel αTi laths growing from prior βTi grain boundaries

The αTi lamellae growing from the βTi grain boundaries into the matrix were present mostly in the alloys without Cu (Figures 4a and 5a). With Cu additions the microstructures (Figures 4b and 5b) exhibited needle-like and parallel αTi plates, grown from the prior βTi and into the matrix. Higher magnification had to be used to see the αTi plates in Ti-6Ta-1.5Zr-0.2Ru-5Cu (Alloy 3) compared to other alloys. The EDX analyses showed that the alloys without Cu had coarser αTi lamellae with more Ta, whereas the alloys with Cu had parallel αTi plates with more Ta and Cu than the nominal composition.

Figure 6 shows Alloy 4 (Ti-2Ta-8Mo-8Sn) with and without Cu. The microstructure was apparently single-phase cored dendritic, and any second phase was in a small proportion, and could not be analysed accurately by EDX.

3.2 Thermo-mechanical testing

Hot deformation behaviour of the as-received Ti-6Al-4V reference material and Ti-10.1Ta-1.7Nb-1.6Zr alloys was evaluated and Figure 7 shows the stress-strain curves obtained from uniaxial compression testing. The microstructures as a function of deformation temperature and strain rates are shown in Figures 8-11. The strain rates for Ti-6Al-4V were higher at both temperatures compared to Ti-10.1Ta-1.7Nb-1.6Zr. For 10 s^{-1} strain rate the Ti-6Al-4V at 950 °C was higher than 0.1 s^{-1} strain rate.

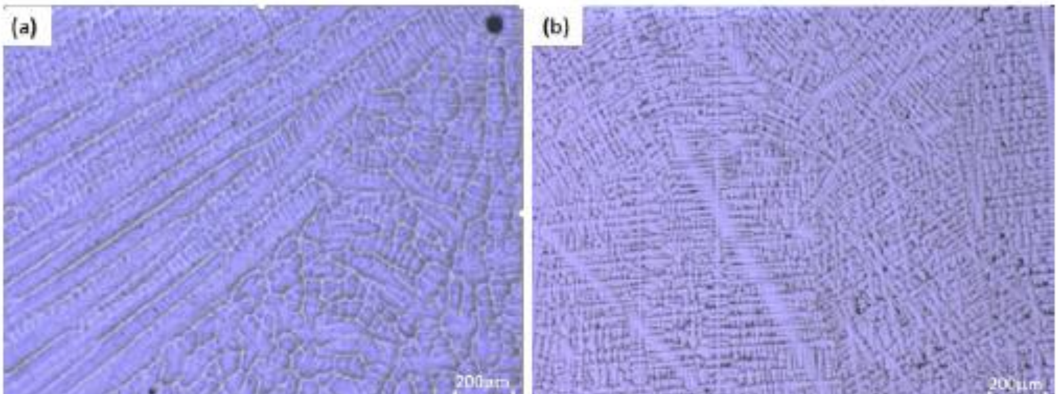

Figure 6: Optical micrographs of as-cast: (a) Ti-2Ta-8Mo-8Sn and (b) Ti-2Ta-8Mo-8Sn-5Cu (wt%) showing mainly a cored dendritic structure, with small proportions (Ti_2Cu)

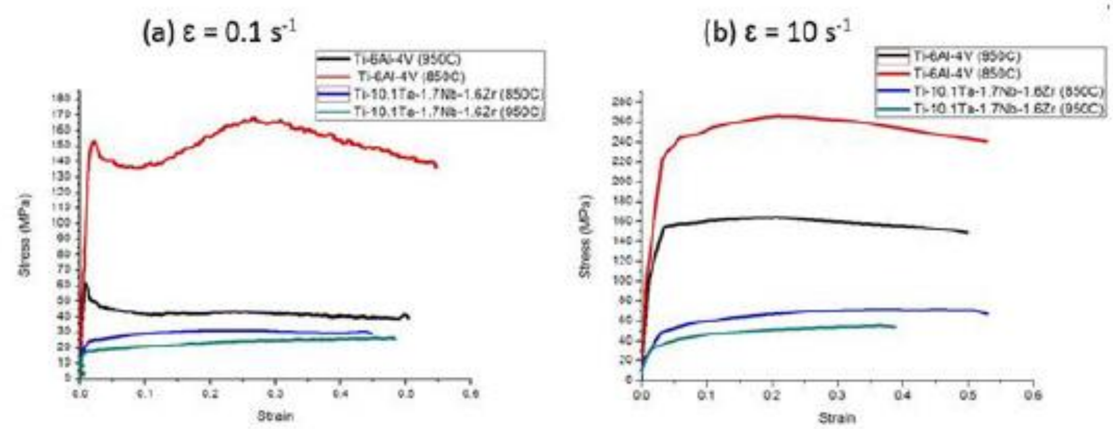

Figure 7: Stress-strain curves of the as-received Ti-6Al-4V and Ti-10.1Ta-1.7Nb-1.6Zr (wt%) alloys deformed at 850 °C and 950 °C, at: (a) 0.1 s^{-1} and (b) 10 s^{-1} strain rates

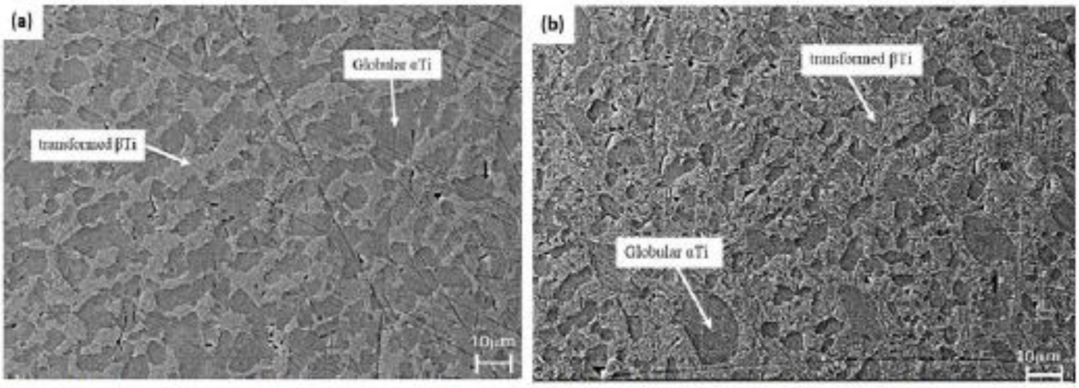

Figure 8: SEM-BSE images of Ti-6Al-4V deformed at 0.1 s^{-1} strain rate at: (a) 850 °C and (b) 950 °C, showing βTi matrix (light contrast) and αTi globules (dark contrast)

The SEM-BSE images (Figure 8) show αTi globules within the transformed βTi matrix. At 950 °C, the αTi globules decreased in size. There were coarser αTi globules and grain coarsening at 850 °C (Figure 9a), and finer αTi globules at 950 °C (Figure 9b).

At 850 °C, TTNZ comprised coarse αTi particles (Figure 10a), whereas at 950 °C there were fine αTi particles (Figure 10b). Figure 11 shows microstructures of globular αTi grains, and the βTi matrix. The αTi globules appeared to be coarser at 950 °C (Figure 11b), than at 850 °C (Figure 11a).

4. Discussion

4.1 α + β alloys

As the phase proportions for Ti-6Al-4V (Figure 1) and Ti-6Ta-1.5Zr-0.2Ru (Figure 2a) were similar, it is expected that Ti-6Ta-1.5Zr-0.2Ru could replace Ti-6Al-4V and have similar properties.

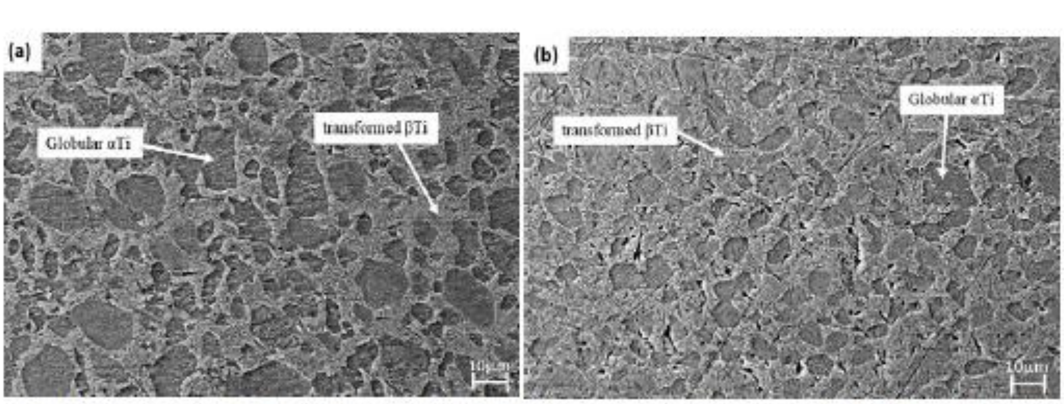

Figure 9: SEM-BSE images of Ti-6Al-4V (wt%) deformed at 10 s^{-1} strain rate at: (a) 850 °C and (b) 950 °C, showing βTi-matrix (light contrast) and αTi globules (dark contrast)

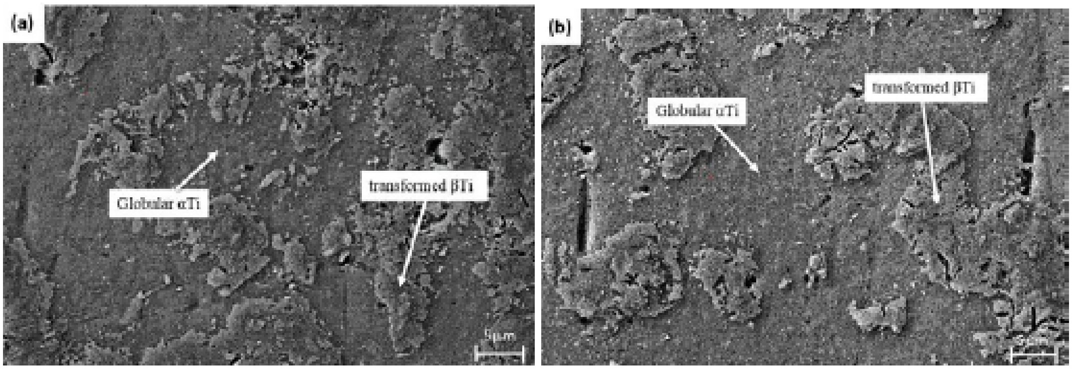

Figure 10: SEM-BSE images of Ti-10.1Ta-1.7Nb-1.6Zr (wt%) deformed at 0.1 s^{-1}strain rate at: (a) 850 °C and (b) 950 °C, showing αTi particles in βTi matrix

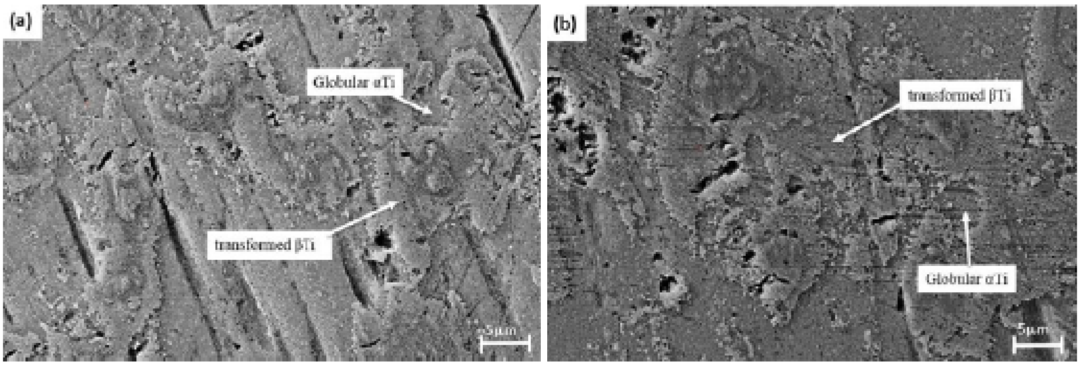

Figure 11: SEM-BSE images of Ti-10.1Ta-1.7Nb-1.6Zr (wt%) deformed at 10 s^{-1}strain rate at: (a) 850 °C and (b) 950 °C, showing αTi particles and βTi matrix

The phase proportion diagram in Figure 2b shows that the αTi phase proportions decreased slightly and Ti_2Cu formed when Cu was added to the alloy. The βTi phase proportion was not affected by the addition of Cu.

Alloys 1-3 (Table 1) had similar morphologies, although Alloy 4 had a dendritic microstructure. Due to Alloy 4 not being clearly two-phase (there could have been a small amount of a second phase, but insufficient for the microstructure targeted), no further analysis was done on that alloy. Possibly, the alloy solidified as apparently single-phase because of the high cooling rate from arc-melting, which was not at equilibrium, whereas Thermo-Calc shows equilibrium phases and compositions. However, this shows that Alloy 4 was more cooling-rate dependent than the other alloys. Alloys 1-3 with Cu additions formed the Ti_2Cu phase, which would improve the antibacterial properties of the alloys (Jin et al, 2005) and make them suitable candidates to replace the existing Ti alloys.

4.2 Thermo-mechanical testing

The thermo-mechanical results for Ti-10.1Ta-1.7Nb-1.6Zr showed that ductility improved at higher temperature (950 °C) and lower strain rate (0.1 s^{-1}), and at lower temperature (850 °C) and higher strain rate (10 s^{-1}). The ductility of Ti-6Al-4V improved at lower deformation temperature, consistent with Prozesky et al. (2017) and Dos Santos et al. (2017). An increased strain rate (10 s^{-1}) led to increased flow stress, compared to 0.1 s^{-1}, and increasing the temperature (950 °C) gave reduced flow stress for both Ti-6Al-4V and Ti-10.1Ta-1.7Nb-1.6Zr alloys. The Ti-6Al-4V alloy had higher flow stress (170 MPa at 0.1 s^{-1} and 270 MPa at 10 s^{-1}) than Ti-10.1Ta-1.7Nb-1.6Zr (35 MPa 0.1 s^{-1} and 75 MPa at10 s^{-1}) at 850 °C. The Ti-6Al-4V and Ti-10.1Ta-1.7Nb-1.6Zr alloys had steady-state flow stress at 950 °C, and continuous flow softening at 850 °C for both 0.1 s^{-1} and 10 s^{-1} strain rates.

The Ti-6Al-4V alloy deformed at 850 °C and 0.1 s^{-1} had elongated αTi laths (Figure 6a), which grew into globular α grains at 950 °C and 10 s^{-1} (Figure 7b). This suggested that globularisation of αTi occurred from the higher strain rate and increased deformation temperature. Thus, a higher deformation temperature and strain rate gave a finer Ti-6Al-4V microstructure. The deformed Ti-6Al-4V microstructures were different from the initial microstructure, which were fully αTi lamellar microstructures.

The microstructures of the TTNZ alloy before and after deformation (Figures 8 and 9) were similar, with globular αTi grains. At 850 °C and 10 s^{-1} (Figure 9a), and at 950 °C and 0.1 s^{-1} (Figure 8b), there were finer αTi globules, similar to the initial microstructure. The coarser αTi globules at 850 °C and 0.1 s^{-1} (Figure 8a) and 950 °C and 10 s^{-1} (Figure 9b) suggested that a combination of lower temperature and higher strain rate, and/or a higher temperature and lower strain rate, would produce finer microstructures.

5. Conclusions

The Ti-8Nb-4Zr alloys studied had bimodal microstructures comprising αTi laths in a transformed β matrix. Alloys without Cu (Alloys 2 and 3) had coarser αTi lamellae with more Ta, whereas the alloys with Cu had parallel αTi plates with higher Ta and Cu contents. All the alloys with Cu formed sufficient Ti_2Cu, except for Alloy 4 which had only small amounts. Alloy 4 was the only unsuccessful alloy, as it did not have a sufficientyly high proportion of the second phase as the other alloys.

Higher flow stresses were obtained at higher strain rates (10 s^{-1}) and lower temperature (850 °C). At 850 °C, the Ti-6Al-4V alloy had higher flow stresses (170 MPa at 0.1 s^{-1} and 270 MPa at10 s^{-1}) than Ti-10.1Ta-1.7Nb-1.6Zr (35 MPa 0.1 s^{-1} and 75 MPa at10 s^{-1}). The Ti-6Al-4V and Ti-10.1Ta-1.7Nb-1.6Zr alloys had steady-state flow stresses at 950 °C, and continuous flow softening at 850 °C for both 0.1 s^{-1} and 10 s^{-1} strain rates.

Acknowledgements

This work was supported by the National Research Foundation [Grant numbers 41292, STNT170905261815].

Contribution of each author

K Dyal Ukabhai undertook calculations, experiments and wrote the paper; K T Nape, L Spotose and M Mavundla undertook calculations and experiments; I A Mwamba gave advice on some aspects and was the Mintek co-supervisor; M O Bodunrin gave advice on calculations and thermomechanical simulations; L H Chown co-supervised all the students, hosted the postdoctoral fellow and helped with the interpretation; and L A Cornish conceived the overall project, co-supervised the students, helped with interpretation and checked the writing of the paper.

References

1. Bodunrin M.O. 2018. Hot deformation and corrosion behaviour of low-cost α+β titanium alloys with aluminium, vanadium and iron additions, School of Chemical and Metallurgical Engineering, University of the Witwatersrand, Johannesburg. PhD Thesis, *1-293*.
2. Bundy K J, Marek M and Hochman R F. 1983. In vivo and in vitro studies of the stress-corrosion cracking behaviour of surgical implant alloys. Journal of Biomedical Materials Research *17, 467-87*.
3. Burnstein A, Reilly D and Martens M. 1976. Aging of bone tissue: mechanical properties. Journal of Bone and Joint Surgery *58 (1), 82-86*.
4. Calin M, Zhang L C and Eckert J. 2007. Tailoring of microstructure and mechanical properties of a Ti-based bulk metallic glass-forming alloy. Scripta Materialia *57 (12), 1101-1104*.
5. Choubey A, Balasubramaniam R and Basu B. 2004. Effect of replacement of V by Nb and Fe on the electrochemical and corrosion behaviour of Ti–6Al–4V in simulated physiological environment. Journal of Alloys and Compounds *381 (1), 288-294*.
6. Dos Santos M W B. 2017. Investigation of the mechanical behaviour and microstructural evolution of titanium alloys under superplastic and hot forming conditions. Ecole des Mines d'Albi-Carmaux Polytechnic School of Engineering of the University of Sao Paulo (EPUSP).
7. Eisenbarth E, Velten D, Müller M, Thull R and Breme J. 2004. Biocompatibility of β-stabilizing elements of titanium alloys. Biomaterials *25, 5705-13*.
8. Geetha M, Singh A K, Asokamani R and Gogia A K. 2009. Ti based biomaterials, the ultimate choice for orthopaedic implants – A review. Progress in Materials Science *54 (3), 397-425*.
9. Jha B K and Kumar V. 2010. Role of thermo-mechanical simulation in the development of special steel products. Proceedings of National Conference and 2nd Gleeble User Workshop RDCIS Ranchi 1-10.
10. Jin L G X, Liu E, Yu F, Shu X and Wang H. 2015. Microstructure, corrosion and tribological and antibacterial properties of Ti-Cu coated stainless steel. Journal of the Mechanical Behaviour of Biomedical Materials *50, 23–32*.
11. Khan W, Marew T and Kumar N. 2006 Immobilization of drugs and biomolecules on in situ copolymerized active ester polypyrrole coatings for biomedical applications. Biomedical Materials *1 (4), 235-241*.
12. Kuroda D, Niinomi M, Morinaga M, Kato Y and Yashiro T. 1998. Design and mechanical properties of new β type titanium alloys for implant materials, A Structure and Material Properties, Microstructural Process. Materials Science and Engineering A *243, 244-249*.
13. Li Y, Yang C, Zhao H, Qu S, Li X and Li Y. 2014. New developments of Ti-based alloys for biomedical applications. Journal of Materials *7 (3), 1709-1800*.
14. Lindahl O and Lindgren A G H. 1967. Cortical bone in man: II. Variation in tensile strength with age and sex. Acta Orthopaedica Scandinavica *38, 141-147*.
15. Meng Q, Guo S, Liu Q, Hu L and Zhao X. 2014. A β-type TiNbZr alloy with low modulus and high strength for biomedical applications. Progress in Natural Science: Materials International *24, 157-162*.
16. Mitragotri S and Lahann J. 2009. Physical approaches to biomaterial design. Nature Materials *8, 15-23*.
17. Navarro M, Michiardi A, Castaño O and Planell J A. 2008. Biomaterials in orthopaedics. Journal of the Royal Society Interface *5 (27), 1137-1158*.
18. Okazaki Y and Gotoh E. 2005. Comparison of metal release from various metallic biomaterials in vitro. Biomaterials *26 (1), 11-21*.
19. Persson G R and Renvert S. 2014. Cluster of bacteria associated with peri-implantitis. Clinical Implant Dentistry and Related Research *16 (6), 783-793*.
20. Prozesky D J, Bodunrin M O and Chown L H. 2017. Hot-deformation behaviour of α+β Ti-Al-V-Fe experimental alloys. AIP Conference Proceedings. 1896 1160019-1-6 https://doi.org/10.1063/1.5008194.
21. Schutz R W. 1996. Ruthenium enhanced titanium alloys. Platinum Metals Review *40 (2), 54-61*.
22. Shaikh A A, Kashyap B P and Chauthai A. 2015. Identification of Favorable Hot Working Condition for Ti-6Al-4V Alloy. National Conference on Thermo-mechanical processing of Steels & 5th Gleeble User Workshop, India, *78-91*.
23. Sidambe A T. 2014. Biocompatibility of advanced manufactured titanium implants—a review. Materials *7 (12), 8168-8188*.
24. Stenlund P, Omar O, Brohede U, Norgren S, Norlindh B, Johansson A, Lausmaa J, Thomsen P and Palmquist A. 2015. Bone reponse to a novel Ti-Ta-Nb-Zr alloy. Acta Biomaterialia *20, 165-175*.
25. Nang S, Banerjee R, Stechschulte J and Fraser H L. 2005. Comparison of microstructural evolution in Ti-Mo-Zr-Fe and Ti-15Mo biocompatible alloys. Journal of Materials Science: Materials in Medicine *16 (7), 679-685*.
26. Tamilselvi S, Raman V and Rajendran N. 2006. Corrosion behaviour of Ti–6Al–7Nb and Ti–6Al–4V ELI alloys in the simulated body fluid solution by electrochemical impedance spectroscopy. Electrochimica Acta *52 (3), 839-846*.
27. Vanderhasten M. 2008. Ti-6Al-4V: Deformation map and modelisation of tensile behavior.
28. Katholieke Universiteit Leuven. Doctoral Thesis, *1-150*.
29. Zhang L C, Kim K B, Yu P, Zhang W Y, Kunz U and Eckert J. 2007. Amorphization in mechanically alloyed (Ti, Zr, Nb)– (Cu, Ni)–Al equiatomic alloys. Journal of Alloys and Compounds *428, 157-163*.
30. Zhang L C, Klemm D, Eckert J, Hao Y L and Sercombe T B. 2011. Manufacture by selective laser melting and mechanical behaviour of a biomedical Ti–24Nb–4Zr–8Sn alloy. Scripta Materialia *65 (1), 21-24*.

NEW Ti-Cu BASED ALLOYS FOR BIOMEDICAL APPLICATIONS

L. Spotose and L.A. Cornish

School of Chemical and Metallurgical Engineering, and DSI-NRF Centre of Excellence in Strong Materials, University of the Witwatersrand, Johannesburg

Biometallic materials are used in different parts of the body for biological artificial replacement and to improve lives[1]. The prerequisite for these metallic implants is low elastic modulus, good biocompatibility, high strength and corrosion resistance, and the ability to inactivate bacteria. Commercially pure titanium and its alloys have been extensively utilized as suitable biometallic implants due to their coherent properties with hard tissue.

The mechanical properties of Ti alloys depend on the microstructure, including volume fraction of specific phases, grain size and distribution and type of precipitates. The Ti-6Al-4V alloy is the most widely-used (α+β) alloy due to its superior strength, corrosion resistance and good integration with the bone (osseointegration)[3]. However, its high elastic modulus causes stress-shielding to the adjacent bone. The continuous use of Ti-6Al-4V alloys poses concerns due to adverse tissue reaction caused by V ions. Aluminum has the potential to cause Alzheimer's disease. This has encouraged the development of metallic alloys with nontoxic and allergy-free elements.

Fluids in the oral environment may cause metallic implants to corrode, which can trigger bacterial colonization leading to tissue inflammation and peri-implantitis[4]. Then progressive bone loss occurs around an osseointegrated implant. Copper additions to Ti alloys inactivate bacteria on implants[2], which is associated with the precipitation of Ti_2Cu[4].

Suitable compositions were identified using Thermo-Calc and the TTTI3 database, with similar phase proportions to Ti-6Al-4V. Copper was added at 5 wt% since this is the minimum for antimicrobial properties[4]. Samples of 10g were made for: Ti-6Ta-1.5Zr, Ti-6Ta-1.5Zr-0.2Ru, Ti-6Ta-1.5Zr-5Cu and Ti-6Ta-1.5Zr-0.2Ru-5Cu (mass%). The mixed powders were compacted and arc melted to make buttons, which were sliced down the centre, and mounted in MultiFast Black resin. Samples were prepared metallographically, and polished with colloidal silica and hydrogen peroxide (5:1) solution, then etched with Kroll's reagent. The microstructures were examined using a ZEISS Sigma 300 VP scanning electron microscope.

The microstructures were (αTi) lamellae growing from the prior (βTi) grain boundaries (Fig. 1). The Ti-6Ta-1.5Zr-0.2Ru had light contrast retained (βTi) and dark contrast (αTi) phases (Fig. 1b). More (αTi) with dark contrast with small (βTi) and small very light Ti_2Cu phases were found in the Ti-6Ta-1.5Zr-5Cu (Fig. 1c). Traces of original light contrast dendrites and dark contrast α phase, and small very light Ti_2Cu precipitates seen in the Ti-6Ta-1.5Zr-0.2Ru-5Cu (Fig, 1d). The EDX analyses showed that light contrast phases had higher Ta contents. High Cu contents confirmed the Ti_2Cu precipitates. The XRD patterns of Ti-6Ta-1.5Zr and Ti-6Ta-1.5Zr-0.2Ru only showed peaks of (αTi) phase, and both Cu-containing alloys had peaks of (αTi), (βTi), and Ti_2Cu phase.

From the measured compositions in the experimental alloys, the targeted phases were found, including Ti_2Cu precipitates for antibacterial properties after Cu additions.

References
1. Geetha, M., Singh, A.K., Asokamani, R., Gogia, A.K., (2009) Prog. Mater. Sci. 54(3), 397.
2. Fowler, L., Engqvist, H. and Öhman-Mägi, C., (2019) Materials. 12(22), 1.
3. Li, Y., Yang, C., Zhao, H., Qu, S., Li, X. and Li, Y. (2014) Materials. 7(3), 1709.
4. Zhang, E., Ren, J., Li, S., Yang, L., Qin, G. (2016) Biomed. Materials. 11(6), 1.

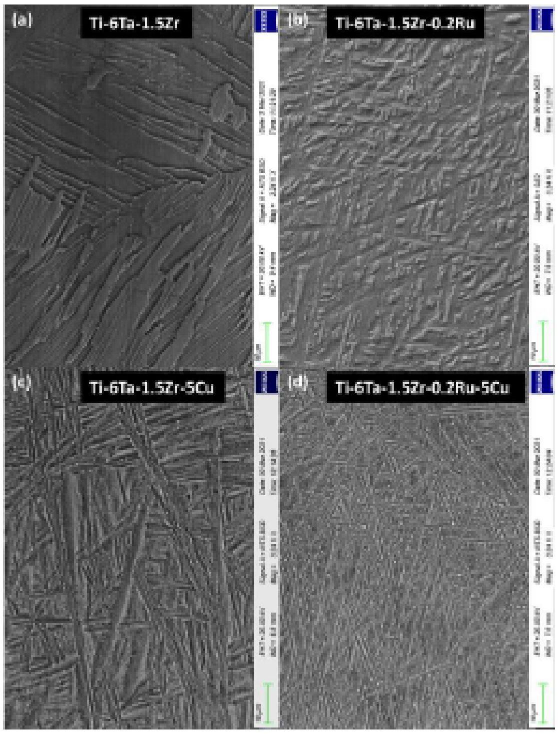

Figure 1. SEM-BSE images of the as-cast alloys: (a) Ti-6Ta-1.5Zr showing (αTi) lamellae growing into the matrix, (b) Ti-6Ta-1.5Zr-0.2Ru with retained (βTi) and dark contrast (αTi), (c) Ti-6Ta-1.5Zr-5Cu with irregular dark contrast (αTi) and small very light Ti_2Cu precipitates, and (d) Ti-6Ta-1.5Zr-0.2Ru-5Cu showing needle-like laths and small very light Ti_2Cu precipitates.

Corresponding author: *2187508@students.wits.ac.za*

A MICROSTRUCTURAL ANALYSIS OF A Ti-Ta-Cu-Nb-Zr ALLOY

N.G. Hashe[1], L. Fowler[2], W.E. Goosen[3], S. Norgren[2], N.D. Masia[4], L.A. Cornish[4], C. Öhman-Mägi[2], L.H. Chown[4], S. Magadla[1], K.T. Nape[4], M. Mavundla[4] and L. Spotose[4]

[1]Department of Physics, Nelson Mandela University, Port Elizabeth, [2]Department of Engineering Science, Uppsala University, Uppsala, Sweden, [3]CHRTEM, Nelson Mandela University, Port Elizabeth, [4]School of Chemical and Metallurgical Engineering, and DST-NRF Centre of Excellence in Strong Materials, hosted by the University of the Witwatersrand, Johannesburg

Titanium and its alloys are used in the medical industry as implants because of their biocompatibilities and excellent mechanical and physical properties[1]. The Ti-6Al-4V alloy is used as an implant material due to its high corrosion resistance and excellent biocompatibility[1]. However, there are concerns about the toxicity of aluminium and vanadium[2]. The other concern is the formation of the adherent biofilms around the surface area of the implants[3]. Therefore, the current research is aimed at replacing V and Al with Ta, Nb and Zr to produce a biocompatible alloy with antibacterial[4] and osseointegrative properties that has a similar microstructure to that of an alpha-beta Ti-6Al-4V alloy.

The Ti-10.1Ta-1.7Nb-1.6Zr (wt%) alloy produced by Stenlund *et al.*[5] was studied further. Titanium and Zr sponges were mixed with Ta and Nb wires and compressed into a 7 kg lump, which was melted four times in vacuum in an Electron Beam furnace for homogeneity. The Ti-10.1Ta-1.7Nb-1.6Zr alloy was mixed with 3 mass% Cu and the mixture was melted five times in a custom built arc-furnace. Annealing was done in a sealed quartz-ampoule at 1.333 mbar (after flushing) in a conventional furnace. Heat treatment was done at 980 °C for 10 hours, followed by 798 °C for 6 hours, with a final rapid salt-brine water quench. The annealing temperatures were chosen to obtain the alpha Ti (hcp) and beta Ti (bcc)[5]. After heat treatment, the samples were prepared metallographically and analysed by scanning electron microscopy (SEM) and X-ray diffraction (XRD).

Backscattered SEM imaging (Fig. 1) shows that the microstructure of the Ti-Ta-Cu-Nb-Zr alloy was lamellar, which are reported to have a high fatigue crack propagation resistance and high fracture toughness[6]. There were small, irregular regions of a much darker phases (indicated by a white arrow) , within the dark phase (indicated by a white star). Energy dispersive spectroscopy (EDX) showed the light contrast phase (indicated by a black arrow) had more Ta and Cu, with less Nb than the dark phase. However, the Nb content was less than 1 mass%, so the results were too near the detection limit to be reliable. The dark phase was identified as alpha Ti since it had more Ti. The small regions of the darkest phase were too small to analyse accurately with EDX.

The XRD patterns only showed alpha-Ti (Fig, 2). The pattern for the heat treated samples also showed apparent preferred orientation, which was surprising considering that the pattern from the as-cast sample was more random. Further work is required to identify the darkest phase, and XRD needs to be repeated with a more suitable X-ray source in order to quantify the phases present in the material.

References:

1. Geetha, M. *et al.* (2009) Prog. Mat. Sci. 54, 397.
2. Niinomi M. and Nakai M. (2011) Int. J. Biomater. 2011, 1.
3. Lorenzetti, M. *et al.* (2015) Appl. Mater. Interfaces 7, 1644.
4. Magadla, S. *et al.* (2019) Euromat 2019 Abstracts, 2288.
5. Stenlund, P. *et al.* (2015) Acta Biomat. 20, 165.
6. Filip, R. *et al.* (2003) J. Mat. Proc. Techn. 133, 84.

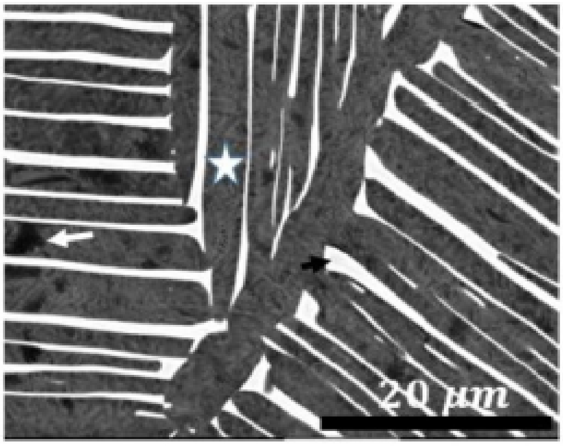

Figure 1. SEM-BSE image showing the typical microstructure of Ti-Ta-Nb-Zr-Cu alloy with three phases.

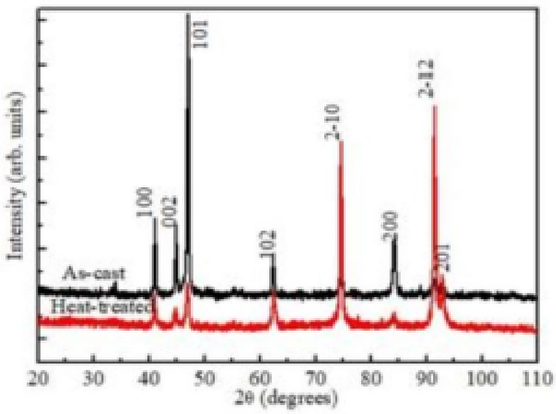

Figure 2. XRD patterns of the as-cast and heat treated Ti-Ta-Cu-Nb-Zr alloy, showing only alpha-Ti.

Corresponding author: nobom.hashe@mandela.ac.za